Geodetic Imaging of Fault System Activity

Geodetic Imaging of Fault System Activity

A dissertation presented

by

Eileen Louise Evans

to

The Department of Earth and Planetary Sciences

in partial fulfillment of the requirements

for the degree of

Doctor of Philosophy

in the subject of

Earth and Planetary Sciences

Harvard University

Cambridge, Massachusetts

May 2014

Dissertation Advisor: Professor Brendan J. Meade Eileen Louise Evans

Geodetic Imaging of Fault System Activity

Abstract

Geodetic observations provide kinematic constraints on the behavior of tectonically active fault systems. Estimates of earthquake cycle activity derived from these constraints may depend on modeling assumptions and/or regularization of a geodetic inverse problem, which is often poorly conditioned. Common model assumptions may affect kinematic solutions and conclusions about physical properties of faults and fault zones. For example, within a geometrically complex fault system, parameterization of nearby faults may affect slip estimates on an individual fault. In addition, fault slip models are often regularized by assuming that slip varies smoothly in space, which may artificially smear slip estimates beyond physical boundaries. As an alternative to smooth regularization, the applied mathematics field of compressed sensing provides a suite of methods for recovering sparse solutions. Applied to GPS observations of the 2011 Tohoku earthquake, compressed sensing algorithms enable imaging of spatially localized slip during and following the earthquake, and identification of a sharp boundary between coseismic and postseismic slip. Similar algorithms recover quantized solutions and may be applied to models of plate boundary deformation. Beginning with a dense array of tectonic micro-plates bounded by mapped faults in North America, these methods can be used to detect coherent motions of groups of micro-plates behaving as larger active blocks, effectively quantifying the complexity of North America plate boundary deformation. By improving our ability to identify and compare kinematic constraints on

earthquake cycle processes, we are able to characterize the spectrum of earthquake cycle behaviors and gain a deeper understanding of earthquake phenomenology and physics.

Contents

List of Figures

List of Tables

Acknowledgements

I would like to express my sincere gratitude to those who have supported my work throughout the years. First, I am grateful to my advisor Brendan Meade for the opportunity to pursue this research and for his guidance over the past six years. Brendan's enthusiasm for earthquake science has inspired and motivated me since we began working together. His wealth of knowledge and acute scientific insight constantly challenge me to become a better scientist. I thank him for the years he has spent contributing to my education and helping me grow into a rigorous and scholarly research scientist.

Many other scientists have provided valuable assistance towards my research. I would like to thank the members of my thesis committee: John Shaw, James Rice, and Miaki Ishii for their thoughtful comments and help on my dissertation, and also for their help and insights throughout the past six years. I am also grateful to Richard O'Connell for his support of my research during my graduate career.

I am also truly fortunate to have been a member of the Active Tectonics research group. I am particularly grateful to Jack Loveless, who patiently taught me about inverse theory and block modeling. I also thank Meredith Langstaff for being a wonderful group-mate for our entire time at Harvard, and special thanks to Phoebe Robinson for being a great colleague and a great friend. Thanks especially to Bridget Mastandrea for keeping our

research group running smoothly. I am additionally grateful for our close involvement with the Shaw Structural Geology group. Thanks to current group members Kristian Bergen and Joe Stockmeyer, and past members Judith Hubbard and Amanda Hughes Kiser. Thanks also to my office mates Natalya Gomez, Carling Hay, Emmy Smith, and Uyanga Bold.

I am incredibly indebted to the Harvard University Department of Earth and Planetary Sciences for being my home away from home for the past six years. This department has allowed me to pursue my scientific curiosity among a remarkable collection of intelligent scientists who are also kind and fascinating people. This department has been the source of numerous lasting friendships and countless happy memories. For encouraging this supporting and friendly environment, I thank all the professors, staff, and students, especially Sarah Colgan, Chenoweth Moffat, and Maryorie Grande.

Thank you to my friends and family who have provided love and support throughout these six years. Thank you to everyone I have been lucky enough to be friends with during my time at Harvard, including Allie Gale, Rita Parai, Shannon Koplitz, and Eloise Marais. Thank you to Mom, Dad, and Ian for your endless encouragement and patience, especially Dave, for introducing me to Earth Science. Finally, thank you to Kevin for being there for me every step of the way.

Chapter 1

Introduction

The goal of this work is to provide quantitative kinematic constraints on the behavior of tectonically active fault systems, based on geodetic observations of earthquake cycle activity. Imaging the kinematic behavior of a fault or fault system allows us to make predictions that can be tested against other observables and hypotheses about fault mechanics. However, common model assumptions, including regularization of poorly conditioned geodetic inverse models, may affect kinematic solutions and conclusions about physical properties of faults and fault zones. By identifying and quantifying the influence of these assumptions, we can improve our ability to rigorously test scientific hypotheses and gain a deeper understanding of earthquake phenomenology and physics.

The precision and density of modern geodetic observations provide an unprecedented opportunity for understanding the kinematics of fault systems relating to seismic hazard potential and crustal dynamics. Geodetic observations, such as the global positioning system (GPS), record surface deformation due to earthquake cycle processes. In the last several decades, advancements in geodetic observation techniques have matured to allow the measurement of deformation with precision better than 1 mm/yr. In addition, the number of

GPS stations has increased dramatically in many regions of tectonic interest: Japan operates an array of about 1000 continuous GPS stations, and there are almost 2000 continuous GPS stations in Western North America. Continuous GPS stations allow us to observe surface deformation throughout the earthquake cycle.

Interpreting geodetic observations in terms of earthquake cycle kinematics requires models of how faults and fault systems deform the earth's crust. In the interseismic period of the earthquake cycle, surface deformation is the result of both plate motion (block translation) and smooth interseismic strain accumulation due to locked faults. Within a complex fault system, the signals due to interseismic strain accumulation on multiple faults may overlap. Models of an individual fault in the system must rigorously account for these effects by interpreting geodetic observations within a three-dimensional kinematically consistent block model. Ensuring kinematic consistency within the fault zone avoids introducing slip artifacts that limit the interpretability of the final model.

Coseismic geodetic observations record surface displacements due to an earthquake, and can be used to constrain models of earthquake slip on the fault. Fault slip models are often regularized by assuming that slip varies smoothly in space, which may artificially smear slip estimates beyond physical boundaries. As an alternative to smooth regularization, the applied mathematics field of compressed sensing provides a suite of methods for recovering sparse solutions. Applied to coseismic GPS observations, compressed sensing algorithms enable imaging of spatially localized slip during and following the earthquake. These methods provide unprecedented opportunities for comparing geodetic imaging results with other observables, because they provide a reproducible algorithmic means for defining a spatially

compact region of fault slip. In particular, understanding the relationship between coseismic slip during an earthquake and postseismic afterslip in the weeks to months following an earthquake has implications for the thermal and frictional behavior of subduction zones. So far, studies comparing coseismic and postseismic slip have been limited by the inability of smooth imaging methods to identify well defined slip boundaries. By identifying spatially compact slip regions in the co- and postseismic earthquake cycle regimes, compressed sensing methods allow us to test hypotheses about the behavior of subduction zones.

Similar compressed sensing methods may also be applied to kinematic block models of interseismic deformation. The number and geometry of microplates in a block model are typically hand selected, with boundaries representing a limited subset of the large number of potentially seismogenic faults. Integrated with interseismic GPS velocities, compressed sensing methods allow the most important faults to be selected algorithmically. Beginning with a three-dimensional block model that includes all mapped faults, a compressed sensing technique called total variation denoising detects the coherent motion of groups of microplates behaving as larger active blocks, based on interseismic GPS velocities. The ability to algorithmically identify the best kinematic model to describe interseismic deformation allows us to effectively quantify the complexity of a plate boundary and directly address long-standing debates about the nature of continental deformation.

This thesis is organized into five chapters including this Introduction. Chapter 2 presents an interseismic imaging study of the Hayward fault in the San Francisco Bay Area. We estimate spatially variable creep on the Hayward fault within a three-dimensional kinematically consistent block model to rigorously account for the complicated strain accumulation signa-

tures associated with nearby faults. We are able to image spatially variable creep on the Hayward fault that is consistent with independent observations of surface creep, historical seismicity, and geology. Chapters 3 and 4 present the results of imaging coseismic and postseismic slip due to the 2011 Tohoku earthquake. Using sparsity-based regularization techniques, we identify a sharp boundary between coseismic and postseismic slip at $\sim$45 km depth. This boundary may be interpreted as coincident with the transition from velocity strengthening to velocity weakening frictional behavior, providing insight into the thermal structure of the subduction zone. Sharp boundaries also allow us to test hypotheses about the role of stress transfer in promoting postseismic afterslip. Chapter 5 applies a similar sparsity based regularization technique (total variation denoising) to a kinematic block model of Western North America. This technique allows the most important faults to be selected algorithmically, and we are able to effectively quantify the complexity of the Pacific-North America plate boundary zone by reducing the total number of model blocks from 144 to 20. In this way, the observations guide the decision of which faults from the original fault map are most important, providing a deterministic strategy for approaching ambiguity in block model selection.

Chapter 2

Geodetic constraints on San Francisco Bay Area fault slip rates and potential seismogenic asperities on the partially creeping Hayward fault

The Hayward fault in the San Francisco Bay Area (SFBA) is sometimes considered unusual among continental faults for exhibiting significant aseismic creep during the interseismic phase of the seismic cycle while also generating sufficient elastic strain to produce major earthquakes. Imaging the spatial variation in interseismic fault creep on the Hayward fault is complicated due to the interseismic strain accumulation associated with nearby faults in the SFBA, where the relative motion between the Pacific plate and the Sierra block is partitioned across closely spaced sub-parallel faults. To estimate spatially variable creep on the Hayward fault, we interpret geodetic observations with a three-dimensional kinematically consistent block model of the SFBA fault system. Resolution tests reveal that creep rate variations with a length scale of < 15 km are poorly resolved below 7 km depth. In addition,

An amended version of this Chapter was published with John P. Loveless and Brendan J. Meade in the Journal of Geophysical Research–Solid Earth, Vol. 117, (B3), 2012.

creep at depth may be sensitive to assumptions about the kinematic consistency of fault slip rate models. Differential microplate motions result in a slip rate of 6.7 ± 0.8 mm/yr on the Hayward fault and we image along-strike variations in slip deficit rate at ∼15 km length scales shallower than 7 km depth. Similar to previous studies, we identify a strongly coupled asperity with a slip deficit rate of up to 4 mm/yr on the central Hayward fault that is spatially correlated with the mapped surface trace of the 1868 M_W=6.9–7.0 Hayward earthquake and adjacent to gabbroic fault surfaces.

2.1 Introduction

In the San Francisco Bay Area (SFBA), motion between the Pacific plate and Sierra Block is partitioned across 7 major subparallel right-lateral faults with <20 km spacing [e.g., Freymueller et al., 1999]. From west to east, these include the San Gregorio, San Andreas, Hayward, Rodgers Creek, Calaveras, Green Valley, and the Greenville faults (Figure 2.1). The Hayward fault lies in the center of the SFBA fault system accommodating ∼20% of the total slip budget [e.g., Graymer et al., 2002; Schmidt et al., 2005; d'Alessio et al., 2005], and has been interpreted as the SFBA fault most likely to rupture in a M_W=6.7 or larger earthquake in the next 20 years [2007 Working Group on California Earthquake Probabilities, 2008] based on paleoseismic estimates of earthquake recurrence intervals and geologic and geodetic fault slip rate estimates. The last major ($M_W \approx 7$) Hayward fault earthquake occurred in 1868, with a reported surface rupture from Fremont in the south to San Leandro in the north (Figure 2.1) [Lawson, 1908; Yu and Segall, 1996; Bakun, 1999; Toppozada and Branum, 2004].

The Hayward fault is both geometrically [Graymer et al., 2005; Waldhauser and Ellsworth, 2002; Hardebeck et al., 2007] and kinematically complex [Lienkaemper et al., 2001; Simpson et al., 2001; Schmidt et al., 2005]. Nearly vertical along most of its trace, the Hayward fault dips eastward south of Fremont, as illuminated by relocated seismicity [Waldhauser, 2002; Manaker, 2005; Hardebeck et al., 2007], and likely merges at depth with the Calaveras fault immediately to the east [Ponce et al., 2004; Waldhauser, 2002; Graymer et al., 2005]. Surface creep observations from creepmeters [Bilham and Whitehead, 1997] and alignment arrays [Lienkaemper et al., 2001; Simpson et al., 2001] show that sections of the Hayward fault creep aseismically with surface creep rates ranging from <4 mm/yr on the northern Hayward fault to 8 mm/yr near Fremont. Estimates of spatially variable creep on the Hayward fault from inversions of GPS and InSAR data [Bürgmann et al., 2000; Schmidt et al., 2005] suggest that the distribution of interseismic fault coupling is also spatially heterogeneous, ranging from 0 to 8 mm/yr over <15 km length scales both along strike and downdip. Dynamically driven models [e.g., Savage and Lisowski, 1993; Simpson et al., 2001; Malservisi et al., 2003] of creep on the Hayward fault have been interpreted to agree favorably with geodetically inferred estimates of creep at depth.

Imaging the interseismic creep on the Hayward fault is complicated because the geodetic observations that provide the greatest resolution of activity at depth [Schmidt et al., 2005] are also influenced by the overlapping interseismic elastic strain fields associated with each of the closely spaced faults of the SFBA fault system [e.g., Freymueller et al., 1999]. Thus, to some extent, estimates of Hayward fault creep at depth depend on assumptions about the behavior of the rest of the SFBA fault system. Previous geodetically constrained kinematic models

of Hayward fault behavior may be categorized into three classes: 1) those that incorporate spatially dense InSAR measurements near the Hayward fault but do not assume that slip rates are kinematically consistent [Schmidt et al., 2005], 2) those that assume SFBA fault slip rates are kinematically consistent but do not include spatially dense InSAR measurements near the Hayward fault [Murray and Segall, 2001; d'Alessio et al., 2005; Johnson and Fukuda, 2010] and 3) those that both assume SFBA fault flip rates are kinematically consistent and include InSAR measurements [Bürgmann et al., 2000].

Here we develop a kinematically consistent three-dimensional block model of the SFBA fault system constrained by both GPS and spatially dense InSAR observations that provide the greatest resolution of fault activity at depth. We simultaneously estimate microplate rotations, kinematically consistent fault slip rates, and spatially variable slip deficit at depth on the Hayward fault. This particular reference model is not constrained by a priori geologic slip rate constraints or surface creep measurements, so that the model may be tested against these observations. We perform checkerboard resolution tests on the Hayward fault within the three-dimensional SFBA block model to assess the resolving ability of the data and determine the extent to which creeping behavior can be imaged at depth. To understand how the assumption of kinematically consistent slip rates affects Hayward fault creep rate estimates, we develop a series of idealized two-fault deep dislocation models that may explain differences between this and some previous studies.

2.2 Interseismic deformation in fault systems

Interseismic deformation in fault systems such as the SFBA includes the contribution of earthquake cycle processes associated with multiple faults. The quasi-static earthquake cycle contribution from SFBA faults has been approximated with deep dislocation [Bürgmann et al., 2000; Schmidt et al., 2005], and block models [Murray and Segall, 2001; d'Alessio et al., 2005; Johnson and Fukuda, 2010]. In the deep dislocation formulation, the net surface velocity field resulting from a partially creeping fault such as the Hayward is described as the sum of the deep dislocation and creep contributions, $\tilde{\mathbf{v}}_{\text{net}} = \tilde{\mathbf{v}}_{\text{deep}} + \tilde{\mathbf{v}}_{\text{creep}}$. Partial creep refers to aseismic fault creep at rates at or below the long term slip rate.

In this study, we estimate partial creep on the Hayward fault in terms of slip deficit within a kinematically consistent block model of the SFBA fault system, assuming steady state interseismic behavior, similar to previous studies of subduction zone environments [e.g., Wallace et al., 2004; Bürgmann et al., 2005; Loveless and Meade, 2010; McCaffrey, 2009]. In the block model formulation, the upper crust is divided into microplates bounded by faults, and fault slip rates are linearly proportional to the differential rotation rates at block boundaries, so that slip rates are implicitly kinematically consistent [Matsu'ura et al., 1986; Bennett et al., 1996; Souter, 1998; McCaffrey, 2002; Meade and Hager, 2005; Meade and Loveless, 2009]. Kinematic consistency is defined such that a path integral of motion (slip rates and plate rotations) across the plate boundary sums to the total relative tectonic plate motion, independent of path [Minster and Jordan, 1987; Humphreys and Weldon, 1994]. Interseismic fault slip rates are determined by the rotation rate of adjacent microplates [Souter, 1998], and the elastic contribution to the surface velocity field depends on the

degree of slip deficit along these faults [Meade and Hager, 2005]. In this formulation, the resulting velocity field due to a partially creeping fault is equal to the contribution from the total static block offset minus the contribution to the velocity field due to the elastic slip deficit, $\tilde{\mathbf{v}}_{\text{net}} = \tilde{\mathbf{v}}_{\text{block}} - \tilde{\mathbf{v}}_{\text{slip deficit}}$. Estimates of interseismic creep and slip deficit rates map into the other as $\dot{\mathbf{s}}_{\text{creep}} = \dot{\mathbf{s}}_{\text{long term}} - \dot{\mathbf{s}}_{\text{slip deficit}}$. We determine creep rates on the Hayward fault from directly estimated slip deficit rates. The particular linear block model formulation used here [Meade and Loveless, 2009] is similar to that used in other SFBA studies [Matsu'ura et al., 1986; Murray and Segall, 2001; d'Alessio et al., 2005] with the addition of spatially variable fault coupling on the Hayward fault, and without geologic fault slip rate assumptions [Johnson and Fukuda, 2010].

2.3 Block modeling with spatially variable fault coupling and InSAR observations

For this study we have modified the block model formulation [Meade and Loveless, 2009] to include InSAR observations. The linear block model formulation, explicitly stated for GPS velocities in terms of linear operators by Meade and Loveless [2009], interprets interseismic geodetic velocities, $\mathbf{v}_{\text{I}}$, as resulting from a combination of microplate or block rotations, $\mathbf{v}_{\text{B}}$, quasi-static earthquake cycle processes, $\mathbf{v}_{\text{E}}$, and residual velocities, $\mathbf{v}_{\text{r}}$:

$$\mathbf{v}_{\text{I}} = \mathbf{v}_{\text{B}} + \mathbf{v}_{\text{E}} + \mathbf{v}_{\text{r}} \tag{2.1}$$

A homogeneous internal strain rate may also be included in the velocity field decomposition, but since we do not estimate internal strain in this study, we do not include it

here. The discussion that follows extends, and requires, the mathematical framework detailed previously in Meade and Loveless [2009]. Velocities due to elastic earthquake cycle processes are modeled assuming that all faults are fully coupled between the surface and an inferred locking depth using rectangular dislocations [Okada, 1985] in a homogeneous elastic half space [e.g., Savage, 1983; Matsu'ura et al., 1986]. We describe these velocities, $\mathbf{v}_{\mathrm{CSD}}$, as resulting from interseismic elastic strain accumulation across a locked fault, represented by removing the coseismic slip deficit from the static block offset. Where geodetic data are sufficiently dense and/or where rectangular elements inadequately describe fault geometry, we incorporate a continuous mesh of triangular dislocation elements to allow coupling rate estimates on a smoothly interpolated three-dimensional fault surface. We simultaneously estimate elastic coseismic slip deficit on each of these triangular dislocation elements [Comninou, 1973; Jeyakumaran et al., 1992; Thomas, 1993; Meade, 2007]. Incorporating $\mathbf{v}_{\mathrm{CSD}}$ and the velocities due to slip on triangular dislocation elements, $\mathbf{v}_{\mathrm{TDE}}$ into equation 2.1 outlines the linear forward problem [Meade and Loveless, 2009].

$$\mathbf{v}_{\mathrm{I}} = \mathbf{v}_{\mathrm{B}} - (\mathbf{v}_{\mathrm{CSD}} + \mathbf{v}_{\mathrm{TDE}}) + \mathbf{v}_{\mathrm{r}} \tag{2.2}$$

We expand the formulation here to include InSAR line-of-sight measurements. Unlike GPS East-North-Up velocities, InSAR data record one component of interseismic velocity, $\widehat{\mathbf{v}}_{\mathrm{I}}$, in the satellite look direction. For the satellite data included in this study, the look vector has east, north, and up components given by $l = [0.389, -0.078, 0.918]$. To account for orbital baseline unknowns in the InSAR measurements, we simultaneously solve for a best fitting quadratic ramp from the data. We choose a quadratic ramp because InSAR

orbital errors are approximately quadratic in space [Zebker et al., 1994]. The solution does not change significantly with a linear ramp. We decompose the line-of-sight velocities, $\widehat{\mathbf{v}}_{\mathrm{I}}$, as in equation 2.2, considering line of sight velocities, $\widehat{\mathbf{v}}_{\mathrm{q}}$, due to the additional ramp parameter:

$$\widehat{\mathbf{v}}_{\mathrm{I}} = \widehat{\mathbf{v}}_{\mathrm{B}} - (\widehat{\mathbf{v}}_{\mathrm{CSD}} + \widehat{\mathbf{v}}_{\mathrm{TDE}}) + \widehat{\mathbf{v}}_{\mathrm{r}} + \widehat{\mathbf{v}}_{\mathrm{q}} \tag{2.3}$$

The velocity components defined in equation 2.3 are related to the estimated block model parameters using the linear operators defined by Meade and Loveless [2009], with the addition of the linear operator $\mathbf{P}_{\mathrm{L}}$, which converts East-North-Up velocities to a line-of-sight range change rate to ENU velocities based on the look vector l.

$$\mathbf{P}_{\mathrm{L}} = \begin{bmatrix} l_e & l_n & l_u & & 0 & 0 & 0 \\ & & & \ddots & & & \\ 0 & 0 & 0 & & l_e & l_n & l_u \end{bmatrix} \tag{2.4}$$

For each component of the velocity field decomposition, InSAR LOS velocities must be converted from XYZ velocities to East-North-Up velocities, and reduced to a line-of-site range change rate by pre-multiplying terms from Meade and Loveless [2009] by $\mathbf{P}_{\mathrm{L}}$. For example, the block rotation rate is explicitly written as

$$\widehat{\mathbf{v}}_{\mathrm{B}} = \mathbf{P}_{\mathrm{L}}\mathbf{P}_{\mathrm{V_S}}\mathbf{G}_{\mathrm{B_S}}\boldsymbol{\Omega} \tag{2.5}$$

in which $\mathbf{P}_{\mathrm{V_S}}$ is a geometric transformation that converts XYZ rotation velocities at InSAR observation locations into East-North-Up velocities; $\mathbf{G}_{\mathrm{B_S}}$ is the generalized matrix of partial derivatives for each InSAR observation point with respect to the rotation vector, and $\boldsymbol{\Omega}$

contains the elements of a Cartesian rotation vector. Finally we estimate a quadratic ramp to account for uncertainties in the orbital parameters assumed in InSAR processing. These uncertainties can map into the derived velocity field as a quadratic form varying in latitude and longitude [Zebker et al., 1994]. Because the line-of-sight contribution of the quadratic ramp is calculated in the look direction, we do not have to convert the ramp parameters to East-North-Up:

$$\widehat{\mathbf{v}}_{\mathrm{q}} = \mathbf{G}_{\mathrm{q}}\mathbf{q} \tag{2.6}$$

$\mathbf{G}_{\mathrm{q}}$ contains 6 columns for every InSAR line-of-sight observation for each coefficient in the quadratic ramp, and $\mathbf{q}$ is a 6-by-1 array containing the ramp coefficients.

In order to estimate block model parameters, we use a weighted least squares inversion to simultaneously estimate block rotations, $\mathbf{\Omega}^{\mathrm{est}}$, smoothed coupling on triangular dislocation elements, $\mathbf{t}^{\mathrm{est}}$:

$$\begin{bmatrix} \mathbf{\Omega}^{\mathrm{est}} \\ \mathbf{t}^{\mathrm{est}} \\ \mathbf{q} \end{bmatrix} = \left[\left(\mathbf{G}^{\top}\mathbf{W}\mathbf{G} \right)^{-1} \mathbf{G}^{\top}\mathbf{W} \right] \begin{bmatrix} \tilde{\mathbf{v}}_{\mathrm{GPS}} \\ \widehat{\mathbf{v}}_{\mathrm{SAR}} \\ \mathbf{s}_{\mathrm{obs}} \\ 0 \\ \mathbf{t}_{\mathrm{bc}} \end{bmatrix} \tag{2.7}$$

in which $\mathbf{G}$ is the generalized combined Jacobian relating the estimated parameters to GPS velocities, $\widehat{\mathbf{v}}_{\mathrm{SAR}}$, and a priori slip rate observations, $\mathbf{s}_{\mathrm{obs}}$. We additionally impose smoothing constraints on the mesh of triangular dislocation elements by minimizing the gradient of

the slip distribution. We select a smoothing value that maintains realistic coupling values. The vector $\mathbf{t}_{\mathrm{bc}}$ depends on the boundary conditions on the mesh of triangular dislocation elements. Relative data weights are determined by the weighting matrix $\mathbf{W}$:

$$\mathbf{W} = \begin{bmatrix} \mathbf{C}_{\mathrm{GPS}}^{-1} & 0 & 0 & 0 & 0 \\ 0 & \beta_{\mathrm{SAR}}\mathbf{C}_{\mathrm{SAR}}^{-1} & 0 & 0 & 0 \\ 0 & 0 & \beta_{\mathrm{obs}}\mathbf{C}_{\mathrm{obs}}^{-1} & 0 & 0 \\ 0 & 0 & 0 & \beta^{*}\mathbf{I} & 0 \\ 0 & 0 & 0 & 0 & \beta_{\mathrm{bc}}\mathbf{C}_{\mathrm{bc}}^{-1} \end{bmatrix} \tag{2.8}$$

in which $\mathbf{C}_{\mathrm{GPS}}^{-1}$, $\mathbf{C}_{\mathrm{SAR}}^{-1}$, $\mathbf{C}_{\mathrm{obs}}^{-1}$, and $\mathbf{C}_{\mathrm{bc}}^{-1}$ are the GPS, SAR, a priori observation, and boundary condition covariance matrices, respectively. Weights of each data set relative to GPS velocities are given by constants β_{SAR}, β_{ap}, β^{*}, β_{bc}. $\mathbf{I}$ is the identity matrix associated with the smoothing constraint.

2.4 Geodetic observations and reference block model geometry

The geodetic data that we consider are 191 nominally interseismic GPS velocities and 15,000 PS-InSAR (Permanent Scatterer) line-of-sight range change rates collected from 1992 to 2000 by the European Remote Sensing satellites ERS-1 and ERS-2 [Bürgmann et al., 2006] (Figure 2.1). Survey mode GPS velocities in the SFBA are those reported by d'Alessio et al. [2005], augmented by 6 GPS velocities at sites in the Pacific (sites KWJ1, CHAT, KOKB, MKEA, THTI, MAUI) and 9 in eastern North America (sites WES2, BARN, THU1, THU3, SCH2, BRMU, ALRT, STJO, KELY) to constrain far-field plate motions. Because this study is focused on understanding steady interseismic fault system behavior, we do not

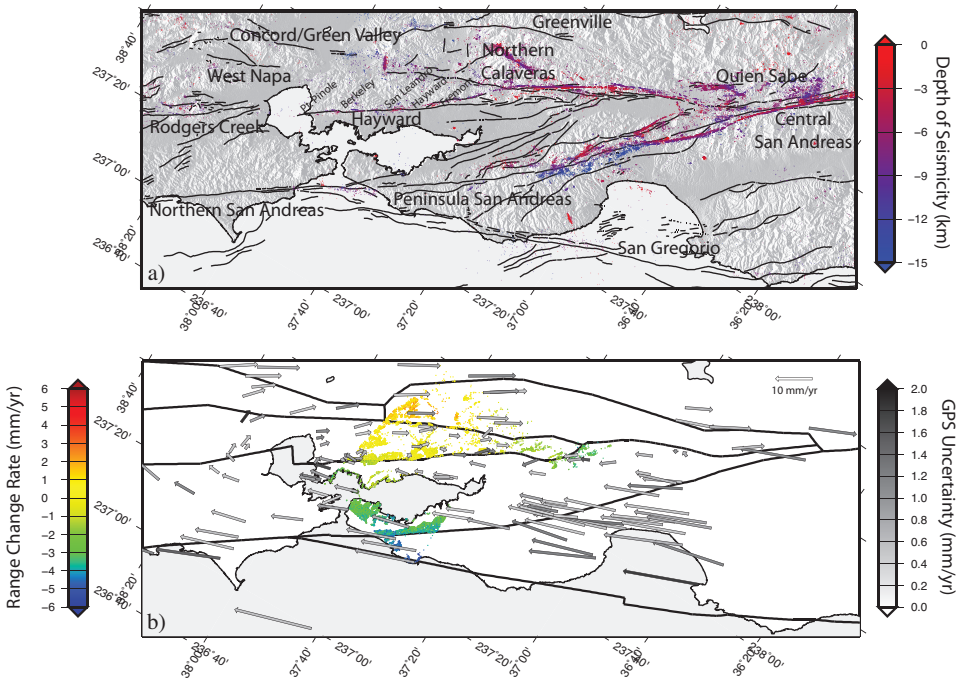

Figure 2.1: Inputs into the SFBA block model. a) San Francisco topography and mapped fault locations; seismicity [Waldhauser and Ellsworth, 2002] shown colored by depth of hypocenter. b) Block boundaries based on mapped fault locations shown as bold black lines. Bay Area GPS velocities shown as vectors colored by uncertainty. Filtered InSAR range change rates from Bürgmann et al. [2006].

include velocities from GPS stations that have documented postseismic deformation following the M_W=6.7–7.0 1989 Loma Prieta Earthquake [Bürgmann et al., 1997]. The InSAR data [Bürgmann et al., 2006] are filtered to remove observations that may be affected by seasonal groundwater effects and local spatially incoherent motions by removing all observations on Quaternary units, and retaining only range change rates of greater than −10 mm/yr and less than 10 mm/yr. We additionally remove observations differing from the mean of all stations within 5 km by more than 1 mm/yr. The resulting filtered InSAR observations are then cropped to remove observations in the Santa Cruz mountains and the Southern Calaveras fault (Figure 2.1) that may be biased by ongoing postseismic deformation from the Loma Prieta Earthquake. The final InSAR data set retains the 15,000 most coherent

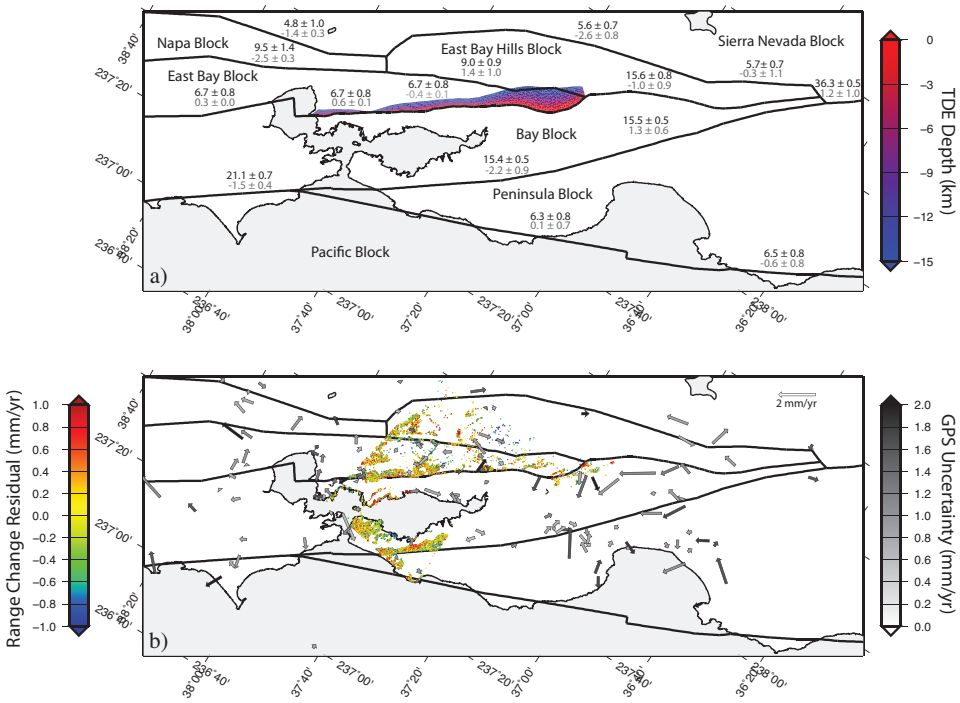

Figure 2.2: Output of the SFBA block model. a) Block geometry with labeled blocks. On-fault estimated strike-slip rates are shown in black, dip-slip rates in grey. Negative dip-slip rate is tensile. Mesh of triangular dislocation elements used to estimate spatially variable coupling colored by depth of element. b) Residual InSAR range change rates and GPS velocities.

observations. There are 7,144 observations within 5 km of either side of the Hayward fault, although data density decreases toward the south due to the presence of Quaternary units and vegetation. Within the block model formulation, we account for uncertainties in satellite orbits by simultaneously estimating a best fitting quadratic ramp as described in (§2.3) [e.g., Pritchard et al., 2002; Zebker et al., 1994].

The block geometry for a reference SFBA model is informed by mapped active faults [Graymer et al., 2002] and previous regional crustal deformation studies (Figure 2.1). We use a reference block model geometry that is similar to d'Alessio et al. [2005]. Our SFBA plate boundary block model is divided into six blocks between the Pacific block to the west

and the Sierra Nevada block to the east (Figure 2.2). The San Francisco peninsula block is separated from the Pacific block by the San Gregorio fault and bounded by the San Andreas fault in the east. East of the San Andreas fault is the Bay block, bordered on the east by the Rodgers Creek, Hayward, and Calaveras faults. The East Bay block lies between the Hayward and Rodgers Creek faults to the west and the Northern Calaveras fault to the east. The northeast SFBA contains the Napa Block, bounded by the West Napa fault in the west and the Green Valley and Concord faults in the east. The Greenville fault separates the East Bay Hills block from the Sierra Nevada block, which bounds the entire SFBA fault system to the east. To complete the plate boundary, we include a coarse representation of the North America block east of the Sierra Nevada block.

The most notable geometric difference between this reference block model and previous models [d'Alessio et al., 2005; Johnson and Fukuda, 2010] is that we do not include the Great Valley fault as a structure sub-parallel to the SAF. Instead, we hypothesize that the Greenville fault in the east SFBA transfers slip to the Quien Sabe fault (Figure 2.1). Repeating micro-earthquakes on this structure indicate that it is distinct from the neighboring southern Calaveras fault and may actively creep [Templeton et al., 2008]. This difference in model geometry is consistent with the idea that all of the slip in the SFBA is fed from San Andreas and San Gregorio faults in central California and is discussed in the results section. All faults other than the Hayward fault are represented using rectangular dislocation elements [Okada, 1985] that are assumed to be locked from the surface to an effective locking depth during the interseismic stage of the seismic cycle. InSAR data near the trace of the Hayward fault [Schmidt et al., 2005; Bürgmann et al., 2006] are spatially dense enough to

enable us to constrain spatial variations in fault coupling in this region. Although nearly vertical for most of its trace, the Hayward fault dips east south of Fremont, CA, and likely merges with the Calaveras fault at depth [Waldhauser and Ellsworth, 2002; Manaker, 2005; Graymer et al., 2005; Hardebeck et al., 2007]. The geometry of the Hayward fault is represented by a three-dimensional mesh of 1006 triangular dislocation elements [Comninou, 1973; Jeyakumaran et al., 1992; Thomas, 1993; Meade, 2007], derived from relocated seismicity and geologic mapping [Murray-Moraleda and Simpson, 2009]. We estimate spatially variable coupling on the portion of the Hayward fault north of the step over to the Calaveras fault east of San Jose. In addition to the reference model described above, we have tested block boundary geometries with and without step overs on the Calaveras-Concord-Green Valley system and in San Pablo Bay and find negligible differences in slip rate estimates on SFBA faults.

2.5 Estimated fault slip and creep rates

We jointly invert GPS and InSAR data for the best fitting set of block rotation vectors and fault slip rates (§2.3). Because there are approximately two orders of magnitude more InSAR observations than GPS observations, the InSAR data as a whole have a dominant influence on the solution unless they are downweighted. In our reference model the weighting ratio of the InSAR data relative to the GPS data, β_{SAR}, is set to 0.1 so that no individual InSAR pixel has more of an influence over the solution than the GPS velocity with the smallest uncertainty (§2.3). We also regularize the solution by smoothing the slip deficit rates on the mesh of triangular dislocation elements by minimizing the gradient of coupling rate

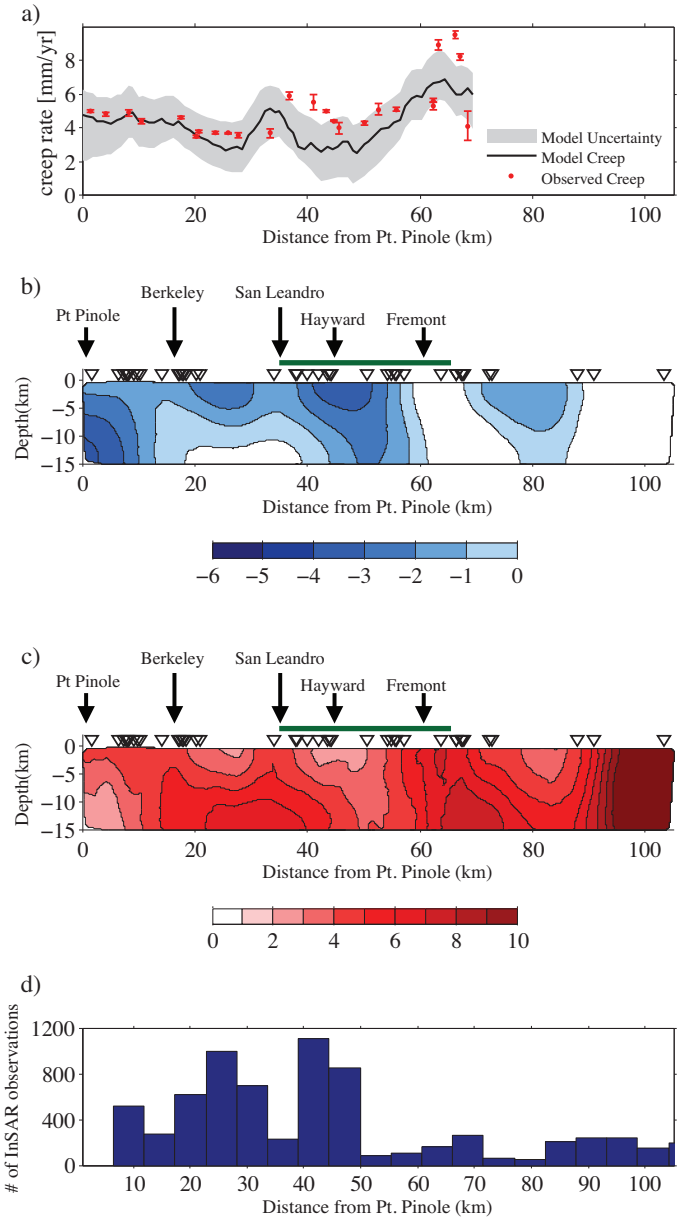

Figure 2.3: Creep and slip deficit on the Hayward Fault. a) Observed creep rates and estimated creep (estimated long term slip − estimated coupling) on the surface triangular dislocation elements of our reference coupling distribution shown with 67% confidence bounds. b) Reference slip deficit distribution on the Hayward fault estimated on a mesh of triangular dislocation elements. High coupling rates (dark blue) correspond to locked regions. Low slip deficit rates (white) represent creeping sections. Black triangles represent GPS station locations. Green bar represents the observed surface trace of the 1868 Hayward earthquake. c) Reference creep distribution (estimated long term slip minus estimated slip deficit rate) for the fault surface. d) Histogram showing density of SAR data points within 5 km of either side of the fault.

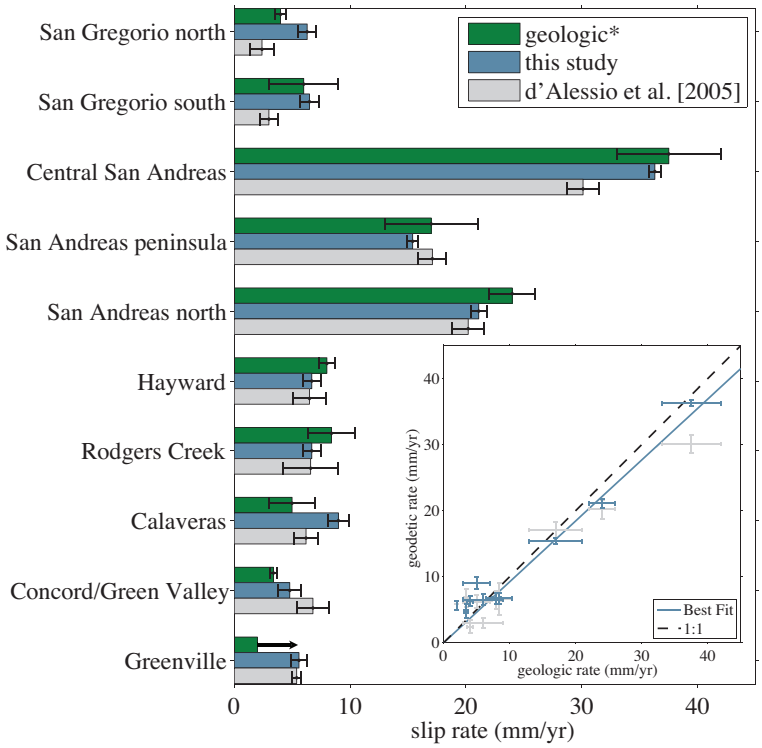

Figure 2.4: Slip rate comparison for this and previous SFBA studies. Inset shows geologic vs. geodetic rates for each fault. Inset: comparison of geologic and geodetic rates for this study and d'Alessio et al. [2005], best fit line shown in blue, dashed line is 1:1. *References for Geologic slip rates: San Gregorio north [Simpson et al., 1997], San Gregorio south [Weber et al., 1993], Central San Andreas [Segall, 2002], San Andreas peninsula [Hall et al., 1999], San Andreas north [Niemi and Hall, 1992], Hayward [Lienkaemper and Borchardt, 1996], [Budding et al., 1991], Calaveras [Kelson et al., 1996] Concord [Borchardt et al., 1999], Greenville [Berger et al., 2010].

between adjacent triangles [e.g., Harris and Segall, 1987; Maerten et al., 2005]. We choose the smoothing constant, β^*, based on the resolution tests described below. The reference model (Figure 2.2 and Figure 2.3) with $\beta^* = 5$ reproduces the SFBA GPS velocity field and InSAR range change rates with a mean residual GPS velocity magnitude of 1.4 mm/yr (WRSS per station = 6.1) and mean residual InSAR range change rate of 0.4 mm/yr.

Geodetic slip rate estimates on SFBA faults from this study and d'Alessio et al. [2005]

are compared with geologic slip rate estimates in Figure 2.4. Plotting geodetic slip rates against geologic slip rates, the best fit line through the origin is indistinguishable from a 1-to-1 line at the 95% confidence level (Figure 2.4, inset). We estimate a slip rate of 9.0±0.9 mm/yr on the Calaveras fault, which is faster than both the previous geologic slip rate estimate of 5.0±2 mm/yr [Simpson et al., 1999] and the previous geodetic estimate of 6.2 ± 1.0 [d'Alessio et al., 2005] (Figure 2.4). A slip rate estimate of 5.6±0.7 mm/yr on the Greenville fault is consistent with a recent study estimating a minimum geologic fault slip rate of 2 mm/yr from offset sediments [Berger et al., 2010] (Figure 2.4). A slip rate of 5.7±0.7 mm/yr on the Quien Sabe fault is also consistent with estimates of 11 cm of creep offset over 22 years of observations estimated from repeating microearthquakes on the fault [Templeton et al., 2008], although the use of repeating microearthquakes as creepmeters is ambiguous [Sammis and Rice, 2001]. We estimate 36.3±0.5 mm/yr on the central San Andreas fault south of Hollister. This is consistent with previous geodetic estimates in this region [Johanson and Bürgmann, 2005], and with estimates north of Parkfield, CA [Argus and Gordon, 1990; Segall, 2002; Becker et al., 2005; Meade and Hager, 2005; Schmalzle et al., 2006]. This agreement supports the idea that slip transfers directly into the SFBA from the San Andreas and San Gregorio faults in central California.

We estimate that the Hayward fault is fully to partially creeping along its entire length and down to at least 7 km depth (Figure 2.3). Although short wavelength features (<15 km) cannot be robustly resolved below 7 km depth (see resolution tests in §2.6), Figure 2.3 shows the complete slip deficit and creep rate estimates from the reference model, in which the Hayward fault extends to 15 km depth. Above 7 km, slip deficit rates appear to decrease, and

creep rates increase, with depth. We estimate the long-term fault slip rate on the Hayward fault to be 6.7±0.8 mm/yr, which is 1 to 4 mm/yr lower than previous estimates of long-term slip rates on the Hayward fault [d'Alessio et al., 2005; Lienkaemper and Borchardt, 1996; Graymer et al., 2002] (Figure 2.4). Similar to previous Hayward fault studies [e.g., Simpson et al., 2001; Schmidt et al., 2005], we find maximum coupling rates of 4.3±1.4 mm/yr at depth beneath Pt. Pinole, although the lack of InSAR data at the northern end of the Hayward fault limits resolution here. High surface creep rates near Pt. Pinole (4.1±2.1 mm/yr) and near Fremont, CA (7.2±1.5 mm/yr) are generally consistent with observations [Bilham and Whitehead, 1997; Lienkaemper et al., 2001] (Figure 2.3a). Within 67% confidence bounds, model surface creep rate estimates and creep rate measurements agree at 19 of the 25 alignment array observation locations [Lienkaemper et al., 2001]. The southern portion of the creep distribution shows a rapid increase in creep rate at the surface and at depth, supporting the hypothesis that the Hayward fault merges around 90 km from Pt. Pinole with the Calaveras fault to the east [Lienkaemper and Galehouse, 1998; Waldhauser and Ellsworth, 2002; Ponce et al., 2004; Williams, 2005; Manaker, 2005; Graymer et al., 2005]. A period of decreased creep on the southern Hayward fault from 1989 to 1996 following the 1989 M_W=7.0 Loma Prieta earthquake [Lienkaemper, 1997; Lienkaemper et al., 2001] would be captured in the InSAR data spanning 1992–2000, and included in the slip distribution estimated here, which represents an average over this time period. However, because the density of InSAR observations within 5 km of the Hayward fault decreases north of Fremont (Figure 2.3), where the decrease in creep rate was most dramatic [Lienkaemper, 1997; Lienkaemper et al., 2001], we do not expect a large affect in the creep distribution (assuming

creep rate changes were not persistent at depth). Between San Leandro and Fremont, spatially coincident with the surface rupture in the 1868 Hayward earthquake [Lawson, 1908] and a 25 km long gabbroic body on both faces of the Hayward fault [Graymer et al., 2005], we estimate a 20 km long segment with slip deficit rates of up to 3.7±1.2 mm/yr at the surface (Figure 2.3b).

2.6 Hayward fault resolution tests

To determine how well the current distribution of GPS and InSAR observations can be used to resolve coupling on the Hayward fault in the context of the elastic block model used here, we perform a series of checkerboard resolution tests [e.g., Bürgmann et al., 2005; Loveless and Meade, 2010]. We create a synthetic coupling distribution in a checkerboard pattern (Figure 2.5) in which patches of 20 km by 7.5 km are assigned coupling rates alternating between 10 mm/yr and 0 mm/yr. We run forward block models (using the same geometry as the reference model) with this known coupling distribution to generate synthetic GPS velocities and synthetic InSAR range change rates at the same observation coordinates as the real data. Inverting the synthetic geodetic data to see how well a known slip deficit distribution can be recovered provides an assessment of the resolving ability of the data at different points along the fault and allows us to systematically test the sensitivity to variations in weighting parameters.

The resolved coupling distribution varies based on the contribution to the solution of InSAR data relative to GPS data and on the degree of spatial smoothing [e.g., Menke, 1984]. When the ratio β_{SAR} is equal to one, every InSAR range change rate is given the

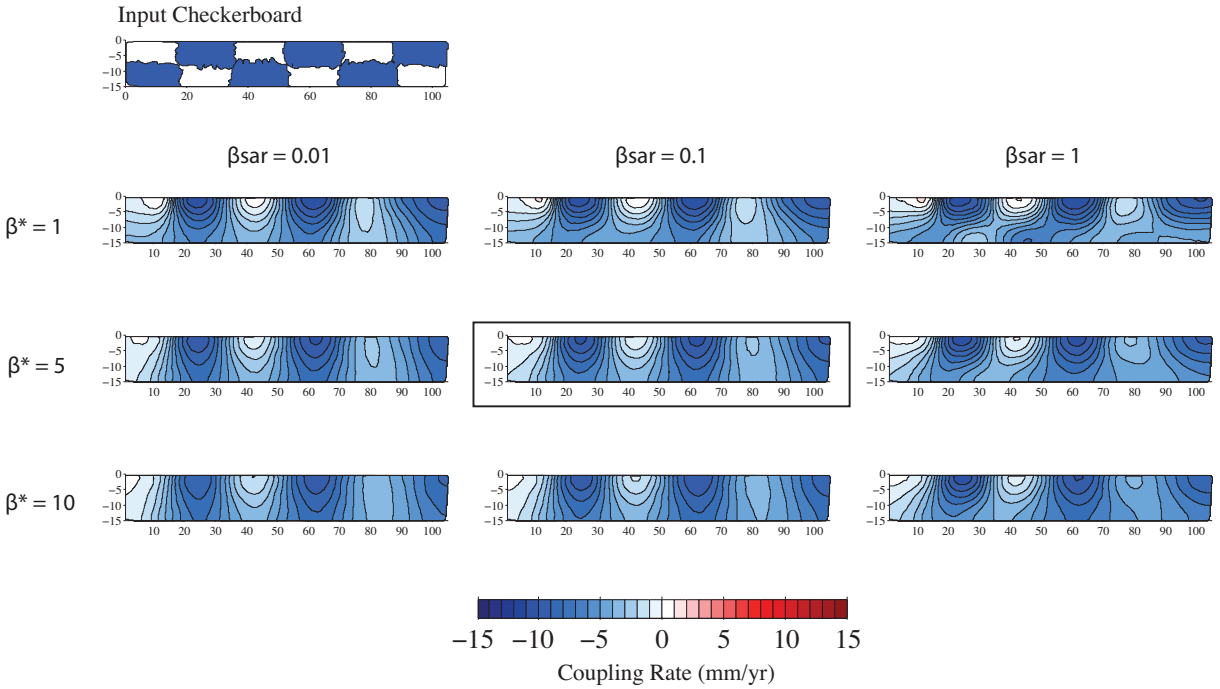

Figure 2.5: Checkerboard resolution tests. We assign a known coupling distribution (Input Checkerboard) to the Hayward fault mesh of triangular dislocation elements, generate synthetic GPS and InSAR surface observations with a forward model, and invert to recover the input coupling distribution. Contribution to the solution from InSAR relative to GPS, β_{SAR}, increases from left to right. The smoothing constant β^* increases from top to bottom. Constants corresponding to the reference model shown with black box.

same weight as each GPS velocity. Higher β_{SAR} values improve spatial resolution on the triangular dislocation elements due to the greater density of InSAR observations near the fault. Decreasing the smoothing constant β^* for a given data weight ratio sharpens the boundaries of the checkerboard pattern. Figure 2.5 shows the results of 9 realizations of the checkerboard resolution test with weighting ratio ranging from $\beta_{\mathrm{SAR}} = 0.01$ to $\beta_{\mathrm{SAR}} = 1$ and smoothing values ranging from $\beta^* = 1$ to $\beta^* = 10$. Features at ∼15 km wavelength are resolvable where $\beta^* = 1$, $\beta_{\mathrm{SAR}} = 1$ (Figure 2.5). At distances of 40–70 km south of Pt. Pinole, this resolution test overestimates coupling by ∼1 mm/yr at the surface and underestimates

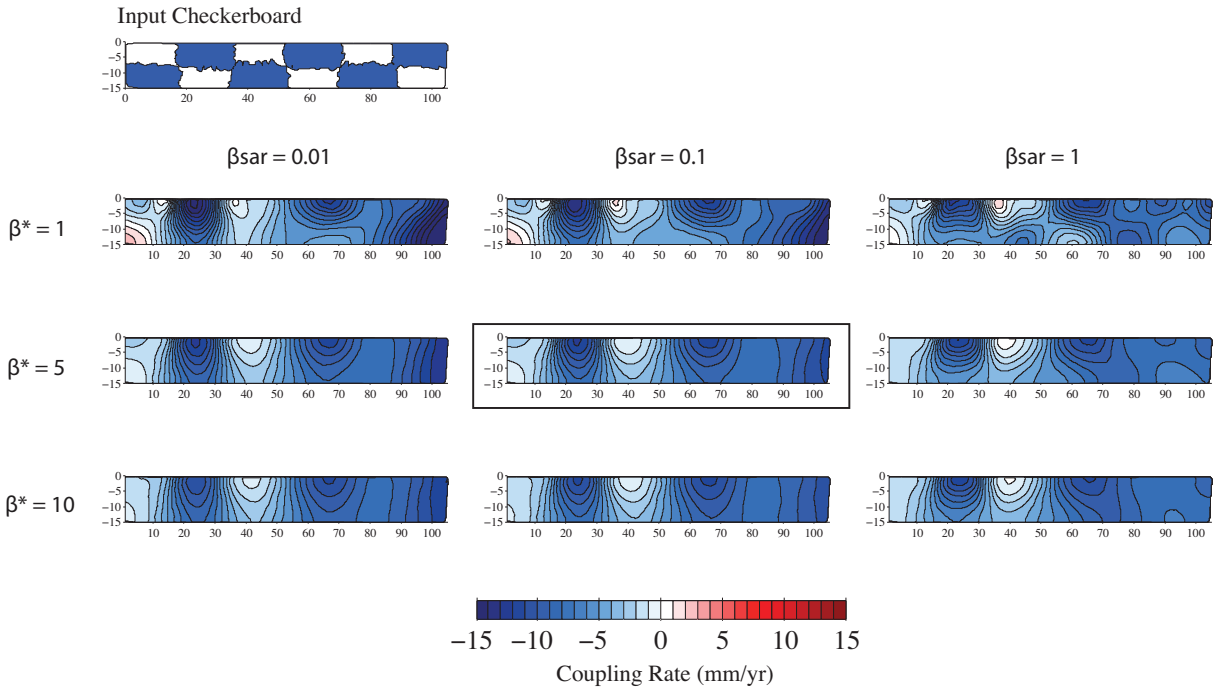

Figure 2.6: Checkerboard resolution tests with noise added. Noise sampled from a normal distribution with standard deviation of 0.5 mm/yr and added to synthetic GPS and SAR rates. We assign a known coupling distribution (Input Checkerboard) to the Hayward fault mesh of triangular dislocation elements and generate synthetic GPS and InSAR surface observations with a forward model. We then add noise sampled from a normal distribution with standard deviation of 0.5 mm/yr and invert to recover the input coupling distribution. Contribution to the solution from InSAR relative to GPS, β_{SAR}, increases from left to right. The smoothing constant β^* increases from top to bottom. Constants corresponding to the reference model shown with black box.

coupling by ∼2 mm/yr at 10 km depth. Farther south than 70 km, resolution at depth deteriorates such that we recover only 5 mm/yr of the input 10 mm/yr patch at depth between 70 and 90 km from Pt. Pinole (Figure 2.5).

Adding noise to the synthetic velocities computed from the forward model reduces resolution of the recovered coupling distribution (Figure 2.6). We add noise sampled from a normal distribution with a standard deviation of 0.5 mm/yr to the synthetic velocities and range change rates. At low smoothing values of $\beta^* = 1$, estimated coupling rates overshoot

the input coupling rates by up to 8 mm/yr. Increasing smoothing to $\beta^* = 5$ and $\beta^* = 10$ resolves coupling rates between 0 and 10 mm/yr, but cannot resolve sharp boundaries between patches. In general, estimated coupling rates still recover the checkerboard pattern on the northern part of the triangular mesh and at the surface, but lose resolution south of about 60 km from Pt. Pinole and below 7 km depth. Higher β_{SAR} values improve spatial resolution on the triangular dislocation elements, but higher smoothing values are required to recover coupling magnitudes similar to input values (Figure 2.6). We choose a smoothing value of $\beta^* = 5$ and weight ratio of $\beta_{\mathrm{SAR}} = 0.1$ for our reference model to capture along strike coupling variations with minimal overshoot in the coupling rate estimates (Figure 2.3).

The resolution tests demonstrate that we are able to resolve coupling features of 15–20 km in wavelength along strike, especially 10–80 km south of Pt. Pinole. At high smoothing weights, resolution at depth deteriorates. With an InSAR weight $\beta_{\mathrm{SAR}} = 0.1$, and smoothing weight $\beta^* = 5$, the checkerboard resolution tests are not successful at recovering slip deficit features <15 km in length below 7 km depth. In interpreting model results, slip deficit estimates deeper than 7 km should be considered within the context of these resolution tests.

2.7 Simple models of the effects of kinematically consistent and inconsistent fault systems on creep distributions

Creep rate estimates on the Hayward fault at depth suffer not only from poor resolution, but are also sensitive to model assumptions about the kinematic consistency of closely spaced SFBA faults. For example, Hayward fault creep rates at depth estimated with a

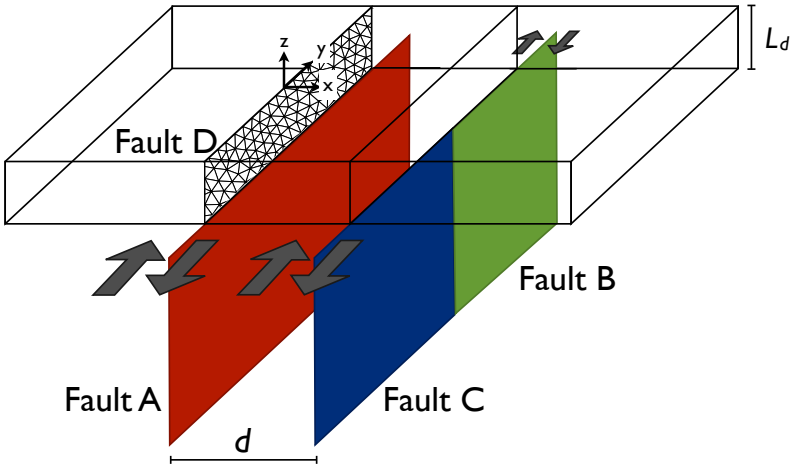

Figure 2.7: Simple model setup. Faults A, B and C are very long parallel strike slip fault segments in a homogeneous elastic halfspace extending from a locking depth L_d to infinite depth and separated by distance d. Fault D is a mesh of triangular dislocation elements between the locking depth, L_d and the surface, and is assumed to be fully locked. When Faults B and C slip at the same rate, the system is kinematically consistent. Kinematic inconsistency can be introduced by assuming an a priori slip rate on Fault B that is inconsistent with Fault C. Estimates of nonzero slip on fault D represent modeling artifacts.

kinematically consistent SFBA fault system model [Bürgmann et al., 2000] differ from those derived from models with kinematically inconsistent fault slip rates [Schmidt et al., 2005]. To understand how assumptions of kinematic consistency affect creep rate estimates, we develop a simple model consisting of a pair of very long parallel strike slip faults modeled as deep dislocations in a homogeneous elastic halfspace. Fault slip rates and geometry are assumed to be similar to that of the SFBA fault system. The two very long parallel strike-slip faults, separated by distance $d = 20$ km are subdivided into four fault segments A-D (Figures 2.7 and 2.8). Fault segment A extends from $-d/2$ on the x-axis to infinity in both

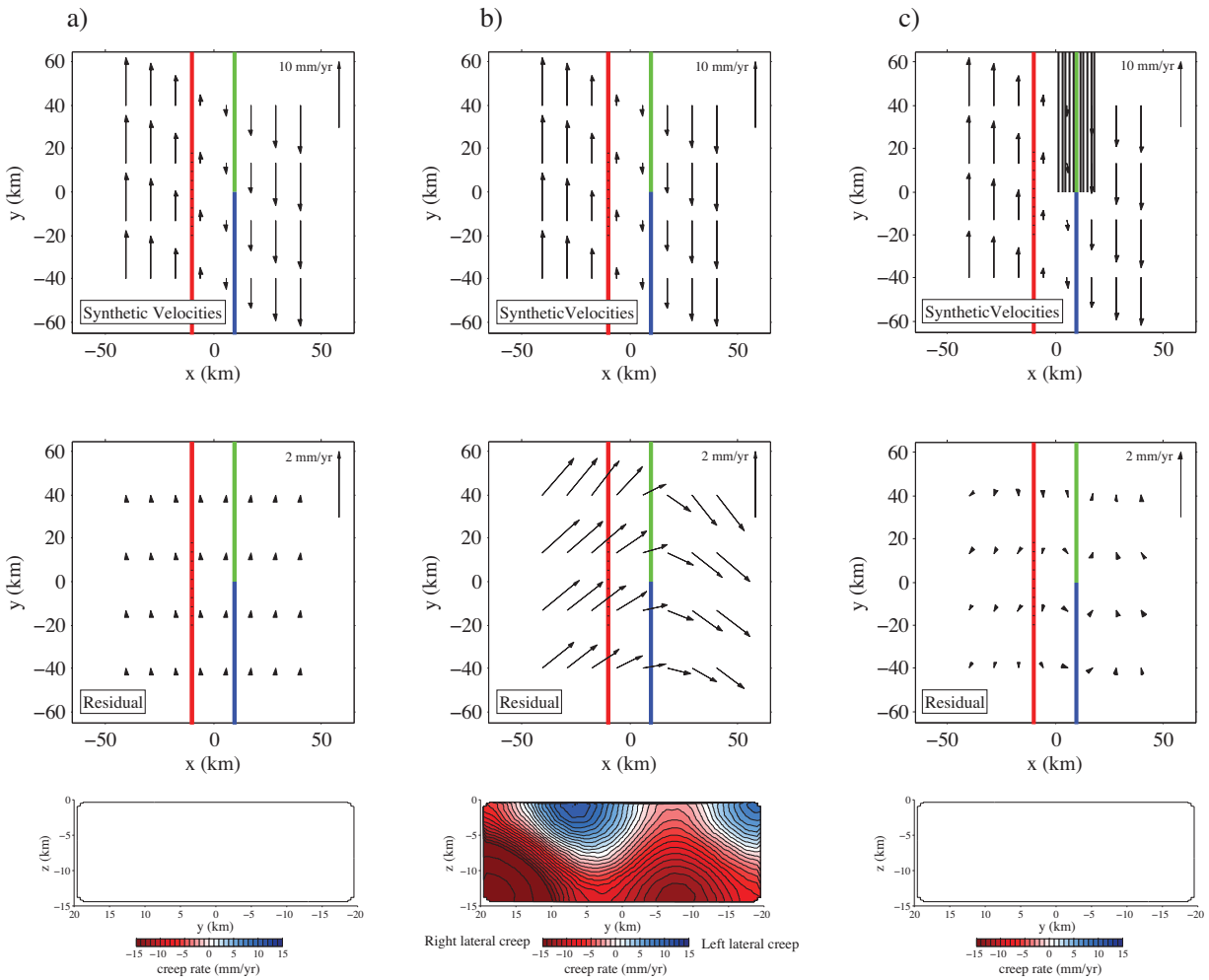

Figure 2.8: Kinematic consistency toy model results. The top row shows kinematically consistent forward velocities. a) Kinematically consistent synthetic velocities generated by a forward model with slip rates of 10 mm/yr on faults A, B and C. When synthetic velocities are inverted assuming kinematic consistency, no modeling artifacts map onto the mesh of triangular dislocations. b) Kinematically consistent synthetic velocities generated with slip rates of 10 mm/yr on faults A, B, and C. When forward velocities are inverted assuming an a priori slip rate of 5 mm/yr imposed on fault C (green), this produces artificial slip on the triangular dislocations. c) In this forward model, 10 mm/yr of right lateral slip near fault C is distributed over 11 parallel faults. Faults A and B slip at 10 mm/yr. Approximating diffuse slip with a single fault C produces negligible modeling artifacts.

the $+y$ and $-y$ directions, slipping continuously below some depth L_d. Parallel to fault A, fault B extends from $+d/2$ on the x-axis but extends to infinity in the $+y$ direction, and fault C also begins at $+d/2$ on the x-axis but extends to infinity in the $-y$ direction. Both B and C slip continuously below L_d. When faults B and C slip at the same rate, this is identical to a single through going vertical strike slip fault, and the model is kinematically consistent. This model configuration allows us to introduce a slip rate discontinuity by changing the slip rate on fault B, creating a kinematically inconsistent set of fault slip rates. We additionally include fault D as a 20 km long mesh of 312 triangular dislocation elements between the locking depth and the surface above fault A, centered at $y = 0$. We assume fault D is fully locked.

We define a set of synthetic observation points on the free surface of the elastic halfspace, and calculate synthetic velocities from a forward model with prescribed slip rates. These synthetic velocities are inverted for estimates of slip rates on the deep dislocations and spatially variable creep on fault D. In contrast to the block model in which we directly estimate slip deficit rates, this simple model is constructed in the deep dislocation framework, and we directly estimate creep rates on fault D. We generate synthetic observation velocities assuming a fully locked upper crust, therefore non-zero slip estimated on fault D will be a model artifact, allowing us to evaluate the influence of kinematic inconsistency on creep distributions resolved on nearby faults.

To demonstrate the differences between kinematically consistent and inconsistent models of kinematically consistent deformation, we generate synthetic velocities computed from a kinematically consistent forward model (Figure 2.8a) such that the slip rates on faults A,

B, and C are all equal to 10 mm/yr. We then invert these velocities within their original framework for slip on the faults and on the triangular dislocations. In this case of retaining kinematic consistency within the inversion, we recover 10 mm/yr slip rates on faults A, B, and C, and resolve negligible artificial slip on the triangular dislocation elements (Figure 2.8a). To understand the effects of kinematically consistent models, we invert these velocities for fault slip a second time, assigning a priori slip rate constraints of 10 mm/yr on faults A and C and 5 mm/yr on fault B. Kinematic inconsistency arises because a path integral of slip across the positive half of the fault system now differs from the path integral of slip across the negative half of the fault system. The residual velocity field now contains edge effects due to the jump in slip rate along strike (Figure 2.8b), and mesh of triangular dislocation elements is the only source of additional surface deformation available to accommodate the difference between the kinematically consistent forward field and the imposed deep slip rates. In this case, kinematic inconsistency within the model creates artifacts that map into a near-surface creep distribution on fault D (Figure 2.8b). The magnitude and spatial distribution of artificial slip depend on the smoothing parameters and geometry of the fault system. In the synthetic case shown in Figure 2.8b, this results in a maximum right lateral creep rate of 28 mm/yr and a maximum left lateral creep rate of 11 mm/yr.

Although mapped fault traces are finite, traveling from stable North America to the Pacific plate without accommodating the geodetically [Argus and Gordon, 1990; Argus and Heflin, 1995] or geologically [DeMets et al., 1994] observed total tectonic deformation would imply path dependence to relative plate tectonic motions. Maintaining kinematic consistency within a plate boundary model therefore requires the assumption of fault system continuity,

in which continuous structures may represent deformation accommodated by diffuse deformation or poorly exposed faults.

As an example, consider Figure 2.8c, in which 10 mm/yr of right-lateral slip is distributed over eleven parallel faults ($1/6^{\text{th}}$ km spacing), representing a case where deformation is more distributed. Even though deformation is distributed, the model is kinematically consistent because the total amount of slip does not vary across the system. As before, solving for creep on fault D recovers zero creep. We then model the same synthetic velocities with a slightly different model geometry, where the 11 parallel faults are represented as a single fault slipping at 10 mm/yr. Because the simplified geometry maintains kinematic consistency, inverting velocities predicted by the diffuse deformation model with this simplified single fault geometry produces negligible modeling artifacts on the near surface creep distribution. At the scale of the simple model used here, creep rate estimates on fault D are weakly sensitive to the exact geometry at the junction of faults B and C, so long as the slip budget is kinematically consistent. Based on these simple models, it is possible that differences between our reference creep estimate and previous creep estimates [Schmidt et al., 2005] may result from different assumptions about the kinematic consistency of the SFBA fault system.

2.8 Discussion

We find that geodetically constrained slip rate estimates from our reference block model agree, within reported uncertainties, with geologic slip rate estimates along 6 of 10 SFBA faults (Figure 2.4). Our slip rate estimate on the Hayward fault of 6.7±0.8 mm/yr is 1

to 4 mm/yr lower than previous geologic and geodetic estimates [d'Alessio et al., 2005; Schmidt et al., 2005; Simpson et al., 2001]. Because the Hayward fault may merge with, and transfer slip from, the Calaveras fault at its southern end, the geologic slip rate of 8.0±2.0 mm/yr estimated by Lienkaemper and Borchardt [1996] at Union City, CA, may not be representative of slip rate on the northern portion of the Hayward fault. Slip rates on the Calaveras and Greenville faults are slightly faster (∼40% and ∼100% respectively) than geologic estimates [Kelson et al., 1996; Berger et al., 2010] (Figure 2.4), suggesting that structures east of the Hayward fault may currently accommodate more than twice the slip of the Hayward fault itself. In particular, because the estimated interseismic slip rate of 9.0±0.9 mm/yr on the partially creeping Calaveras fault [Manaker et al., 2003] exceeds that of the Hayward fault by 40%, the Calaveras fault may be capable of producing earthquakes that are larger or more frequent than those on the Hayward fault.

We estimate the long-term fault slip rate on the Hayward fault to be 6.7±0.8 mm/yr, and find maximum slip deficit rates of 4.2±1.4 mm/yr at depth beneath Pt. Pinole, although data density severely limits resolution in this region. Between San Leandro and Fremont, slip deficit rates reach up to 3.7±1.2 mm/yr at the surface. This 20 km region of high slip deficit rate is consistent in length and location with the observed surface rupture in the 1868 Hayward fault earthquake [Lawson, 1908]. Over 150 years, temporally invariant behavior of this patch would produce moment accumulation equivalent to a $M_W \approx 6.6$ earthquake, estimated with an empirical area-slip scaling relationship [Wells and Coppersmith, 1994]. Although deep features are poorly resolved, a fully locked patch on the Hayward fault at depth is not required to accumulate sufficient moment to generate a major earthquake over

Hayward fault recurrence intervals of 161±65 years [Lienkaemper et al., 2010]. The pattern and magnitude of fault creep in the reference model are most consistent with the shallow creep distribution of Bürgmann et al. [2000], in which SFBA faults are represented as kinematically consistent deep dislocations.

A correlation between geodetically imaged interseismic fault coupling and historical earthquake rupture location may be interpreted as consistent with the hypothesis of characteristic fault behavior [Shimizaki and Nakata, 1980; Schwartz and Coppersmith, 1984] and persistent seismic asperities [Lay and Kanamori, 1980]. In this idealized view, episodic earthquakes of similar magnitude occur at a characteristic location, and the ruptured portion of the fault remains locked during the interseismic period. Although the characteristic earthquake concept may oversimplify fault behavior, studies of interseismic coupling in subduction zones off Japan [Yamanaka and Kikuchi, 2004; Nishimura et al., 2004; Loveless and Meade, 2010], Sumatra [Konca et al., 2008], South America [Moreno et al., 2010], and Alaska [Cross and Freymueller, 2007; Suito and Freymueller, 2009] also suggest that fault patches that are strongly coupled during the interseismic period are colocated with the hypocenters or rupture areas of large earthquakes.

On the other hand, there is also evidence that creeping regions may not be temporally invariant. Coral records offshore of Sumatra suggest time and space variable patterns of strain accumulation over multiple earthquake cycles [Natawidjaja et al., 2004], and coupled asperities at the New Britain trench off the coast of Papua New Guinea suggest that interseismically locked regions may not have controlled the locations of historic earthquakes [Park and Mori, 2007]. Another possibility is that the 1868 earthquake was able to rupture

through a region of low coseismic slip deficit rather than be confined to the most strongly coupled patches [e.g., Malservisi et al., 2003, 2005]. Large historical events have also occurred along the Japan trench [Nishimura et al., 2004] and offshore Sumatra [Konca et al., 2008], in regions of low estimated coupling. Numerical models show that earthquake rupture on a fault with heterogenous frictional properties may not be confined to a velocity weakening patch imbedded within an otherwise velocity strengthening fault [Kaneko and Lapusta, 2008]. Similar models show that earthquakes may rupture through weakly coupled regions between separate highly coupled asperities [Kaneko et al., 2010] and the nature of the earthquake rupture may not be consistent over multiple earthquake cycles, consistent with interpretation of seismic observations [e.g., Thatcher, 1990; Freymueller et al., 2008]. Thus, low slip deficit rates surrounding a 20 km asperity on the Hayward fault may not preclude a longer 1868-type rupture extending from Berkeley to south of Fremont [e.g., Yu and Segall, 1996].

Partially creeping behavior on the Hayward fault may be associated with complex lithologically modulated variations in frictional behavior of the rocks on either side of the Hayward fault. The region of partial creep we observe between San Leandro and Fremont is spatially coincident with a 25 km long gabbro body on the east face of the Hayward fault [Graymer et al., 2005] (Figure 2.9). The adjacent west face consists of gabbro above 6 km depth and metagreywacke below. Although resolution of spatially variable creep is poor at depth, we image maximum slip deficit rates within this asperity near the surface. The collocation of a strongly coupled, though still creeping zone, with proximal gabbro units is notable given the apparent prevalence of this kinematic behavior in subduction zones where gabbro is

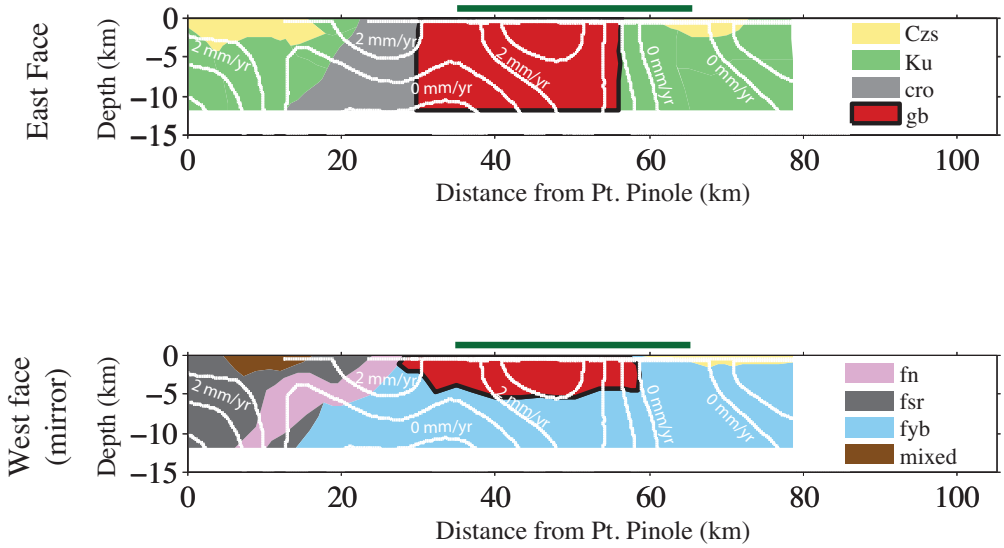

Figure 2.9: Fault surface geology reproduced from Graymer et al. [2005] with coupling rate contours. Jurassic gabbro (gb) shown in red. Top: Eastern face of the Hayward fault. Bottom: Western face (mirror image) of the Hayward fault. Green bar represents the observed surface trace of the 1868 Hayward earthquake. Rock types are Czs: Cenozoic sedimentary rocks, Ku: Upper Cretaceous sandstone, shale and minor conglomerate, cro: undivided Jurassic serpentinite, gabbro, basalt, and keratophyre, with minor sedimentary rocks, gb: Jurassic gabbro, fn: Upper Cretaceous sandstone and shale, fsr: melange, fyb: Cretaceous metagreywacke, mixed: tectonically interleaved sandstone, metasandstone, melange, and serpentinite [Graymer et al. 2005].

regularly present [Liu and Rice, 2009]. Experiments to determine the frictional properties of gabbro at low temperatures and pressures reveal a complex range of behaviors. Morrow and Lockner [2001] performed failure and frictional sliding tests on rock samples collected in situ along the Hayward fault and found that all of the samples, consisting of gabbro, coarse gabbro, keratophyre, altered keratophyre, basalt, sandstone and serpentinite, exhibit velocity strengthening behavior at room temperature and pressures of 30–200 MPa. At an effective pressure of 30 MPa, the coarse gabbro is the least velocity strengthening of Hayward fault rocks. A similar set of experiments by Marone and Cox [1994] show that the velocity dependence of gabbro depends on contact roughness and total fault displacement, such that

under 5 MPa normal stress at ambient temperatures, a smooth gabbro surface exhibits velocity weakening behavior while rough gabbro is velocity strengthening at slip distances less than 50 mm. At near surface temperatures and pressures, most rocks have been found to be velocity strengthening enabling interseismic creep, with creep rate magnitude a function of the frictional parameters, stress history, and boundary conditions [Marone, 1998]. Frictional experiments on dry gabbro have suggested that the transition from velocity strengthening to velocity weakening occurs at temperatures between 250 and 510° C at atmospheric pressures [He et al., 2007]. Assuming pressure effects on frictional parameters are negligible, these experiments would suggest that the near surface transition from velocity strengthening to velocity weakening occurs near a depth of 8.3 km assuming a regional geothermal gradient of 30° C/km. While current geodetic data are insufficient to provide kilometer-scale resolution downdip, experimental results are consistent with geodetically constrained estimates of a creep transition midway through the upper crust.

2.9 Conclusion

To better constrain the kinematic parameters necessary for quantitative seismic hazard assessment and understand the interseismic behavior of the Hayward fault, we invert GPS and InSAR data with a kinematically consistent block model of the SFBA fault system to estimate Bay Area fault slip rates and spatially variable slip deficit rates on the Hayward fault. Checkerboard resolution tests on the Hayward fault reveal that slip deficit features <15 km long are well resolved along strike at the surface, but cannot be robustly resolved deeper than 7 km with published GPS and InSAR data. Simple models of a two-fault

system suggest that, at scales comparable to that of the SFBA fault system, estimated creep rates at depth are sensitive to assumptions about the kinematic consistency of slip rates on neighboring faults, and may contribute to differences between this and previous estimates of creep rates at depth on the Hayward fault. We identify a strongly coupled asperity with a slip deficit rate of 3.7±1.2 mm/yr at the surface near San Leandro, CA. Spatial correlation between high slip deficit rates and gabbroic fault surfaces adjacent to the mapped surface trace of the 1868 M_W=6.9–7.0 suggests that partially creeping fault behavior may be associated with complex lithologically modulated variations in frictional properties. Further insight into whether or not geodetically imaged asperities limit the rupture extent of future earthquakes on the Hayward fault may be gained through dynamic slip models that are evolved forward in time from present day conditions.

Chapter 3

Geodetic imaging of coseismic slip and postseismic afterslip: Sparsity promoting methods applied to the great Tohoku earthquake

Geodetic observations of surface displacements during and following earthquakes such as the March 11, 2011 great Tohoku earthquake can be used to constrain the spatial extent of coseismic slip and postseismic afterslip, and characterize the spectrum of earthquake cycle behaviors. Slip models are often regularized by assuming that slip on the fault varies smoothly in space, which may result in the artificial smearing of fault slip beyond physical boundaries. Alternatively, it may be desirable to estimate a slip distribution that is spatially compact and varies sharply. Here we show that sparsity promoting state vector regularization methods can be used to recover slip distributions with sharp boundaries, representing an alternative end-member result to very smooth slip distributions. Using onshore GPS observations at 298 stations during and in the ∼2 weeks following the Tohoku earthquake, we

An amended version of this Chapter was published with Brendan J. Meade in Geophysical Research Letters, Vol. 39, 2012.

estimate a band of coseismic slip between 30 and 50 km depth extending 500 km along strike with a maximum slip of 64 m, corresponding to a minimum magnitude estimate of M_W=8.8. Our estimate of afterslip is located almost exclusively downdip of the coseismic rupture, with a transition between 40 and 50 km depth and an equivalent moment magnitude M_W=8.2. This depth may be interpreted as coincident with the transition from velocity strengthening to velocity weakening frictional behavior, consistent with the upper limit of cold subduction estimates of the thermal structure of the Japan trench.

3.1 Introduction

The March 11, 2011 great Tohoku earthquake off the east coast of Japan has been the focus of numerous studies to determine the spatial extent of coseismic slip in order to assess the degree to which the earthquake ruptured portions of the subduction zone inferred to be strongly coupled prior to the earthquake, the extent of near trench slip, and the relationship with afterslip following the earthquake. Answering each of these questions requires the solution of an inverse problem where geodetic [Sato et al., 2011; Kido et al., 2011], teleseismic [e.g., Fujii et al., 2011; Kiser and Ishii, 2012], strong motion [e.g., Yokota et al., 2011], tsunami run-up [Mori et al., 2011], and tsunami waveform and strain gauge [Fujii et al., 2011] observations are used to infer the spatial distribution of fault slip, typically assuming a linear mapping.

Currently there is significant diversity in estimates of coseismic slip. Coseismic slip at or very near the trench has been estimated from GPS offsets [Loveless and Meade, 2011a; Pollitz et al., 2011], high frequency GPS [Yue and Lay, 2011], teleseismic observations [Fujii

et al., 2011; Ide et al., 2011], GPS and teleseismic observations [Simons et al., 2011], tsunami observations [Maeda et al., 2011], and joint inversion of GPS, teleseismic, strong motion, and tsunami observations [Yokota et al., 2011]. However, other estimates of the coseismic slip have been interpreted as suggesting little slip along the trench itself based on static GPS offsets [Ozawa et al., 2011; Miyazaki, 2011], GPS and tsunami observations [Simons et al., 2011], and joint inversions of GPS, teleseismic, and strong motion observations [Lee et al., 2011; Koketsu et al., 2011]. Estimates of maximum slip range from 18 m [Loveless and Meade, 2011a] to 60 m [Simons et al., 2011; Yue and Lay, 2011].

Variation in coseismic slip estimates also affects our ability to quantify the spatial relationship between coseismic slip and short-term postseismic deformation on the subduction zone interface. A broad region of afterslip following the Tohoku earthquake estimated from 15 days of postseismic GPS observations is centered downdip of, but largely overlaps with, the coseismic slip estimate [Ozawa et al., 2011]. Afterslip downdip of coseismic slip has been observed following multiple large earthquakes [Chlieh et al., 2004; Miyazaki and Larson, 2008; Chlieh et al., 2007; Paul et al., 2007; Vigny et al., 2011; Hsu et al., 2002], and is often attributed to a transition between velocity weakening behavior and velocity strengthening behavior on the fault [e.g., Tse and Rice, 1986; Marone et al., 1991; Scholz, 1998]. However, rigorous comparison of slip during and after the Tohoku main shock has been limited by our ability to sharply resolve and compare spatial patterns of coseismic slip and afterslip.

Here we estimate both co- and postseismic slip distributions using a sparsity promoting solution method to recover sharp boundaries to slip, providing an alternative to smoothed slip estimates. We demonstrate through synthetic resolution tests that sparsity promoting

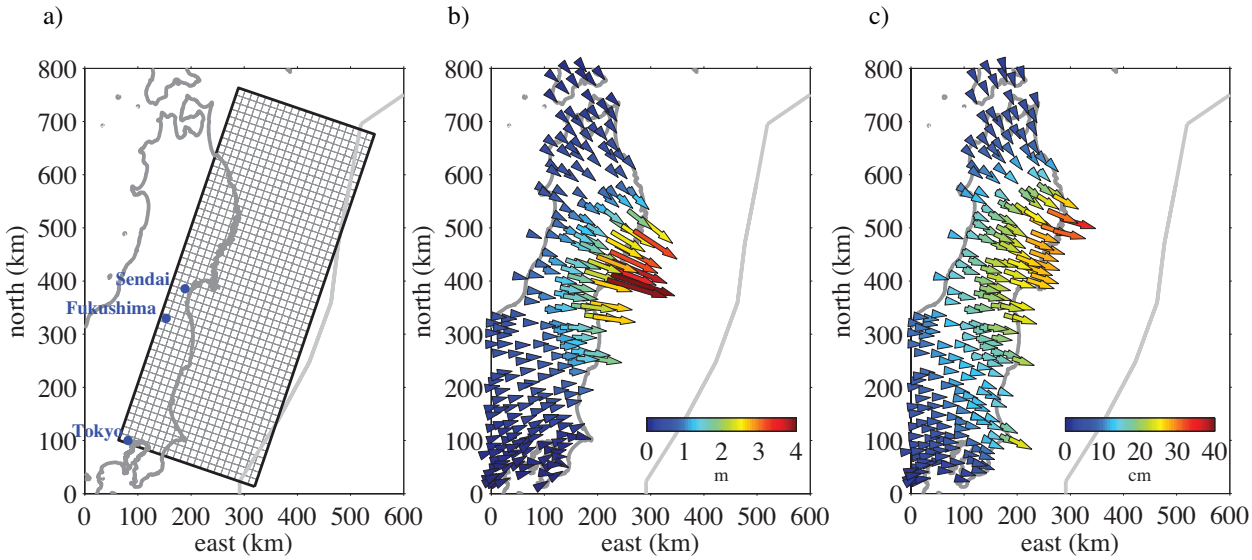

Figure 3.1: Figure showing model inputs: Japan coastline shown in in dark grey, trench shown in light grey a) idealized planar fault geometry: strike 199°, dip 15°; b) coseismic displacements (from the Geospatial Information Authority of Japan processed by U.S. Jet Propulsion Laboratory: ftp://sideshow.jpl.nasa.gov/pub/users/ARIA); c) postseismic displacements [Ozawa et al., 2011].

regularization can recover sharp boundaries to slip, and solve for slip during the Tohoku earthquake on an idealized planar array of rectangular dislocation elements [Okada, 1985]. We compare sparsity promoting and smoothed estimates of coseismic slip to afterslip in the 15 days following the earthquake, and image a localized band of afterslip directly downdip of coseismic rupture.

3.2 SPARSITY PROMOTING ESTIMATION THROUGH ℓ_1 REGULARIZATION

The problem of estimating fault slip from geodetic observations is well studied and regularly applied to constrain the rupture extent of large earthquakes. Typically the displacements, $\mathbf{d}$, due to slip on fault patches, $\mathbf{m}$, are calculated using analytic Greens functions, $\mathbf{G}$, for slip on a rectangular dislocation in a homogeneous elastic half space [Okada, 1985],

forming the linear system $\mathbf{Gm} = \mathbf{d}$. It is often the case that the problem is under-determined (more fault patches than data) and $\mathbf{G}$ may be poorly conditioned in the sense that some elements lie near the null space and therefore solutions tend to be extremely sensitive to noise in the data. To minimize this sensitivity, a regularization constraint is applied to the state vector, $\mathbf{m}$ (alternatively, minimizing a cost function containing a term that compares the values of adjacent fault elements [Chlieh et al., 2007, e.g.,] achieves the same goal), and fault slip estimates are obtained by minimizing the sum of squares of the residual displacements, $\mathbf{Gm} - \mathbf{d}$, along with the constrained state vector, $\mathbf{m}$ [e.g., Harris and Segall, 1987; Maerten et al., 2005]. This may also be written as a damped least squares problem where parameter α is included in the minimization to damp oscillations and drive the state vector toward a common value with increasing α: $\min \|\mathbf{Gm} - \mathbf{d}\|_2 + \alpha\|\mathbf{m}\|_2$.

Absolute value (ℓ_1) regularization approaches designed to recover sparse state vectors have been applied in reflection seismology problems in the last four decades [e.g. Claerbout and Muir, 1973; Santosa and Symes, 1986], and have been recently applied to teleseismic P wave filtering [Yao et al., 2011]. While this approach introduces a non-linear state vector regularization, optimal solutions can be found using standard quadratic programming approaches [Boyd and Vandenberghe, 2004]. Interest in ℓ_1 regularization has increased markedly over the last decade with the development of a theoretical understanding of how it very likely recovers the ℓ_0 pseudo-norm, which gives the number of non-zero elements in the state vector [Donoho, 2006; Candès et al., 2006]. A state vector is considered sparse if the total number of non-zero elements is much less than the total number of elements in the state vector, and efficient algorithms now exist to solve problems of the

form: min $\|\mathbf{Gm} - \mathbf{d}\|_2 \ + \ \lambda\|\mathbf{m}\|_1$ in which λ controls the sparsity of the state vector. The constrained form of this regularized optimization problem is referred to as the least absolute shrinkage and selection operator (lasso) [Tibshirani, 1996],

$$\min \|\mathbf{Gm} - \mathbf{d}\|_2 \text{ subject to } \|\mathbf{m}\|_1 \leq \tau \tag{3.1}$$

in which the value of τ controls the tradeoff between sparseness of the solution slip distribution and model fit to the data, and which can be solved efficiently using a spectral projected gradient root finding algorithm (spgl1) [van den Berg and Friedlander, 2009], which we use here. Applied to earthquake slip distributions, ℓ_1 regularization produces a compact representation of slip, and may be considered an alternative end-member to smoothed ℓ_2 regularized solutions.

Figure 3.2 *(following page)*: Resolution test demonstrating recovery of a known slip distribution with sparsity promoting and smooth regularization techniques. The 33% least resolved rectangular dislocations shown in gray. a) input slip distribution consisting of 30 m of slip on a 9800 km^2 rectangular subset of 50 rectangular dislocations; b) sparsity promoting recovery of input distribution shown in a); c) damped least squares recovery of input slip distribution show in a; d) input slip distribution with 30 m of slip on a 56 km wide fault patch extending from the base of the model fault to the trench made up of 280 rectangular dislocations; e) sparsity promoting recovery of input distribution shown in d); f) damped least squares recovery of input slip distribution shown in d); g) input slip distribution with 30 m of slip imposed on a subset of 44 of the rectangular dislocations in the shape of a ring; h) sparsity promoting recovery of input slip distribution shown in g); i) damped least squares recovery of input slip distributions shown in g).

Figure 3.2: (continued)

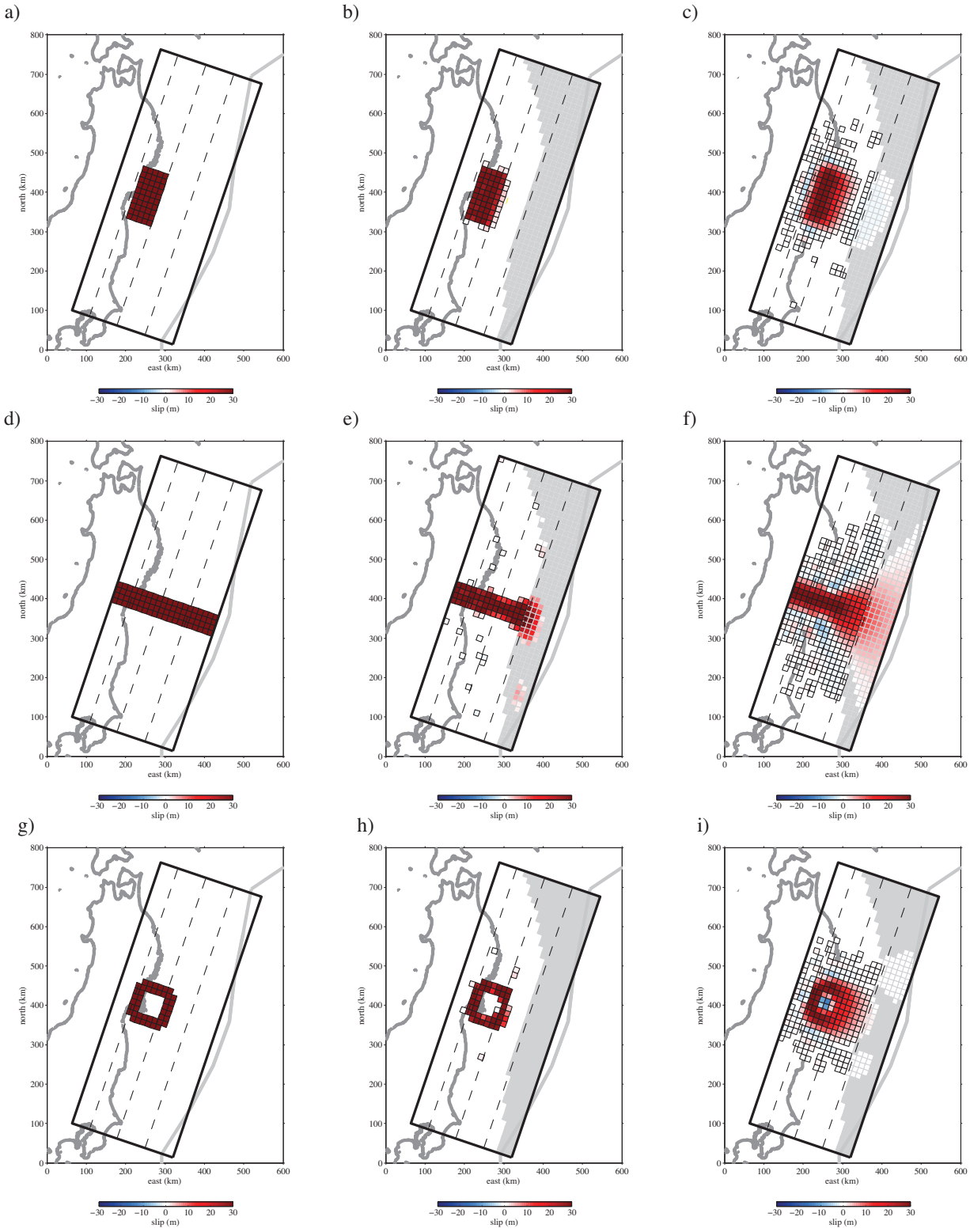

3.3 GPS data, model geometry, and resolution tests

We consider 298 onshore coseismic (data from the Geospatial Information Authority of Japan processed by U.S. Jet Propulsion Laboratory: ftp://sideshow.jpl.nasa.gov/pub/users/ARIA) and 15 days of postseismic [Ozawa et al., 2011] GPS observations, including only GPS observation locations that appear in both catalogs to avoid bias due to station location. Due to potential complexities in vertical deformation associated with subduction erosion on the Japan subduction zone [Heki, 2004], we consider only the horizontal components of the observations. Seven seafloor observations [Sato et al., 2011; Kido et al., 2011] record the coseismic rupture, however they also contain at least two weeks of the postseismic period as well, and are therefore not included in this comparison. We use simplified representation of the Japan subduction zone parameterized as a planar array of 1000 rectangular dislocation elements [Okada, 1985] with dimensions of 700 km along strike and 280 km downdip. Each rectangular element has dimensions of 196 km^2. The simplified single planar fault dips 15° with a strike of 199° (Figure 3.1).

To test the ability of sparsity promoting regularization to recover a known slip distribution, we perform a set of resolution tests. Because ℓ_1 regularization methods are designed to recover sparse solutions, the slip distribution used to generate synthetic velocities must also be sparse. Instead of performing a checkerboard resolution test, which requires 50% of the model fault to slip, we impose 30 m of slip on three different subsets of rectangular dislocations. For the resolution tests, the convergence criterion in the spgl1 algorithm [van den Berg and Friedlander, 2009] is set to an optimality tolerance of 10^{-4}. A smoothed solution may produce slip estimates that are small, but will rarely be exactly equal to zero. In con-

trast, sparsity promoting regularization results in a state vector in which most elements are exactly zero. For consistent interpretation of both distributions, we consider recovery of slip less than 50 cm as identifying a non-slipping dislocation. This precludes the interpretation of low magnitude smoothing artifacts that may extend estimated rupture areas significantly.

We impose 30 m of slip on a 9800 km^2 rectangular subset of 50 of the rectangular dislocations (Figure 3.2a). A forward model of this slip distribution generates synthetic observation displacements. We then invert the synthetic observation displacements to recover the known slip distribution using sparsity promoting regularization as well as damped least squares. In these tests, no synthetic noise is added. ℓ_1 regularized recovery of the slip distribution produces a maximum slip of 36.5 m ($\tau = 1500$), identifies all of the known slipping dislocations, and falsely identifies 15 (2%) of the non-slipping rectangular dislocations (Figure 3.2b). The damped least squares recovery of the slip distribution produces a maximum slip of 37.7 m ($\alpha = 10^{-8}$), identifies all of the slipping rectangles, but falsely identifies 95 (10%) slipping rectangular dislocations (Figure 3.2c).

To test recovery of slip as a function of depth, we impose 30 m of slip on a 56 km wide fault patch extending from the base of the model fault to the trench made up of 280 rectangular dislocations (Figure 3.2d). With no synthetic noise, the ℓ_1 regularized recovery of the slip distribution produces a maximum slip of 43.7 m ($\tau = 2300$), identifies all of the known slipping dislocations, and falsely identifies 14 (6%) of the non-slipping rectangular dislocations (Figure 3.2e). The damped least squares recovery of the slip distribution produces a maximum slip of 38.4 m ($\alpha = 10^{-8}$), identifies all of the slipping rectangles, but falsely identifies 270 (38%) slipping rectangular dislocations (Figure 3.2f).

To test the ability of sparsity promoting regularization to recover small-scale variations, 30 m of slip are imposed on a subset of 44 of the rectangular dislocations in the shape of a ring (Figure 3.2g). With an optimality tolerance of 10^{-4}, and no synthetic noise, the ℓ_1 regularized recovery of the slip distribution produces a maximum slip of 52 m, identifies all of the known slipping dislocations, falsely identifies 9 (1%) of the non-slipping rectangular dislocations (Figure 3.2h), but also fails to recover 2 of the known slipping dislocations. The damped least squares recovery of the slip distribution produces an average of 33 m of slip, identifies all of the slipping rectangles, but falsely identifies 124 (13%) slipping rectangular dislocations (Figure 3.2i).

In addition to checkerboard style resolution tests, another measure of model resolution for an underdetermined inverse problem is by calculation of matrix $\mathbf{R}_m = \mathbf{G}^{\mathrm{T}}\mathbf{G}$, in which $\mathbf{G}$ is the generalized Jacobian relating station location to slip on rectangular dislocations. For an underdetermined inverse problem, $\mathbf{R}_m$ is a nonidentity symmetric matrix, and the trace of $\mathbf{R}_m$ provides a quantitative measure of the resolution of the model. Figure 3.3 shows the trace of $\mathbf{R}_m$ mapped onto its respective rectangular dislocations. The magnitude of the trace of $\mathbf{R}_m$ decreases to near zero less than 20 km from the trench, and therefore rectangular dislocations near the trench are poorly resolved. We additionally identify the 33% least resolved rectangular dislocations (Figure 3.3).

In all of the resolution tests, sparsity promoting regularization falsely identifies fewer slipping rectangular dislocations than damped least squares, and is therefore less likely to artificially smear fault slip rates beyond their physical extent. Both regularization methods lose recovery ability with distance from the coast (Figure 3.3). The most poorly resolved

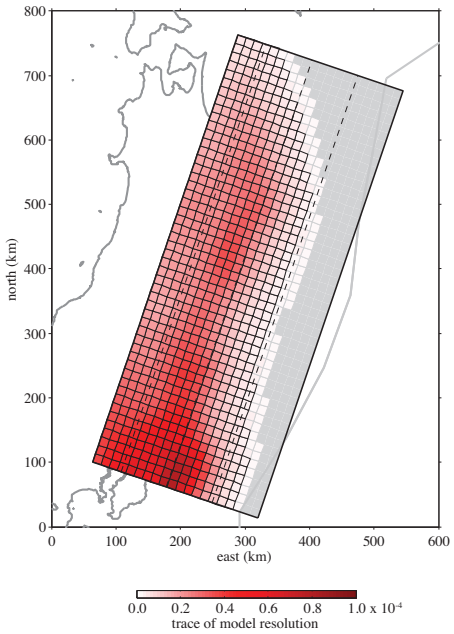

Figure 3.3: Trace of the matrix $\mathbf{R}_m = \mathbf{G}^{\mathrm{T}}\mathbf{G}$ mapped onto rectangular dislocations. Rectangular dislocations with larger magnitudes are better resolved. Dislocations shown in grey or with grey outlines represent the 33% least resolved rectangular dislocations.

33% of rectangular dislocations occur shallower than about 20 km depth (Figures 3.3, 3.2, 3.7), suggesting slip on the shallowest portion of the subduction zone interface cannot be resolved using onshore GPS data [e.g., Loveless and Meade, 2010].

3.4 τ SELECTION

The value of τ in the least absolute shrinkage and selection operator controls the tradeoff between sparseness of the solution slip distribution and model fit to the data. When τ is very small, the ℓ_1 norm of the solution is constrained to be small, so the solution will be sparse, but the fit to the data may be poor. Likewise, increasing τ weakens the constraint on the ℓ_1 norm, improving model fit to the data, but the solution may not be sparse. We quantify model fit with mean residual displacement (MRD). Conditions for sparse recoverability are based

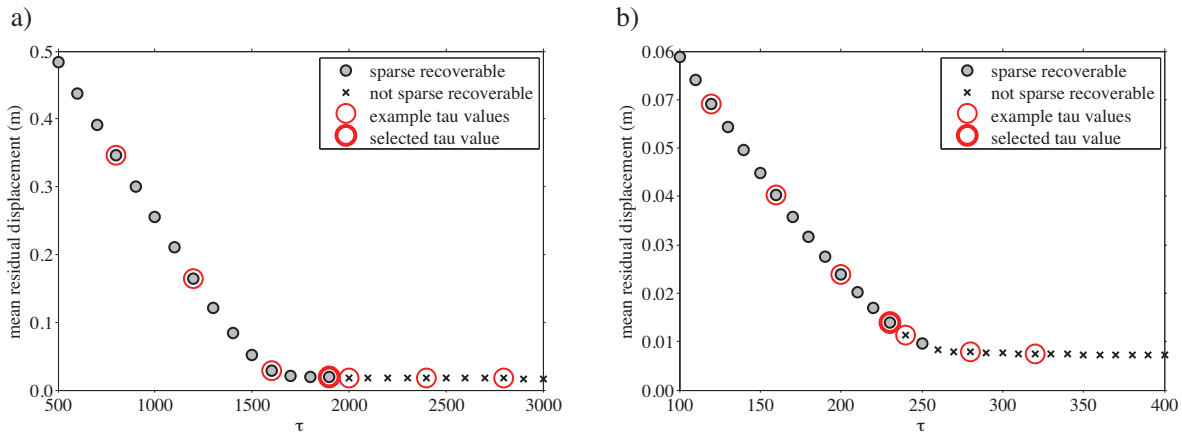

Figure 3.4: τ selection a) Mean residual displacement for increasing τ for coseismic slip distributions. Example slip distributions shown in 3.5. b) Mean residual displacement for increasing τ for postseismic slip distributions. Example slip distributions shown in 3.5 and 3.6.

on the Donoho-Tanner phase transition [Donoho and Tanner, 2009], relating the number of nonzero estimated parameters to problem size. For a problem of the size we consider here, with 596 observations and 1000 estimated parameters, a slip distribution may be considered sparse recoverable when the ratio of nonzero estimated parameters to total observations is less than 0.26. These values show that our system is underdetermined and the estimated number of non-zero model parameters satisfies the Donoho-Tanner condition for ℓ_0 recovery.

To select a τ value, we choose the distribution with the best fit to the data, defined by the smallest MRD, that still satisfies conditions for a sparse recoverable problem [Donoho and Tanner, 2009]. This choice is illustrated in Figure 3.4, which shows decreasing MRD with increasing τ for both coseismic (Figure 3.4a) and postseismic (Figure 3.4b) regimes. Solutions satisfying the Donoho-Tanner constraints for sparse recoverability are represented with gray circles. The postseismic case shows some oscillation between sparse and dense solutions for $\tau = 230$ to $\tau = 260$, so we choose the τ with the lowest MRD below this

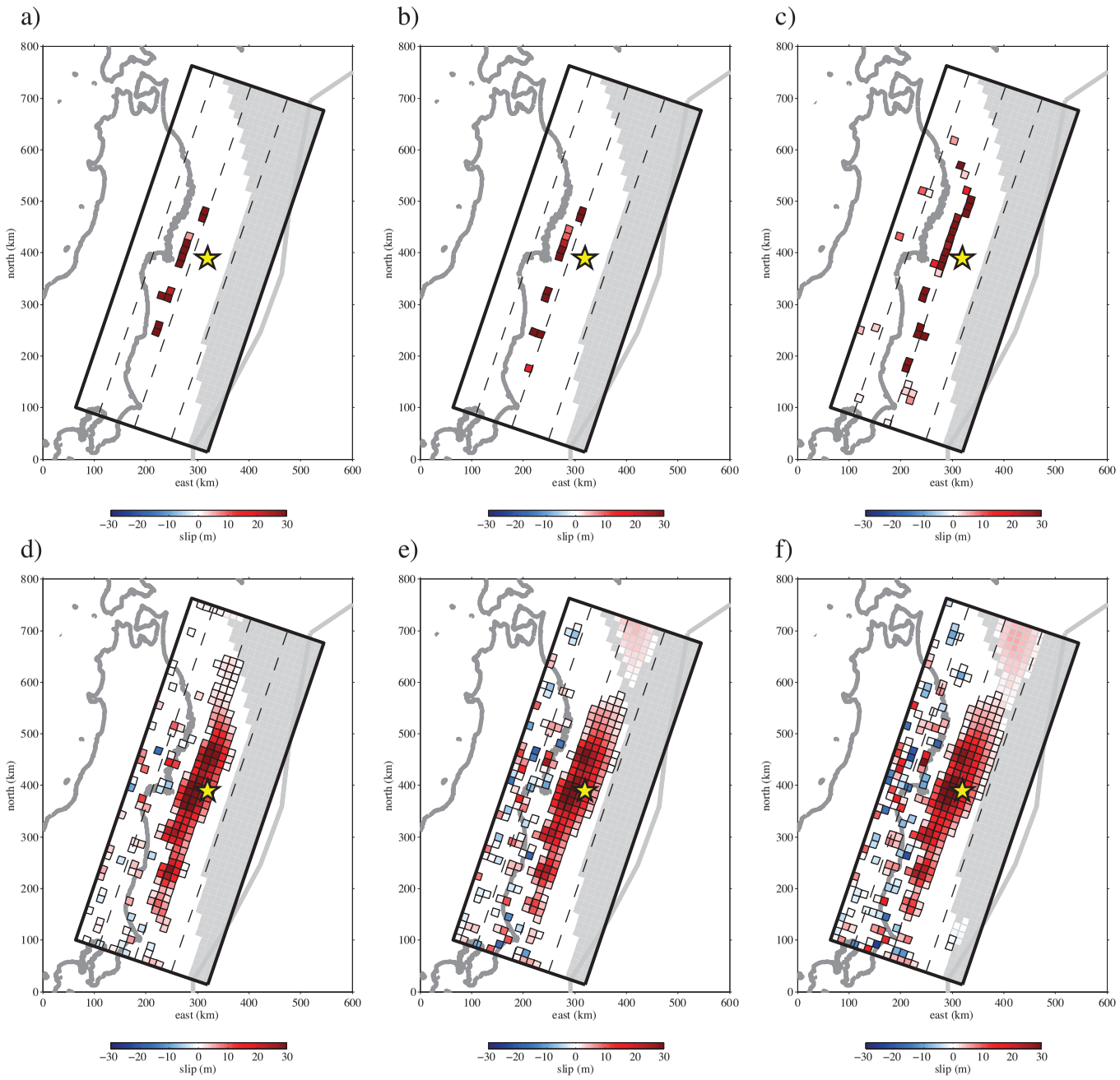

Figure 3.5: Estimated coseismic slip distributions for values of tau circled in 3.4a. a) $\tau = 800$, b) $\tau = 1200$, c) $\tau = 1600$, d) $\tau = 2000$, e) $\tau = 2400$, f) $\tau = 2800$.

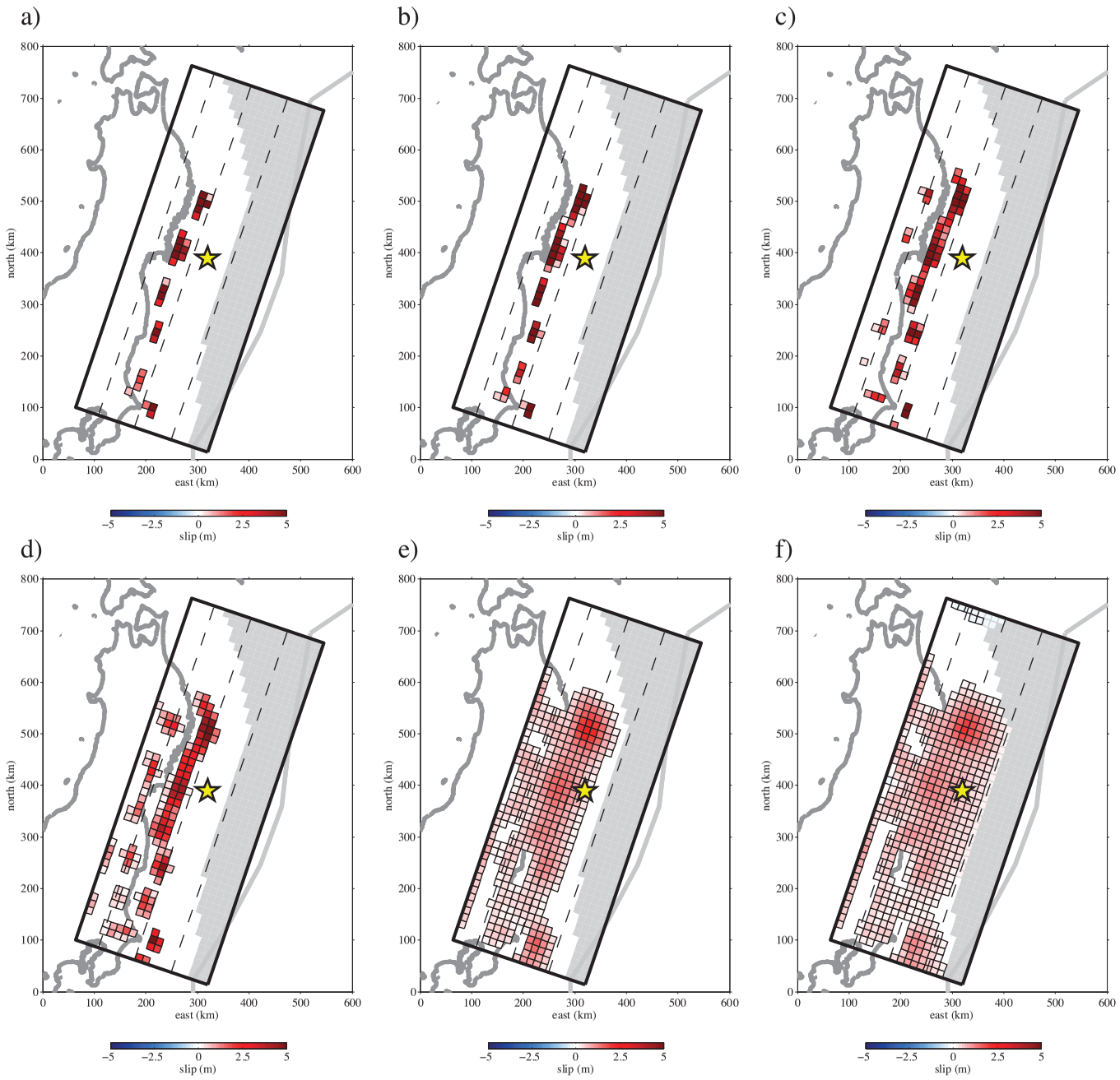

Figure 3.6: Estimated postseismic slip distributions for values of tau circled in 3.4b. a) $\tau = 120$, b) $\tau = 160$, c) $\tau = 200$, d) $\tau = 240$, e) $\tau = 280$, f) $\tau = 320$.

transition range.

To demonstrate the change in slip distribution with increasing τ, we show example slip distribution for τ values ranging from $\tau = 800$ to $\tau = 2800$ in the coseismic case (Figure 3.5) and $\tau = 120$ to $\tau = 320$ in the postseismic case (Figure 3.6). The τ values for the example distributions are outlined in red in Figure 3.4, as are the final selected values: $\tau = 1900$ (coseismic) and $\tau = 230$ (postseismic).

Due to the presence of observational noise in real geodetic observations, the convergence criterion for the minimization algorithm (SPGL1, http://www.cs.ubc.ca/ mpf/spgl1/)[van den Berg and Friedlander, 2009] is relaxed to an optimality tolerance of 8×10^{-3}.

3.5 Coseismic and postseismic slip distributions

Sparsity promoting estimation of coseismic slip ($\tau = 1900$) identifies a linear trend of 10-60 m slip in a relatively narrow depth range between 20 and 40 km depth and extending 500 km along strike (Figure 3.7a). This slip distribution results in a mean residual displacement of 0.02 m at the 298 GPS stations (Figure 3.8a). We estimate a moment for this distribution of 2.1×10^{22} Nm, and a moment magnitude of M_W=8.8 (assuming shear modulus $\mu = 58$ GPa, calculated from Nishida et al. [2008]), which represents a minimum magnitude estimate because slip may occur up-dip of the shallowest slip estimated here, but cannot be recovered with the onshore data.

For comparison, we estimate coseismic slip using underdetermined damped least squares. With a smoothing parameter $\alpha = 10^{-4}$, the area of maximum estimated slip extends about 200 km along strike and is concentrated in the depth range between 30 and 40 km, with

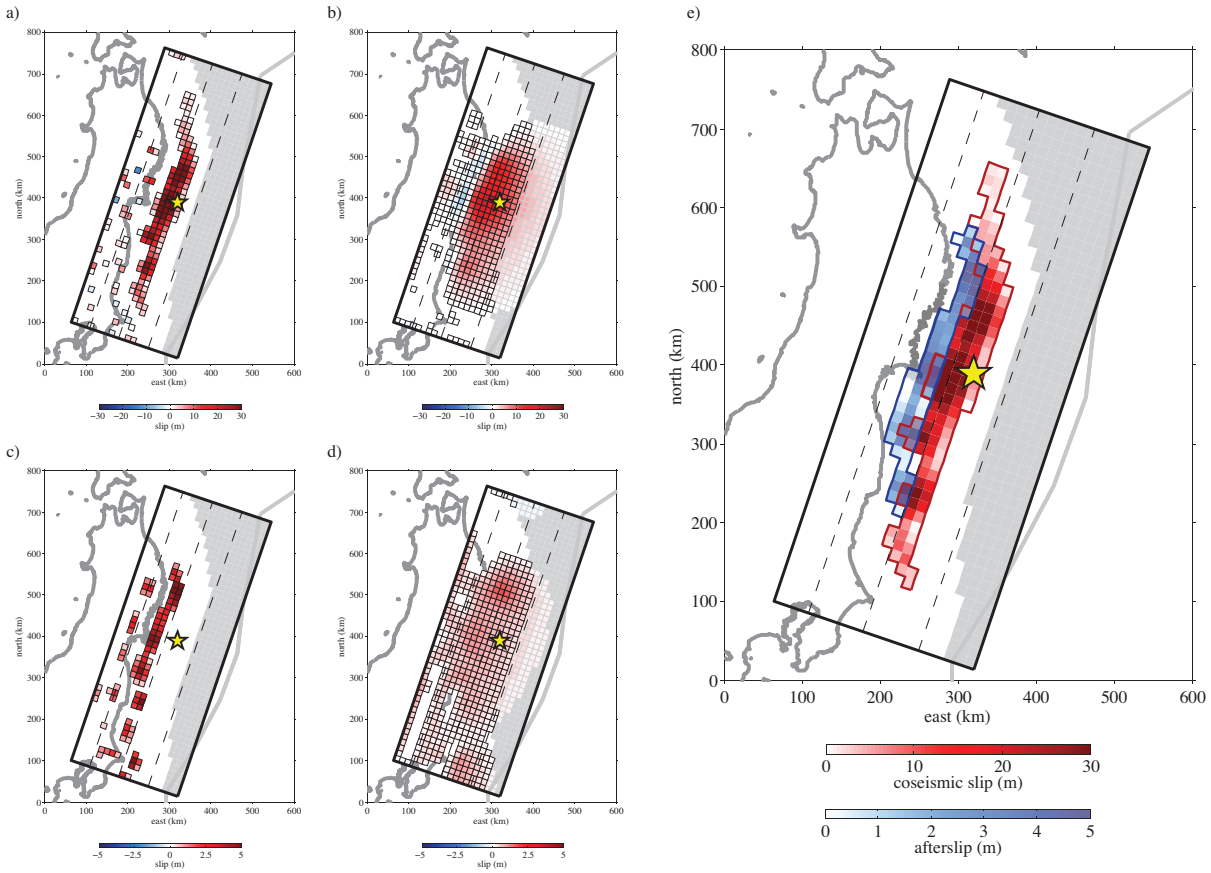

Figure 3.7: Comparison of sparsity promoting and smooth regularization methods for coseismic slip and postseismic afterslip. The 33% least resolved rectangular dislocations shown in gray. a) Sparsity promoting estimate of coseismic slip; b) Damped least squares estimate of coseismic slip; c) Sparsity promoting estimate of postseismic afterslip; d) Damped least squares estimate of postseismic afterslip; e) Combined coseismic and postseismic slip: largest contiguous coseismic slipping region shown in red, and largest contiguous postseismic region shown in blue. The distributions overlap in 13 rectangular dislocations between 40 and 50 km depth.

a maximum estimated slip of 21 m (Figure 3.7b). This slip distribution results in a mean residual displacement of 0.02 m (Figure 3.8b). We estimate a moment of 2.5×10^{22} Nm and a moment magnitude of M_W=8.9 for the smooth distribution. For consistent interpretation of both regularization methods, as with the resolution tests, we consider recovery of slip

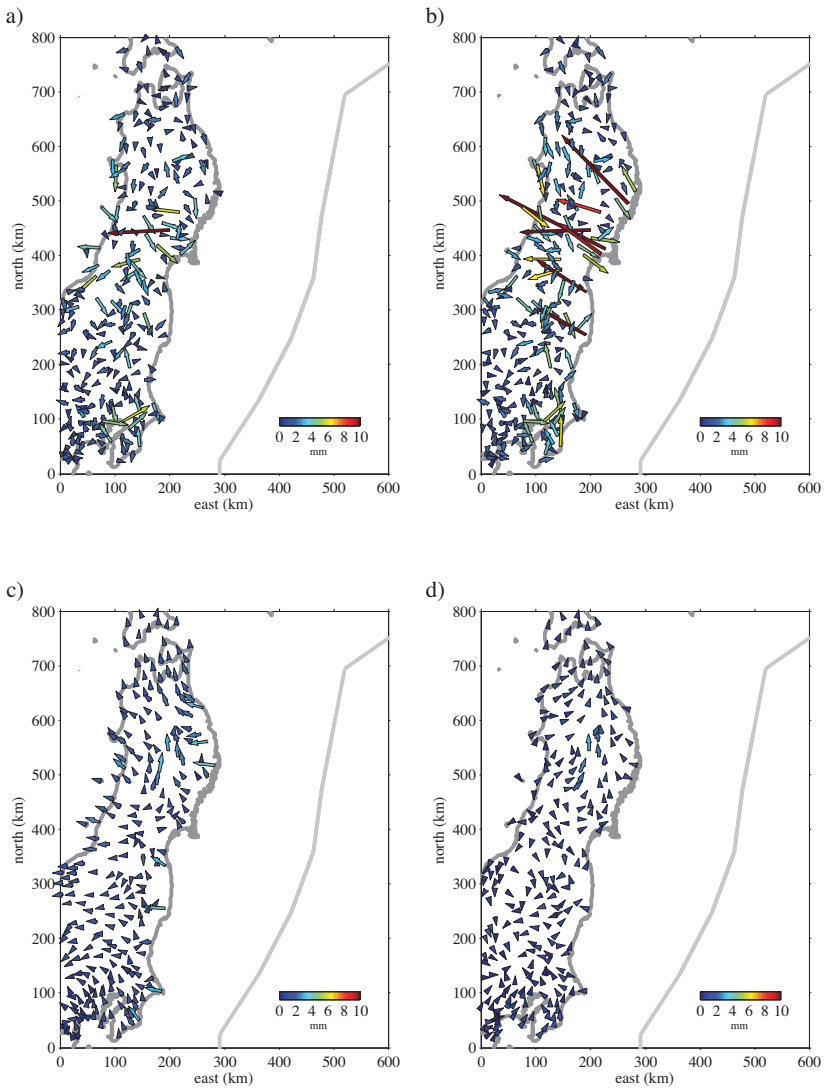

Figure 3.8: Residual displacements for a) sparsity promoting coseismic slip distribution, b) damped least squares coseismic slip distribution, c) sparsity promoting postseismic afterslip distribution, and d) damped least squares postseismic afterslip distribution.

greater than 50 cm as identifying a slipping dislocation in both sparsity promoting and damped-least-squares estimates of coseismic slip.

Surface displacements in the postseismic period of the earthquake cycle may be attributed to a combination of afterslip, viscoelastic relaxation, and poroelastic rebound. For simplicity and for direct comparison with coseismic slip, we attribute all postseismic deformation to af-

terslip, as did Ozawa et al. [2011]. Estimated afterslip magnitudes are therefore a maximum. We estimate ℓ_1 regularized postseismic afterslip with the same process as with coseismic slip, with $\tau = 230$. The sharply varying estimate of afterslip identifies a linear trend of 1–4 m slip downdip of the coseismic estimate at 40 km depth. Estimated afterslip does not propagate as far as coseismic slip, extending 200 km along strike (Figure 3.7c). Total estimated afterslip is equivalent to a moment of 2.6×10^{21} Nm, and M_W=8.2. This slip distribution results in a mean residual displacement of 0.01 m (Figure 3.8c).

As with coseismic slip, we also estimate afterslip using underdetermined damped least squares. With a smoothing parameter $\alpha = 10^{-4}$, the area of maximum estimated slip extends about 200 km along strike and is concentrated in the depth range between 30 and 40 km (Figure 3.7d). We estimate an equivalent moment of 2.3×10^{21} Nm, and M_W=8.3. This slip distribution results in a mean residual displacement of 0.01 m (Figure 3.8d). For afterslip distributions, we consider recovery of slip greater than 20 cm as identifying a slipping dislocation in both sparsity promoting and damped-least-squares estimates of afterslip.

3.6 Discussion

We estimate postseismic afterslip following the Tohoku earthquake almost completely downdip of and distinct from the region of coseismic slip. To directly compare the sharply varying estimates of coseismic and postseismic slip, we identify the largest contiguous slipping patches in both distributions (Figure 3.7e). The two regimes are largely distinct from one another, overlapping at 13 rectangular dislocations (1% of the total modeled fault surface area). Overlap between the lower extent of contiguous coseismic slip and the upper bound

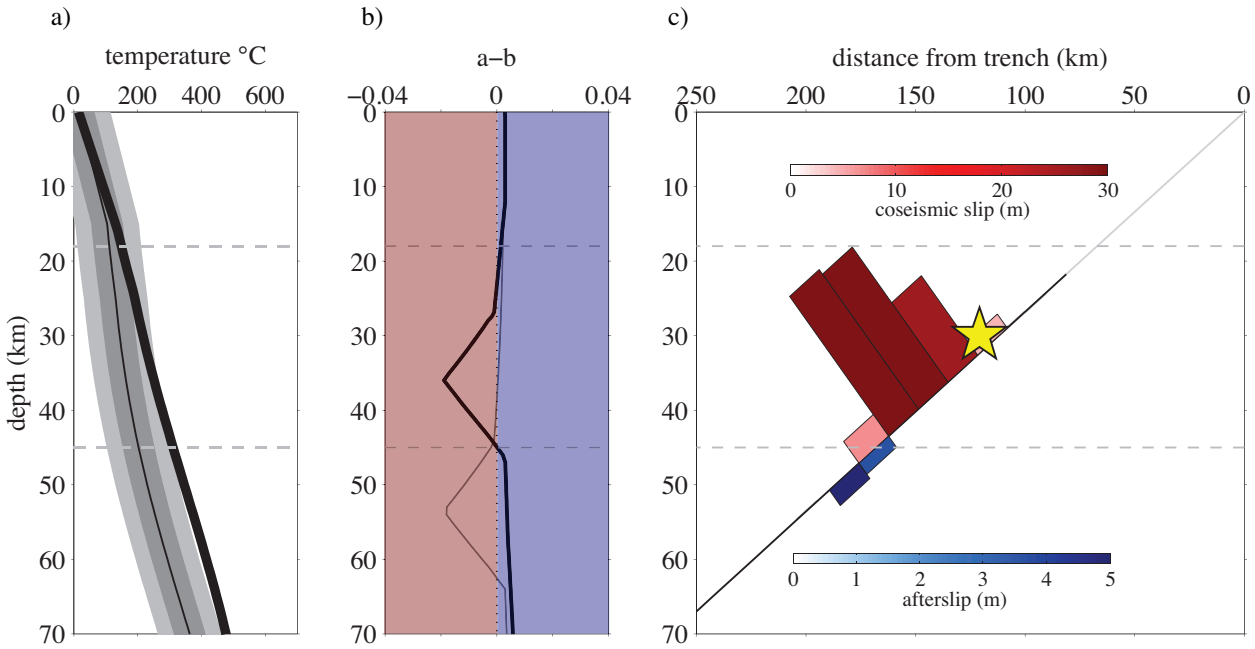

Figure 3.9: Sparse slip distributions and subduction zone temperature. a) Temperature profile +/−50 and 100° C from Peacock and Wang [1999], and temperature profile based on modified a-b profile (thick black line) b) a-b from He et al. [2007], calculated from temperature profile of Peacock and Wang [1999] (grey line) and adjusted based on transition between coseismic slip and postseismic afterslip (black line) negative a-b values are velocity weakening (pink), and positive a-b values are velocity strengthening (blue) c) cross section of model fault surface showing slip rates and hypocenter (yellow star). Dashed gray lines represent predicted region of velocity weakening. The updip portion of the fault is shown in gray where resolution is limited.

of postseimic afterslip occurs between 40 and 50 km depth. This afterslip distribution is in contrast to the distribution estimated by Ozawa et al. [2011], where afterslip spans a broad region of the fault and almost completely overlaps with the region of estimated coseismic rupture. Our smoothed distributions of co- and postseismic slip estimated with damped least squares are consistent with the spatial extent of slip estimated by Ozawa et al. [2011], in which smoothness is imposed by damping roughness within a Bayesian framework [Yabuki and Matsu'ura, 1992]. These smooth distributions limit the identification of a potentially sharp mechanical boundary between the two regimes. Although neither coseismic nor postseismic

slip distribution extends more shallowly than 25 km depth, we do not suggest the absence of up-dip slip, only that onshore geodetic data alone are insufficient to uniquely resolve near trench behavior (§3.3, Loveless and Meade [2010]).

The spatial distinction between regions of coseismic and postseismic slip may be attributed to a transition from velocity weakening frictional properties, where earthquakes nucleate, to velocity strengthening frictional properties that allow for stable sliding [e.g., Tse and Rice, 1986; Marone et al., 1991; Scholz, 1998]. Rock friction experiments on gabbro [He et al., 2007], and granite gouge [Blanpied et al., 1995] suggest a temperature controlled transition from velocity weakening to velocity strengthening behavior at 250–300° C. Using a temperature profile model of the subduction zone off the coast of Tohoku [Peacock and Wang, 1999] the lower transition from velocity weakening to velocity strengthening should occur at 65 km depth, over 20 km deeper than the imaged transition between co- and postseismic slip. To demonstrate a potential application of sharply resolved slip distributions, we use the imaged transition zone depth to modify the temperature profile on the subduction zone. The modified temperature profile is within the 50–100° C uncertainty in the Peacock and Wang [1999] above 50 km, and the modified a-b profile predicts velocity weakening in the depth range of 18-43 km (Figure 3.9).

3.7 Conclusion

Sparsity promoting estimation techniques can recover compact and sharply varying slip distributions that fit geodetic observations as well as smoothed distributions, and allow quantitative assessment of the spatial relationship between coseismic slip and the rest of

the earthquake cycle. Sparsity promoting estimates of slip in the great Tohoku earthquake identify a linear trend of slip between 20 and 40 km depth with a maximum coseismic slip of 64 m, and a narrow transition zone between coseismic slip and postseismic afterslip at depths of 40–50 km. Interpreted as a transition in idealized temperature-dependent frictional behavior from velocity weakening to velocity strengthening, this depth range is consistent with the warmest limit of estimated temperature profiles of the Japan trench subduction zone. In this sense, the ability to image sharp boundaries to co- and postseismic slip provides new images of earthquake cycle processes that may be used to constrain the thermal structure of subduction zones and the depth profile of frictional behavior.

Chapter 4

Sparse imaging of postseismic afterslip following the 2011 Tohoku earthquake

Geodetic observations following the 2011 M_w 9.0 Tohoku earthquake record time-dependent surface motions and provide constraints on the spatial and temporal evolution of postseismic afterslip. Postseismic afterslip behavior bears on hypotheses related to static stress transfer, characteristic rupture theory, and the existence of mechanical asperities. By assuming that afterslip should be consistent with stress transfer theory, we explore multiple solution methods to identify co- and postseismic slip models that fit GPS observations and are consistent with predictions from Coulomb failure stress. Traditional geodetic imaging methods rely on the assumption that slip varies smoothly, which limits resolution of slip boundaries that may impact interpretation of the physical properties of the fault. As an alternative, we apply a sparsity-promoting ℓ_1 regularization algorithm (lasso) to estimate postseismic afterslip based on horizontal GPS displacements during and in the year following the Tohoku earthquake. Sharpened imaging of co- and postseismic slip identifies spatially distinct slipping patches, that are most consistent with afterslip predicted by Coulomb failure stress.

4.1 Introduction

The nature of postseismic deformation following large earthquakes has been the subject of considerable research to understand the physical properties of the seismogenic crust and subduction zone mechanics. Observations of large postseismic deformation have been used to infer frictional properties of subduction zone faults [e.g., Chlieh et al., 2007; Paul et al., 2007; Evans and Meade, 2012] and estimate rheological properties of the mantle and upper crust [e.g. Ueda, 2003; Panet et al., 2010; Kogan et al., 2011; Hoechner et al., 2011; Hu and Wang, 2012; Rousset et al., 2012; Lubis et al., 2012; Kogan et al., 2013]. The location of quasi-static postseismic afterslip relative to coseismic rupture has frequently been estimated downdip of the coseismic rupture [Hsu et al., 2002; Chlieh et al., 2004, 2007; Paul et al., 2007; Vigny et al., 2011], and both up- and downdip [e.g., Hsu et al., 2006], although afterslip roughly co-located with coseismic slip has also been observed [e.g., Lubis et al., 2012]. Following the 2011 Tohoku earthquake, static afterslip in the 14–564 days after the earthquake has been observed both downdip of the coseismic rupture [Ito et al., 2011; Fukuda et al., 2013; Diao et al., 2013; Evans and Meade, 2012] and largely overlapping with coseismic rupture [Ozawa et al., 2011].

The geometry of co- and postseismic slip, and the extent of overlap between these regimes, may depend on estimation method [Evans and Meade, 2012]. This uncertainty limits interpretation of these regions in terms of the physical and thermal properties of the subduction zone. Sparse estimation methods such as the least absolute shrinkage and selection algorithm (lasso) [Tibshirani, 1996] that take advantage of breakthroughs in compressive sensing [Donoho, 2006; Candès et al., 2006] are able to identify sparse, sharply bounded slip regions,

in which slip goes to zero over most of the fault plane. The ability to define compact and finite regions of slip allows slip estimates to be directly compared with other observables on the fault surface. Assessing whether or not these sharply bounded estimates are a better representation of fault behavior remains a challenge.

In the absence of direct (i.e., on fault) observations of the relative locations of co- and postseimic slip, stress transfer calculations such as Coulomb failure stress (CFS) change and rate and state friction theory make predictions about postseismic phenomena. CFS change following large earthquakes has been used to predict aftershock locations [e.g., King et al., 1994; Harris and Segall, 1987; Pollitz and Sacks, 2002; Ishibe, 2011], and as a potential mechanism to explain regional earthquake sequences [e.g., Stein et al., 1994; Pollitz and Sacks, 2002; Pollitz, 2004; Wiseman and Bürgmann, 2011]. In terms of aseismic afterslip on the seismogenic fault, CFS has also been used to predict the location and intensity of afterslip [e.g., Barbot et al., 2009]. However, this type of analysis may be limited by uncertainty in the geometry of the main shock [Steacy et al., 2004].

We estimate postseismic afterslip from GPS observations over one year following the 2011 Tohoku earthquake and solve for time-dependent afterslip on an idealized planar array of rectangular dislocation elements [Okada, 1985, 1992] using a sparsity promoting solution method to recover sharp boundaries to afterslip. We compare this sharp slip distribution with CFS predicted by coseismic slip estimates. To explore the range of physically plausible postseismic afterslip models that explain geodetic data, we then develop a method to identify co- and postseismic slip models that are most consistent with predictions from CFS change using both sharp and smooth estimation methods. We find that sparse, sharply bounded co-

and postseismic slip distributions, as opposed to slip distributions with smooth boundaries, are more consistent with the theory that afterslip will be promoted in regions of positive CFS change.

4.2 Sparse estimation theory

A suite of recent regularization methods take advantage of the sparsity promoting properties of absolute value (ℓ_1 norm) regularization, as discussed in §3.2. In the least absolute shrinkage and selection algorithm (lasso) [Tibshirani, 1996], which we use here, the trade-off between sparseness of the solution and model fit to the data is controlled by tunable parameter τ:

$$\min \|\mathbf{Gm} - \mathbf{d}\|_2 \text{ subject to } \|\mathbf{m}\|_1 \leq \tau \tag{4.1}$$

in which $\mathbf{d}$ is the data vector containing horizontal GPS displacements, $\mathbf{m}$ is the solution vector of slip on rectangular dislocations, and $\mathbf{G}$ is the matrix of analytic Greens functions for calculating surface displacements from slip on a rectangular dislocation in a homogeneous elastic half space [Okada, 1985]. We solve the lasso optimization using a spectral projected gradient root finding algorithm [van den Berg and Friedlander, 2009].

4.3 GPS data and Model Geometry

We consider 1178 GPS stations with observations of the March 11, 2011 Tohoku earthquake and for one year (March 12, 2011 to March 12, 2012) following the earthquake (data from the Geospatial Information Authority of Japan) (Figure 4.1). We use only GPS ob-

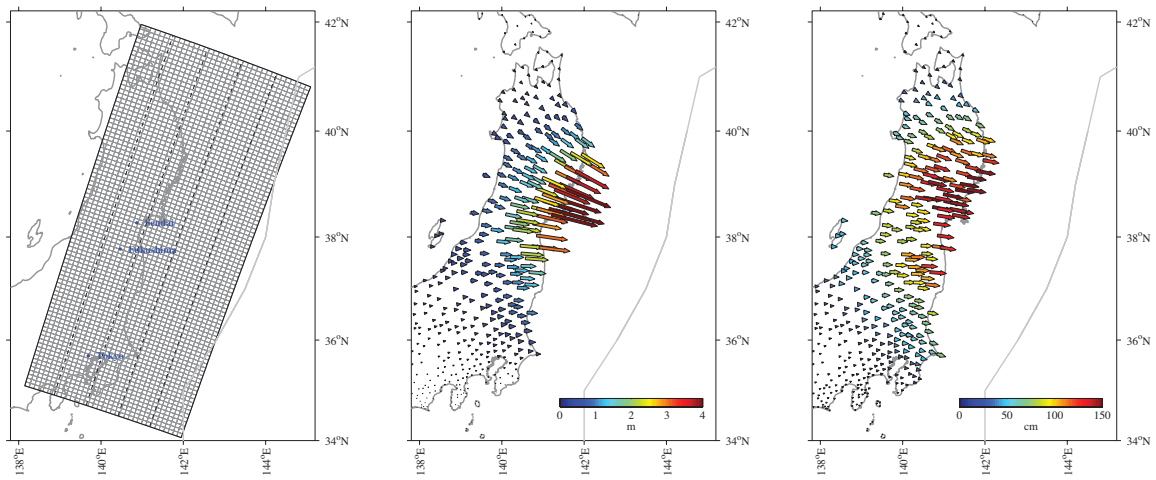

Figure 4.1: Model inputs (a) Rectangular planar mesh consisting of 3080 rectangular dislocations. Model fault extends 700 km along strike and 280 km down dip. (b) Coseismic displacements for Tohoku earthquake c) Cumulative postseismic displacements in 366 days following the earthquake.

servations with missing data on no more than 10 days in the 367 days considered (2012 is a leap year), and additionally require that no more than four consecutive days are missing. For each GPS station with missing observations, we interpolate for the missing data using a piecewise cubic Hermite interpolation (done with the interp1 function in MATLAB) in both the east position and north position. Due to potential complexities in vertical deformation associated with subduction erosion on the Japan subduction zone, [Heki, 2004] we consider only horizontal components of the observations. We do not include displacements from the seven seafloor observations that recorded the coseismic rupture [Sato et al., 2011; Kido et al., 2011] because they also contain at least two weeks of the postseismic period, and we seek to explicitly differentiate between co- and postseismic deformation.

We consider a planar fault extending 700 km along strike and 380 km downdip, with a strike of 199° and a dip of 15° to the northwest and divided into 3080 rectangular dislocations with dimensions 8 km by 10 km (Figure 4.1a). We simplify the subduction zone so that we

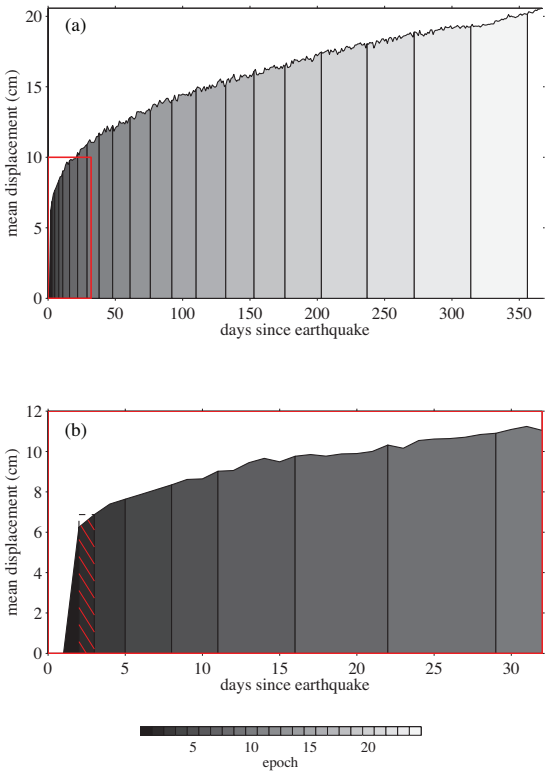

Figure 4.2: Mean cumulative displacement and division of postseismic epochs for (a) 366 days following the earthquake and (b) 35 days following the earthquake. Epochs are based on mean displacements consistent with the second day following the earthquake (epoch 2), shown with red hatching.

consider here the influence of imaging method alone, and not variations in fault geometry. The planar geometry is determined by fitting a rectangular plane to the triangulated mesh of Simons et al. [2011]. All postseismic deformation in the year considered is attributed to elastic afterslip on these rectangular dislocations, and we do not consider viscoelastic effects. Therefore these postseismic estimates likely overestimate slip values and equivalent moment magnitude estimates, especially later in the postseismic period, as some viscoelastic deformation may be attributed to afterslip. However, in the 564 days following the Tohoku earthquake, viscoelastic effects are not required to explain the data [Diao et al., 2013].

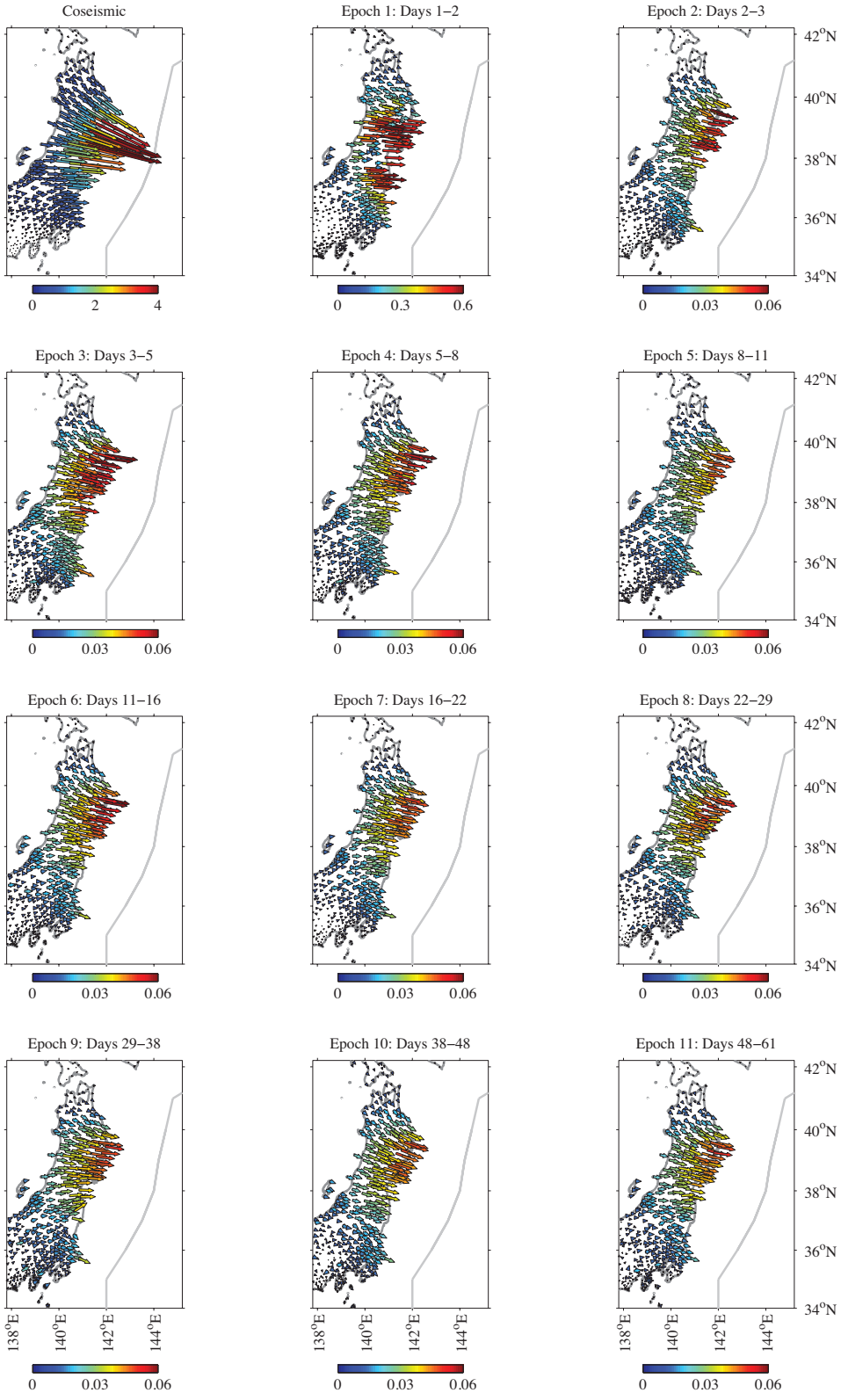

Figure 4.3: Observations for coseismic slip and postseismic epochs 1–11. The color bar axis changes over the first three figures.

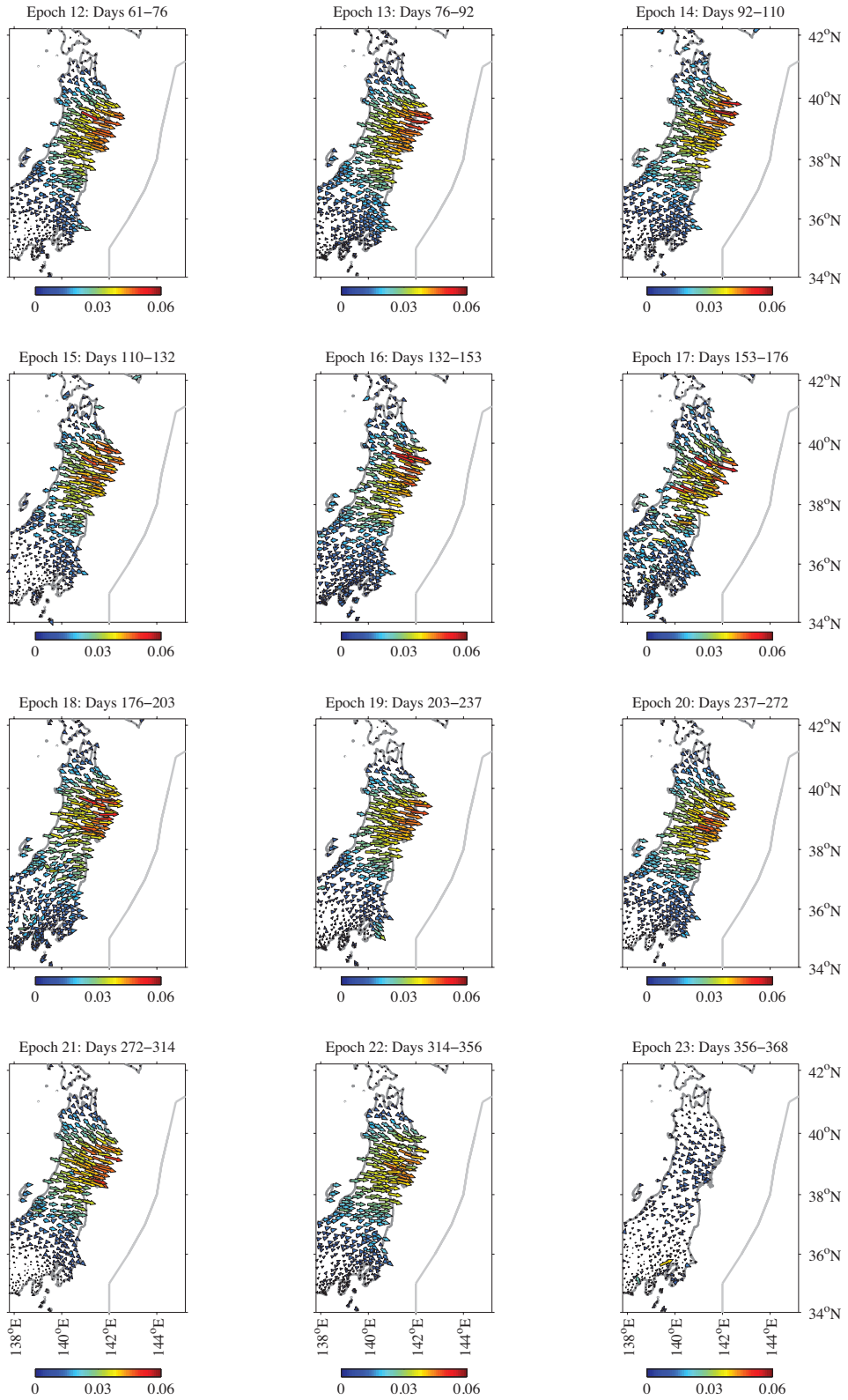

Figure 4.4: Same as Figure 4.3 for postseismic epochs 12–23.

To image postseismic deformation as it evolves in time while maintaining an approximately equal signal-to-noise ratio, we divide the 366-day postseismic period into 23 discrete time epochs of increasing duration such that each timestep includes approximately equal mean displacements (similar to Diao et al. [2013]). The magnitude of postseismic GPS displacements decrease dramatically after the earthquake, and mean displacement in the day following the earthquake (March 12, 2011) are approximately an order of magnitude larger than in the second day following the earthquake (March 13, 2011). Therefore we take mean displacement in the second day following the earthquake (March 13, 2011) as a benchmark (3 cm) for selecting the time epochs for the rest of the postseismic period. We then combine subsequent days until the mean displacement in the combined epoch is equal to that of the second postseismic day: the second day following the earthquake is a single time epoch, days 3-5 following the earthquake are another epoch, days 5-8 are another epoch, and so on for a total of 23 postseismic epochs (Figure 4.2). The final epoch (days 356-366) only contains 10 days and does not reach the threshold mean displacement, with a mean displacement in this epoch of only 1 cm. Additionally, for each postseismic epoch we consider the GPS observations in the reference frame of 12 stations in northern Hokkaido that do not experience displacements due to postseismic deformation in the time period considered. The GPS displacements for each postseismic epoch are shown in Figures 4.3 and 4.4.

To assess the power of the GPS observations to constrain fault behavior, we quantify resolution on the model fault plane as the sum of the displacements at all GPS stations due to unit dip slip on that element (i.e., the sum of the row of the generalized Jacobian related to a given rectangular dislocation) (Figure 4.5). Where this value is large, we expect good

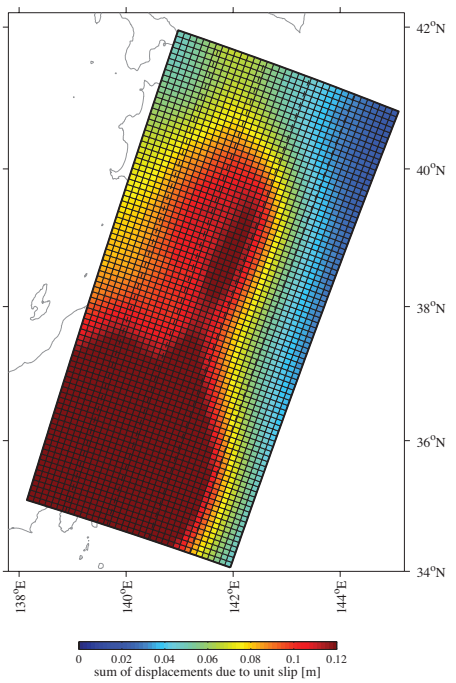

Figure 4.5: Model resolution quantified as the sum of the displacements at all GPS stations due to unit slip on that element (i.e., the sum of the row of the generalized Jacobian related to a given rectangular dislocation).

resolution of features on the fault plane, and we expect poor resolution where this value is small. In particular, depths shallower than ∼30 km depth are poorly resolved.

4.4 Imaging postseismic afterslip: Non-negative slip estimates

4.4.1 Selecting the τ parameter

The parameter τ in the lasso constraint (Equation 4.1) controls the tradeoff between the sparsity of the solution and fit to the data. When τ is zero, all elements in the solution vector are zero. As τ increases, elements in the solution vector become active, and the solution becomes less sparse. This behavior is shown in Figure 4.6a, in which each colored line represents an element in the solution vector. For increasing τ, we plot the value of

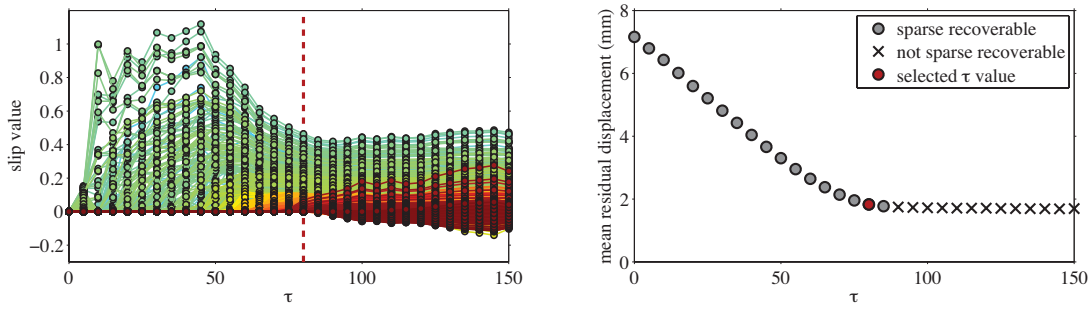

Figure 4.6: τ selection process (shown for epoch 2). a) Each colored line represents slip on a rectangular dislocation element, i.e., an element in the solution vector, for a given value of regularization parameter τ. We select the largest value of τ for which all slip is positive. b) As τ increases, the solution becomes less sparse and the mean residual displacement decreases as fit to the data improves. We additionally ensure that the selected τ value satisfies conditions for sparse recovery. Conditions for sparse recovery are determined by the Donoho-Tanner phase transition [Donoho and Tanner, 2009].

each element (i.e., the slip magnitude on each dislocation). In addition, as the solution becomes less sparse, fit to the data, as measured by mean residual displacement (MRD), improves (Figure 4.6b). We also seek to satisfy conditions for sparse recovery, as defined by the Donoho-Tanner phase transition [Donoho and Tanner, 2009], which relates the number of nonzero estimated parameters to problem size (Figure 4.6b). If the number of nonzero estimated parameters in an underdetermined system is below the Donoho-Tanner phase transition, the solution satisfies the Donoho-Tanner condition for ℓ_0 recovery. For a problem of the size we consider here, with 1178 east and north GPS observations and 3080 estimated parameters, a slip distribution is considered sparse recoverable when the ratio of nonzero estimated parameters to total observations is less than 0.55, or when there are less than 1345 nonzero estimated parameters (slipping dislocations). To find a solution that satisfies conditions for sparse recovery and fits the data well, we select the largest value of τ for which all slip is positive and the solution satisfies conditions for sparse recovery. We follow

this procedure to select distinct τ values for coseismic slip (March 11, 2011), and for each postseismic epoch.

4.4.2 Results from lasso estimation: Part I

To estimate a coseismic slip distribution to compare with postseismic slip, we follow the τ selection algorithm described above to select $\tau = 3500$ with an optimality tolerance of 0.1. This slip distribution fits the coseismic GPS observations with a mean residual displacement of 4.6 cm. We estimate a mean coseismic slip of 35 m on 99 slipping rectangular dislocations with a maximum slip of 124 m, which is ∼60 m greater than other maximum slip estimates for the Tohoku earthquake [Simons et al., 2011; Yao et al., 2011]. The sparseness of this selected solution may indicate that additional slip occurs up-dip where resolution is poor, but the data can be fit just as well with large slip magnitudes where resolution is better.

For the first day of postseismic afterslip (March 12, 2011), we identify $\tau = 924$ with an optimality tolerance of 8×10^{-2}. As with the coseismic estimate, this is the largest (least sparse) τ value for which all afterslip is positive. Here, we estimate slip on 634 dislocations with a maximum slip of 6 m and mean slip of 1.5 m on the slipping dislocations, and fit the GPS observations for this day with a mean residual displacement of 3.4 cm (Figure 4.7). On the second day of postseismic afterslip (March 13, 2011), we identify $\tau = 84.1$ with an optimality tolerance of 10^{-3} (this optimality tolerance is applied to all subsequent epochs). Over the next 20 epochs we estimate slip on 488–1530 dislocations (in epochs 15 and 5, respectively). Maximum slip ranges from 0.3 m in epoch 20 to 1.5 m in epoch 16. In all epochs, we image slip extending ∼600 km along strike and in the depth range of ∼40–50 km. We do not image significant changes in the location and intensity of afterslip (Figures 4.7 and

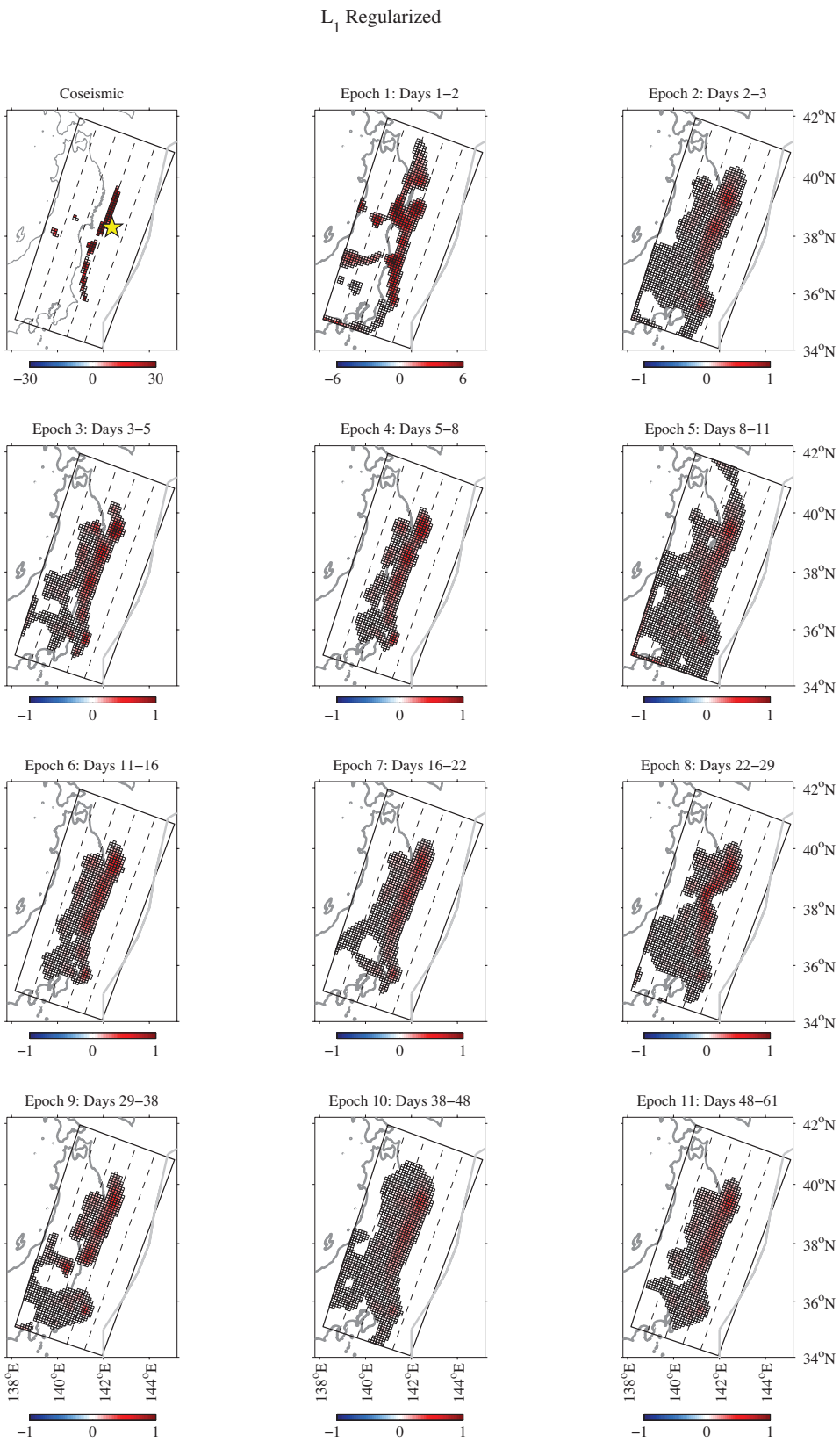

Figure 4.7: Estimated coseismic slip and postseismic afterslip for epochs 1–11. The color bar axis changes over the first three figures.

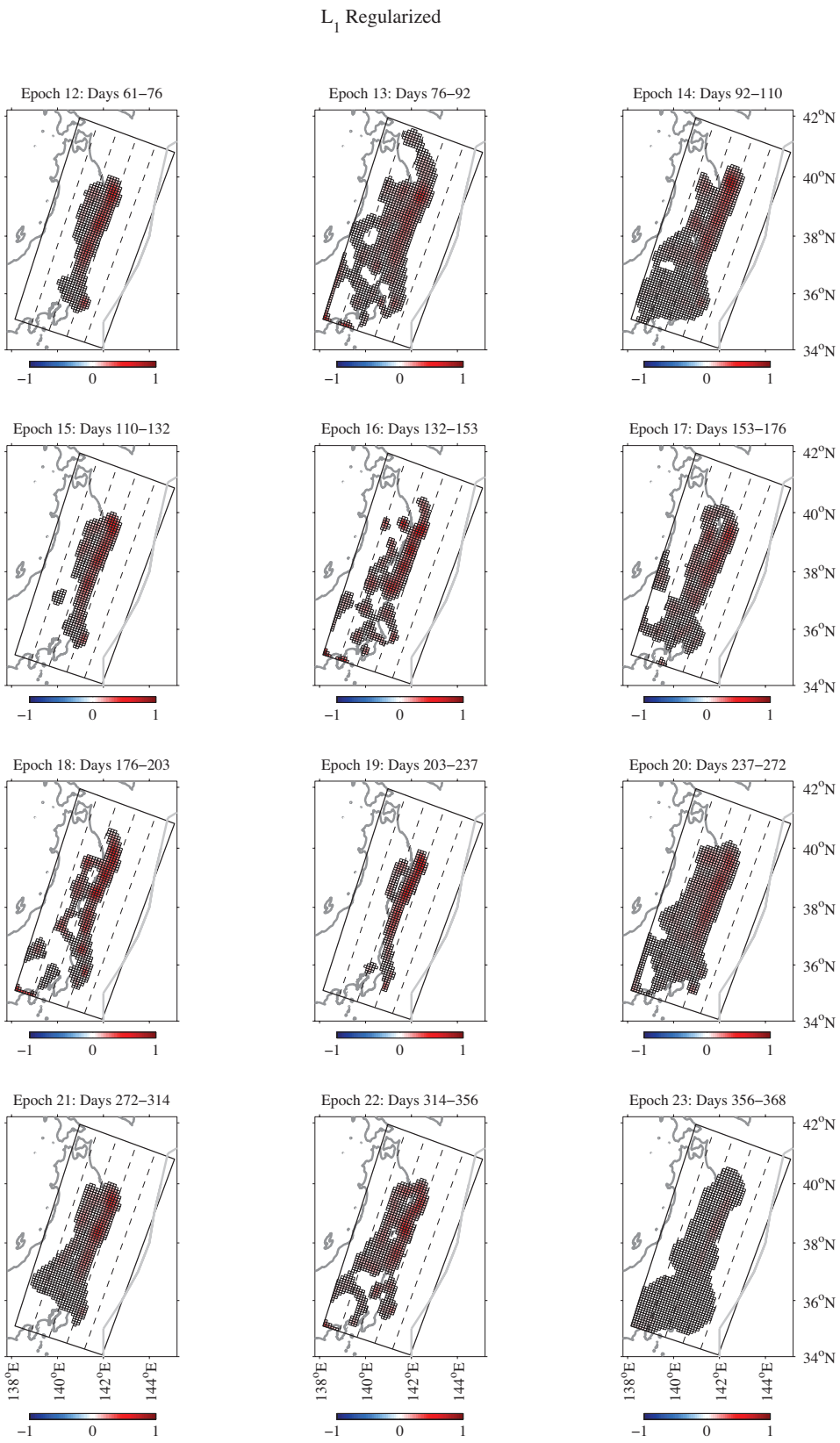

Figure 4.8: Same as Figure 4.7 for postseismic epochs 12–23.

4.8). These afterslip estimates fit the GPS observations with mean residual displacements of 0.2-0.8 cm/epoch. Table 4.1 contains additional statistics for these afterslip estimates.We estimate a total equivalent earthquake moment magnitude for the year days following the earthquake of M_W=8.96. Afterslip in the first day following the earthquake is an equivalent magnitude of M_W=8.4, and equivalent magnitudes of M_W=7.8 per epoch for the rest of the year. These magnitudes are all larger than the cumulative moment magnitude of aftershocks in each epoch, which is M_W=7.9 for the rest of the day on March 11, 2011, M_W=7.2 on March 12, and ranges between M_W=6.3 and M_W=7.3 in each postseismic epoch to follow (earthquake data from Japan Meteorological Agency (JMA)).

EPOCH	τ	Correlation Coefficient	slip/epoch (m)	nonzero elements	mean slip/epoch (m)	max slip/epoch (m)	Mw/epoch	mrd/epoch (cm)
Coseismic	3500.0	-	3500.0	99	35.35	124.9	8.8	4.64
1	924.0	-0.05	924.0	634	1.46	6.2	8.4	3.40
2	84.1	-0.05	84.1	1248	0.07	0.4	7.8	0.18
3	99.0	-0.08	99.0	799	0.12	1.0	7.8	0.28
4	82.2	-0.06	82.2	634	0.13	0.7	7.7	0.28
5	92.2	-0.07	92.2	1530	0.06	0.6	7.8	0.25
6	84.0	-0.06	84.0	734	0.11	0.6	7.8	0.27
7	77.1	-0.05	77.1	802	0.10	0.4	7.7	0.27
8	85.0	-0.03	85.0	1036	0.08	0.5	7.8	0.24
9	81.6	-0.06	81.6	824	0.10	0.5	7.7	0.51
10	83.6	-0.05	83.6	1256	0.07	0.4	7.8	0.41
11	76.0	-0.05	76.0	876	0.09	0.4	7.7	0.34
12	61.9	-0.06	61.9	521	0.12	0.5	7.7	0.43
13	99.5	-0.06	99.5	1153	0.09	0.6	7.8	0.34
14	86.1	-0.05	86.1	1138	0.08	0.5	7.8	0.35
15	61.9	-0.03	61.9	488	0.13	0.5	7.7	0.49
16	88.3	-0.03	88.3	625	0.14	1.5	7.8	0.55
17	79.0	-0.07	79.0	857	0.09	0.4	7.7	0.69
18	83.0	0.03	83.0	636	0.13	0.8	7.8	0.78
19	52.9	0.07	52.9	331	0.16	0.6	7.6	0.54
20	88.1	-0.05	88.1	1092	0.08	0.3	7.8	0.36
21	65.2	-0.05	65.2	778	0.08	0.4	7.7	0.47
22	82.5	-0.01	82.5	744	0.11	0.5	7.7	0.51
23	24.8	0.03	24.8	1205	0.02	0.1	7.4	0.36

Table 4.1: Summary of results for lasso solution in Section §4.4.2

4.4.3 Results from lasso estimation: Part II

Because postseismic epochs 2-22 were selected based on constant mean GPS displacement, we expect the total afterslip in these epochs to be consistent. We therefore additionally

consider afterslip solutions in which we identify only three separate τ values: 1) a τ value for coseismic slip (March 11, 2011), 2) a τ value for the day following the earthquake (March 12, 2011), and 3) a τ value for the second day following the earthquake (March 13, 2011), which we apply to this and all subsequent time epochs (Figure 4.2). In this case, estimated coseismic slip and postseismic afterslip in epochs 1 (March 12, 2011) and 2 (March 13, 2011) are identical to the estimates described above, with coseismic $\tau = 3500$ with an optimality tolerance of 0.1, and $\tau = 924$ for epoch 1 with an optimality tolerance of 8×10^{-2}. On the second day of postseismic afterslip, we identify $\tau = 84.1$ with an optimality tolerance of 10^{-3}, which we apply to this and all subsequent epochs. In this case, over the next 20 epochs we estimate slip on 473-1280 dislocations (in epochs 18 and 7, respectively). Maximum slip ranges from 0.4 m in epoch 15 to 1.7 m in epoch 16. These afterslip estimates fit the GPS observations with mean residual displacements of 0.2-0.8 cm/epoch (Figures 4.9 and 4.10). Table 4.2 contains additional statistics for these afterslip estimates.

We estimate a total equivalent earthquake moment magnitude for the year days following the earthquake of M_W=8.7. Afterslip in the first day following the earthquake is an equivalent magnitude of M_W=8.5, and equivalent magnitudes of M_W=7.8 per epoch for the subsequent epochs.

4.4.4 Discussion of sparse afterslip estimates

Afterslip does not appear to migrate significantly in the time intervals considered, consistent with previous time-dependent postseismic studies [Fukuda et al., 2013; Diao et al., 2013; Johnson et al., 2012]. The location of persistent afterslip downdip of coseismic slip, and minimal overlap between the regimes, may suggest a boundary between rate-weakening

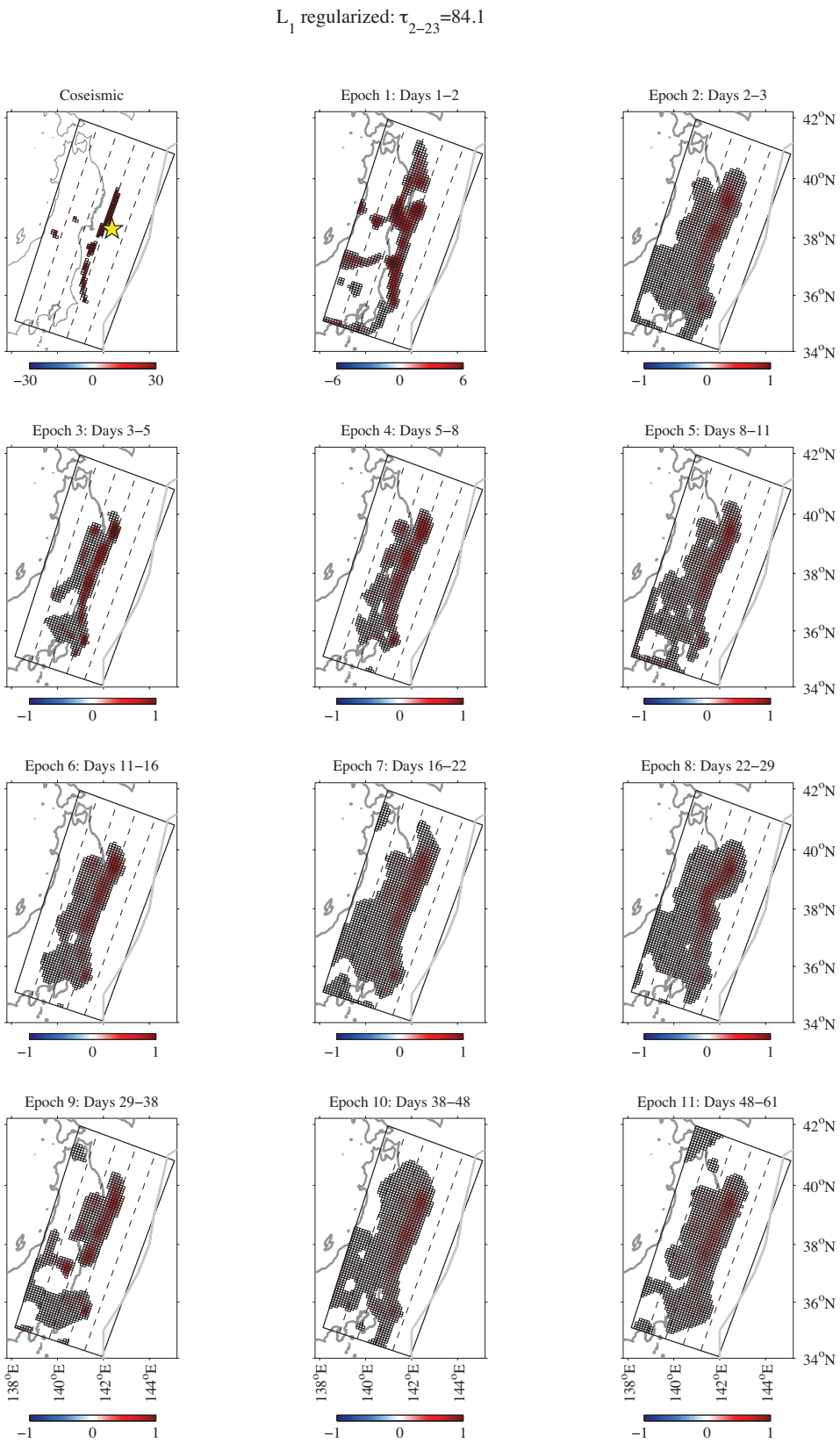

Figure 4.9: Estimated coseismic slip and postseismic afterslip for epochs 1–11. Sparsity parameter τ is selected based on epoch 2, and applied to all subsequent epochs. The color bar axis changes over the first three figures.

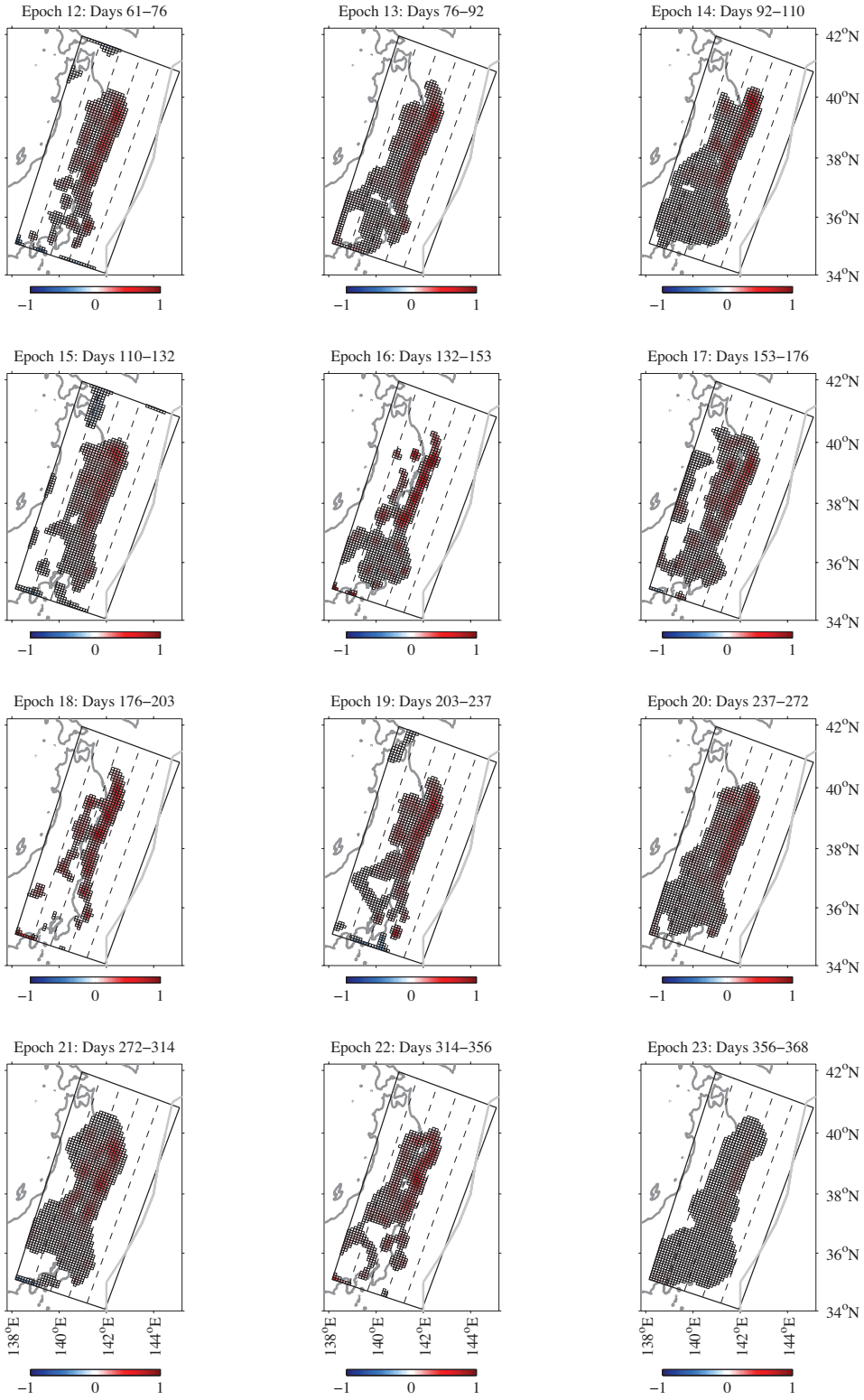

Figure 4.10: Same as Figure 4.9 for postseismic epochs 12–23.

EPOCH	τ	Correlation Coefficient	slip/epoch (m)	nonzero elements	mean slip/epoch (m)	max slip/epoch (m)	Mw/epoch	mrd/epoch (cm)
Coseismic	3500.0	-	3500.0	99	35.35	124.93	8.8	4.6
1	924.0	-0.05	924.0	634	1.46	6.22	8.4	3.40
2	84.1	-0.05	84.1	1248	0.07	0.44	7.8	0.18
3	84.1	0.03	84.1	540	0.16	1.35	7.8	0.32
4	84.1	-0.06	83.8	636	0.13	0.63	7.8	0.27
5	84.1	-0.07	84.1	1032	0.08	0.45	7.8	0.26
6	84.1	-0.06	84.1	789	0.11	0.60	7.8	0.27
7	84.1	-0.05	81.0	1280	0.06	0.35	7.8	0.26
8	84.1	-0.02	84.1	1241	0.07	0.41	7.8	0.24
9	84.1	-0.06	82.4	816	0.10	0.51	7.8	0.50
10	84.1	-0.05	84.1	1269	0.07	0.39	7.8	0.41
11	84.1	-0.04	79.5	1204	0.07	0.37	7.8	0.33
12	84.1	-0.06	70.5	747	0.09	0.40	7.8	0.38
13	84.1	-0.06	84.1	975	0.09	0.45	7.8	0.37
14	84.1	-0.06	84.1	1166	0.07	0.56	7.8	0.35
15	84.1	-0.05	67.8	982	0.07	0.39	7.8	0.46
16	84.1	0.04	84.1	701	0.12	1.74	7.8	0.55
17	84.1	-0.08	82.5	980	0.08	0.41	7.8	0.68
18	84.1	0.04	83.8	473	0.18	0.90	7.8	0.77
19	84.1	-0.05	69.9	778	0.09	0.48	7.8	0.46
20	84.1	-0.05	84.1	1055	0.08	0.34	7.8	0.37
21	84.1	-0.05	77.3	1179	0.07	0.40	7.8	0.41
22	84.1	-0.01	83.6	725	0.12	0.49	7.8	0.51
23	24.8	0.03	24.8	1205	0.02	0.13	7.4	0.36

Table 4.2: Summary of results for lasso solution in Section §4.4.3, with $\tau_{2-23} = 84.1$

and rate-strengthening fault behavior.

Stress perturbation calculations such as Coulomb failure stress (CFS) change and rate and state friction make predictions about the location and intensity of postseismic afterslip [e.g., Barbot et al., 2009]. To assess the extent to which slip distributions estimated here are consistent with stress transfer due to CFS, we calculate static CFS changes (σ_{CFS}) due to our estimate of the Tohoku coseismic slip distribution, projected onto the fault [e.g., King et al., 1994]:

$$\sigma_{\mathrm{CFS}} = \tau_\beta - \mu(\sigma^*_\beta) \tag{4.2}$$

where τ_β is the shear stress on the failure plane, σ^*_β is the effective normal stress (normal stress minus pore fluid pressure), and μ is the coefficient of friction. To illustrate this concept, we calculate CFS changes in two dimensions due to a smooth thrust slip distribution on a

dipping fault plane, projected onto planes parallel to the fault (Figure 4.11a). We expect afterslip to be promoted on the fault plane where CFS change is positive, and restricted where CFS change is negative. The distribution of expected afterslip depends on the initial earthquake slip distribution, and if we consider an earthquake with sharp boundaries, the CFS change distribution changes (Figure 4.11b).

We expect fault regions of positive cumulative CFS change to promote postseismic afterslip, and regions of negative CFS change to suppress afterslip. To assess the consistency of our estimates of postseismic afterslip with these predictions, we calculate CFS changes projected onto the model fault plane, and a find the correlation coefficient between this CFS change and the estimated afterslip for each postseismic time epoch. Afterlip may alter stress on coseismically stressed fault patches, so for each postseismic epoch, we recalculate the CFS change due to cosesimic slip and cumulative postseismic afterslip.

We calculate 95% confidence bounds on the correlation coefficient with a non-parametric bootstrap [Efron, 1979]. We take $\mu = 0.6$, but CFS calculation on the fault plane is insensitive to this value. Because the shallow portion of the fault is poorly resolved, we calculate correlation coefficients only on the best-resolved 50% of the fault plane (Figure 4.5).

When we estimate a new tau value for every epoch, CFS change does not correlate well with estimated afterslip in the year following the earthquake. The correlation coefficients for only four of the subsequent time epochs are positive, and none of the correlations are distinguishable from zero within the 95% confidence bounds (Figure 4.12a).

Afterslip distributions calculated with a single value of tau for epochs 2-22 are only slightly more consistent with CFS change than the distributions in which tau is re-selected

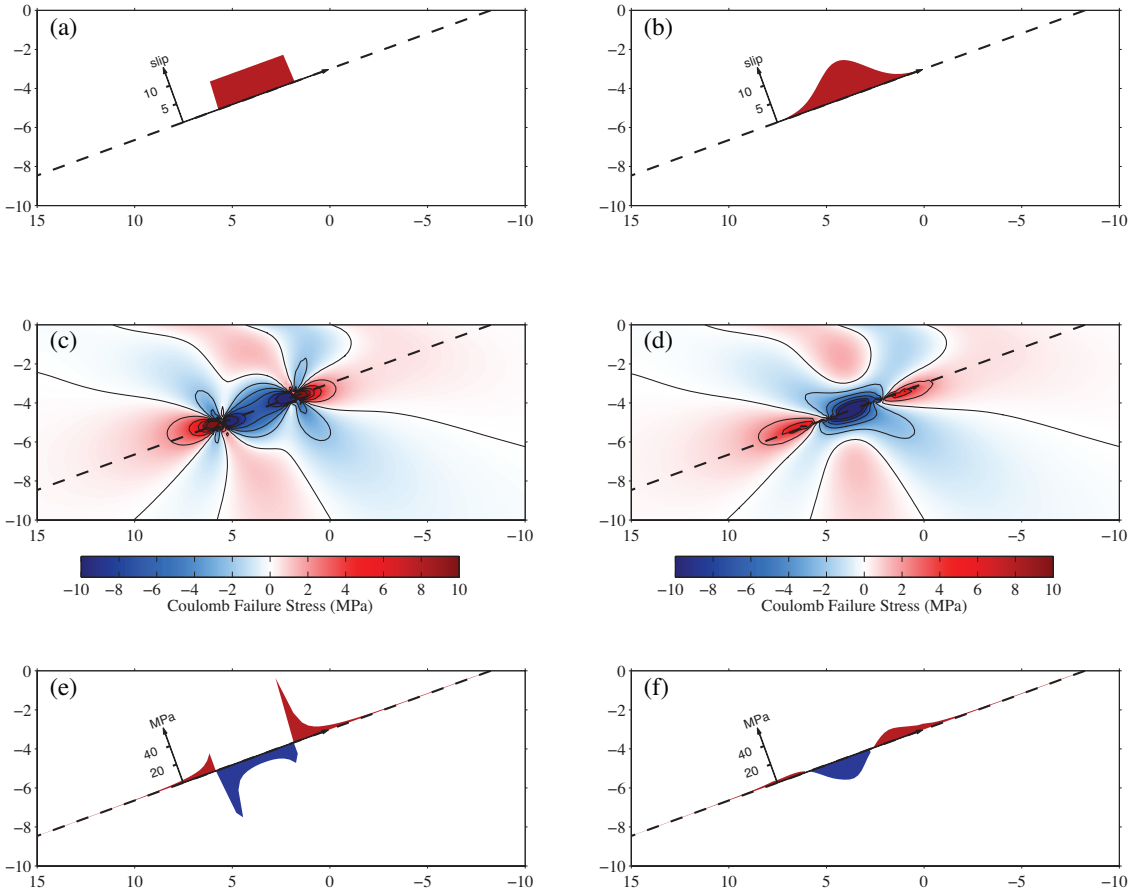

Figure 4.11: Coulomb failure stress (CFS) calculated in 2 dimensions for a) a sharp slip distribution and b) a smooth slip distribution. Panels c) and d) show calculated CFS change in 2 dimensions on lines parallel to the fault. Panels e) and f) show CFS change on the fault.

every epoch. The correlation coefficients for seven of the subsequent time epochs are positive, between 0.01 and 0.12, suggesting some consistency between afterslip and stress transfer, although only two of these correlations are positive within the 95% confidence bounds (Figure 4.12b). This also suggests that slip distributions that are compact and sharply bounded may be more consistent with the hypothesis that afterslip is promoted in regions of positive static CFS change.

An assessment of the extent to which postseismic phenomena are consistent with coseismic CFS changes depends largely on the slip estimates used to calculate stress change [e.g.,

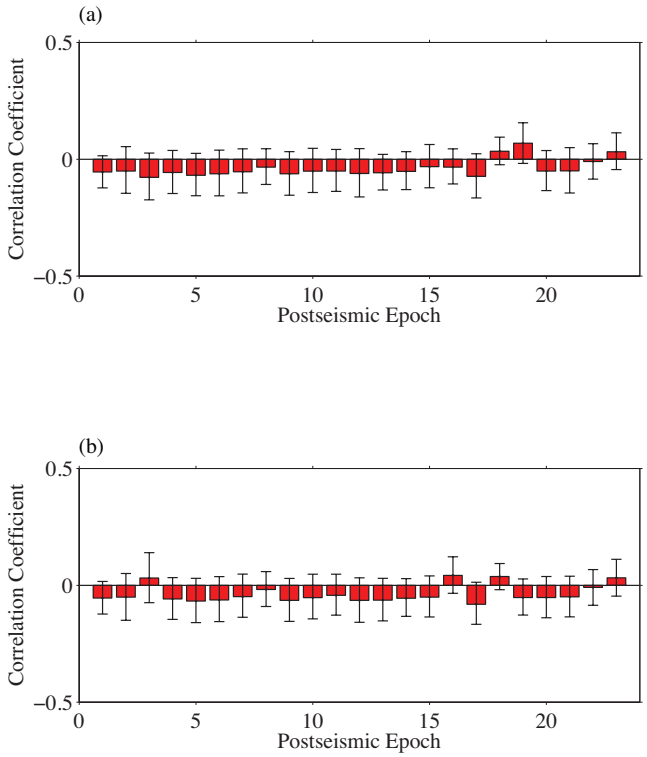

Figure 4.12: Correlation coefficients between cumulative Coulomb failure stress and afterslip distribution per epoch. a) Correlation coefficients for lasso solutions in which a new τ parameter is chosen every epoch. b) Correlation coefficients for lasso solutions in which the τ parameter is chosen for epoch 2, and applied to all subsequent epochs.

Steacy et al., 2004]. Therefore an alternative set of co- and postseismic distributions may be more consistent with the physical expectations from CFS. Furthermore, slip estimated with inverse methods other than the lasso likely result in different slip and stress change distributions. To identify a solution method and set of tuning parameters that give an afterslip estimate that is most consistent with CFS change due to a coseismic slip estimate, we explore several additional estimation methods.

4.5 Estimation methods for Coulomb stress calculation and comparison

In addition to the lasso, we explore three smoothing methods for estimating regularized slip distributions with which to estimate cosesimic stress changes and compare with afterslip estimates: 1) Damped least squares, 2) incorporating an augmented smoothing matrix into an overdetermined weighted least squares problem, 3) spatially variable smoothing [e.g., Menke, 1984].

1) Damped least squares

A straightforward method for solving an underdetermined problem is with damped least squares:

$$\min \|\mathbf{Gm} - \mathbf{d}\|_2 \; + \; \lambda \|\mathbf{m}\|_2 \tag{4.3}$$

where $\mathbf{G}$ is the generalized Jacobian as described in §4.2, $\mathbf{m}$ is the solution slip vector, $\mathbf{d}$ is the data vector, and λ is a scalar tunable parameter that controls the strength of regularization. The first term in the damped least squares formulation minimizes data misfit, and the second term regularizes the data fit by simultaneously minimizing the length/magnitude of the solution vector itself. The smoothing parameter λ controls the strength of this regularization or damping. This term causes all values in the solution to approach zero with increasing λ, and therefore the solution becomes more smooth to the limit at which the solution is all zeros, for very large λ.

2) Augmented smoothing matrix

Augmenting the generalized Jacobian $\mathbf{G}$ with a smoothing matrix $\mathbf{S}$ transforms an otherwise underdetermined problem to an overdetermined least squares problem:

$$\min \|\mathbf{W'}_{\mathrm{d}}(\mathbf{G'm} - \mathbf{d'})\|_2 \tag{4.4}$$

such that

$$\mathbf{G'} = \begin{bmatrix} \mathbf{G} \\ \\ \mathbf{S} \end{bmatrix}, \mathbf{d'} = \begin{bmatrix} \mathbf{d} \\ \\ \mathbf{s} \end{bmatrix}, \mathbf{W'}_{\mathrm{d}} = \begin{bmatrix} \mathbf{W} & \mathbf{0} \\ \\ \mathbf{0} & \beta\mathbf{I} \end{bmatrix} \tag{4.5}$$

The smoothing matrix $\mathbf{S}$ is a square matrix that explicitly defines the desired smoothing properties of the problem, typically based on centroid distances between neighboring mesh elements, so that a dislocation does not slip considerably more or less than its neighbors. Here, S is constructed as follows:

$$\mathrm{S}_{ij} = \frac{-2(\delta_{ij} - 1)}{\mathrm{L}_i \mathrm{d}_{ij}} + \delta_{ij} \frac{-2}{\mathrm{L}_i} \sum_{k=1}^{n} \frac{1}{\mathrm{d}_{ik}} \tag{4.6}$$

so that the diagonal terms are:

$$\mathrm{S}_{ii} = \frac{-2}{\mathrm{L}_i} \sum_{k=1}^{n} \frac{1}{\mathrm{d}_{ik}} \tag{4.7}$$

and the off-diagonal terms are:

$$\mathrm{S}_{ij} = \frac{-2}{\mathrm{L}_i \mathrm{d}_{ij}} \tag{4.8}$$

where L_i gives the sum of distances to neighboring centroid elements:

$$\mathrm{L}_i = \frac{1}{2}\sum_{k=1}^{\mathrm{n}} \mathrm{d}_{ik} \tag{4.9}$$

in which d_{ij} gives the centroid distance between dislocation i and dislocation j, and n is the number of neighboring dislocations to dislocation i [e.g. Desbrun et al., 1999; Maerten et al., 2005]. Augmented data vector $\mathbf{s}$ contains pseudodata setting the discrete second derivative of dislocation slip to zero. Weighting matrix $\mathbf{W}'_{\mathrm{d}}$ is a diagonal matrix containing data and pseudodata variance. For simplicity, we assume all data variance is equal to unity. Scalar parameter β controls the strength of smoothing of the solution. As β increases, differences in slip vector approach zero, and elements in the solution vector approach a homogeneous value.

3) Spatially variable smoothing

The augmented smoothing matrix $\mathbf{S}$ may also be constructed by incorporating additional information about model resolution on each dislocation element. In this case, values in matrix $\mathbf{S}$ corresponding to dislocation elements of high model resolution are decreased to reduce the strength of smoothing in these regions, and and values in $\mathbf{S}$ corresponding to dislocation elements of low model resolution are increased to increase smoothing in these regions. As with the augmented smoothing matrix, pseudodata $\mathbf{s}$ is a vector of zeros, and the scalar tuning parameter β controls the strength of smoothing. To incorporate spatially variable smoothing we modify each row and column of the smoothing matrix $\mathbf{S}$ by the sum of the corresponding row in the generalized Jacobian $\mathbf{G}$, so each element is modified as follows:

$$\mathrm{S}'_{ij} = \mathrm{S}_{ij} v_i v_j \tag{4.10}$$

and

$$v_i = 1 - \frac{1}{m} \sum_{k=1}^{\mathrm{n}} \mathrm{G}_{ik} \tag{4.11}$$

This modification reduces values in the smoothing matrix associated with well-resolved rectangular dislocations, and increases values in the smoothing matrix associated with poorly resolved dislocations.

4.6 Coulomb failure stress to select regularization parameter

We explore the four inverse methods discussed above: lasso, damped least squares, augmented smoothing matrix, and spatially variable smoothing, to identify a solution method most consistent with Coulomb stress change due to a coseismic slip estimate. For each method we consider a wide range of values for the relevant scalar tuning parameter (τ, λ, and β).

As with the lasso afterslip solutions from §4.4, we are interested in how well CFS change predicts, or is correlated with, postseismic afterslip. For a given inverse method, we estimate coseismic slip for each of a wide range of regularization parameters, and use these coseismic estimates to calculate a suite of CFS changes. We then estimate afterslip in the first postseismic epoch (day 1: March 12, 2011) for each of another wide range of regularization parameters specific to that method. To quantify how well CFS change predicts or is correlated with postseismic afterslip, we calculate a correlation coefficient between each CFS distribution and each epoch 1 afterslip distribution as well as 95% confidence bounds on each correlation. Again, we only calculate correlation coefficients for the best-resolved

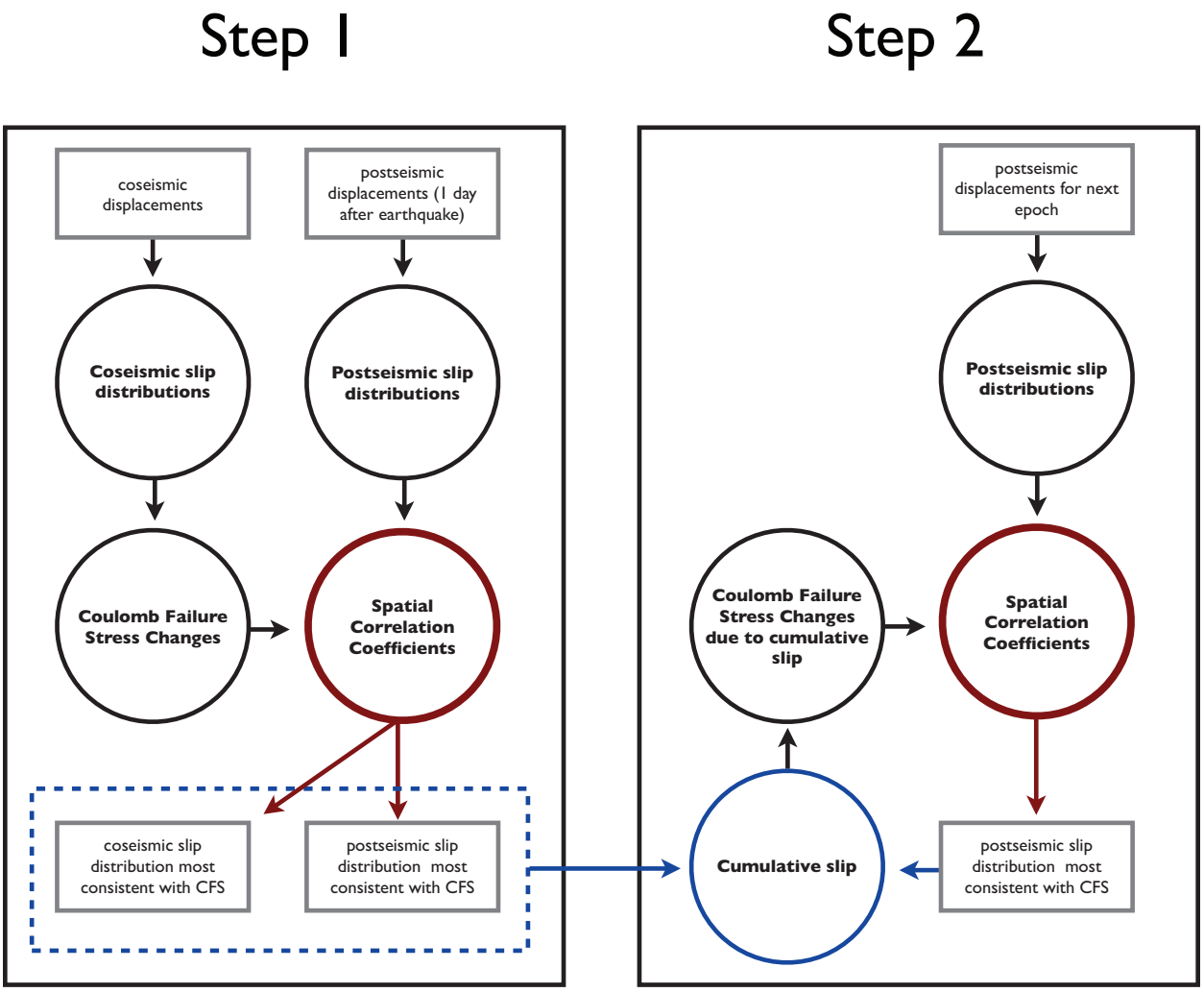

Figure 4.13: Flowchart for workflow in Section §4.6. In step 1, we estimate coseismic and postseismic slip distributions (for the first postseismic day) for each of a wide range of regularization parameters. We calculate CFS change due to each of these estimated coseismic slip distributions. We then calculate a correlation coefficient between each CFS change distribution and each estimated afterslip distribution. The largest correlation coefficient calculated in this way identifies the set of coseismic and postseismic slip distributions that are most consistent with the CFS change. In step 2, we calculate cumulative CFS change due to coseismic and postseismic afterslip, and calculate a correlation coefficient between cumulative CFS and afterslip in the next postseismic epoch. In this way we identify the slip distribution for each subsequent postseismic epoch that is most consistent with the cumulative slip due to coseismic slip and all postseismic afterslip prior to the given epoch.

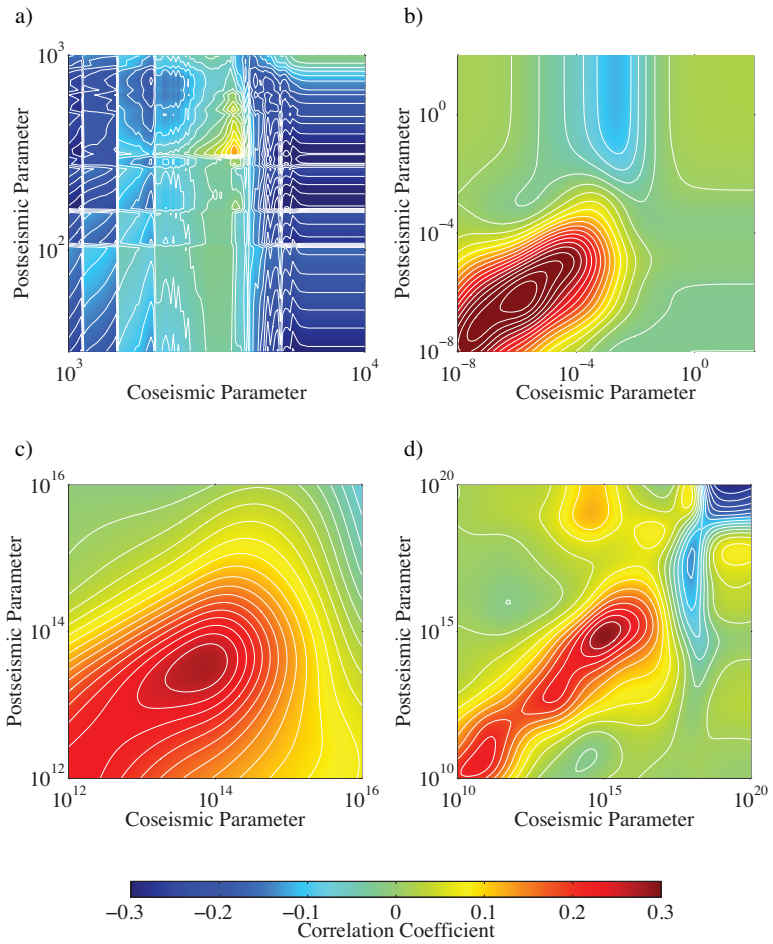

Figure 4.14: Correlation coefficient contour plots a) lasso; b) damped least squares; c) augmented smoothing matrix; d) spatially variable smoothing.

50% of the fault plane. This procedure is outlined as step one in the flowchart in Figure 4.13. The largest correlation coefficient calculated in this way identifies the set of co- and postseismic slip distributions that are most consistent with the hypothesis that afterslip is promoted in regions of positive CFS change (Figure 4.14).

The best correlation coefficient for identifying coseismic slip and afterslip in epoch 1 for each method is shown in Figure 4.15. In all cases, the correlation coefficient is less than 0.5, but positive within 95% confidence bounds, so all of the estimation methods considered here produce a co- and postseismic slip solution that is consistent with CFS.

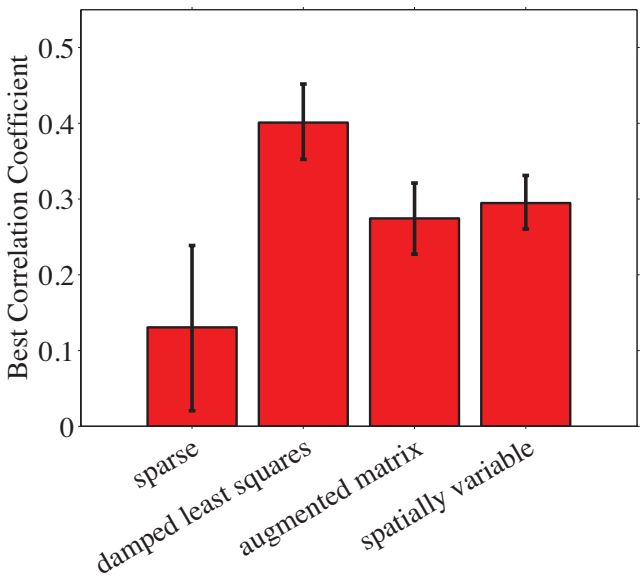

Figure 4.15: Best correlation coefficient for each method (maximum values from each contour plot in Figure 4.14, with 95% confidence intervals.

Next, to identify the afterslip distribution in epoch 2 (day 2: March 13, 2011) that is most consistent with regions of postitive CFS change, we calculate the cumulative CFS change due to coseismic slip and afterslip in epoch 1. We then estimate afterslip in epoch 2 for another wide range of regularization parameters, and calculate a correlation coefficient between the cumulative CFS change and each new afterslip distribution. The largest correlation coefficient identifies the afterslip distribution in epoch 2 that is most consistent with cumulative CFS change, and we can calculate a new cumulative CFS change due to coseismic slip and two postseismic epochs. In this way we identify the slip distribution for each subsequent postseimic epoch that is most consistent with the cumulative slip due to coseismic slip and all postseimic afterslip prior to the given epoch. This procedure is outlined as Step 2 in the flowchart in Figure 4.13.

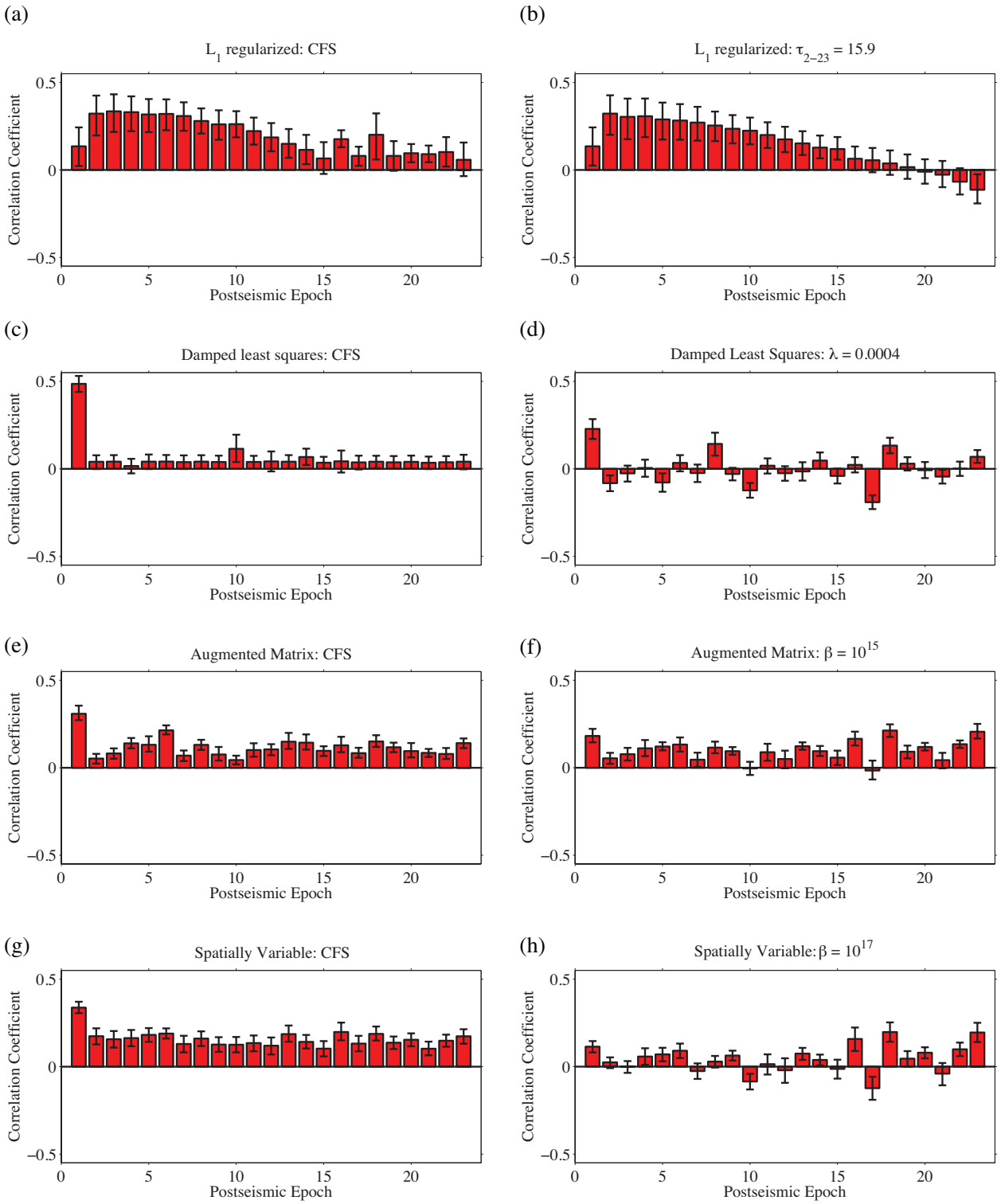

Figure 4.16: Correlation coefficients per epoch for each estimation method. a) lasso; b) lasso for τ values selected based on epoch 2; c) damped least squares for best epoch 1 correlation; d) damped least squares for manually smoothed distributions; e) augmented smoothing matrix for best correlation; f) augmented smoothing matrix for manually smoothed distributions; g) spatially variable smoothing for best correlation; h) spatially variable smoothing for manually smoothed distributions.

4.6.1 Imaging postseismic afterslip consistent with CFS: Lasso

The parameter search and workflow described above identifies the co- and postseismic regularization parameters for each method that give solutions most consistent with Coulomb failure stress change. This process is illustrated in Figures 4.17, 4.18, and 4.19, where we show the selected slip distribution, as well as the calculated cumulative CFS change for each epoch. This method identifies a coseismic $\tau = 3656.2$ for an optimality tolerance of 0.1 and postseismic $\tau = 311.7$ for an optimality tolerance of 8×10^{-2} for the first postseismic epoch, with a correlation coefficient of 0.13 ± 0.1. This coseismic slip distribution is less sparse than that found by the non-negative approach described in §4.4, and the postseismic distribution is more sparse. Here, the mean coseismic slip is 15.4 m on 235 slipping rectangles with a maximum slip of 55 m. The coseismic magnitude for this distribution is more than that estimated in Section 4, at M_w=8.8. The coseismic slip distribution selected in this way fits the data slightly better than the previously estimated distribution, with a mean residual displacement of 4.6 cm. For postseismic epoch 1, we estimate slip on 206 dislocations with a maximum slip of 5.1 m and mean slip of 1.5 m, and we fit the data with a mean residual displacement of 5.9 cm, almost 3 cm worse than we fit epoch 1 in §4.4. However, these slip estimates are consistent with predictions from CFS change, whereas our estimates from §4.4 produced a negative correlation between coseismic stress change and epoch 1 afterslip.

For epoch 2, the slip distribution (for which slip is sparse) that is most consistent with cumulative Coulomb stress change due to coseismic slip and epoch 1 afterslip occurs at $\tau = 15.9$ for an optimality tolerance of 10^{-3}. For this epoch, we image 62 slipping rectangular dislocations, with maximum slip of 1.2 m, and a mean residual displacement of 0.6 cm.

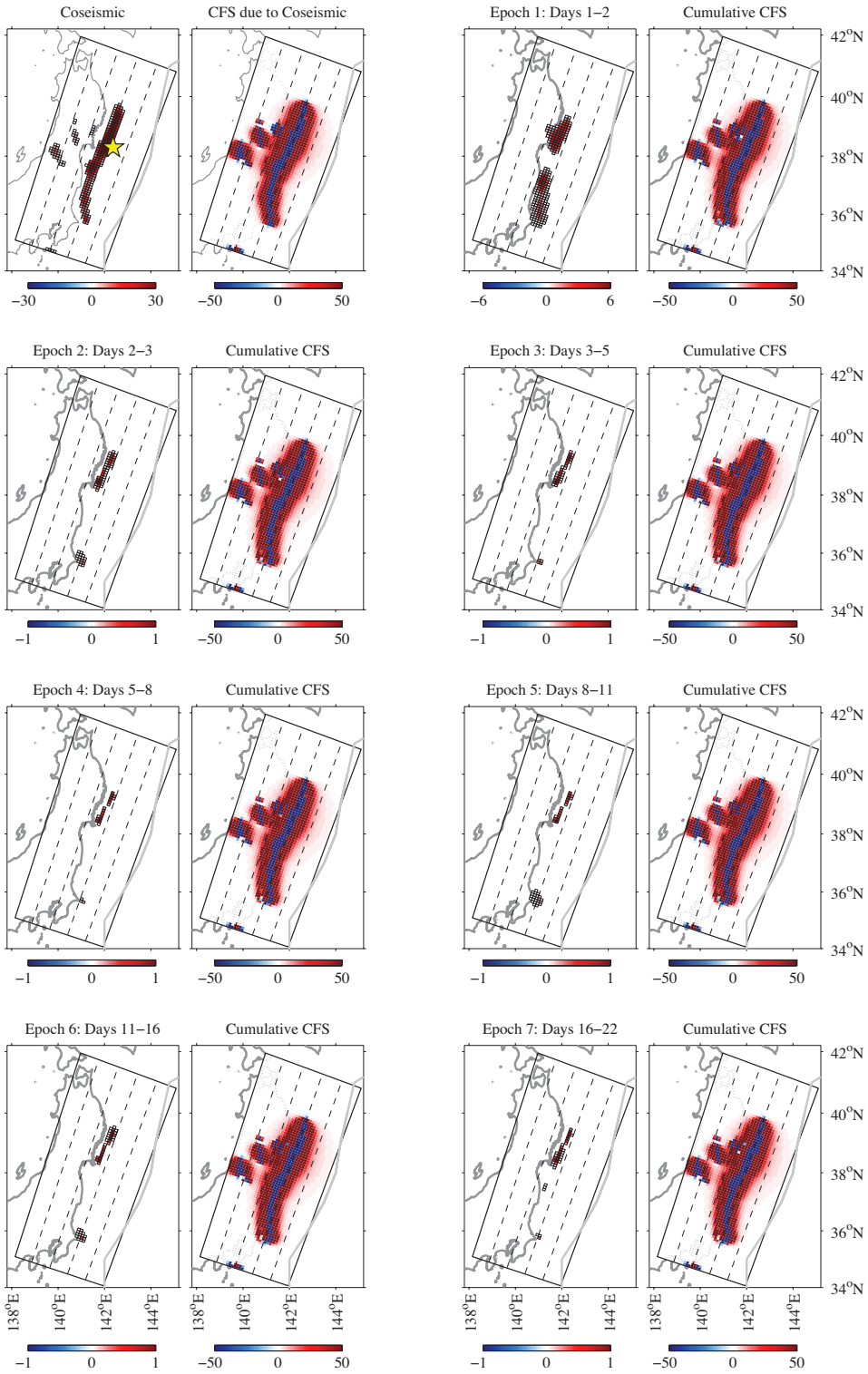

Figure 4.17: Coseismic slip and postseismic afterslip (epochs 1–7) estimated with the lasso, most consistent with Coulomb failure stress, shown with cumulative Coulomb failure stress for each epoch. Slip color bars are in meters, stress color bars are in MPa. The color bar axis changes over the first three figures.

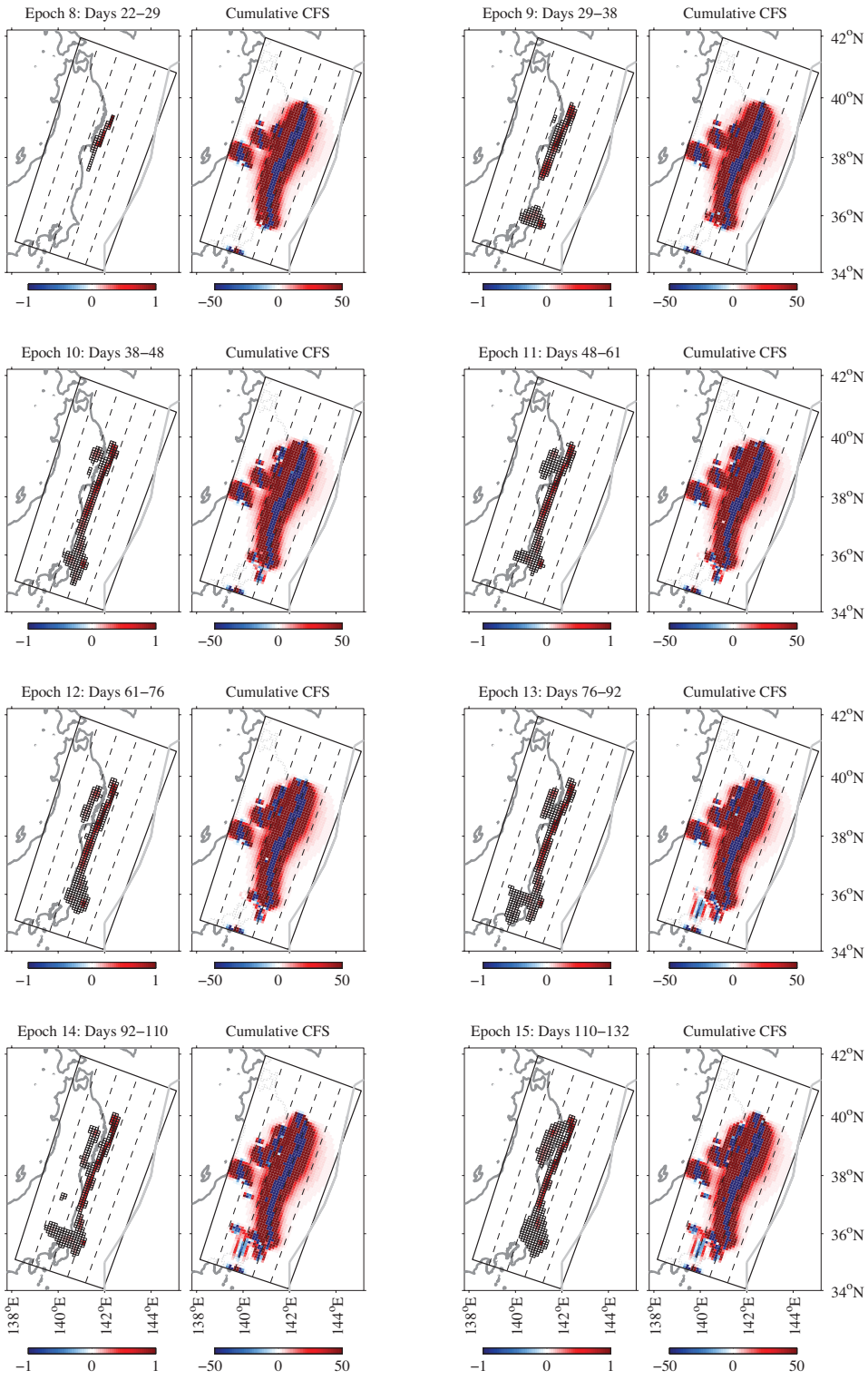

Figure 4.18: Same as Figure 4.17 for postseismic epochs 8–15.

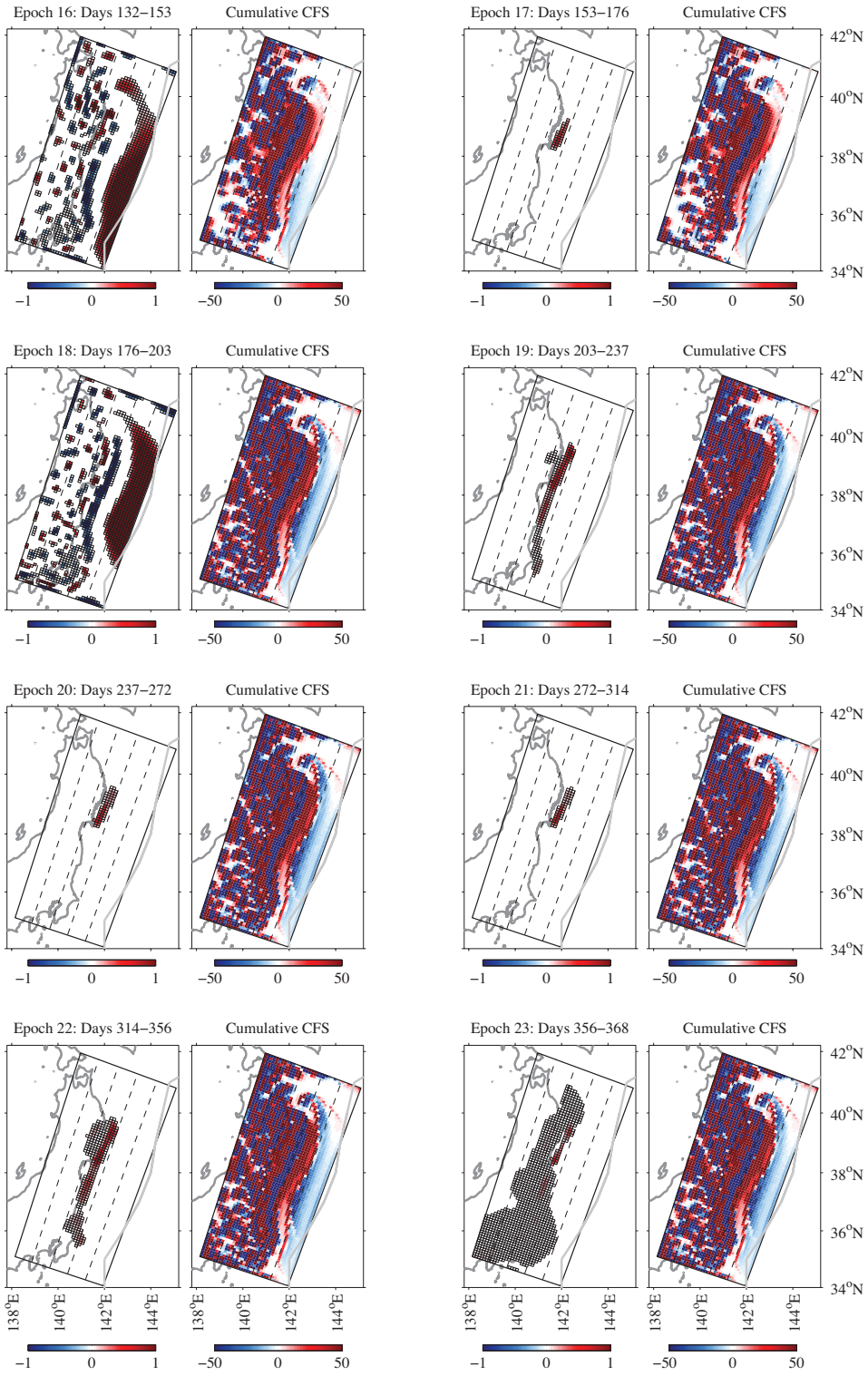

Figure 4.19: Same as Figure 4.17 for postseismic epochs 16–23.

EPOCH	τ	Correlation Coefficient	slip/epoch (m)	nonzero elements	mean slip/epoch (m)	max slip/epoch (m)	Mw/epoch	mrd/epoch (cm)
Coseismic	3656.2	-	3626.4	235	15.43	55.41	8.8	4.58
1	311.7	0.14	311.7	206	1.51	5.13	8.1	5.88
2	15.9	0.32	15.9	62	0.26	1.21	7.3	0.59
3	13.4	0.34	13.4	36	0.37	1.13	7.2	0.78
4	10.0	0.33	10.0	22	0.45	1.01	7.1	0.72
5	10.0	0.32	10.0	42	0.24	0.96	7.1	0.76
6	16.9	0.32	16.9	46	0.37	1.75	7.3	0.67
7	15.9	0.31	15.9	37	0.43	1.65	7.3	0.61
8	14.2	0.28	14.2	42	0.34	1.67	7.2	0.64
9	42.9	0.26	42.9	175	0.25	2.08	7.6	0.65
10	54.2	0.26	54.2	254	0.21	2.10	7.6	0.52
11	48.3	0.22	48.3	259	0.19	2.11	7.6	0.45
12	54.2	0.19	54.2	264	0.21	2.07	7.6	0.46
13	57.5	0.15	57.5	315	0.18	2.12	7.6	0.49
14	57.5	0.11	57.5	295	0.19	1.87	7.6	0.44
15	57.5	0.07	57.5	342	0.17	1.85	7.6	0.50
16	747.2	0.18	368.2	1211	0.30	4.57	8.4	0.48
17	10.0	0.08	10.0	32	0.31	0.60	7.1	0.99
18	1000.0	0.20	430.0	1215	0.35	5.79	8.5	0.69
19	36.1	0.08	36.1	191	0.19	0.88	7.5	0.62
20	12.6	0.10	12.6	55	0.23	0.61	7.2	0.83
21	10.0	0.09	10.0	47	0.21	0.56	7.1	0.76
22	42.9	0.10	42.9	277	0.16	0.87	7.6	0.68
23	25.4	0.06	25.4	1121	0.02	0.52	7.4	0.36

Table 4.3: Summary of results for lasso solution in Section §4.6.1

Afterslip imaged in epoch 2 is also consistent with coseismic stress changes, with a correlation coefficient of 0.3±0.1.

For the rest of the year, CFS remains dominated by coseismic slip. Correlation coefficients are positive within the 95% confidence interval, for all but three postseismic epochs (Figure 4.16). Correlation coefficients decrease until epoch 15, then remain small for the rest of the year. Here we image slip on 32-1215 dislocations per epoch with maximum slip between 0.6 and 5 m per epoch, and mean slip between 0.1 and 0.3 m per epoch on the slipping dislocations. The selected slip distributions for epochs 16 and 18 contain particularly large magnitudes of slip, up to 6 m thrust-sense slip, and up to 3 m normal-sense slip, which are likely due to over-fitting the CFS change constraint on the selected solution, and a lack of data resolution (Figures 4.17, 4.18, and 4.19). We estimate a total equivalent moment magnitude for the 366 days following the earthquake of M_W=9.0. We estimate afterslip in the first day following the earthquake equivalent to a magnitude of M_W=8.1, and we

estimate equivalent magnitudes of M_w=7.1 to 8.3 per epoch for the subsequent 201 days. These afterslip estimates fit the GPS observations with mean residual displacements of 0.6-1.0 cm/epoch, ∼0.4 cm/epoch worse than the imaging in §4.4. However, these afterslip distributions are generally more consistent with CFS change for a given epoch. Table 4.3 contains additional statistics for these afterslip estimates.

EPOCH	τ	Correlation Coefficient	slip/epoch (m)	nonzero elements	mean slip/epoch (m)	max slip/epoch (m)	Mw/epoch	mrd/epoch (cm)
Coseismic	3656.2	-	3626.4	235	15.43	55.41	8.8	4.58
1	311.7	0.14	311.7	206	1.51	5.13	8.1	5.88
2	15.9	0.32	15.9	62	0.26	1.21	7.3	0.59
3	15.9	0.30	15.9	44	0.36	1.11	7.3	0.76
4	15.9	0.31	15.9	43	0.37	1.25	7.3	0.67
5	15.9	0.29	15.9	105	0.15	1.15	7.3	0.71
6	15.9	0.28	15.9	51	0.31	1.25	7.3	0.68
7	15.9	0.27	15.9	64	0.25	1.24	7.3	0.61
8	15.9	0.25	15.9	61	0.26	1.36	7.3	0.63
9	15.9	0.24	15.9	65	0.25	1.35	7.3	0.83
10	15.9	0.22	15.9	58	0.27	1.33	7.3	0.77
11	15.9	0.20	15.9	58	0.27	1.33	7.3	0.67
12	15.9	0.17	15.9	58	0.27	1.33	7.3	0.70
13	15.9	0.15	15.9	84	0.19	1.33	7.3	0.81
14	15.9	0.13	15.9	84	0.19	1.45	7.3	0.72
15	15.9	0.12	15.9	53	0.30	1.49	7.3	0.73
16	15.9	0.06	15.9	119	0.13	1.39	7.3	0.94
17	15.9	0.06	15.9	54	0.30	1.32	7.3	0.95
18	15.9	0.04	15.9	60	0.27	1.41	7.3	1.09
19	15.9	0.02	15.9	70	0.23	1.33	7.3	0.75
20	15.9	-0.01	15.9	80	0.20	1.31	7.3	0.80
21	15.9	-0.03	15.9	36	0.44	1.41	7.3	0.72
22	15.9	-0.07	15.9	72	0.22	1.34	7.3	0.87
23	15.9	-0.11	15.9	739	0.02	0.99	7.3	0.39

Table 4.4: Summary of results for lasso solution in Section §4.6.1, with $\tau_{2-23} = 15.9$

As in §4.4.3, we also consider slip distributions in which the τ value is consistent for postseismic epochs 2-22. In this case, τ=15.9 produces the most consistent slip distribution for epoch 2 relative to the cumulative CFS change due to coseismic slip and 1 day of afterslip. This leads to considerably more coherent slip distributions in terms of slip magnitude and physical extent (Figures 4.20, 4.21, and 4.22). In addition, correlation coefficients decrease monotonically after epoch 3, becoming indistinguishable from zero within the 95% confidence interval after epoch 16 (Figure 4.16). Here we image slip on 36-105 dislocations per epoch with maximum slip decreasing from 0.4 to 0.2 m per epoch, and mean slip ranges between

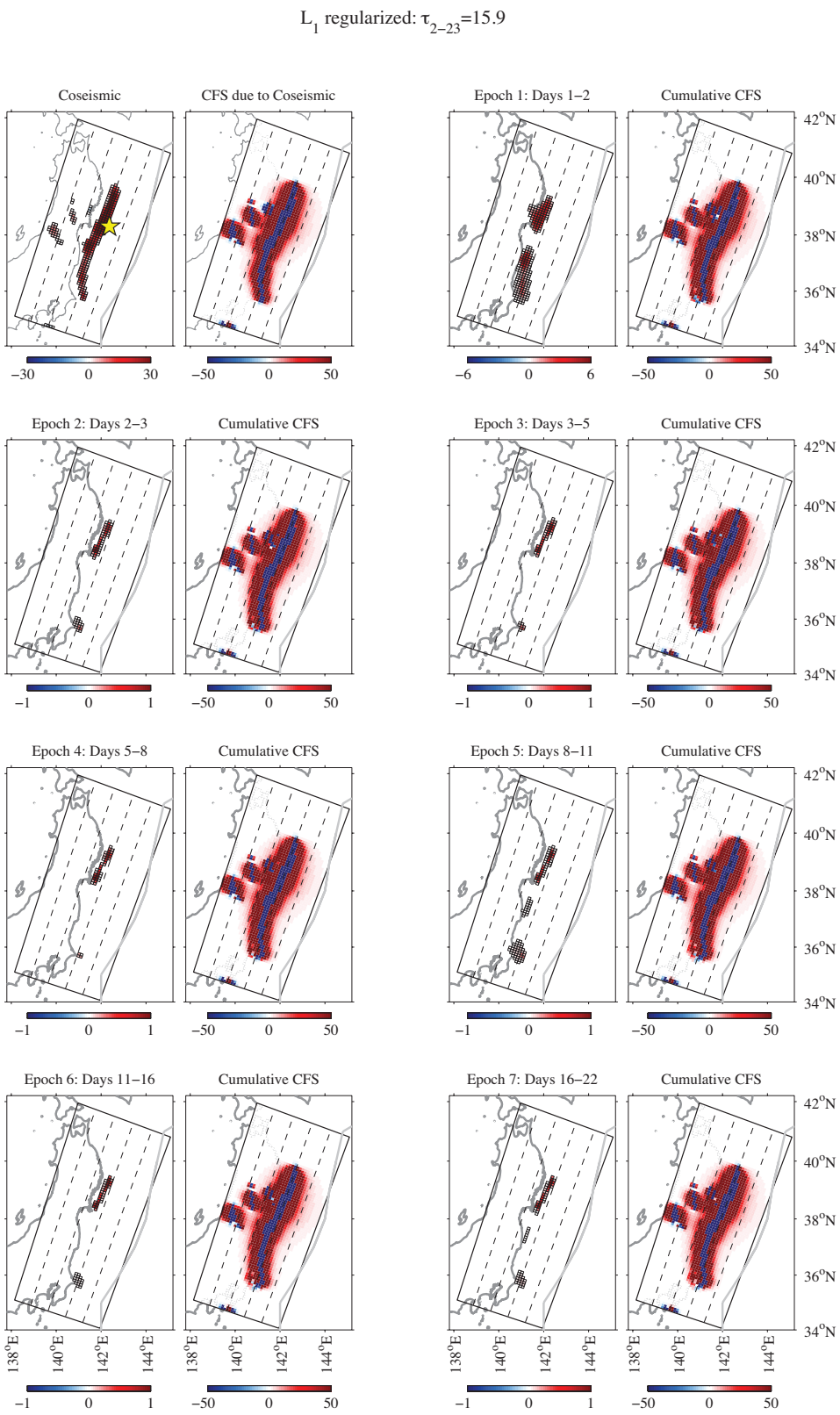

Figure 4.20: Coseismic slip and postseismic afterslip (epochs 1–7) estimated with the lasso. Sparsity parameter τ is selected based on epoch 2, and applied to all subsequent epochs. Shown with cumulative Coulomb failure stress for each epoch. Slip color bars are in meters, stress color bars in MPa. The color bar axis changes over the first three figures.

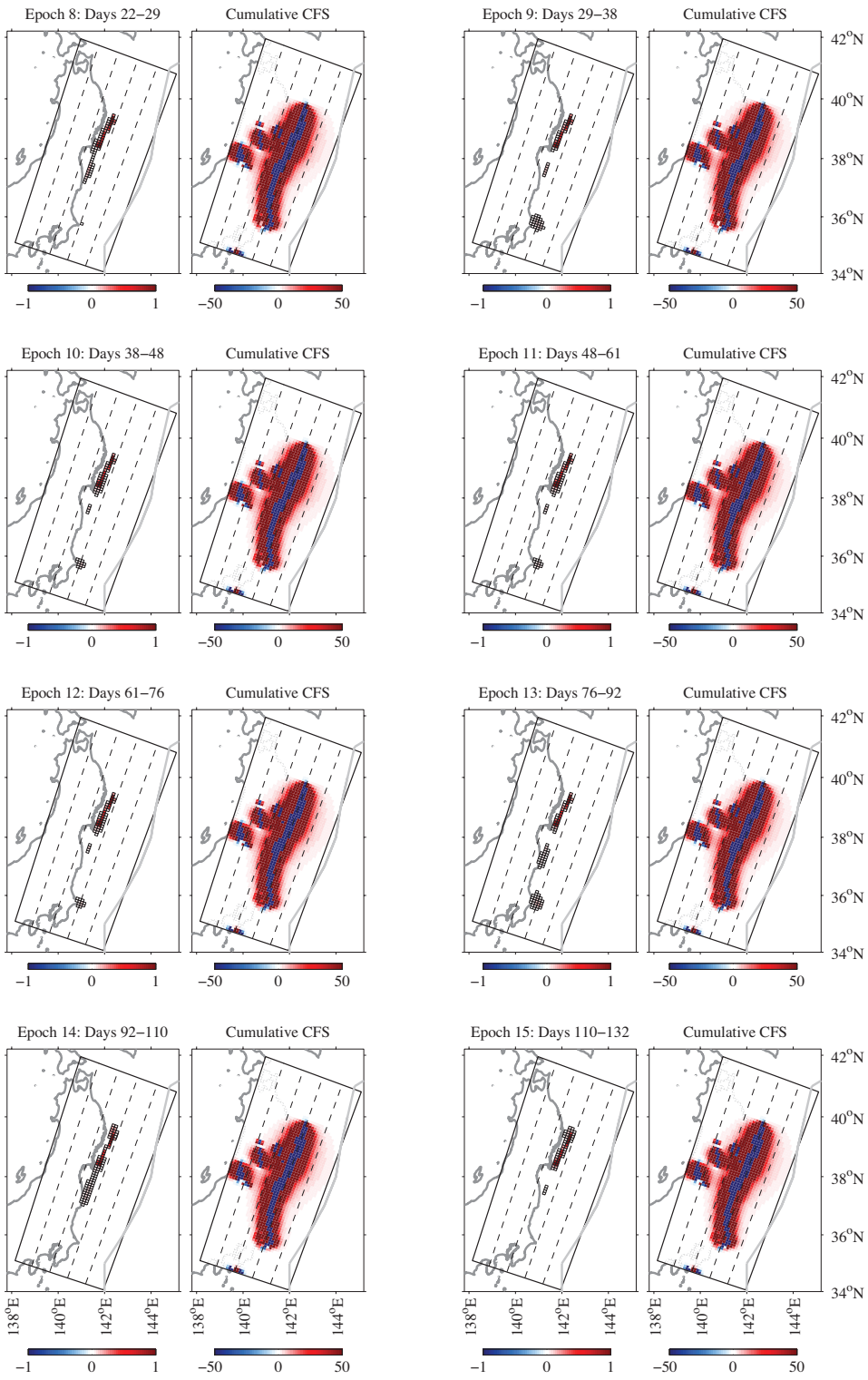

Figure 4.21: Same as Figure 4.20 for postseismic epochs 8–15.

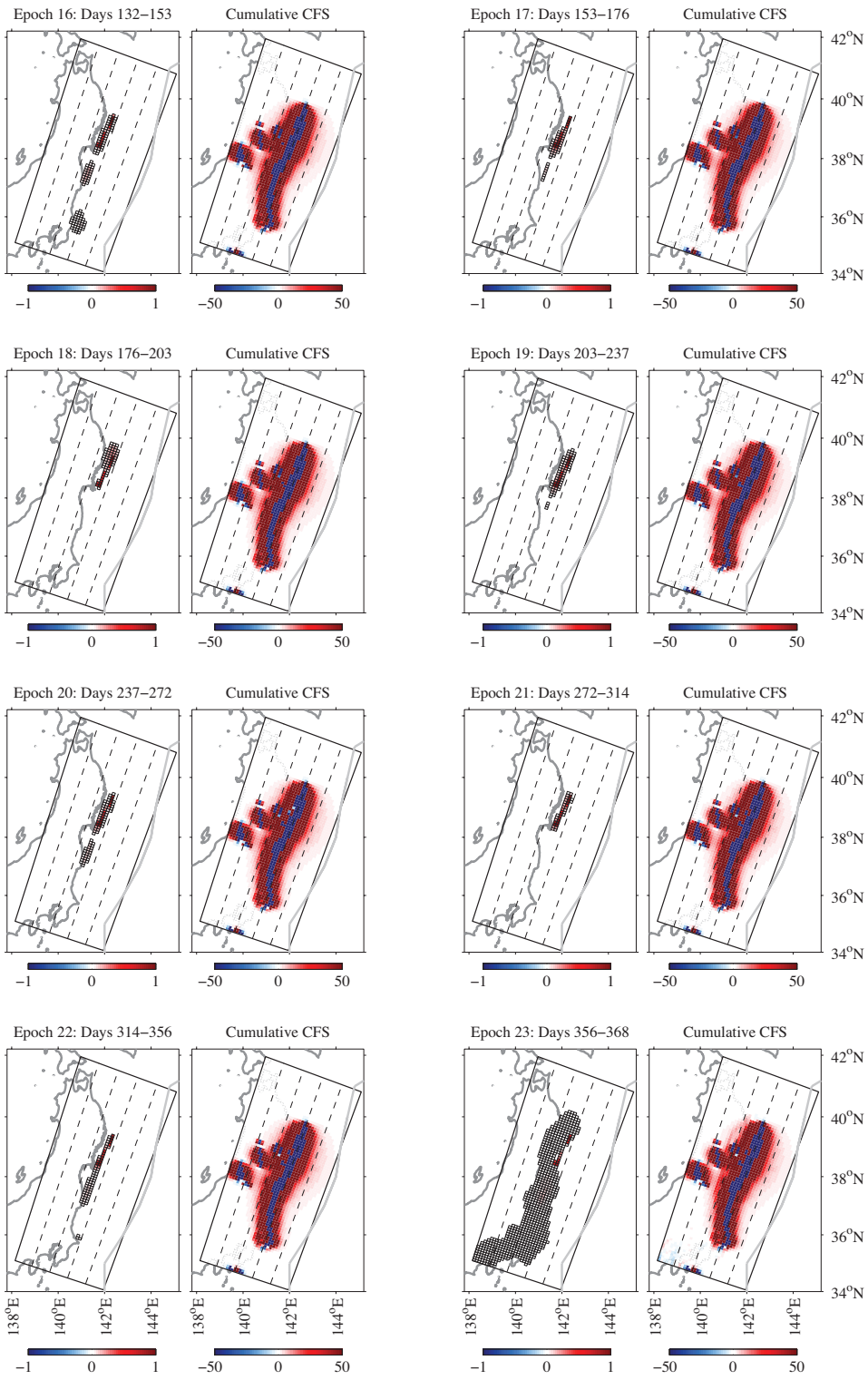

Figure 4.22: Same as Figure 4.20 for postseismic epochs 16–23.

0.2 and 0.4 m per epoch on the slipping dislocations. These afterslip estimates fit the GPS observations with mean residual displacements of 0.6-1.0 cm/epoch, approximately as well as selecting τ based on consistency with CFS. See table 4.4 for additional statistics on these afterslip estimates.

4.6.2 Imaging postseismic afterslip consistent with CFS: Damped least squares

Smooth estimation methods are capable of producing co- and postseismic slip distributions that are as consistent with CFS change as the lasso, if not better. Estimating slip with damped least squares (Equation **??**) produces co- and postseismic slip distributions that are most consistent with CFS change for coseismic smoothing parameter $\lambda = 1.3 \times 10^{-6}$ and postseismic $\lambda = 2.1 \times 10^{-4}$ (Figure 4.14). Here, the mean estimated coseismic slip is 0.23 m with a maximum slip of 43.23 m. The coseismic magnitude for this distribution is high: M_W=9.4. The coseismic slip distribution selected in this way fits the data slightly better than sparse estimates, with a mean residual displacement of 5.3 cm. The correlation between afterslip in postseismic epoch 1 and coseismic CFS is 0.49$\pm$0.1, higher than those found for the lasso solutions, however, the afterslip distribution contains up to 28 m of normal sense slip and up to 48 m of thrust sense slip, and the wavelength of these features is on the order of <50 km. This variance in the solution is unusual among published slip distributions, and is likely the result of over-fitting the CFS constraint on the selected solution. All subsequent correlations are positive. However, a homogeneous slip distribution with slip $\sim$0 m/epoch is most consistent with the calculated CFS change in all but six epochs (Figures 4.23, 4.24, and 4.16). Table 4.5 contains additional statistics for the damped least squares afterslip estimates.

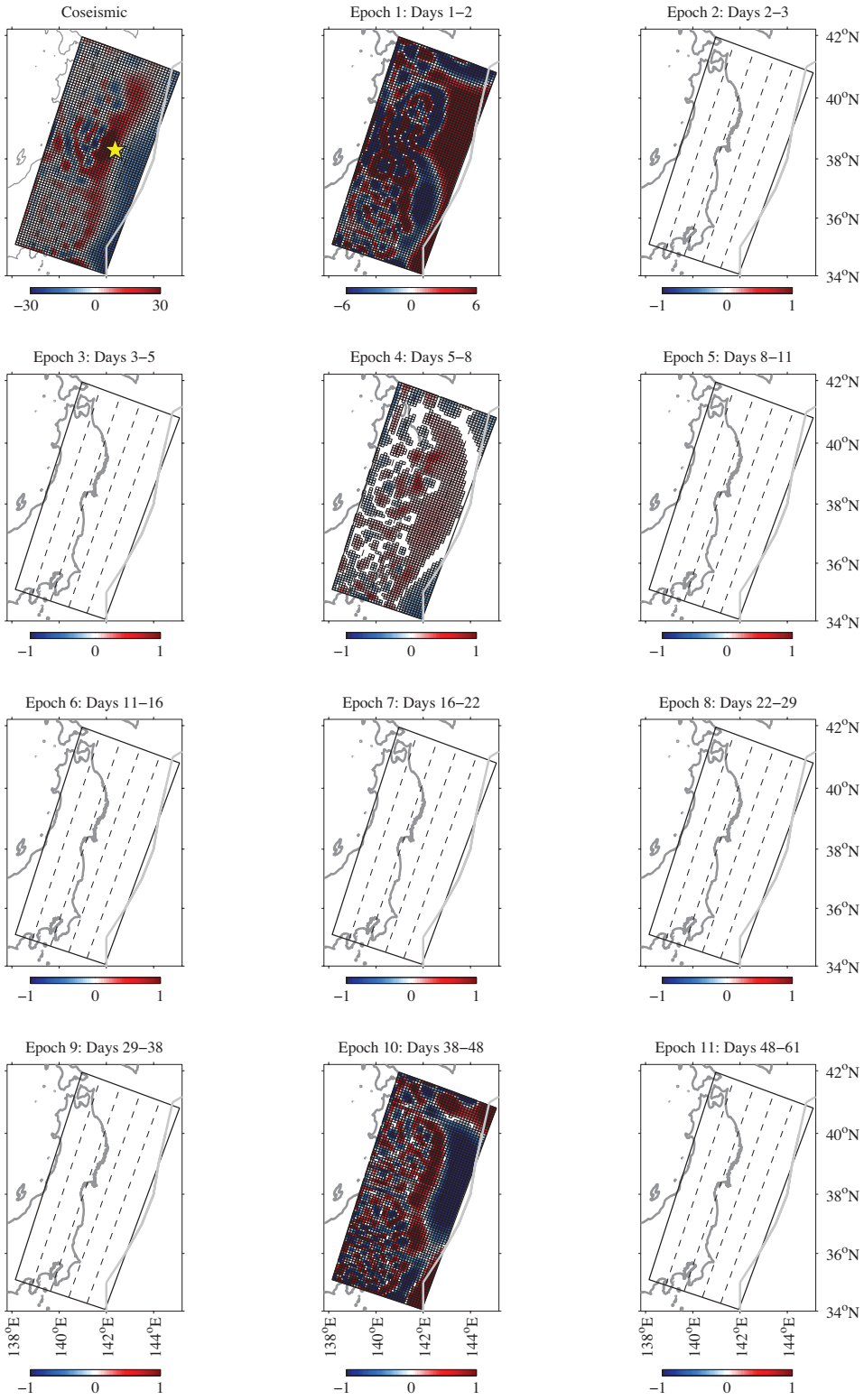

Figure 4.23: Coseismic slip and postseismic afterslip (epochs 1–11) estimated with damped least squares, most consistent with Coulomb failure stress. Slip color bars in meters. The color bar axis changes over the first three figures.

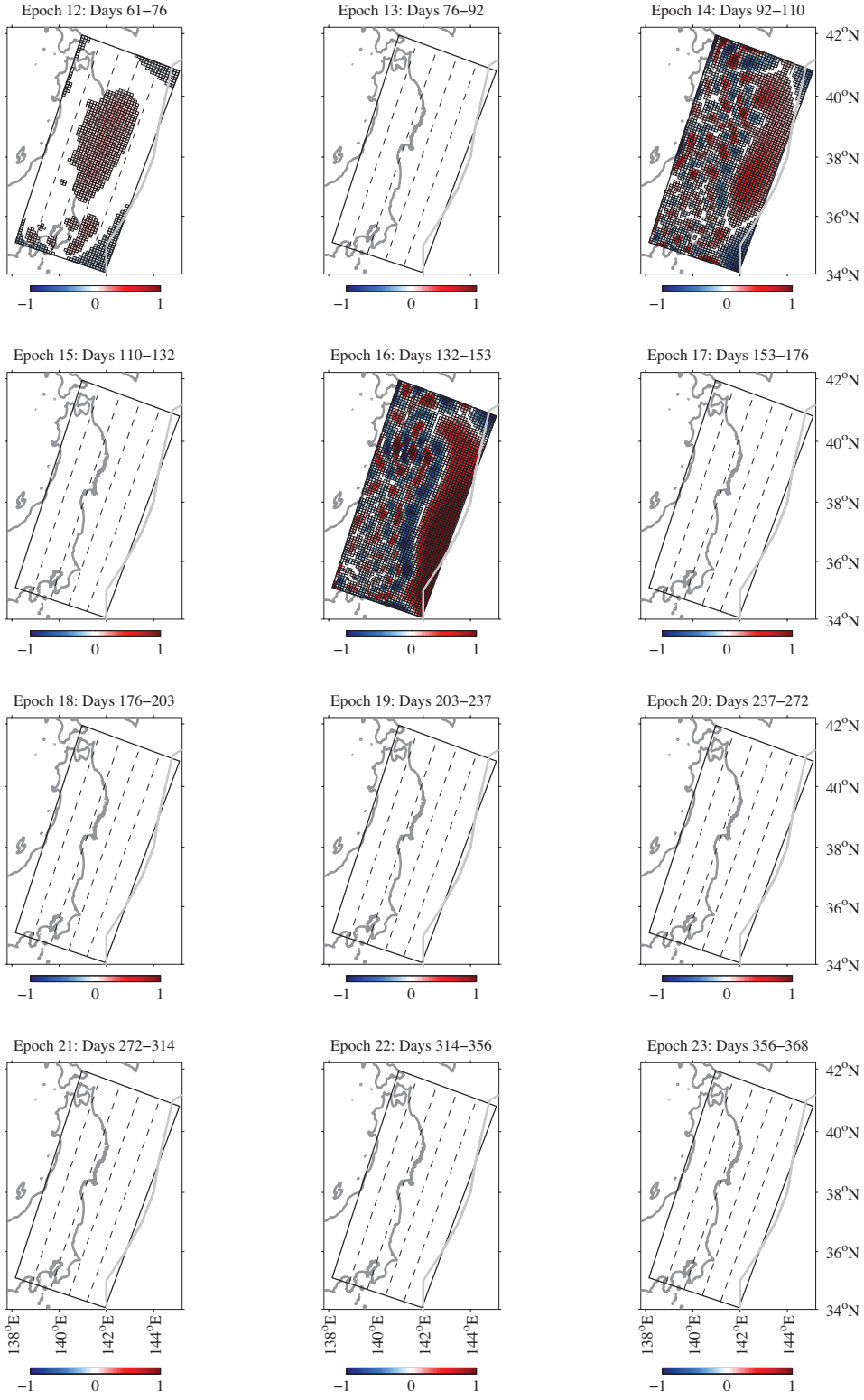

Figure 4.24: Same as Figure 4.23 for postseismic epochs 12–23.

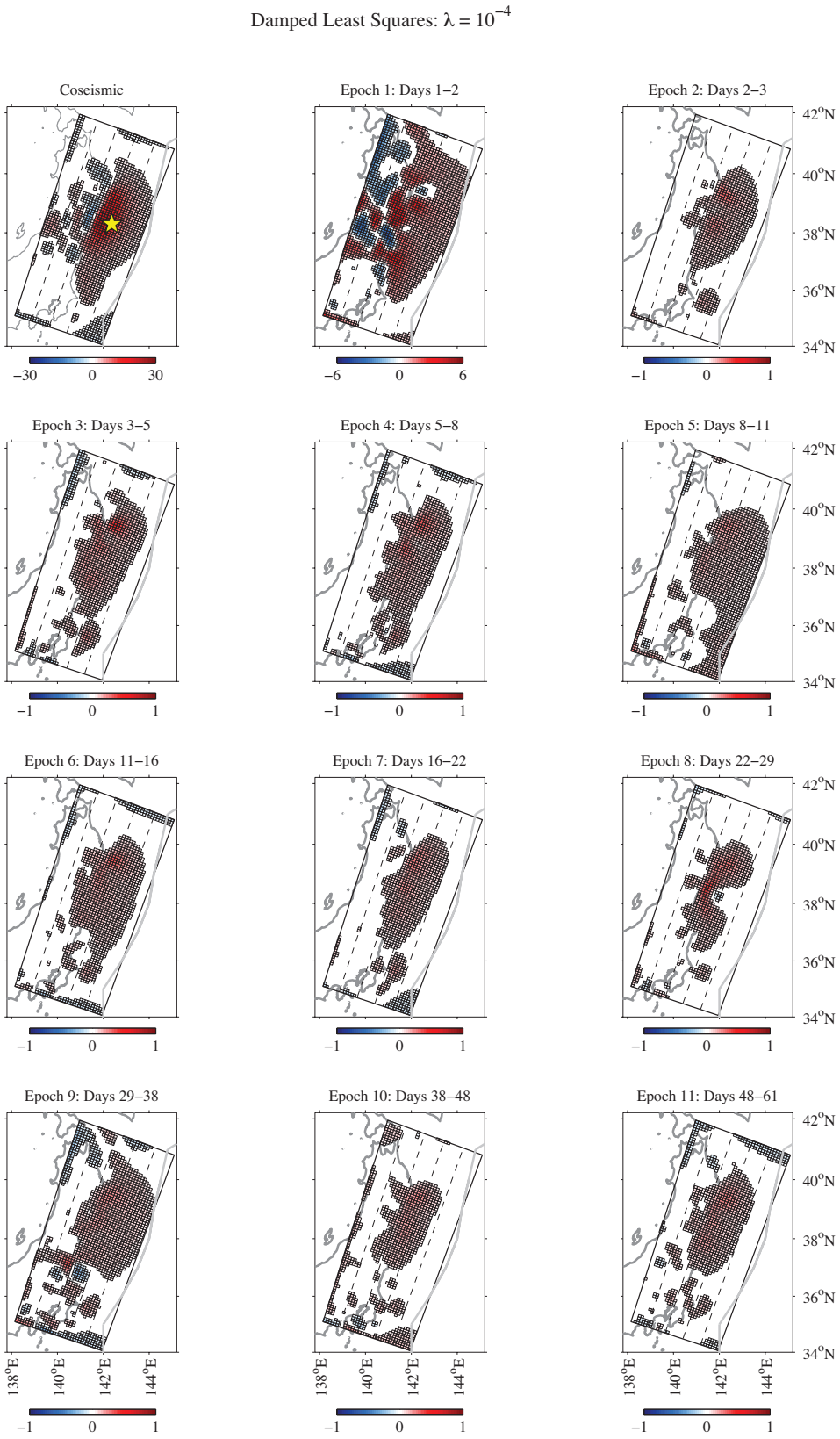

Figure 4.25: Coseismic slip and postseismic afterslip (epochs 1–11) estimated with damped least squares with $\lambda = 10^{-4}$. Slip color bars in meters. The color bar axis changes over the first three figures.

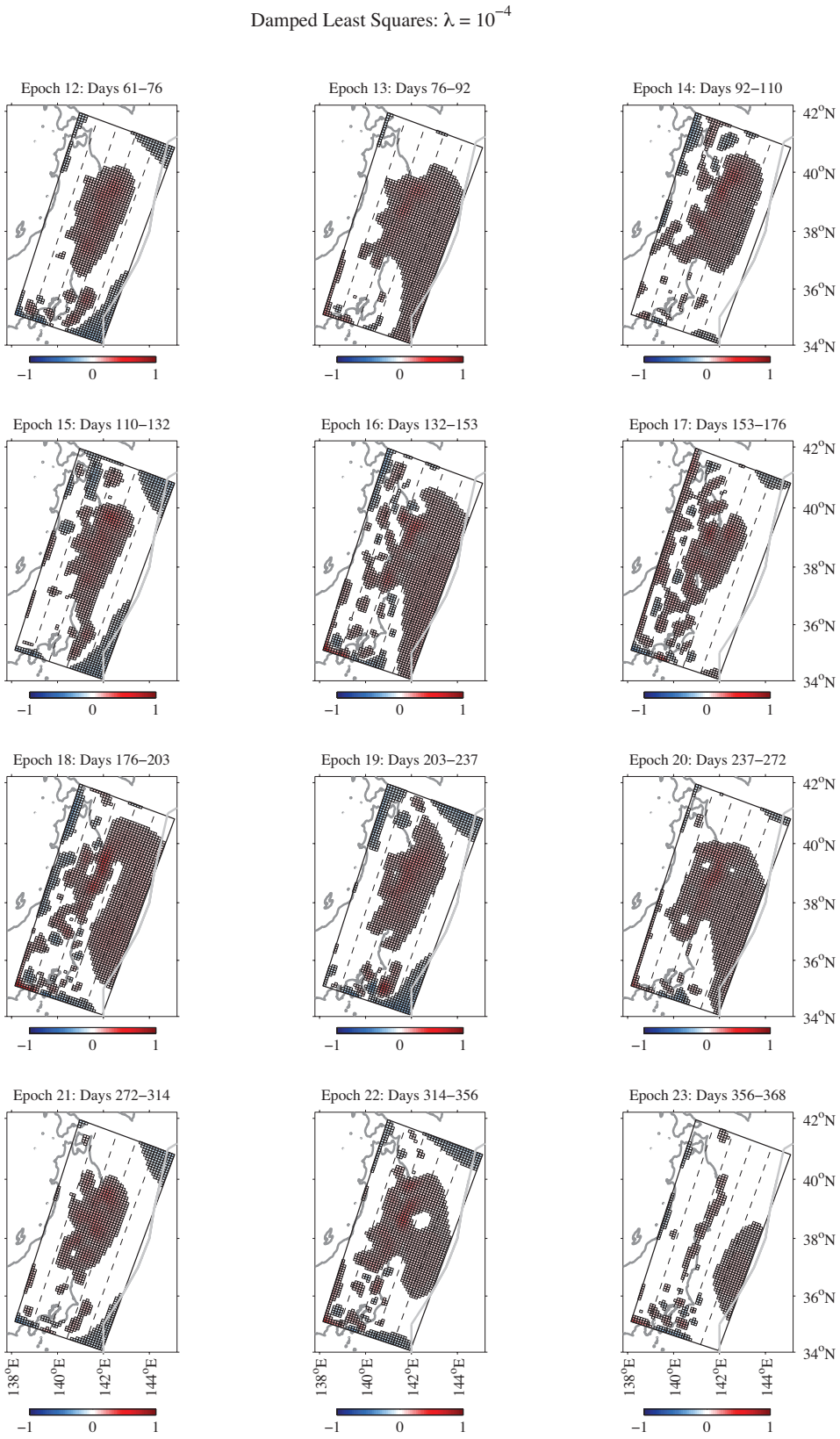

Figure 4.26: Same as Figure 4.25 for postseismic epochs 12–23.

EPOCH	λ	Correlation Coefficient	slip/epoch (m)	mean slip/epoch (m)	max slip/epoch (m)	Mw/epoch	mrd/epoch (cm)
Coseismic	1.26×10^{-6}	-	708.3	0.23	43.23	9.4	5.30
1	5.92×10^{-7}	0.49	3397.3	1.10	48.31	9.3	2.33
2	100	0.04	3.14×10^{-2}	1.02×10^{-5}	2.98×10^{-5}	5.5	0.72
3	100	0.04	3.83×10^{-2}	1.24×10^{-5}	3.50×10^{-5}	5.5	0.88
4	6.09×10^{-6}	0.02	77.5	0.03	0.70	8.1	0.24
5	100	0.04	3.25×10^{-2}	1.06×10^{-5}	2.72×10^{-5}	5.5	0.83
6	100	0.04	3.28×10^{-2}	1.07×10^{-5}	3.20×10^{-5}	5.5	0.80
7	100	0.04	3.00×10^{-2}	9.74×10^{-6}	2.94×10^{-5}	5.5	0.73
8	100	0.04	3.08×10^{-2}	1.00×10^{-5}	3.01×10^{-5}	5.5	0.74
9	100	0.04	3.70×10^{-2}	9.96×10^{-6}	2.98×10^{-5}	5.5	0.95
10	1.84×10^{-7}	0.11	11.3	3.68×10^{-3}	6.18	8.7	0.37
11	100	0.04	2.94×10^{-2}	9.53×10^{-6}	2.88×10^{-5}	5.5	0.79
12	1.12×10^{-4}	0.04	57.0	0.02	0.22	7.9	0.37
13	100	0.04	3.39×10^{-2}	1.10×10^{-5}	3.02×10^{-5}	5.5	0.93
14	1.90×10^{-6}	0.07	129.1	0.04	1.48	8.4	0.31
15	100	0.04	2.58×10^{-2}	8.38×10^{-6}	2.81×10^{-5}	5.4	0.83
16	2.54×10^{-6}	0.04	428.4	0.14	2.74	8.6	0.47
17	100	0.04	2.99×10^{-2}	9.70×10^{-6}	2.85×10^{-5}	5.5	1.06
18	100	0.04	3.12×10^{-2}	1.01×10^{-5}	2.96×10^{-5}	5.5	1.20
19	100	0.04	2.63×10^{-2}	8.55×10^{-6}	2.91×10^{-5}	5.4	0.86
20	100	0.04	3.26×10^{-2}	1.06×10^{-5}	3.06×10^{-5}	5.5	0.92
21	100	0.04	2.72×10^{-2}	8.83×10^{-6}	2.99×10^{-5}	5.4	0.83
22	100	0.04	3.02×10^{-2}	9.81×10^{-6}	2.92×10^{-5}	5.5	0.99
23	100	0.04	1.07×10^{-2}	3.48×10^{-6}	9.06×10^{-6}	5.2	0.49

Table 4.5: Summary of results for damped least squares solution in Section §4.6.2

Because of the inconsistent and likely unphysical behavior in the above slip estimates, we also consider slip distributions with a single smoothing coefficient for the sake of comparison with literature. We estimate coseismic slip and postseismic afterslip for all epochs with a $\lambda = 10^{-4}$ (from Evans and Meade [2012]) (Figures 4.25 and 4.26), which produces a coseismic distribution that is qualitatively similar to several published estimates [e.g., Ozawa et al., 2011; Simons et al., 2011]. In this case, mean coseismic slip is 1.4 m with a maxiumum slip of 23.8 m, and fits the GPS observations with a mean residual displacement of 3.8 cm. The coseismic magnitude for this distribution is estimated to be M_W=9.0. For the postseismic $\lambda = 10^{-4}$ we image maximum slip magnitude decreasing from 4 m in epoch 1 to 0.2-0.7 m per epoch for the rest of the year. Afterslip imaged in epoch 1 is consistent with CFS change, with a correlation coefficient of 0.23±0.1, but afterslip in epoch 2 is less consistent, with a correlation coefficient between cumulative CFS change and afterslip of -0.08 ± 0.1. For the afterslip distributions, we estimate a total equivalent moment magnitude for the 366 days

following the earthquake of M_W=9.12. We estimate afterslip in the first day following the earthquake equivalent to a magnitude of M_W=8.7, and we estimate equivalent magnitudes of M_W=7.8-8.0 per epoch for the subsequent 365 days. These afterslip estimates fit the GPS observations with mean residual displacements of 0.2-0.8 cm/epoch, ∼0.6 cm/epoch better than sparse imaging in §4.6.1, however, these afterslip distributions are slightly less consistent with CFS change than those estimated in §4.6.1 (Figure 4.16). See table 4.6 for additional statistics on damped least squares estimates.

EPOCH	λ	Correlation Coefficient	slip/epoch (m)	mean slip/epoch (m)	max slip/epoch (m)	Mw/epoch	mrd/epoch (cm)
Coseismic	10^{-4}	-	4445.1	1.44	23.78	9.0	3.88
1	10^{-4}	0.23	1215.1	0.395	4.44	8.7	3.00
2	10^{-4}	-0.08	109.2	0.035	0.31	7.9	0.17
3	10^{-4}	-0.03	116.5	0.038	0.47	8.0	0.27
4	10^{-4}	0.01	96.8	0.031	0.34	7.9	0.25
5	10^{-4}	-0.08	126.3	0.041	0.30	7.9	0.24
6	10^{-4}	0.03	102.2	0.033	0.33	7.9	0.24
7	10^{-4}	-0.02	86.3	0.028	0.26	7.9	0.26
8	10^{-4}	0.14	97.2	0.032	0.40	7.9	0.24
9	10^{-4}	-0.03	101.4	0.033	0.35	8.0	0.48
10	10^{-4}	-0.12	117.0	0.038	0.23	7.9	0.40
11	10^{-4}	0.02	81.3	0.026	0.24	7.9	0.32
12	10^{-4}	-0.02	54.2	0.018	0.23	7.9	0.37
13	10^{-4}	-0.01	136.6	0.044	0.30	7.9	0.33
14	10^{-4}	0.05	106.0	0.034	0.26	7.9	0.33
15	10^{-4}	-0.04	47.4	0.015	0.29	8.0	0.45
16	10^{-4}	0.02	140.2	0.046	0.69	8.0	0.53
17	10^{-4}	-0.19	96.4	0.031	0.34	7.9	0.67
18	10^{-4}	0.13	132.1	0.043	0.68	8.0	0.74
19	10^{-4}	0.03	51.1	0.017	0.35	8.0	0.43
20	10^{-4}	-0.01	126.4	0.041	0.33	7.9	0.33
21	10^{-4}	-0.04	68.9	0.022	0.26	7.9	0.40
22	10^{-4}	0.00	102.2	0.033	0.45	8.0	0.49
23	10^{-4}	0.07	53.2	0.017	0.35	7.8	0.33

Table 4.6: Summary of results for damped least squares solution in Section §4.6.2, with $\lambda = 10^{-4}$

4.6.3 Imaging postseismic afterslip consistent with CFS: Augmented smoothing matrix

Estimating slip with an augmented smoothing matrix (Equation 4.5) produces co- and postseismic slip distributions that are most consistent with CFS change for coseismic smoothing parameter $\beta = 6.53 \times 10^{13}$ and postseismic $\beta = 3.3 \times 10^{13}$ (Figure 4.14). These smoothing

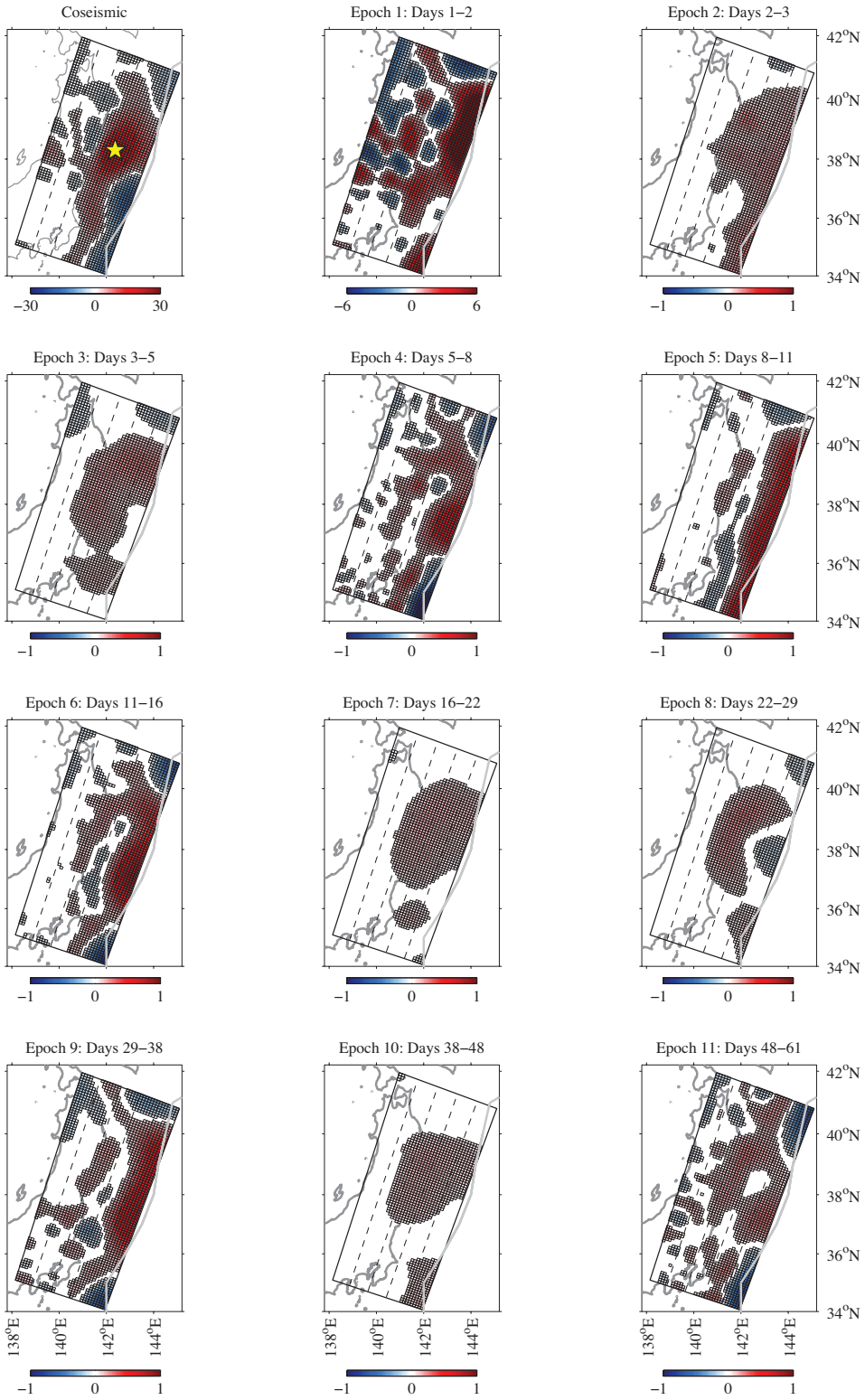

Figure 4.27: Coseismic slip and postseismic afterslip (epochs 1–11) estimated with an augmented smoothing matrix, most consistent with Coulomb failure stress. Slip color bars in meters. The color bar axis changes over the first three figures.

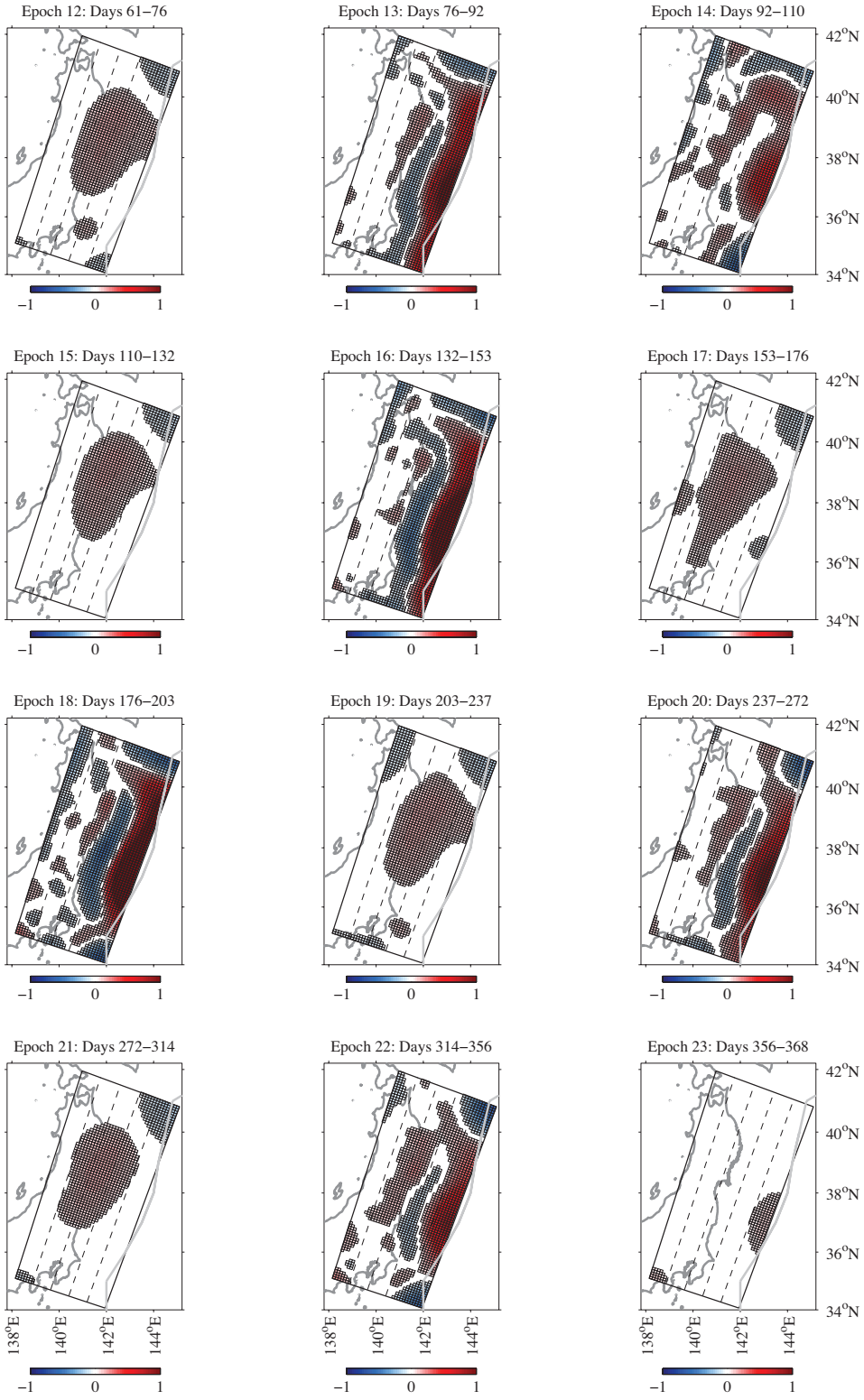

Figure 4.28: Same as Figure 4.27 for postseismic epochs 12–23.

parameters result in a coseismic slip distribution with normal-sense slip magnitudes nearly as large as thrust-sense slip magnitudes (16 m normal slip and 25 m thrust slip). The coseismic magnitude is estimated to be M_W=9.2, with a mean residual displacement of 3.5 cm. The correlation between afterslip in postseismic epoch 1 and static CFS is 0.31±0.1, higher than those found for the lasso solutions, and comparable to those found for the damped least squares estimate. However, as with the damped least squares estimates, the variance in these solutions is unusual among published slip distributions. All subsequent correlations are positive, and range from 0.1±0.06 to 0.2±0.1 (Figure 4.16), with high variance in the slip distributions for epochs 4, 5, 6, 9, 11, 13, 14, 16, 18, 20 and 22, and qualitatively smooth slip in the other epochs (Figures 4.27 and 4.27). Table 4.7 contains additional statistics for afterslip estimates using an augmented smoothing matrix.

EPOCH	β	Correlation Coefficient	slip/epoch (m)	mean slip/epoch (m)	max slip/epoch (m)	Mw/epoch	mrd/epoch (cm)
Coseismic	6.53×10^{13}	-	3689.4	1.20	24.78	9.2	3.54
1	3.30×10^{13}	0.31	2358.2	0.77	11.16	8.9	2.86
2	9.43×10^{13}	0.05	141.7	0.046	0.22	8.0	0.17
3	1.23×10^{15}	0.08	133.2	0.043	0.23	8.0	0.28
4	6.46×10^{12}	0.14	87.2	0.028	0.67	8.2	0.24
5	4.17×10^{13}	0.13	246.7	0.080	0.68	8.2	0.23
6	2.33×10^{13}	0.21	154.1	0.050	0.86	8.2	0.23
7	3.50×10^{15}	0.07	105.8	0.034	0.15	7.9	0.27
8	1.09×10^{15}	0.13	90.7	0.029	0.23	7.9	0.24
9	7.47×10^{13}	0.08	174.7	0.057	0.71	8.2	0.47
10	4.42×10^{15}	0.04	127.4	0.041	0.14	7.9	0.41
11	1.16×10^{13}	0.10	41.2	0.013	0.27	8.1	0.31
12	5.58×10^{15}	0.11	77.8	0.025	0.15	7.9	0.38
13	4.17×10^{13}	0.15	302.0	0.098	1.15	8.3	0.31
14	3.30×10^{13}	0.14	142.6	0.046	0.62	8.1	0.33
15	8.90×10^{15}	0.10	75.7	0.025	0.15	7.9	0.47
16	5.92×10^{13}	0.13	374.2	0.122	1.91	8.4	0.50
17	4.97×10^{15}	0.08	87.7	0.028	0.14	7.9	0.68
18	5.27×10^{13}	0.15	376.4	0.122	2.24	8.4	0.72
19	5.58×10^{15}	0.12	71.7	0.023	0.16	7.9	0.45
20	6.65×10^{13}	0.10	238.4	0.077	1.11	8.2	0.31
21	6.27×10^{15}	0.09	78.9	0.026	0.15	7.9	0.41
22	1.06×10^{14}	0.08	152.5	0.050	0.82	8.2	0.48
23	3.93×10^{15}	0.14	49.8	0.016	0.07	7.7	0.34

Table 4.7: Summary of results for augmented smoothing matrix solution in Section §4.6.3

Because of the dramatic variance in the slip distributions, as in the damped least squares estimation in §4.6.2, we again consider slip distributions with a consistent smoothing coeffi-

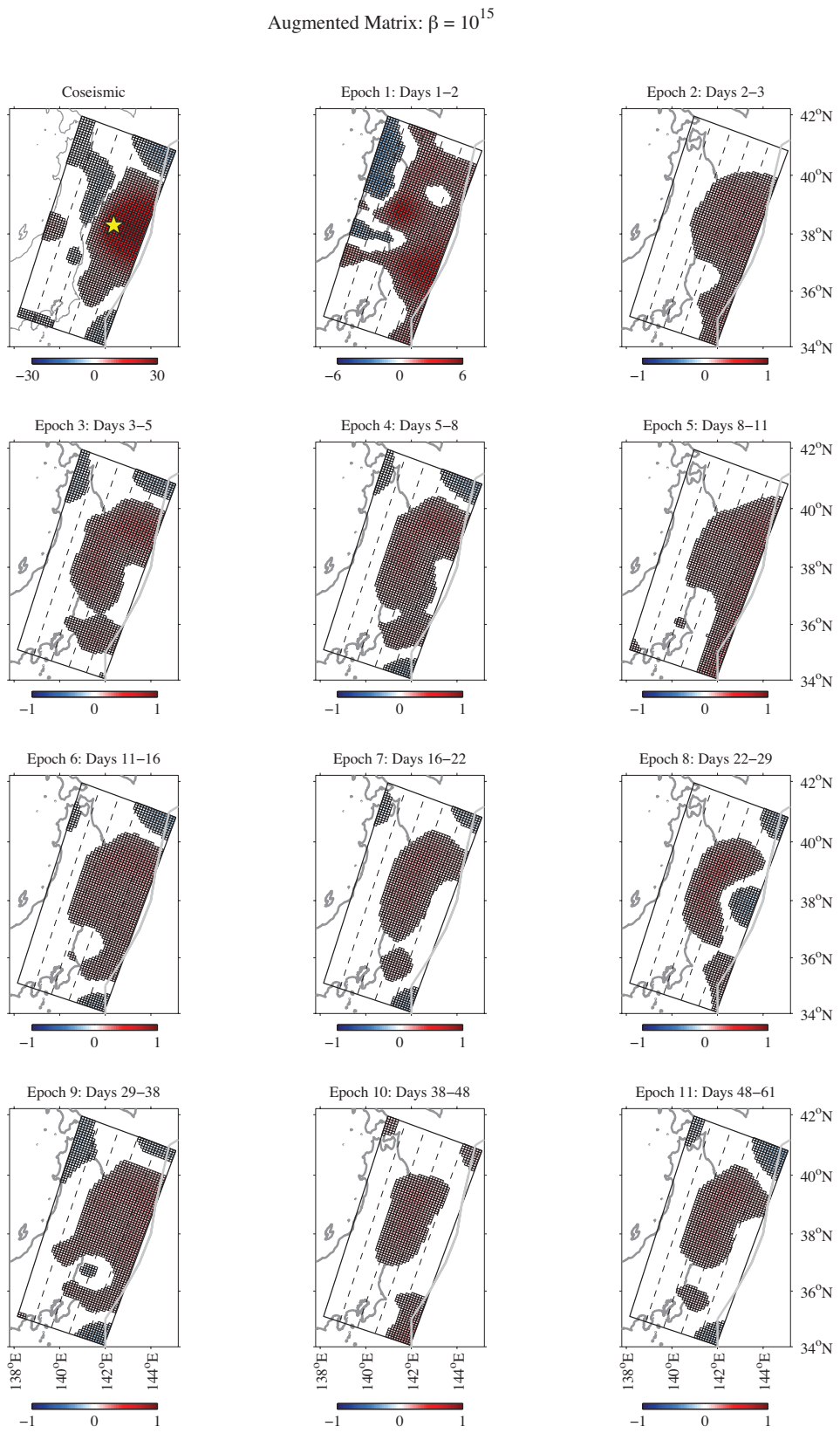

Figure 4.29: Coseismic slip and postseismic afterslip (epochs 1–11) estimated with an augmented smoothing matrix, $\beta = 10^{15}$. Slip color bars in meters. The color bar axis changes over the first three figures.

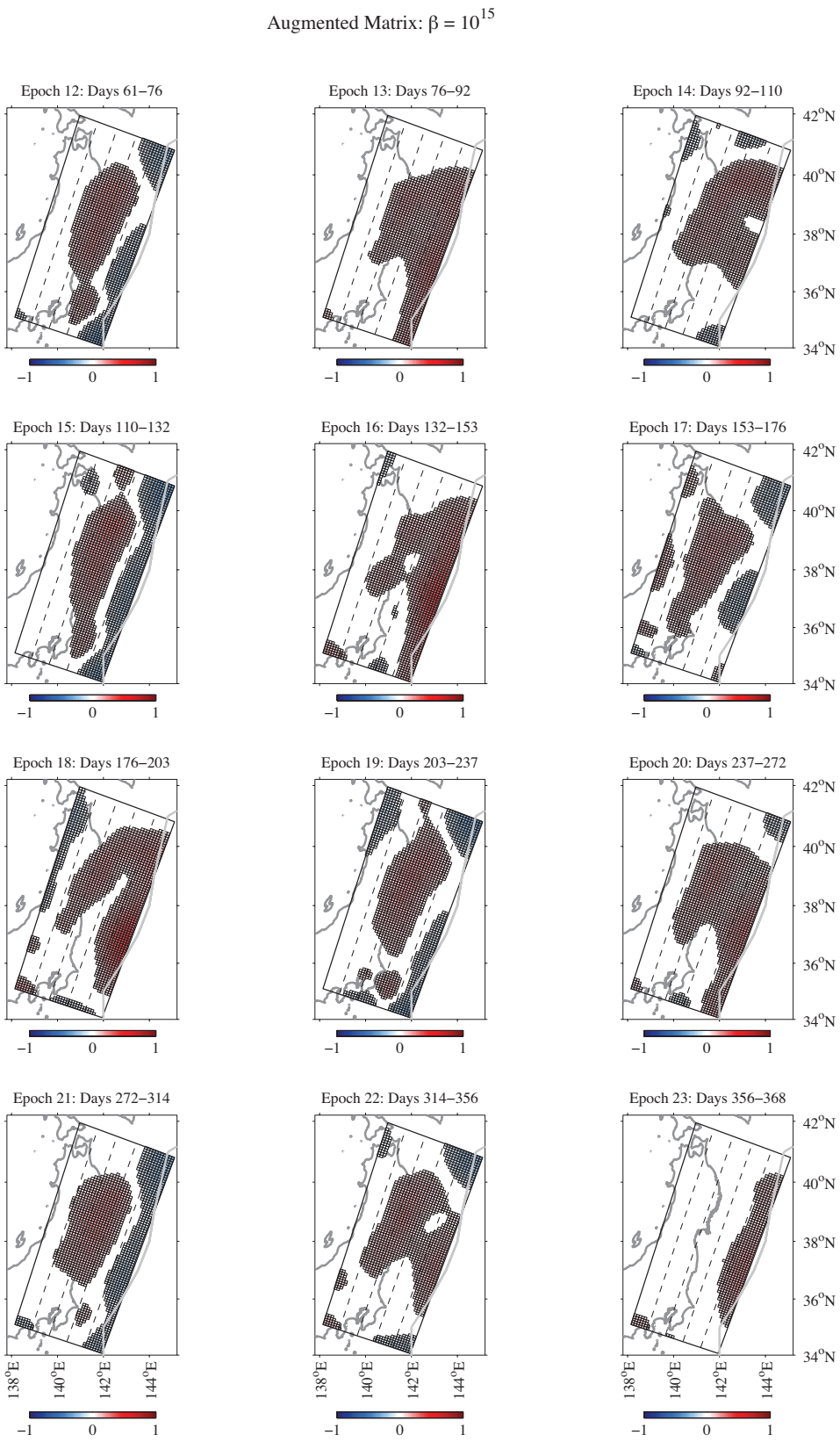

Figure 4.30: Same as Figure 4.29 for postseismic epochs 12-23.

cient for the sake of comparison with literature. We estimate coseismic slip and postseismic afterslip for all epochs with $\beta = 10^{15}$, which produces a coseismic distribution that is qualitatively similar to the damped least squares estimate above. In this case, maximum coseismic slip is 23.1 m, and fits the GPS observations with a mean residual displacement of 4.9 cm. The coseismic magnitude for this distribution is estimated to be M_W=9.1. For the postseismic $\beta = 10^{15}$ we image maximum slip magnitude decreasing from 2.8 m in epoch 1 to 0.2-0.4 m per epoch for the rest of the year (Figures 4.29 and 4.30). Afterslip imaged in all but two postseismic epochs is consistent with cumulative CFS change, with correlation coefficients of 0.05±0.05 to 0.18±0.08, all of which are positive within the 95% confidence interval (Figure 4.16). For the afterslip distributions, we estimate a total equivalent moment magnitude for the 366 days following the earthquake of M_W=9.2. We estimate afterslip in the first day following the earthquake equivalent to a magnitude of M_W=8.7, and we estimate equivalent magnitudes of M_W=7.8-8.0 per epoch for the subsequent 365 days. These afterslip estimates fit the GPS observations with mean residual displacements of 0.2-0.8 cm/epoch. Table 4.8 contains additional statistics for these afterslip estimates using an augmented smoothing matrix with a consistent smoothing parameter.

4.6.4 Imaging postseismic afterslip consistent with CFS: Spatially variable smoothing

Finally, we estimate slip with a spatially variable augmented smoothing matrix (Equations 4.10 and 4.11). This estimation produces co- and postseismic slip distributions that are most consistent with CFS change for coseismic smoothing parameter $\beta = 1.2 \times 10^{15}$ and postseismic $\beta = 8.6 \times 10^{14}$ (Figure 4.14). As with the augmented smoothing matrix

Figure 4.31: Coseismic slip and postseismic afterslip (epochs 1-11) estimated with a spatially variable augmented smoothing matrix, most consistent with Coulomb failure stress. Slip color bars in meters. The color bar axis changes over the first three figures.

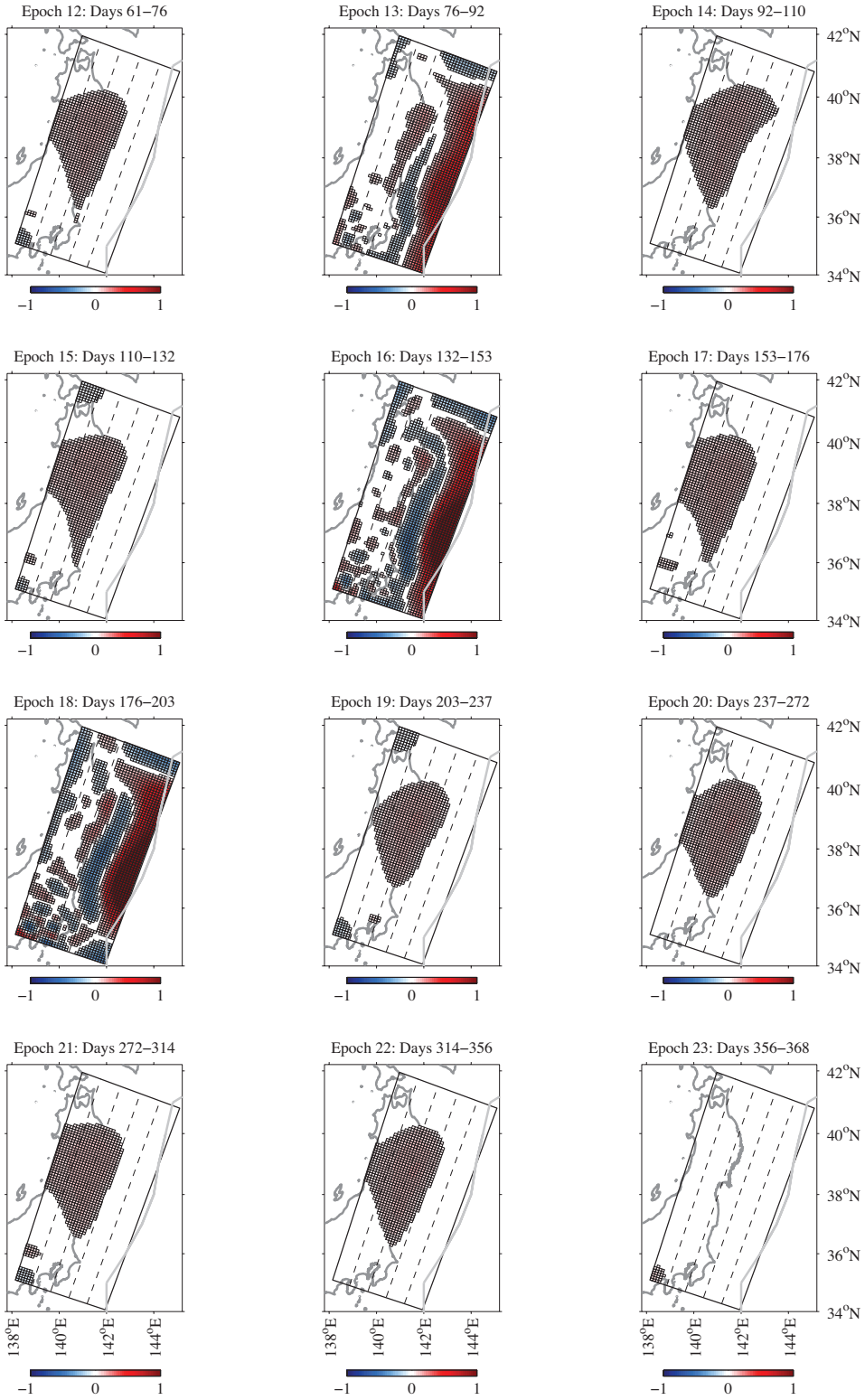

Figure 4.32: Same as Figure 4.31 for postseismic epochs 12-23.

EPOCH	β	Correlation Coefficient	slip/epoch (m)	mean slip/epoch (m)	max slip/epoch (m)	Mw/epoch	mrd/epoch (cm)
Coseismic	10^{15}	-	6709.1	2.18	23.08	9.1	4.85
1	10^{15}	0.18	1447.5	0.47	2.81	8.7	3.18
2	10^{15}	0.05	131.8	0.043	0.15	7.9	0.17
3	10^{15}	0.08	131.7	0.043	0.24	8.0	0.28
4	10^{15}	0.11	105.4	0.034	0.21	8.0	0.25
5	10^{15}	0.12	152.0	0.049	0.20	8.0	0.25
6	10^{15}	0.13	114.0	0.037	0.19	8.0	0.25
7	10^{15}	0.05	89.5	0.029	0.17	7.9	0.26
8	10^{15}	0.12	89.9	0.029	0.23	7.9	0.24
9	10^{15}	0.09	113.2	0.037	0.18	8.0	0.49
10	10^{15}	0.00	123.6	0.040	0.19	7.9	0.40
11	10^{15}	0.09	77.3	0.025	0.18	7.9	0.33
12	10^{15}	0.05	35.3	0.011	0.19	8.0	0.37
13	10^{15}	0.12	158.1	0.051	0.21	8.0	0.33
14	10^{15}	0.09	116.2	0.038	0.18	7.9	0.34
15	10^{15}	0.06	17.7	0.006	0.23	8.0	0.45
16	10^{15}	0.17	172.9	0.056	0.35	8.0	0.53
17	10^{15}	-0.02	76.1	0.025	0.15	8.0	0.68
18	10^{15}	0.21	161.2	0.052	0.38	8.0	0.75
19	10^{15}	0.09	34.1	0.011	0.19	8.0	0.44
20	10^{15}	0.12	135.4	0.044	0.20	7.9	0.34
21	10^{15}	0.04	42.9	0.014	0.19	8.0	0.40
22	10^{15}	0.13	96.3	0.031	0.17	8.0	0.50
23	10^{15}	0.21	66.1	0.021	0.19	7.8	0.34

Table 4.8: Summary of results for augmented smoothing matrix solution in Section §4.6.3, with $\beta = 10^{15}$

estimate, these smoothing parameters result in a coseismic slip distribution with negative (normal-sense) slip magnitudes nearly large as positive (thrust-sense) slip magnitudes (-14m to 23m). The coseismic magnitude for this distribution is estimated to be M_W=9.2, with a mean residual displacement of 3.5 cm. The correlation between afterslip in postseismic epoch 1 and static CFS is 0.34±0.1, higher than those found for the lasso solutions, and comparable to those found for the damped least squares and augmented smoothing matrix estimates. However, as with the damped least squares and augmented smoothing matrix estimates, the variance in many of these solutions is unusual among published slip distributions (Figures 4.31 and 4.32). All subsequent correlations are positive, and range from 0.05±0.04 to 0.17±0.1 (Figure 4.16), with high variance in the slip distributions for epochs 6, 13, 16, and 18, and qualitatively smooth slip in the other epochs. Table 4.9 contains additional statistics for these afterslip estimates that incorporate spatially variable smoothing.

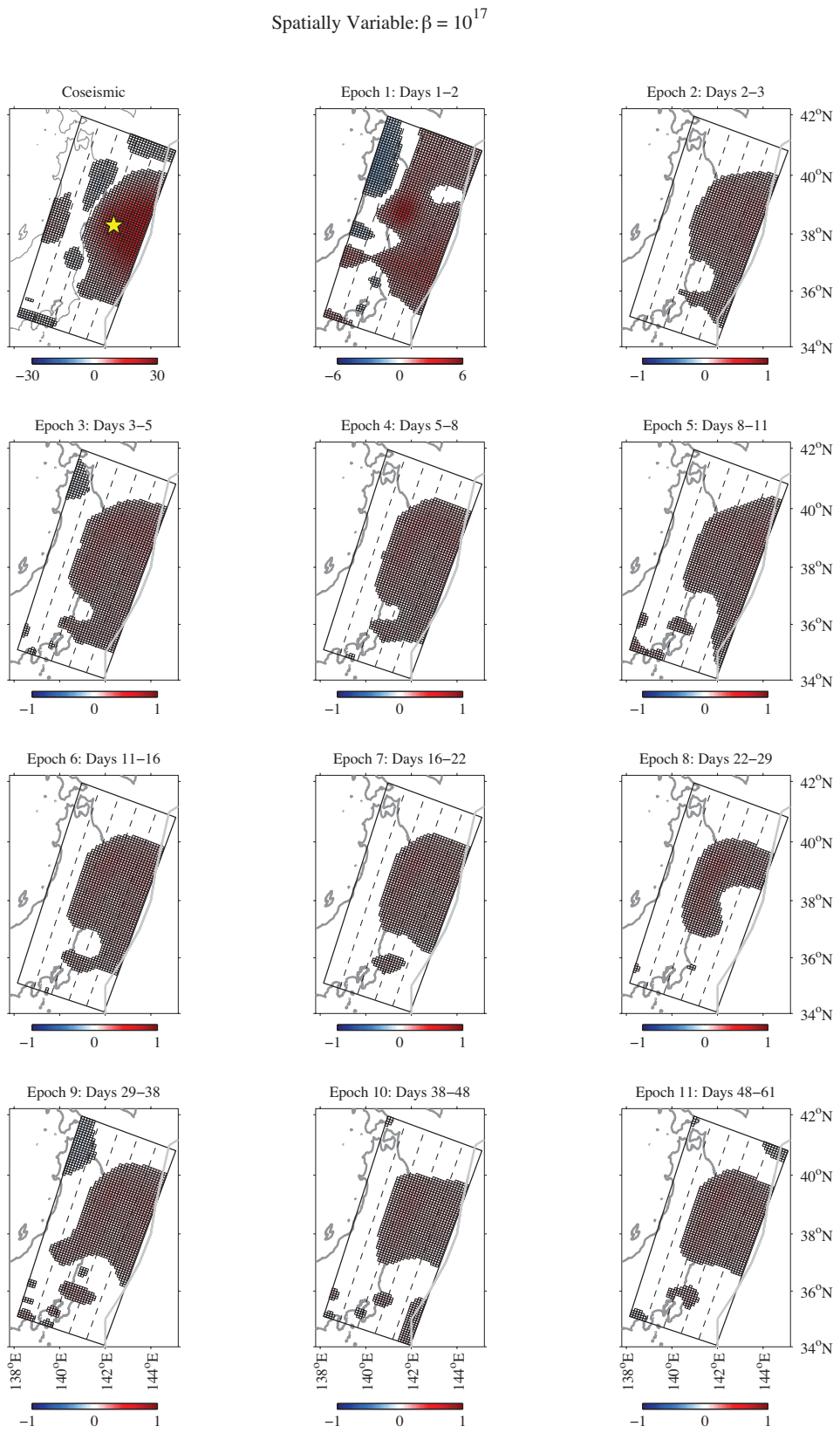

Figure 4.33: Coseismic slip and postseismic afterslip (epochs 1-11) estimated with a spatially variable augmented smoothing matrix, $\beta = 10^{17}$. Slip color bars in meters. The color bar axis changes over the first three figures.

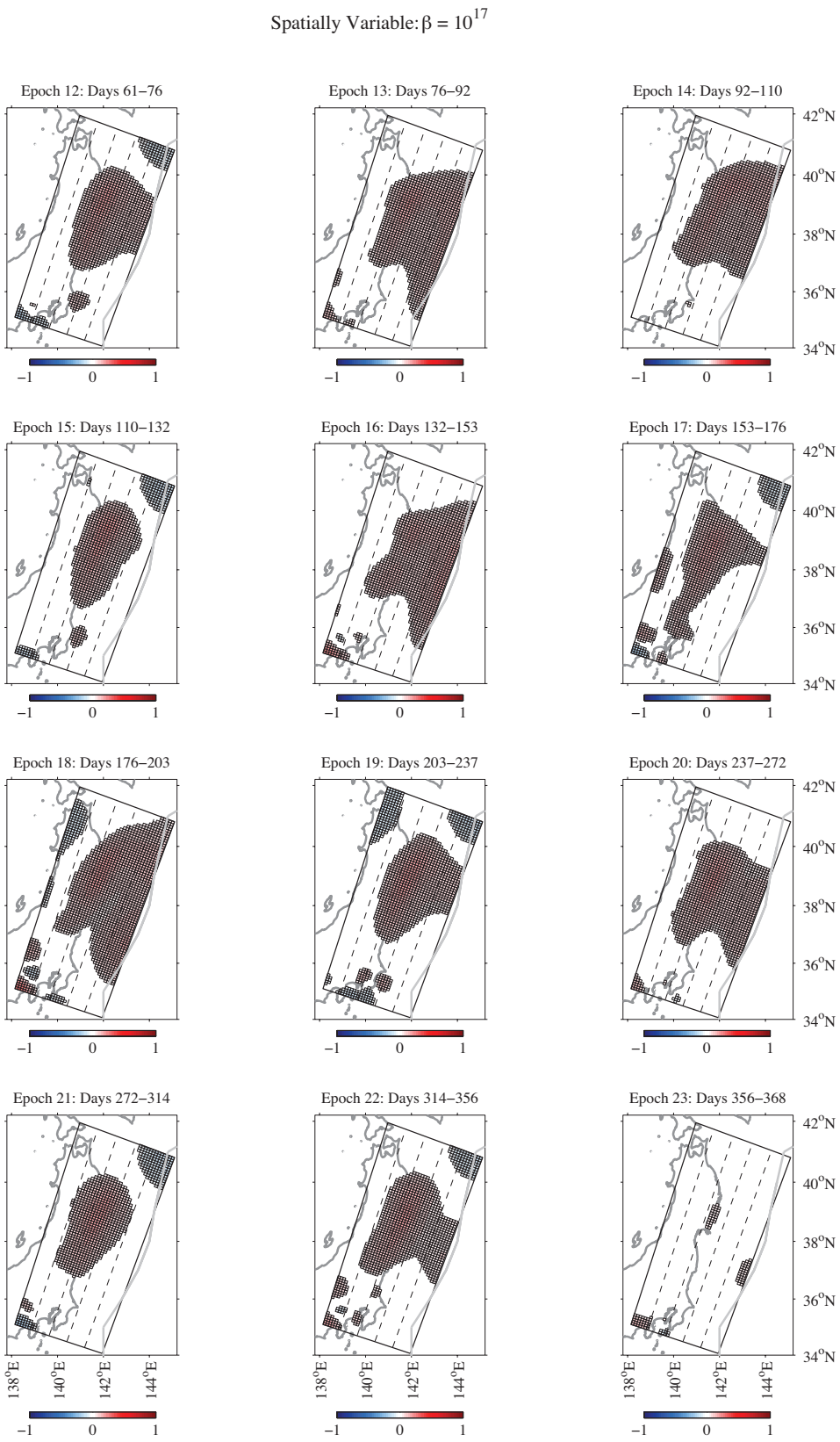

Figure 4.34: Same as Figure 4.33 for postseismic epochs 12-23.

EPOCH	β	Correlation Coefficient	slip/epoch (m)	mean slip/epoch (m)	max slip/epoch (m)	Mw/epoch	mrd/epoch (cm)
Coseismic	1.16×10^{15}	-	3829.3	1.24	23.07	9.2	3.49
1	8.64×10^{14}	0.34	2110.6	0.69	7.93	8.9	2.85
2	1.30×10^{19}	0.17	101.3	0.033	0.11	7.9	0.26
3	1.74×10^{19}	0.16	119.9	0.039	0.14	7.9	0.37
4	1.30×10^{19}	0.16	108.8	0.035	0.13	7.9	0.34
5	9.71×10^{18}	0.18	108.0	0.035	0.11	7.8	0.32
6	3.61×10^{14}	0.19	157.8	0.051	0.82	8.2	0.23
7	1.74×10^{19}	0.13	96.7	0.031	0.11	7.9	0.34
8	7.26×10^{18}	0.16	105.4	0.034	0.13	7.9	0.31
9	9.71×10^{18}	0.13	104.5	0.034	0.12	7.9	0.54
10	9.71×10^{18}	0.13	109.5	0.036	0.12	7.9	0.47
11	7.26×10^{18}	0.13	99.1	0.032	0.12	7.9	0.38
12	7.26×10^{18}	0.12	93.2	0.030	0.12	7.9	0.44
13	1.55×10^{15}	0.19	251.5	0.082	0.78	8.2	0.32
14	7.26×10^{18}	0.14	113.2	0.037	0.12	7.9	0.38
15	9.71×10^{18}	0.10	87.6	0.028	0.12	7.9	0.51
16	1.16×10^{15}	0.20	349.7	0.11	1.62	8.3	0.50
17	7.26×10^{18}	0.13	100.6	0.033	0.12	7.8	0.71
18	1.16×10^{15}	0.19	335.1	0.11	1.73	8.4	0.72
19	5.42×10^{18}	0.14	91.4	0.030	0.13	7.9	0.49
20	5.42×10^{18}	0.15	115.1	0.037	0.13	7.9	0.38
21	9.71×10^{18}	0.10	95.8	0.031	0.12	7.8	0.47
22	5.42×10^{18}	0.15	105.7	0.034	0.13	7.8	0.53
23	4.05×10^{18}	0.17	40.1	0.013	0.07	7.6	0.35

Table 4.9: Summary of results for spatially variable smoothing solution in Section §4.6.4

As with the damped least squares (§4.6.2) and augmented smoothing matrix estimation (§4.6.3), we additionally consider slip distributions with a consistent smoothing coefficient. We estimate coseismic slip and postseismic afterslip for all epochs with $\beta = 10^{17}$, which produces a coseismic distribution that is qualitatively similar to those in the previous sections and (Figure 4.33). In this case, maximum coseismic slip is 17.5 m, and fits the GPS observations with a mean residual displacement of 5 cm. The coseismic magnitude for this distribution is estimated to be M_W=9.1. For the postseismic $\beta = 10^{17}$ we image maximum slip magnitude decreasing from 2.8 to 0.2 m per epoch. Afterslip imaged in epoch 1 is consistent with CFS change within the 95% confidence interval, with a correlation coefficient of 0.11±0.1. Subsequent afterslip distributions are consistent with cumulative CFS in 11 of the remaining postseismic epochs, and are otherwise negative or indistinguishable from zero within the 95% confidence interval (Figure 4.16). For afterslip distributions, we estimate a total equivalent moment magnitude for the 366 days following the earthquake of M_W=9.2.

We estimate afterslip in the first day following the earthquake equivalent to a magnitude of M_W=8.7, and we estimate equivalent magnitudes of M_W=7.9-8.0 per epoch for the subsequent 365 days. These afterslip estimates fit the GPS observations with mean residual displacements of 0.2-0.7 cm/epoch (Figures 4.33 and 4.34). See table 4.10 for additional statistics on these afterslip estimates using spatially variable smoothing.

EPOCH	β	Correlation Coefficient	slip/epoch (m)	mean slip/epoch (m)	max slip/epoch (m)	Mw/epoch	mrd/epoch (cm)
Coseismic	10^{17}	-	6860.3	2.23	17.46	9.1	5.40
1	10^{17}	0.11	1323.8	0.43	2.78	8.7	3.26
2	10^{17}	0.02	127.9	0.042	0.14	7.9	0.17
3	10^{17}	0.00	143.2	0.046	0.19	8.0	0.28
4	10^{17}	0.06	120.1	0.039	0.18	8.0	0.26
5	10^{17}	0.07	135.1	0.044	0.14	7.9	0.25
6	10^{17}	0.09	120.6	0.039	0.18	7.9	0.25
7	10^{17}	-0.03	110.1	0.036	0.16	7.9	0.27
8	10^{17}	0.03	105.6	0.034	0.21	7.9	0.25
9	10^{17}	0.06	115.0	0.037	0.17	8.0	0.49
10	10^{17}	-0.08	126.7	0.041	0.16	7.9	0.40
11	10^{17}	0.01	98.1	0.032	0.17	7.9	0.33
12	10^{17}	-0.02	81.0	0.026	0.17	7.9	0.38
13	10^{17}	0.07	138.2	0.045	0.16	7.9	0.34
14	10^{17}	0.04	121.8	0.040	0.16	7.9	0.34
15	10^{17}	-0.01	70.2	0.023	0.19	7.9	0.46
16	10^{17}	0.16	137.5	0.045	0.24	7.9	0.54
17	10^{17}	-0.12	94.8	0.031	0.16	7.9	0.68
18	10^{17}	0.20	134.1	0.044	0.29	8.0	0.76
19	10^{17}	0.05	74.0	0.024	0.19	7.9	0.45
20	10^{17}	0.08	122.2	0.040	0.17	7.9	0.34
21	10^{17}	-0.04	82.8	0.027	0.18	7.9	0.41
22	10^{17}	0.10	99.1	0.032	0.18	7.9	0.50
23	10^{17}	0.20	46.9	0.015	0.13	7.7	0.34

Table 4.10: Summary of results for spatially variable smoothing in Section §4.6.4, with $\beta = 10^{17}$

4.7 Discussion and Conclusions

Among the many co- and postseismic slip estimates considered in this study, there are still a number of common features. For all of the slip distributions considered, all postseismic afterslip estimates produce a cumulative afterslip in the year following the Tohoku earthquake equivalent to a M_W=8.9-9.2 earthquake, which is larger than the magnitude of coseismic slip

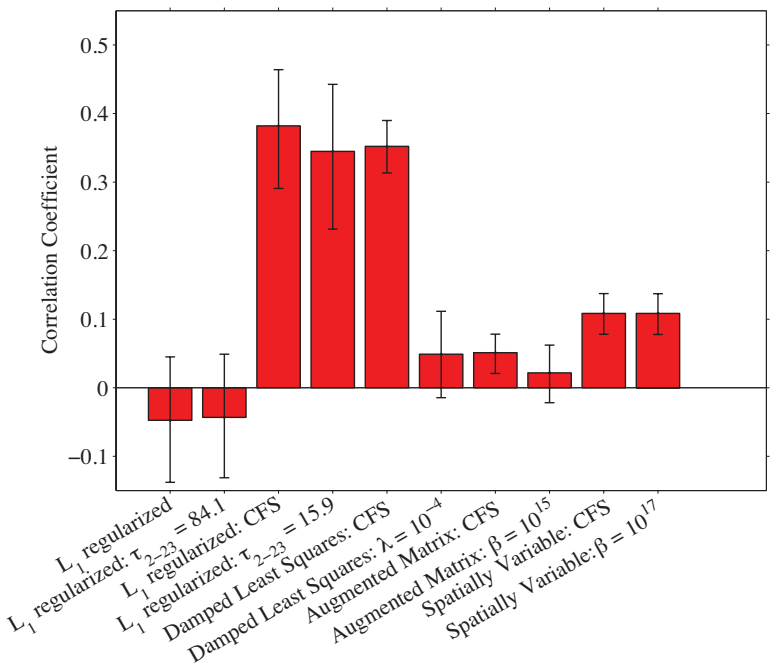

Figure 4.35: Correlation coefficients between CFS due to coseismic slip and one year of cumulative afterslip.

estimated with the same method. Afterslip of greater magnitude than coseismic slip is consistent with previous studies of the Tohoku earthquake and afterslip [Suito et al., 2011; Ozawa et al., 2012], and on the Japan trench following the 1994 Sanriku-Oki earthquake [Yagi et al., 2003], and the 2003 Tokachi-Oki earthquake [Miyazaki, 2004; Miyazaki and Larson, 2008].

We have assumed for this study that afterslip is sensitive to the total CFS change due to coseismic slip and all preceding postseismic slip. Although cumulative CFS is dominated by coseismic stress change, we may have chosen instead to explicitly assume Coulomb stress change for coseismic slip alone is the dominant factor in determining the location and intensity of persistent afterslip. To briefly address this assumption, we consider the cumulative afterslip for each estimation procedure considered in this study, and CFS change due to

coseismic slip estimated with the same estimation procedure. We then calculate the spatial correlation coefficient between cumulative afterslip and coseismic CFS change on the best-resolved 50% of the rectangular dislocations (Figure 4.35). For all but the first two sparse imaging methods (which were estimated without consideration for CFS), these correlations are positive. Given that the stress magnitudes generated coseismically are greater than those generated by afterslip, it is not surprising that the slip estimates are consistent with coseismic CFS alone. However, several of the approaches considered here produce slip distributions that are likely unphysical, and manually smoothed damped least squares and augmented smoothing matrix approaches produce solutions with correlations indistinguishable from zero. Incorporating spatially variable smoothing into the augmented smoothing matrix approach does produce slip distributions that contain mostly positive (thrust-sense) slip and are consistent with this prediction from coseismic Coulomb failure stress change.

Similarly, looking at all of our estimates for co- and postseismic slip, only the spatially variable smoothing method, with $\beta = 10^{17}$ (§4.6.4) produces solutions with a) mostly/completely positive sense slip, b) consistency with CFS change predictions, and c) smooth boundaries to slip. Sharply bounded slip distributions are even more consistent with predictions from CFS change calculations. If we desire a solution with both a) and b), only two of the methods used here are appropriate: sparse estimation methods such as the lasso (§4.6.1), and spatially variable smoothing (§4.6.4). The primary feature that these solution methods have in common is that they produce slip distributions that are localized, and in this sense, sparse estimation methods may be more appropriate than traditional ℓ_2 regularized estimators. For these estimates, postseismic afterslip following the 2011 Tohoku earthquake occurs almost

completely downdip of the coseismic rupture and does not migrate significantly for at least one year after the earthquake.

Chapter 5

Quantized Block Models of Western US Tectonics

Geodetic observations of interseismic deformation provide constraints on microplate rotations, earthquake cycle processes, and slip partitioning across the Pacific-North America plate boundary. These measurements may be interpreted using block models, in which the upper crust is divided into microplates bounded by mapped faults, and slip rates are defined by the relative motions of adjacent microplates. These models integrate the motion of tectonic plates with first-order earthquake cycle processes that couple plates together. The number and geometry of microplates are typically defined with boundaries representing a limited subset of the large number of potentially seismogenic faults. An alternative approach is to include all possible faults in a dense array of microplates, and then deterministically estimate the boundaries at which strain is localized. This approach is possible with a regularization technique called total variation denoising (TVDN) which simultaneously minimizes the ℓ_2 norm of data residuals and ℓ_1 norm of the variation in the estimated state vector. Applied to three-dimensional spherical block models, TVDN reduces the total variation between estimated rotation vectors, creating groups of microplates that rotate together as larger blocks, and therefore localizing fault slip on the boundaries of these larger blocks. Here

we develop a block model comprised of 144 microplates based on detailed fault maps, and deterministically identify the kinematically most important faults in western North America using TVDN regularization. This approach reveals that even in the presence of a diversity of possible fault system geometries, the majority of deformation in western North America is well approximated by slip on a subset of structures at a residual level of 2 mm/yr.

5.1 Introduction

The complexity of continental fault zones has been the focus of numerous studies since the advent of plate tectonics. While discrete fault zones and earthquake activity clearly define narrow regions of concentrated deformation, the apparent number and complexity of these regions has led to a debate about the best means of representing continental deformation: whether as a system of individual rigid microplates, or as a continuous medium [e.g., Molnar, 1988; Thatcher, 1995, 2009]. In particular, several regions of large-scale continental complexity have been identified, including western North America [e.g., Bird, 2003]. Over the last 30 years, global positioning system (GPS) observations have provided a quantitative description of nominally interseismic continental deformation. However, elastic strain accumulation across locked faults produces smooth GPS velocity gradients [e.g., Savage and Burford, 1973; Okada, 1985], making it potentially challenging to identify the individual faults responsible for the largest amount of slip within a fault system or plate boundary zone.

To move beyond qualitative descriptions of apparent complexity, studies of western North America kinematics leveraged discrepancies between path integral constraints and slip obser-

vations from geology [Weldon and Humphreys, 1986; Minster and Jordan, 1987] and geodesy [Minster and Jordan, 1987] to quantify the potential influence of unknown deformation sources required within the plate boundary. This understanding of kinematic consistency evolved into the development of kinematically consistent block models of western North America [Murray and Segall, 2001; McCaffrey, 2002; Meade, 2005], in which the crust is divided into a discrete number of microplates bounded by mapped faults and constrained by geodetic (and/or geologic) observations. Alternatively, other studies have quantified the strain field of western North America not in terms of tectonic microplates, but by representing the plate boundary as a continuously deforming region [e.g., Shen Tu et al., 1998; Flesch et al., 2000]. Finite element models containing major faults seek to describe both tectonic and permanent deformation within the plate boundary [Bird and Baumgardner, 1984; Bird and Kong, 1994; Bird, 2009].

Because block models interpret geodetic observations of interseismic deformation in terms of microplate rotations and earthquake cycle processes [Matsu'ura et al., 1986; Hashimoto and Jackson, 1993; Souter, 1998; Bennett et al., 1996, 1997; Murray and Segall, 2001; McCaffrey, 2002; Meade, 2005], they are a valuable tool for addressing longstanding debates in western North American tectonics and questions of continental complexity. The number and geometry of microplates are typically defined a-priori, with boundaries representing a limited subset of the large number of potentially seismogenic faults. Fixed block model geometries limit interpretation of the complexity of a fault system, because complexity is imposed in the block geometry.

In particularly complex plate boundaries such as western North America, we may wish to

deterministically allow observations of interseismic deformation to independently estimate the kinematically most important faults, and address hypotheses about the nature of continental complexity. Within a block model, we would like to select block boundaries from a large number of potentially seismogenic faults by grouping a large number of small microplates into a smaller number of larger blocks. This is possible with an ℓ_1 regularization technique [e.g., Candès et al., 2006; Donoho, 2006] called total variation denoising (TVDN) [Rudin et al., 1992; Chambolle, 2004]. Applied to three-dimensional spherical block models, TVDN reduces the total variation between estimated rotation vectors, creating groups of microplates that rotate together as larger blocks, and therefore localizing fault slip on the boundaries of these larger blocks. In this way, we seek to find the simplest plate boundary block model (i.e., with the fewest blocks) that fit the data at a given level of resolution.

Geodetic observations of interseismic continental deformation have been used to inform regional kinematic studies in Southern California [Meade, 2005; McCaffrey, 2005; Loveless and Meade, 2011b], the San Francisco bay area [d'Alessio et al., 2005], the Basin and Range [Hammond and Thatcher, 2005; Thatcher et al., 1999; Wernicke et al., 2008; Niemi et al., 2004; Bennett et al., 2003], and the Pacific Northwest [McCaffrey et al., 2007]. Similar geodetic studies have illuminated continental complexity in western Canada and along the Aleutian trench in Alaska [Fletcher and Freymueller, 2003; Freymueller et al., 2008]. Until recently however, quantifying present-day tectonic complexity at the plate-boundary scale was limited by the lack of a unified reference frame for all western North American GPS velocities. Loveless and Meade [2011a] combined 7 velocity fields [McClusky et al., 2001; Shen et al., 2003; Hammond and Thatcher, 2005; Williams et al., 2006; McCaffrey et al., 2007,

and the Plate Boundary Observatory Network velocity field, http://pobweb.unavco.org] into a common reference frame by minimizing velocity misfit between collocated stations in the fields, using a 6-parameter (rotation plus translation) transformation [Loveless and Meade, 2010] for a combined velocity field of 1822 stations.

We use a combined GPS velocity field of Western North America [Loveless and Meade, 2011b] to develop the first block models of the full Pacific-North America plate boundary. Beginning with a block model containing a dense array of microplates, we use total variation denoising (TVDN) as a tool for block model selection, grouping adjacent small microplates into fewer, larger blocks and identifying the kinematically most important block boundaries. These new boundaries are then fed into a traditional block model to estimate block rotations, fault slip rates, and spatially variable coupling on the Cascadia subduction zone for a complete model of western North America crustal deformation. In this way, we are able to quantitatively address the plate boundary complexity required to explain present day interseismic velocities. Beginning with 144 total blocks, we reduce the number of effective blocks to 20-33, and fit data with mean residual velocity of <2 mm/yr.

5.2 Block Modeling

Geodetic observations may be interpreted using block models, in which the upper crust is divided into microplates bounded by mapped faults. Typically, the number and geometry of microplates are defined with boundaries representing a limited subset of the large number of potentially seismogenic faults [Matsu'ura et al., 1986; Hashimoto and Jackson, 1993; Souter, 1998; Bennett et al., 1996, 1997; Murray and Segall, 2001; McCaffrey, 2002; Meade, 2005;

Meade and Loveless, 2009]. In the block model formulation of Meade and Loveless [2009], interseismic velocities are represented as a linear combination of block rotations, elastic strain accumulation due to slip deficit on block-bounding faults and spatially variable coupling on triangular dislocations, and homogeneous internal elastic strain:

$$\tilde{\mathbf{v}}_{\mathrm{I}} = \tilde{\mathbf{v}}_{\mathrm{B}} + \tilde{\mathbf{v}}_{\mathrm{E}} + \tilde{\mathbf{v}}_{\dot{\epsilon}} \tag{5.1}$$

in which $\tilde{\mathbf{v}}_{\mathrm{I}}$ is the vector of inter seismic velocities in spherical coordinates, $\tilde{\mathbf{v}}_{\mathrm{B}}$ is the vector of velocities due to block rotation, $\tilde{\mathbf{v}}_{\mathrm{E}}$ is the vector of velocities due to elastic strain accumulation, and $\tilde{\mathbf{v}}_{\dot{\epsilon}}$ is the vector of velocities due to internal block strain. Written in terms of block rotations, elastic strain accumulation due to triangular dislocation elements, and homogeneous internal strain, the forward problem is:

$$\tilde{\mathbf{v}}_{\mathrm{I}} = [\mathbf{G}_{\mathrm{B}} - \mathbf{G}_{\mathrm{SD}}\ \mathbf{G}_{\mathrm{t}}\ \mathbf{G}_{\dot{\epsilon}}] \begin{bmatrix} \boldsymbol{\Omega} \\ \mathbf{t} \\ \dot{\epsilon} \end{bmatrix} \tag{5.2}$$

in which $\mathbf{G}_{\mathrm{B}}$ contains the Green's functions relating to block rotations, $\mathbf{G}_{\mathrm{SD}}$ contains the Green's functions due to slip deficit on the block-bounding faults, $\mathbf{G}_{\mathrm{t}}$ contains Green's functions due to slip deficit on triangular dislocation elements, and $\mathbf{G}_{\dot{\epsilon}}$ contains Green's functions for homogeneous elastic strain within the block. $\boldsymbol{\Omega}$ is the vector of block rotations, $\mathbf{t}$ is the vector of elastic strain accumulation rates on triangular dislocation elements, and $\dot{\epsilon}$ contains the magnitude of homogeneous elastic strain rates in each block.

5.2.1 Weighted least squares estimator

Present-day GPS observations provide observations of $\tilde{\mathbf{v}}_{\mathrm{I}}$, but we typically do not know the block motions, spatial distribution of strain accumulation on partially coupled faults, or internal block strain rates. A traditional block model estimates these parameters using weighted least squares estimator:

$$\mathbf{m}^{\mathrm{est}} = \left[\left(\mathbf{G}^{\top} \mathbf{W} \mathbf{G} \right)^{-1} \mathbf{G}^{\top} \mathbf{W} \right] \tilde{\mathbf{v}}_{\mathrm{GPS}} \tag{5.3}$$

in which $\mathbf{G}$ is the generalized Jacobian containing $\mathbf{G}_{\mathrm{B}}$, $\mathbf{G}_{\mathrm{SD}}$, $\mathbf{G}_{\mathrm{t}}$ and $\mathbf{G}_{\dot{\epsilon}}$ from equation 5.2. Estimated solution vector $\mathbf{m}^{\mathrm{est}}$ contains the estimated rotation vectors, $\mathbf{\Omega}^{\mathrm{est}}$, estimated slip deficit rates on triangular dislocation elements,$\mathbf{t}^{\mathrm{est}}$, and estimated homogeneous elastic strain rates, $\dot{\epsilon}^{\mathrm{est}}$:

$$\mathbf{m}^{\mathrm{est}} = \begin{bmatrix} \mathbf{\Omega}^{\mathrm{est}} \\ \mathbf{t}^{\mathrm{est}} \\ \dot{\epsilon}^{\mathrm{est}} \end{bmatrix} \tag{5.4}$$

5.2.2 Quantized block model solutions

Within a system of rotating microplates, a fault bounding two blocks with different rotation vectors will have some slip on that fault, whereas if two blocks have an identical Euler pole location and rotation rate, those two blocks effectively behave as a single larger block, and the slip rate on the bounding fault will go to zero (Figure 5.1). We may wish to find a solution in which many blocks have identical rotation vectors, i.e., in which $\mathbf{\Omega}$ is grouped or quantized. Finding a quantized solution provides a strategy for approaching

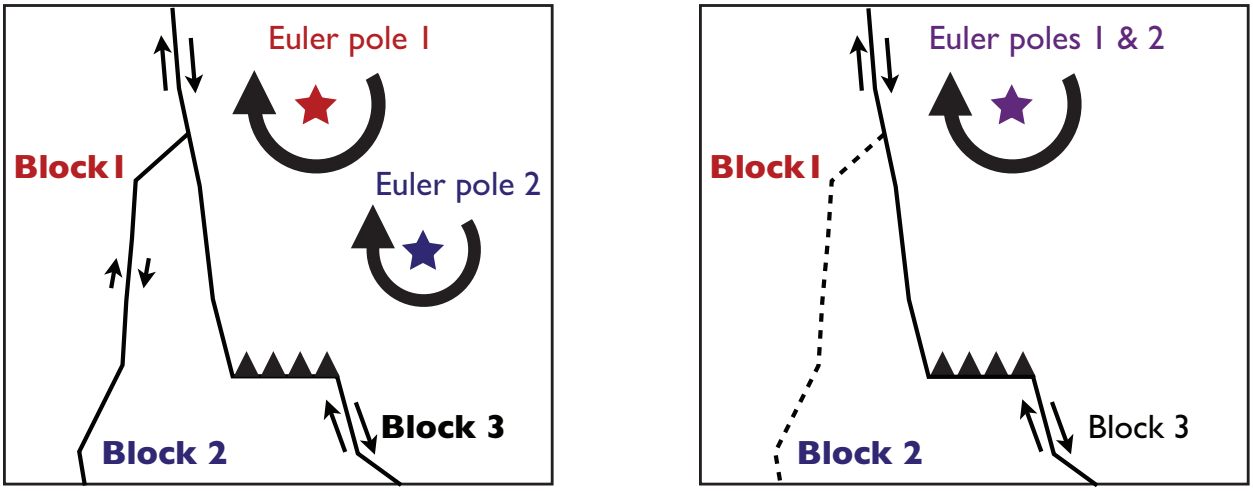

Figure 5.1: Blocks cartoon. Black lines represent faults with relative slip shown with black arrows. Colored stars show Euler pole locations for Blocks 1 and 2. Left: when Block 1 and Block 2 have different rotation vectors, there is some slip resolved on the fault bounding them. Right: when Blocks 1 and 2 have an identical Euler pole and rotation rate, slip on the fault bounding them goes to zero, and they effectively behave as a single larger block.

ambiguity in block model selection: we may include all possible faults in a dense array of microplates, and then algorithmically estimate the boundaries at which strain is localized based on geodetic observations of interseismic deformation.

5.2.3 Total Variation Denoising

It is possible to estimate quantized solutions directly with a regularization technique developed for edge sharpening in image processing: total variation denoising (TVDN) [Rudin et al., 1992; Chambolle, 2004]. TVDN simultaneously minimizes the ℓ_2 norm of the data residuals and ℓ_1 norm of the variation in the estimated state vector. Applied to three-dimensional spherical block models, TVDN minimizes the ℓ_1 norm of variation in the block rotation vectors, and therefore localizing fault slip on the boundaries of these larger blocks:

$$\min \|\mathbf{Gm} - \mathbf{d}\|_2 \; + \; \lambda \|\mathbf{Dm}\|_1 \tag{5.5}$$

where λ is a tunable parameter that controls the strength of the regularization term, and $\mathbf{D}$ is a linear differential operator. Construction of matrix $\mathbf{D}$ for block model implementation is discussed at the end of this section.

Absolute value (ℓ_1) regularization methods designed to recover sparse state vectors have been applied in reflection seismology for decades [e.g., Claerbout and Muir, 1973; Santosa and Symes, 1986], and recently applied to geodetic imaging of sharp coseismic slip distributions [Evans and Meade, 2012]. Under many circumstances, the ℓ_1 norm likely recovers the ℓ_0 pseudo-norm, which gives the number of non-zero elements in the vector of interest [Candès et al., 2006; Donoho, 2006]. Applied to earthquake slip distributions, ℓ_1, regularization minimizes the number of non-zero elements in the solution vector, and produces a compact representation of slip [Evans and Meade, 2012]. In a block model, applying the ℓ_1 norm to vector $\mathbf{Dm}$ limits the number of non-zero differences in the solution vector $\mathbf{m}$, resulting in a grouped or quantized solution. The ℓ_1 regularization introduces a non-linear state vector regularization, but a global minimum can be found using convex optimization methods. Several solvers exist for variations of ℓ_1 regularization, including TVDN. We modify a 1-dimensional version of the TVreg package for Matlab [Jensen et al., 2012; Boyd and Vandenberghe, 2004, 1-D code at http://www.imm.dtu.dk/∼pcha/Regutools/TVreg.m] to accommodate arbitrary problem sizes and constraints.

In terms of a block model, every 3 rows of $\mathbf{D}$ correspond to a block constraint, and each column corresponds to a rotation vector component of a block. $\mathbf{D}$ has dimensions of 3 times

the number of constraints by 3 times the number of blocks. Each constraint limits differences in the rotation vector between two adjacent blocks, for example, if block i is adjacent to block j, we want to minimize the difference in rotation between these blocks:

$$\min\ (\Omega_i - \Omega_j) \tag{5.6}$$

And if block i is also adjacent to block k, we separately constrain the difference in rotation between these blocks:

$$\min\ (\Omega_i - \Omega_k) \tag{5.7}$$

For each block, we want separate rows in the difference matrix for each geographically adjacent block. Because we are constraining the 3-component rotation vector, each block constraint requires three rows. For example, a single block constraint, $\mathbf{C}$ is a 3 x 3n matrix (where n is the total number of blocks) constraining rotation of block i relative to block j, and would be filled in as:

$$\begin{aligned} \mathrm{C}_{q,3i-q+1} &= 1 \\ \mathrm{C}_{q,3j-q+1} &= -1 \\ q &= 1,2,3 \end{aligned} \tag{5.8}$$

Finally, we weight each constraint by the length (l) of the fault that bounds blocks i and j, to avoid biasing the solution towards faults that bound fewer blocks. An example

constraint matrix $\mathbf{C}$ would look like this:

$$\mathbf{C} = l \begin{bmatrix} \dots & 1 & 0 & 0 & \dots & -1 & 0 & 0 & \dots \\ \dots & 0 & 1 & 0 & \dots & 0 & -1 & 0 & \dots \\ \dots & 0 & 0 & 1 & \dots & 0 & 0 & -1 & \dots \end{bmatrix} \tag{5.9}$$

And these constraints are stacked to form difference matrix $\mathbf{D}$.

5.3 GPS data and block model selection method

We constrain deformation in western North America with interseismic observations of a combined velocity field of 1686 observations [Loveless and Meade, 2011b; McClusky et al., 2001; Shen et al., 2003; Hammond and Thatcher, 2005; Williams et al., 2006; McCaffrey et al., 2007, and Plate Boundary Observatory Network velocity field, http://pboweb.unavco.org] (Figure 5.2). These velocity fields are combined into a common reference frame by minimizing velocity misfit between collocated stations in the fields, using a 6-parameter (rotation plus translation) transformation [Loveless and Meade, 2010, 2011b, GSA Data Repository item 2011305]. We omit velocities north of the Canadian border because we do not model potentially complex deformation in western Canada or along the Aleutian trench, and we omit velocities near Yellowstone containing contributions from non-tectonic deformation, resulting in a final velocity field of 1686 observations.

We develop a block model comprised of 144 microplates based on quaternary fault maps [Jennings, 1994; U.S. Geological Survey et al., 2006] (Figure 5.3). We divide the block modeling procedure into two steps: 1) we use TVDN to reduce the number of uniquely rotating blocks, and select the block geometry to be used in modeling deformation in western

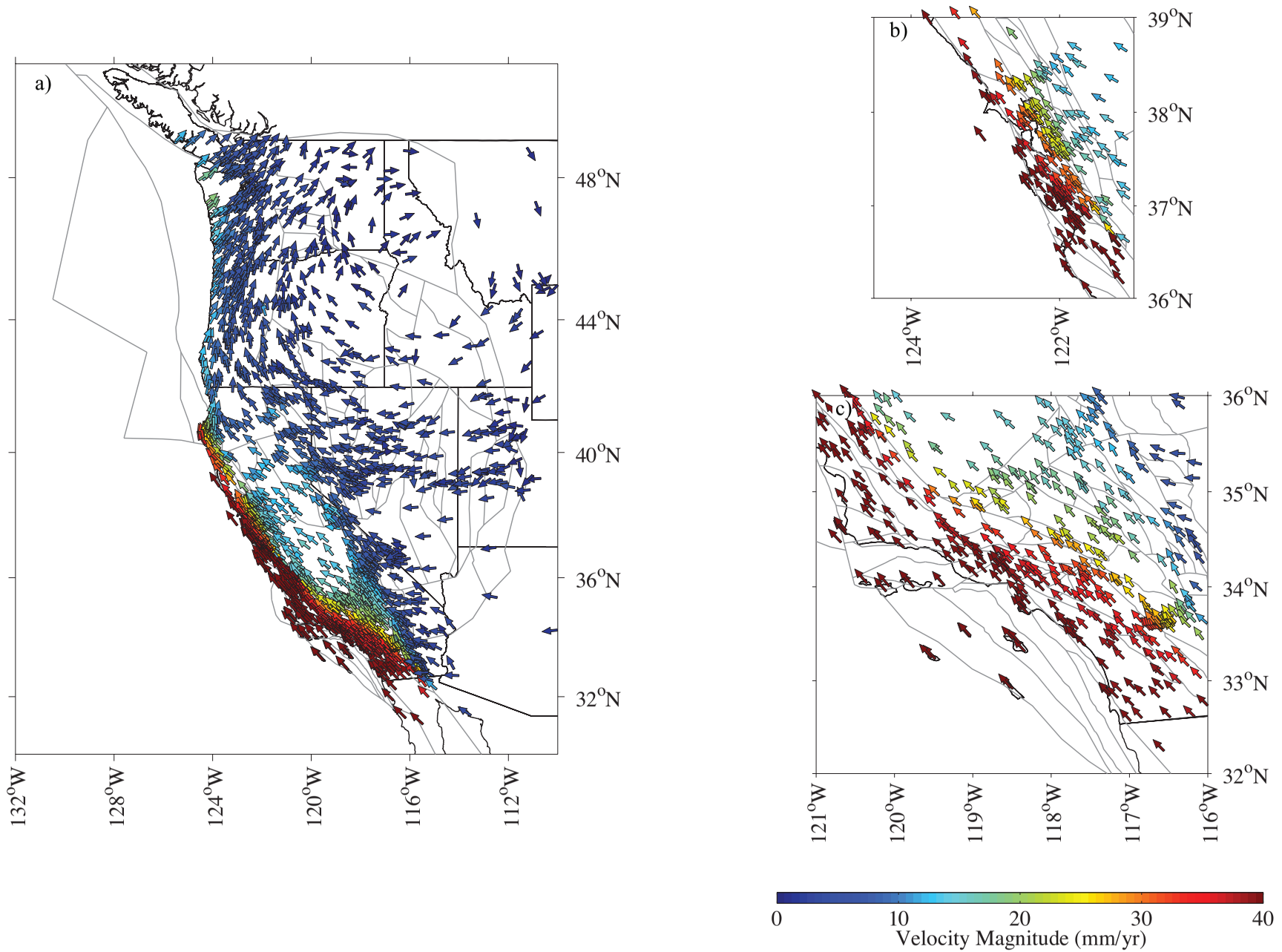

Figure 5.2: Input velocities a) in Western U.S. b) in San Francisco Bay Area c) in Southern California. Arrow sizes are constant, and colors represent velocity magnitude.

North America; then 2) we use the block geometry identified in step 1) for a full block model solution, including spatially variable coupling on the Cascadia subduction zone. This procedure is outlined in the flowchart in Figure 5.4.

To simplify the block model selection problem in step 1), we assume that all deformation is due exclusively to block rotations and strain accumulation on fully locked faults. This assumption simplifies Equation 5.1 to:

$$\tilde{\mathbf{v}}_{\mathrm{I}} = \tilde{\mathbf{v}}_{\mathrm{B}} + \tilde{\mathbf{v}}_{\mathrm{E}} \tag{5.10}$$

so Equation 5.2 becomes:

$$\tilde{\mathbf{v}}_{\mathrm{I}} = [\mathbf{G}_{\mathrm{B}} - \mathbf{G}_{\mathrm{SD}}]\boldsymbol{\Omega} \tag{5.11}$$

which reduces the weighted least squares estimator to:

$$\boldsymbol{\Omega}^{\mathrm{est}} = \left[\left(\mathbf{G}^{\top}\mathbf{W}\mathbf{G}\right)^{-1}\mathbf{G}^{\top}\mathbf{W}\right]\tilde{\mathbf{v}}_{\mathrm{GPS}} \tag{5.12}$$

where $\mathbf{G} = \mathbf{G}_{\mathrm{B}} - \mathbf{G}_{\mathrm{SD}}$. This assumption is not valid near faults that are partially coupled, which is most significant in the northwest United States and southwest Canada due to the Cascadia subduction zone. So that we only estimate block rotations with TVDN, we independently estimate partial coupling on the Cascadia subduction zone [Loveless and Meade, 2011b], and calculate the contribution to the interseismic velocity field from estimated coupling on the Cascadia subduction zone. We then subtract these velocities from the combined velocity field that we use for block model selection step in Figure 5.4.

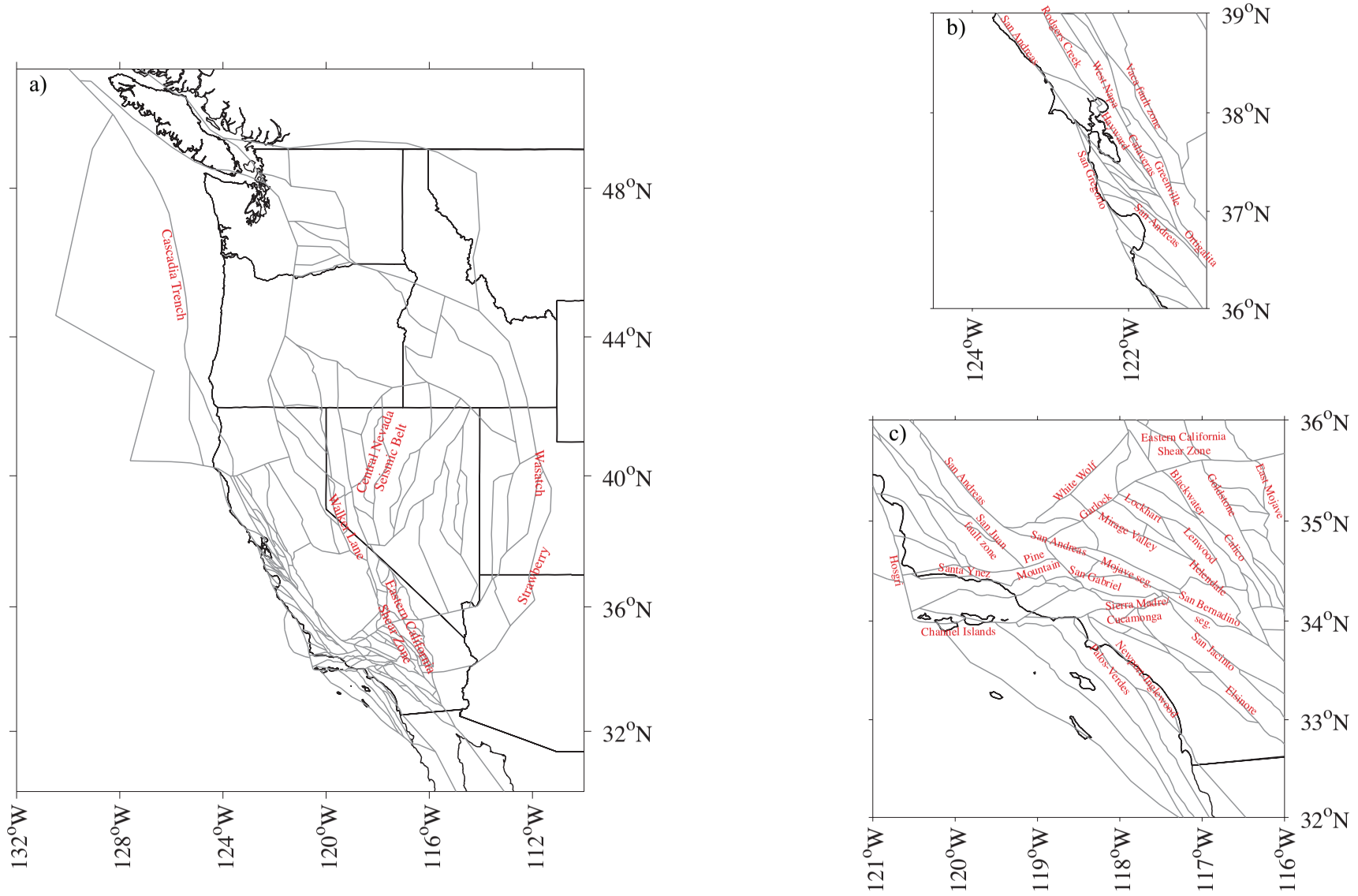

Figure 5.3: Input blocks with fault labels. Gray lines show block boundaries a) in Western U.S. b) in San Francisco Bay Area c) in Southern California.

Once the total number of effective blocks has been reduced algorithmically with TVDN, we use this new block geometry to interpret the full velocity field with a traditional block model (Equation 5.1) using a weighted least squares estimator (Equation 5.3). For the full block model inversion we additionally estimate spatially variable coupling rates on the Cascadia subduction zone. In this case we impose an a-priori Euler pole location of 69.6±0.100 E, -26.6±0.100 N, with a rotation rate 0.81±0.001 [Miller et al., 2001].

5.4 Quantized Block Model Results

Total variation denoising (§5.2.3) Equation 5.5) reduces the effective number of blocks directly by simultaneously estimating block rotations that are quantized. The scalar tuning parameter λ controls the strength of the regularization such that increasing λ reduces the number of independent block Euler poles, i.e., the number of separate blocks. Very small values of λ do not reduce the total number of independently rotating blocks. For large values of λ, model fit to the GPS observations is outweighed by the total variation constraint, resulting in models with very few independently rotating blocks, and therefore very few active faults. We consider block model solutions for λ values from $\lambda = 50$ to $\lambda = 2300$, which incrementally reduces the total number of blocks in the plate boundary from 133 to 3 (Figure 5.5). Dashed lines in Figure 5.5 identify λ values of models that we discuss in this section.

5.4.1 End Member Models

As a benchmark, we first consider the results from a classic block model inversion on the 144-block model. Unsurprisingly, this leads to over-fitting of the GPS velocities, resulting in

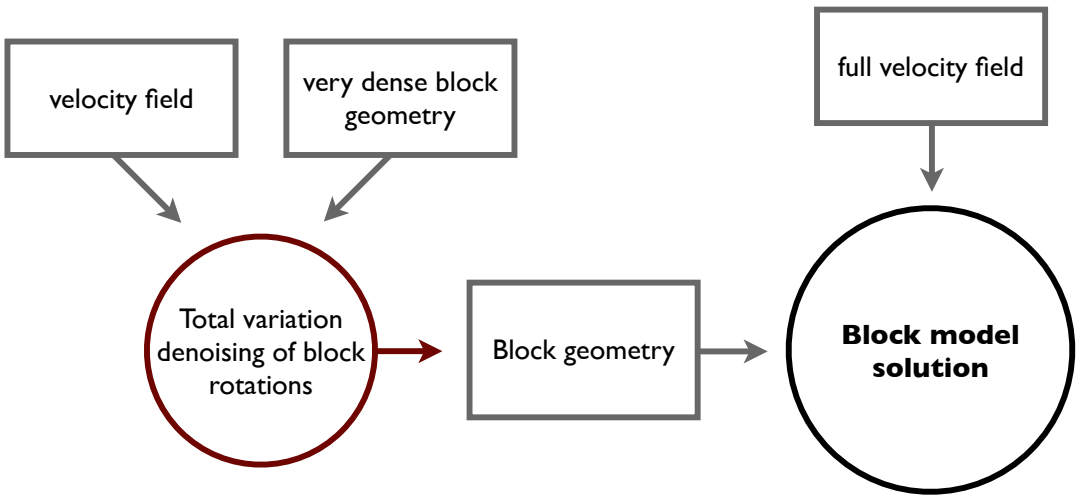

Figure 5.4: Flowchart outlining workflow for TVDN model selection and block model estimation. We use TVDN as a method of block geometry selection based on an original dense block geometry and a modified velocity field (modified to remove the elastic signal due to coupling on the Cascadia subduction zone). The selected block geometry is then fed into the full block model using the full velocity field to estimate block rotation, fault slip rates, and coupling on the subduction zone.

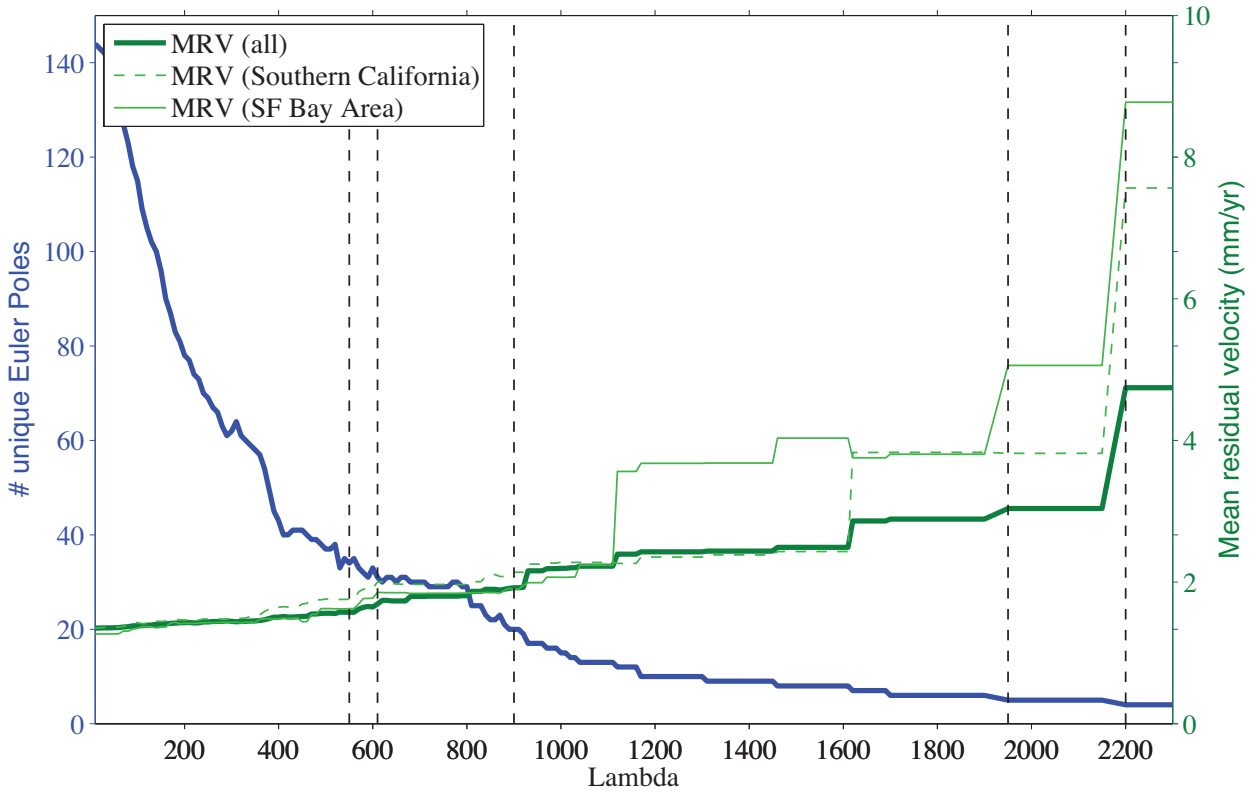

Figure 5.5: Solution behavior for values of λ. Dashed lines identify λ values of models that we discuss in §5.4

non physical block rotations in which a single poorly constrained block may be bounded by high right lateral slip rates on one side, and high left lateral slip rates on the other, leading to artificially high slip rate magnitudes across the boundary (Figure 5.7), motivating the need for a regularized estimator. The locations of the final Euler poles for this and each of the models considered below are shown in Figure 5.6.

As an alternative end-member, for large values of lambda, model fit to the GPS observations is outweighed by the total variation constraint, resulting in models with very few independently rotating blocks, and therefore very few active faults. Figure 5.8 shows the TVDN grouping of the Euler pole locations and rotation rates for two high values of λ: $\lambda = 2200$ and $\lambda = 1950$, resulting in only three and four separate blocks, respectively. We

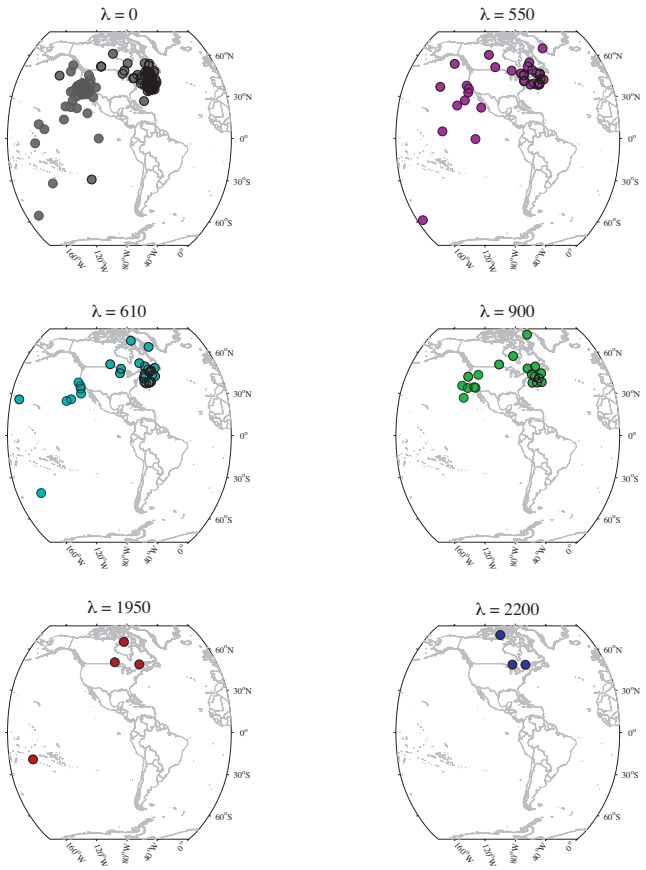

Figure 5.6: Final Euler pole locations for block model solutions. Euler poles associated with negative rotation rates outlined in black. Colors representative of λ value, and are consistent in Figures 5.8 and **??**.

then estimate block rotations, fault slip rates, and spatially variable coupling on the Cascadia subduction zone using the traditional blocks formulation (Equations 5.1 and 5.3). The locations of the final Euler poles for each of the models considered are shown in Figure 5.6. We first consider a model in which the plate boundary is made up of only three blocks: Pacific block, North America block, and the Juan de Fuca block (Figure 5.9), when $\lambda = 2200$. In this extreme case of $\lambda = 2200$, the best fitting boundary between the Pacific and North American blocks follows a fault up the Eastern California Shear Zone, along the eastern side of the great valley up to Mendocino. This boundary is similar to that proposed by Nur et al.

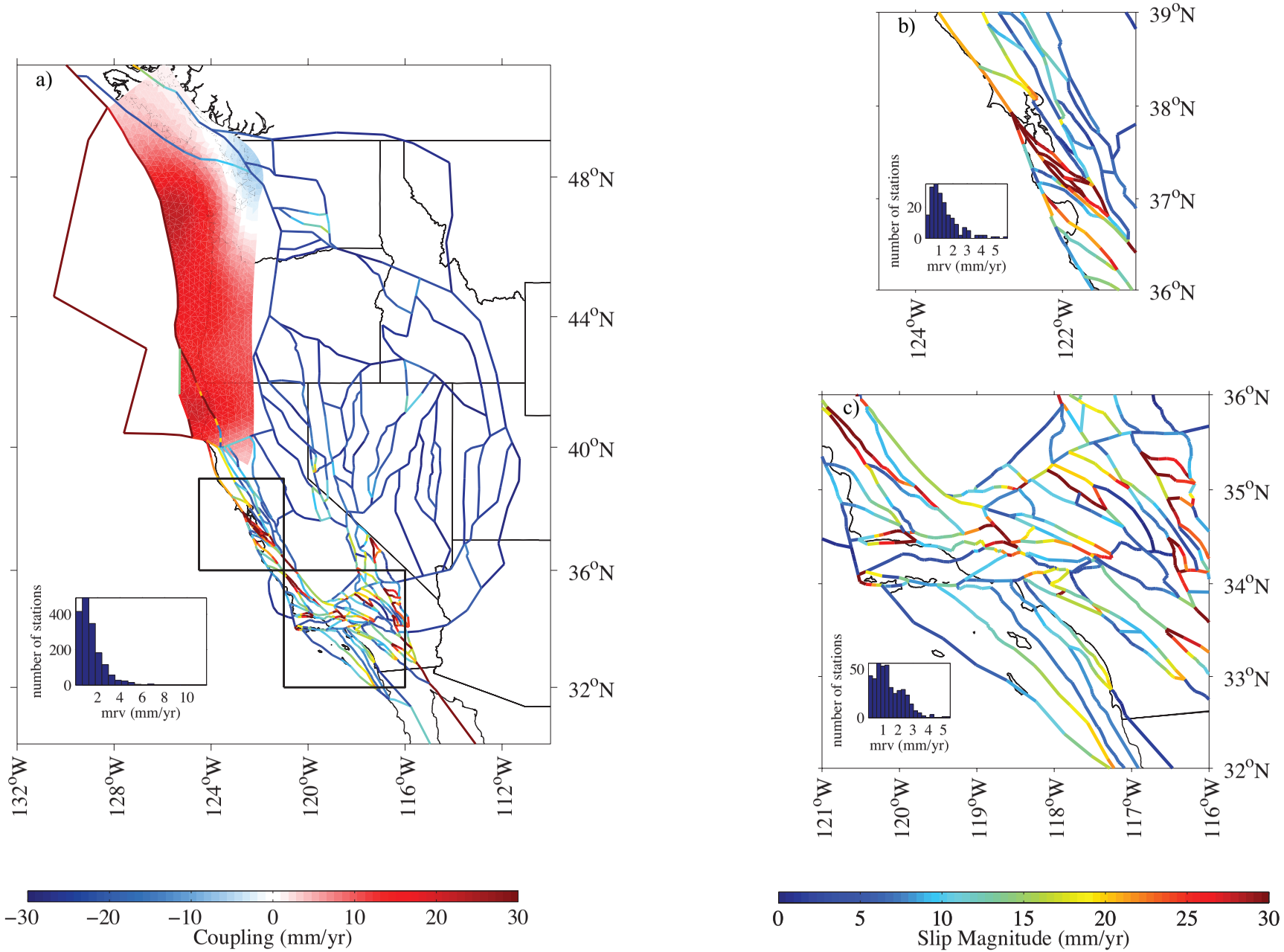

Figure 5.7: Slip rates and spatially variably coupling on the Cascadia subduction zone for solution with $\lambda = 0$ a) in Western U.S. b) in San Francisco Bay Area c) in Southern California. Insets show histograms of residual velocity magnitudes on the region shown.

[1993]; Sleep and Fujita [1997] as a future orientation of the San Andreas fault, however the high slip rates estimated here are clearly not realistic at present. Most notably, this block model fits the data poorly, with a mean residual velocity of ∼4.5 mm/yr (Figure 5.5). Residual velocity directions and magnitudes are shown in Figure 5.10. Individual regions may have particularly high data misfits: Southern California interseismic velocities are fit with a local mean residual velocity of 7.5 mm/yr, and San Francisco Bay Area interseismic velocities are fit with a local mean residual velocity of 8.5 mm/yr (regional mean residual velocities are calculated on the area shown in Figure 5.10b and 5.10b).

Identification of the plate boundary so far east is likely the result of attempting to fit a broad plate boundary zone with a single fault, and slip is modeled east of the Central Valley to compensate for faults that have been removed. Relaxing the total variation constraint slightly to $\lambda = 1950$ introduces a fault along with the San Andreas fault system, resulting in a four block system with a Sierra block between the Pacific and North American blocks [e.g., d'Alessio et al., 2005; Johnson and Fukuda, 2010; Evans et al., 2012] (Figure 5.11). Figure 5.8 shows the TVDN grouping of the Euler pole locations and rotation rates, resulting in four separate blocks. In this case, most plate boundary slip moves to the western boundary, and slip on the eastern fault drops to ∼13 mm/yr. This new west boundary has a slip rate of ∼25 mm/yr and follows the San Andreas fault for much of its strike, with some exceptions. In Southern California, slip follows the Llamo fault and Arrsstre Canyon Narrows fault northeast of the Mojave and San Bernadino segments of the San Andreas fault. North of the creeping segment of the central San Andreas fault, slip transfers onto the Calaveras fault then onto the Hayward fault in the San Francisco Bay area instead of following the San

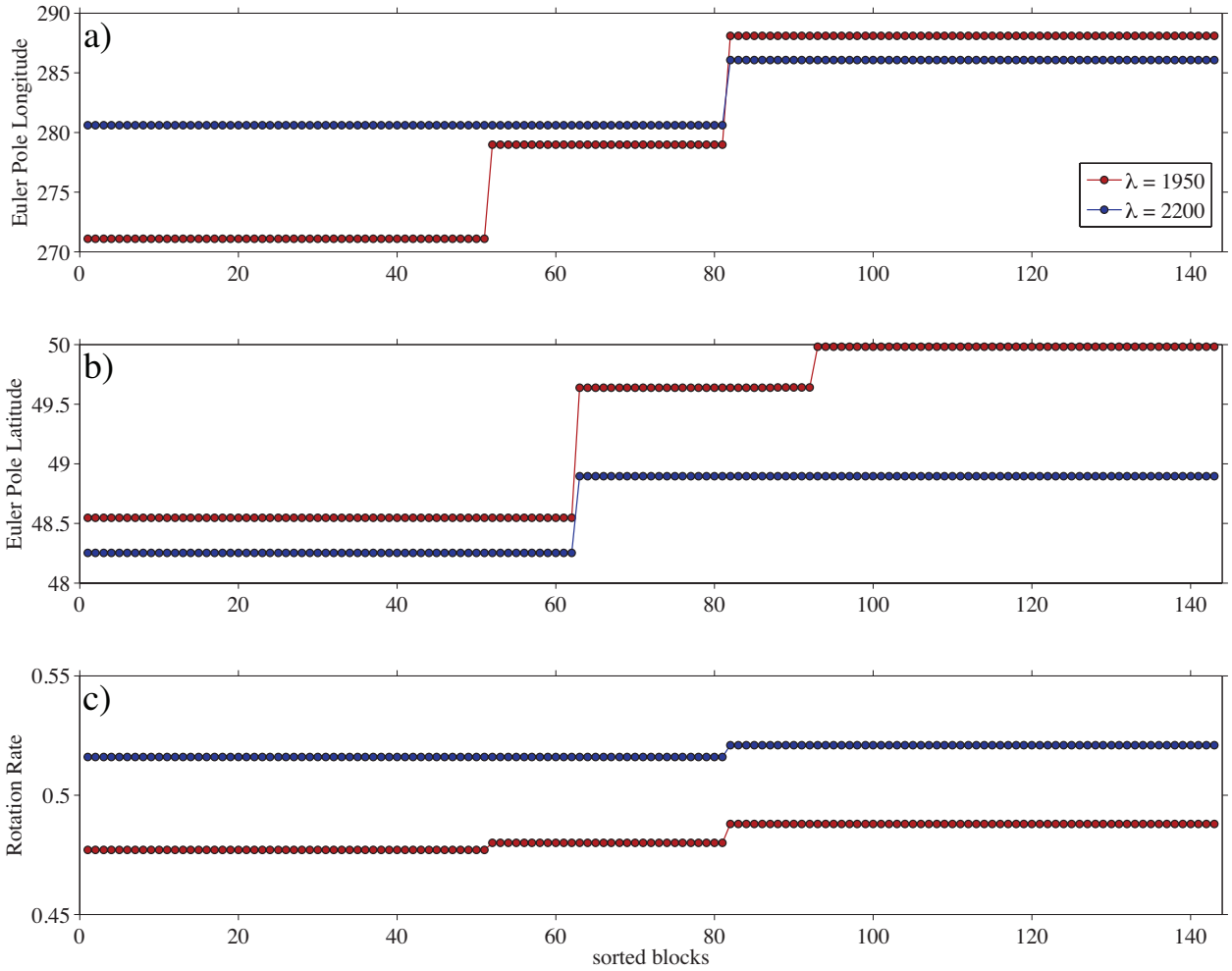

Figure 5.8: $\boldsymbol{\Omega}$ vectors for 3-block and 4-block solutions. a) Euler pole longitudes estimated by TVDN. b) Euler pole latitudes estimated by TVDN. c) Rotation rates estimated by TVDN.

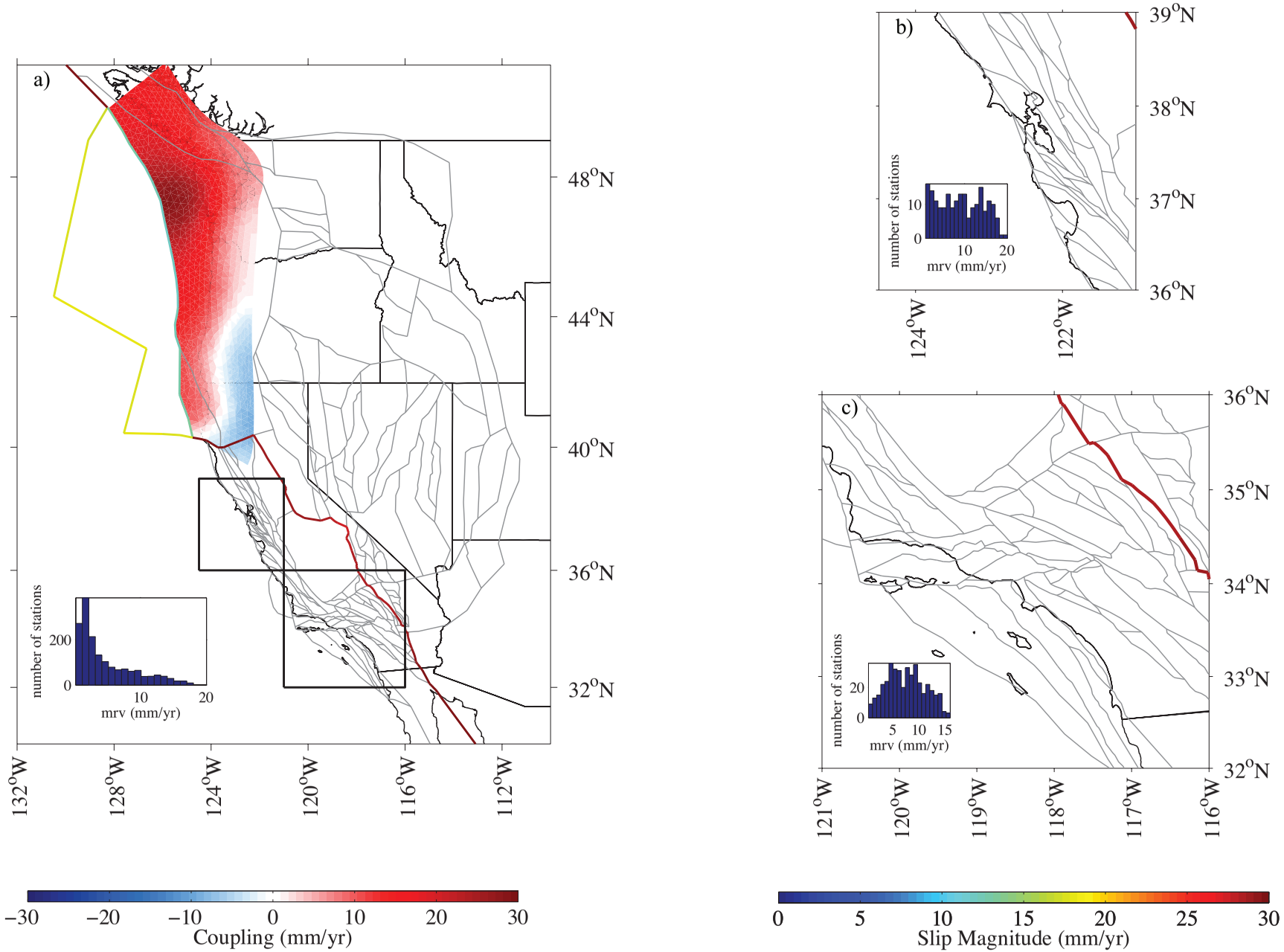

Figure 5.9: Slip rates and spatially variably coupling on the Cascadia subduction zone for 3-block solution ($\lambda = 2200$) a) in Western U.S. b) in San Francisco Bay Area c) in Southern California. Insets show histograms of residual velocity magnitudes on the region shown.

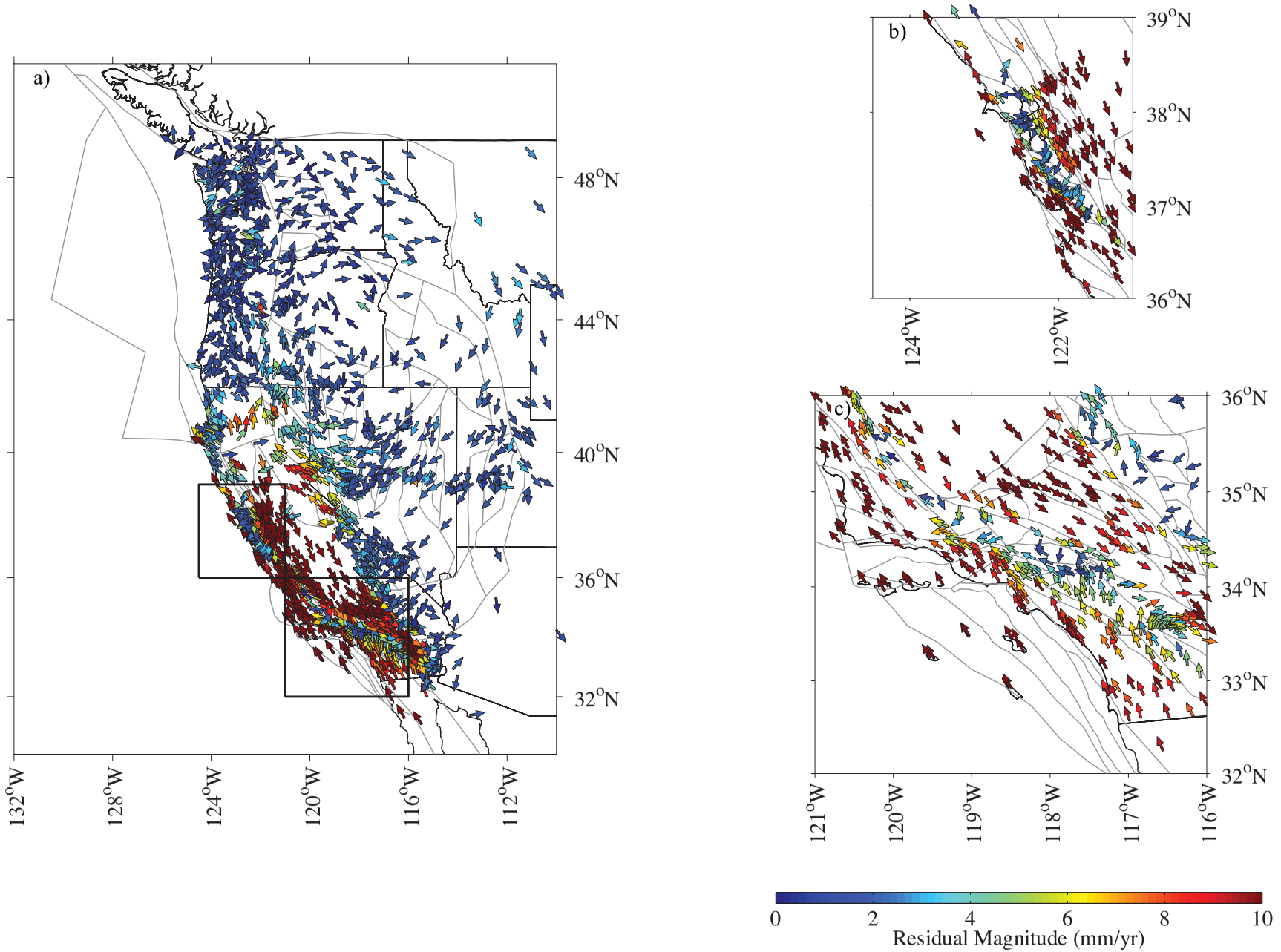

Figure 5.10: Residual velocities for 3-block solution ($\lambda = 2200$) a) in Western U.S. b) in San Francisco Bay Area c) in Southern California.

Andreas. As with the single boundary in the 3-block model, we interpret selection of these faults as likely compensating for faults that have been removed, rather than identifying these specific structures as important plate boundary faults.

Adding this additional block improves fit to the data, with a mean residual velocity of 4.0 mm/yr (Figure 5.5). Southern California interseismic velocities are fit with a local mean residual velocity of 3.8 mm/yr and San Francisco Bay Area interseismic velocities are fit with a mean residual velocity of 5.3 mm/yr. In the San Francisco Bay Area, the highest misfits are located near the Hayward and San Andreas faults. In Southern California, the highest misfits are located between the San Andreas fault and the San Jacinto fault (Figure 5.12).

5.4.2 Fitting GPS velocities with mean residual velocity of 2 mm/yr

We identify a range of solution block model geometries that fit the data with a desired degree of accuracy. For horizontal GPS observations in western North America, we can expect to fit the data with a mean residual velocity magnitude of <2 mm/yr. For λ values less than $\lambda = 900$, we fit the GPS observations with a mean residual velocity of <2 mm/yr across the plate boundary zone. However, this block model solution fits regional observations in Southern California with mean residual velocities 2.13 mm/yr. We fit Southern California with a mrv <2 mm/yr for λ values less than $\lambda = 550$. So we consider block models selected λ values between 550 and 900 to represent the range of solutions that fit our observations with a desired degree of accuracy. Figure 5.13 shows the TVDN grouping of the Euler pole locations and rotation rates for these three values of λ.

In terms of selecting a reference model, we select $\lambda = 610$, as this is the largest λ value for which deformation extends into the interior of North America as far as the Wasatch fault,

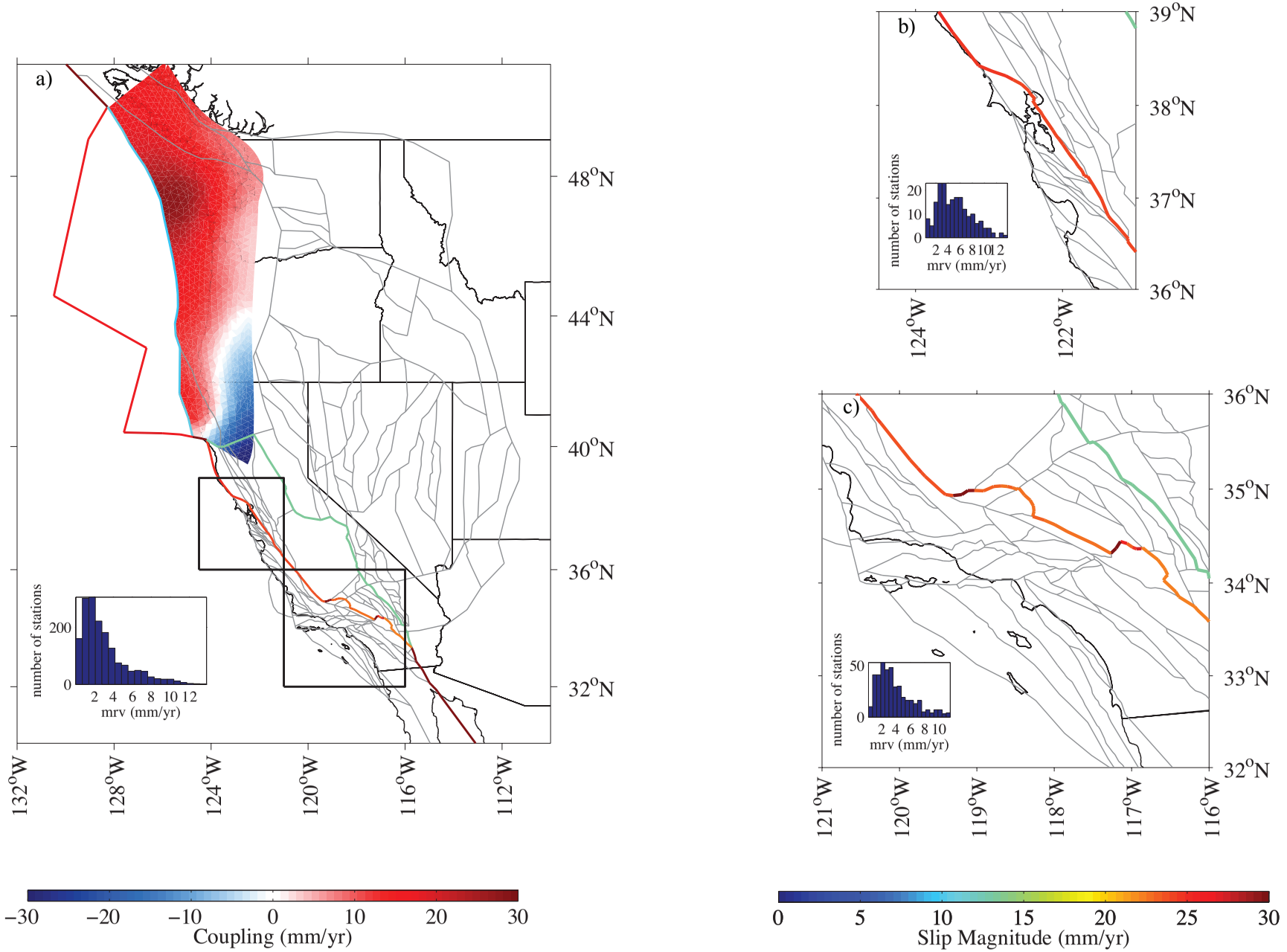

Figure 5.11: Slip rates and spatially variably coupling on the Cascadia subduction zone for 4-block solution ($\lambda = 1950$) a) in Western U.S. b) in San Francisco Bay Area c) in Southern California. Insets show histograms of residual velocity magnitudes on the region shown.

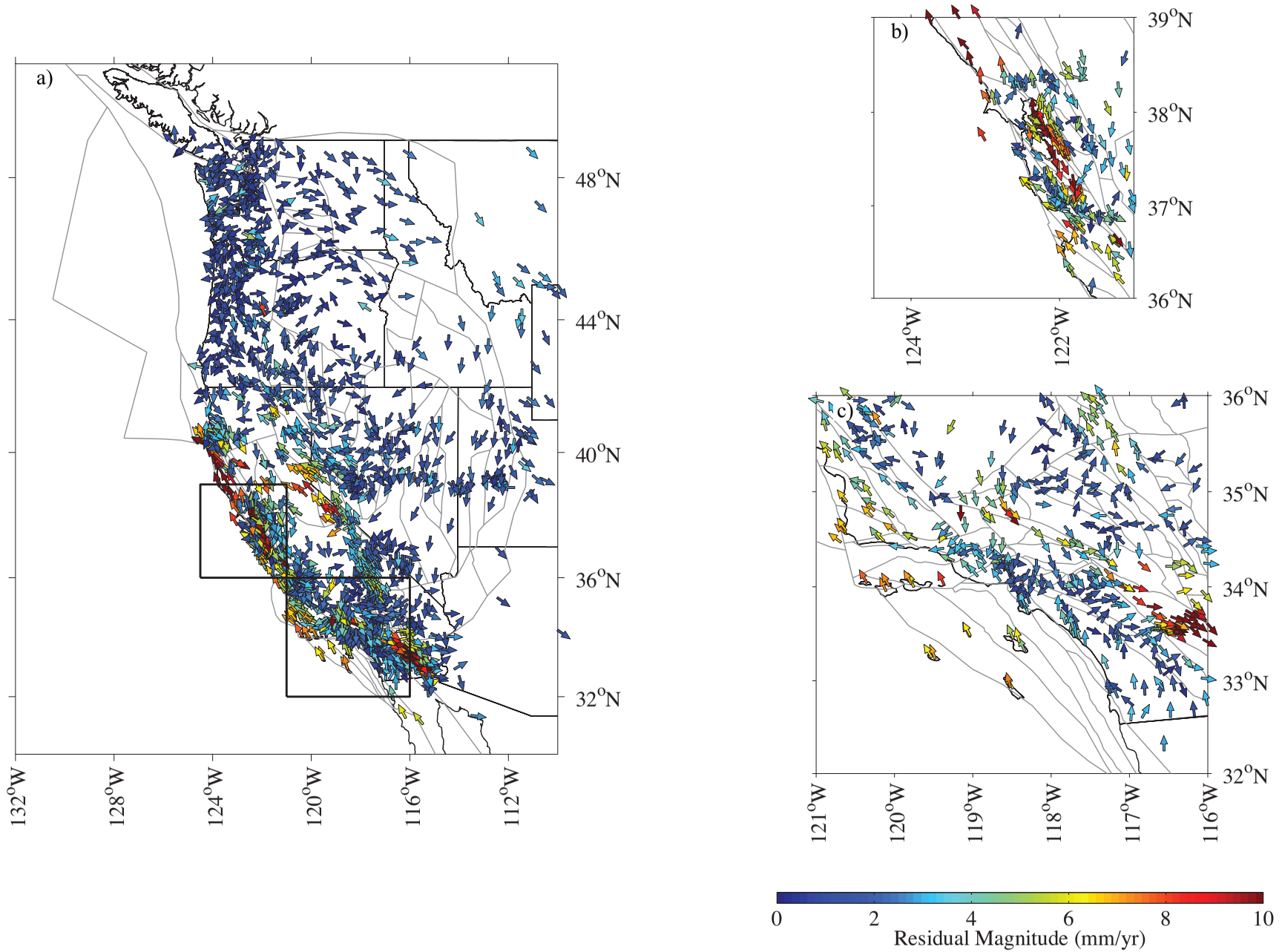

Figure 5.12: Residual velocities for 4-block solution ($\lambda = 1950$) a) in Western U.S. b) in San Francisco Bay Area c) in Southern California.

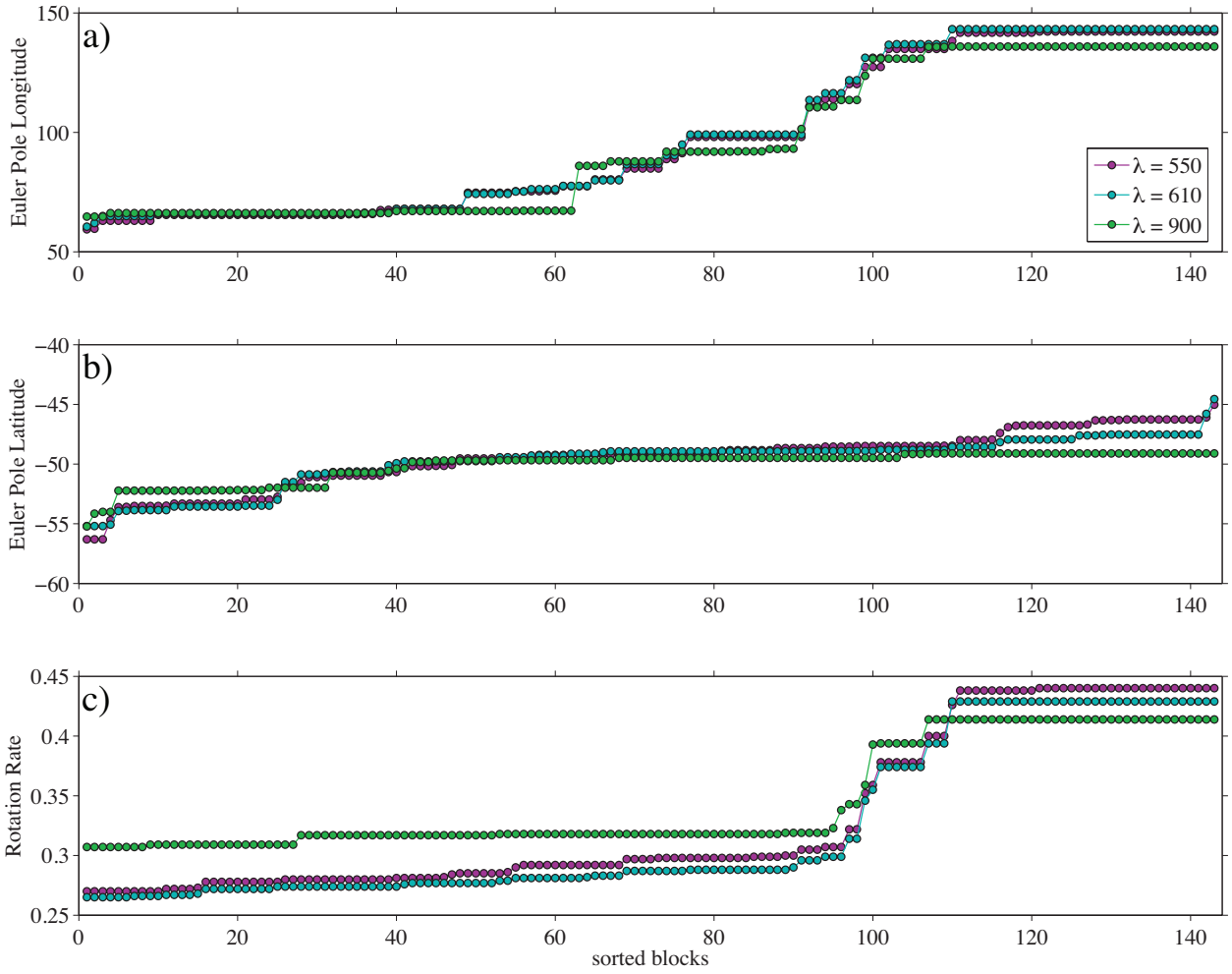

Figure 5.13: $\mathbf{\Omega}$ vectors for reference and comparison solutions. a) Euler pole longitudes estimated by TVDN. b) Euler pole latitudes estimated by TVDN. c) Rotation rates estimated by TVDN.

and this is the smallest λ value at which slip between in central California is concentrated on the San Andreas fault (Figures 5.14 and 5.15). The reference model at $\lambda = 610$ contains 30 blocks, as compared to 33 blocks for $\lambda = 550$ and 20 blocks for $\lambda = 900$ (Figures 5.16-5.19).

The block model formulation produces uncertainty estimates on fault slip rates estimated formally for a given block geometry. These uncertainties therefore do not reflect uncertainties in block and segment geometry, and are therefore much smaller than differences in slip rate on a given fault between the models considered here. Because of this, when reporting model slip rates for a given block geometry, we do not report the formal uncertainties as reported by the block model, and when a range in slip rates is reported, this represents the range of acceptable slip rates among the models considered.

Southern California

We identify 9-15 rotating blocks in southern California, with 10 blocks in the $\lambda = 610$ reference model. The reference model fits GPS observations with a mean residual velocity of 2.00 mm/yr, compared with 1.76 mm/yr ($\lambda = 550$) and 2.13 mm/yr ($\lambda = 900$) in Southern California. The primary tectonic differences between the models considered are related to the total width of the fault zone in this region. In the reference model, only two faults are active west of the San Andreas: the San Gabriel fault adjacent to the Mojave segment of the San Andreas fault, and the San Jacinto fault to the south. Allowing more blocks ($\lambda = 550$), shifts deformation to the west, activating a fault sub-parallel to the San Andreas fault along the San Juan fault zone, and the Pine Mountain and Santa Ynez faults are active between the San Gabriel fault and the Hosgri fault. In both of these models, four faults are active in the ECSZ. In the simpler ($\lambda = 900$) model, the plate boundary in Southern

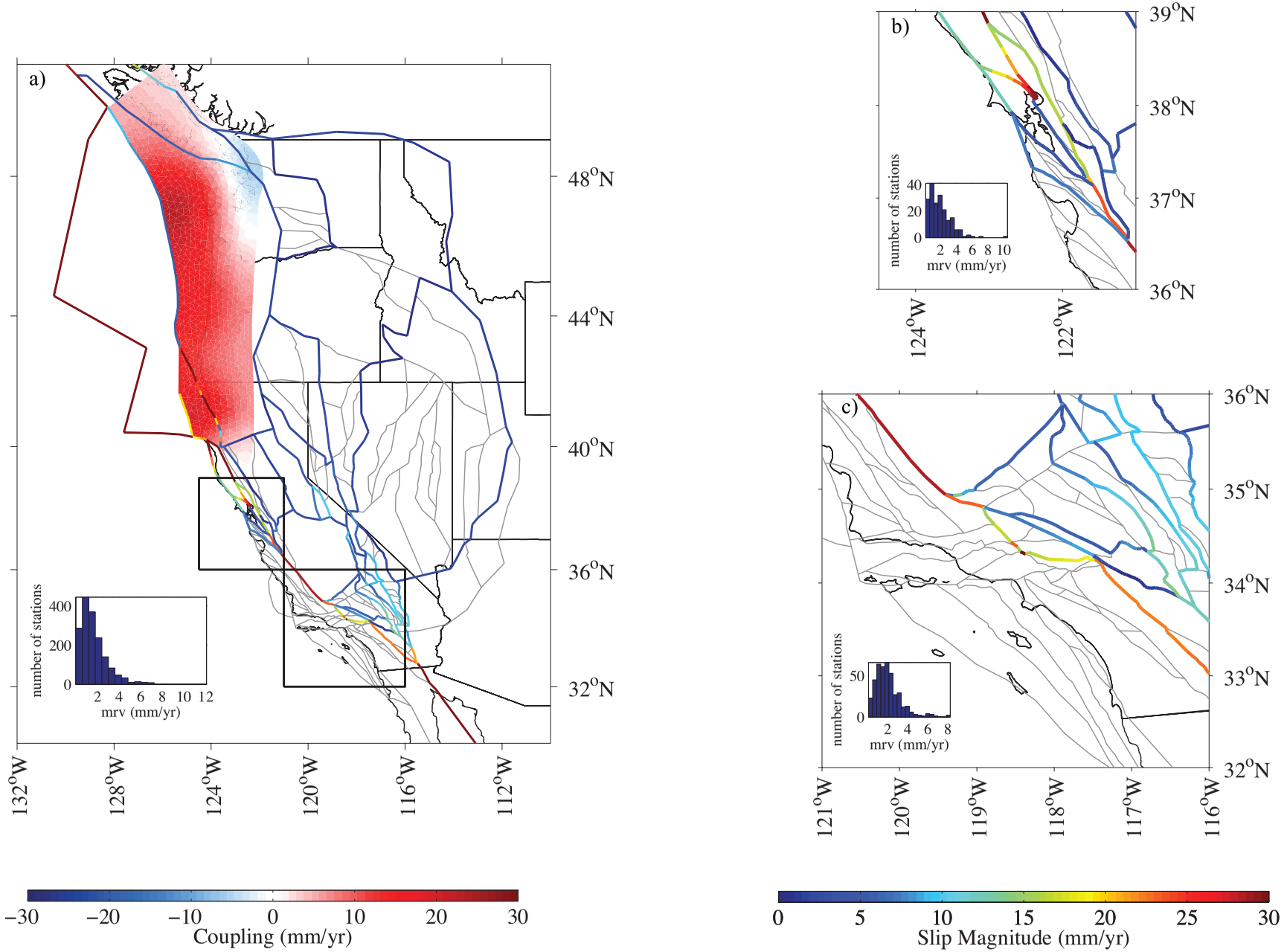

Figure 5.14: Slip rates and spatially variably coupling on the Cascadia subduction zone for $\lambda = 610$ solution a) in Western U.S. b) in San Francisco Bay Area c) in Southern California. Insets show histograms of residual velocity magnitudes on the region shown.

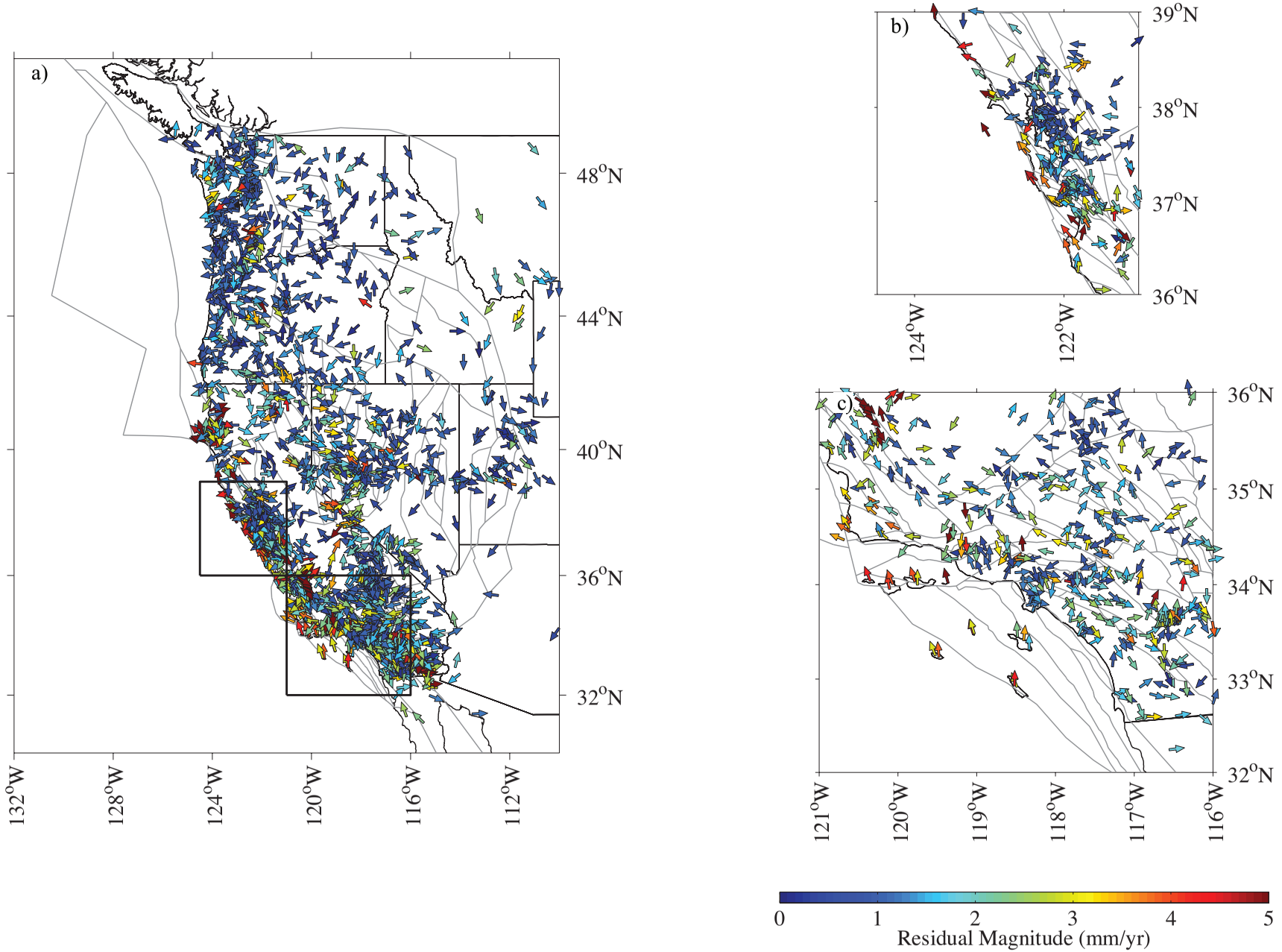

Figure 5.15: Residual velocities for $\lambda = 610$ solution a) in Western U.S. b) in San Francisco Bay Area c) in Southern California.

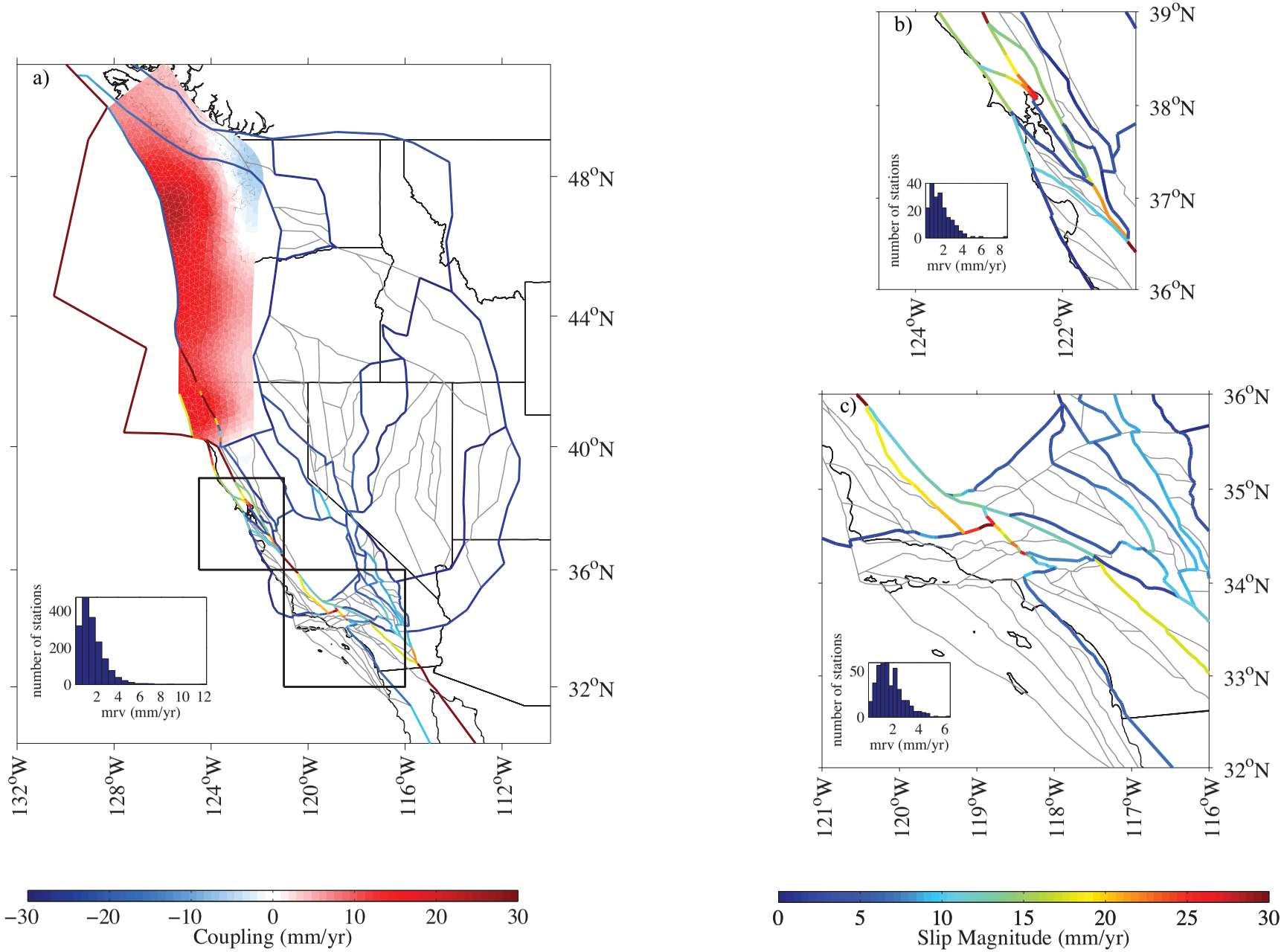

Figure 5.16: Slip rates for $\lambda = 550$ solution a) in Western U.S. b) in San Francisco Bay Area c) in Southern California. Insets show histograms of residual velocity magnitudes on the region shown.

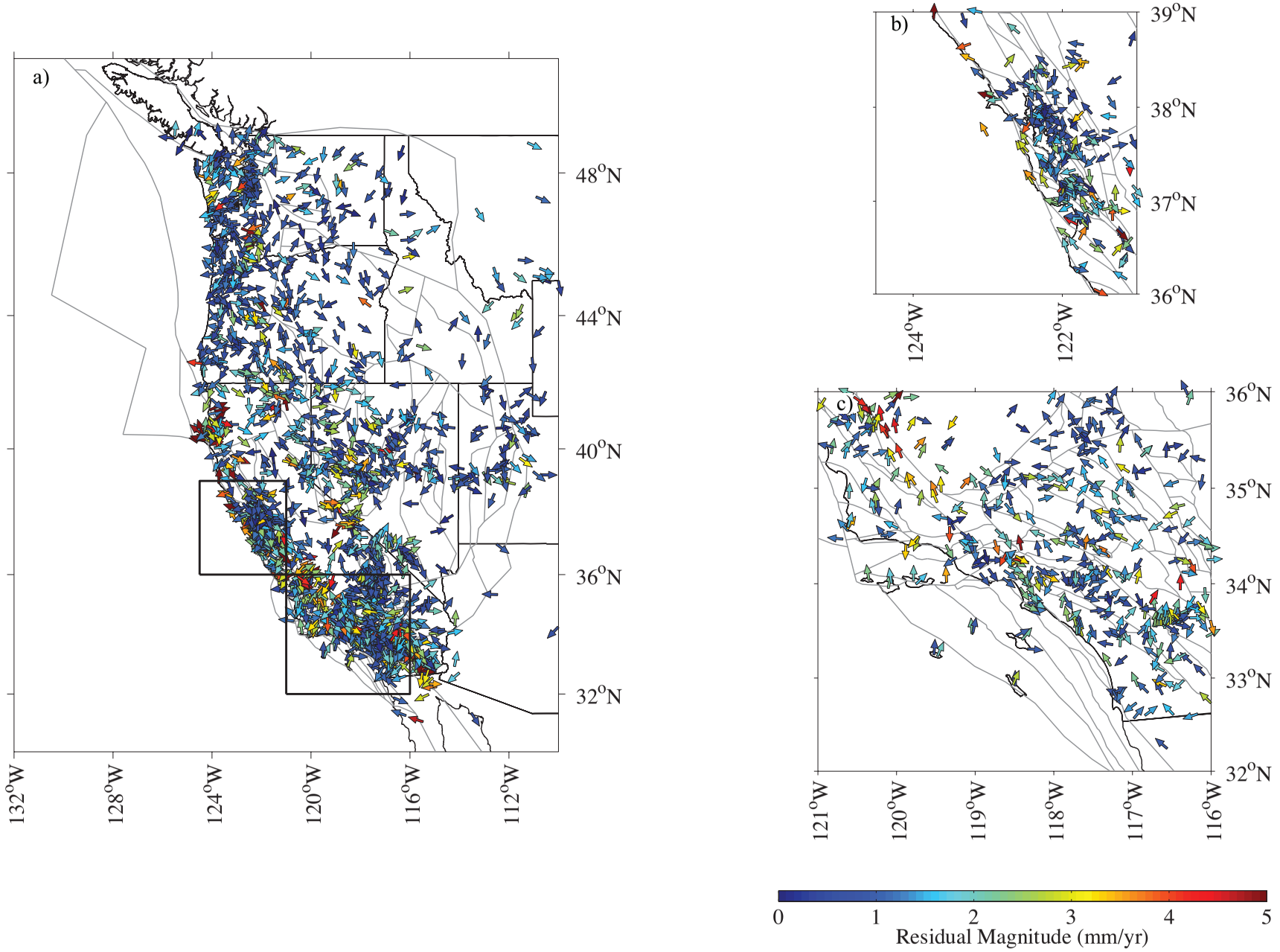

Figure 5.17: Residual velocities for $\lambda = 550$ solution a) in Western U.S. b) in San Francisco Bay Area c) in Southern California

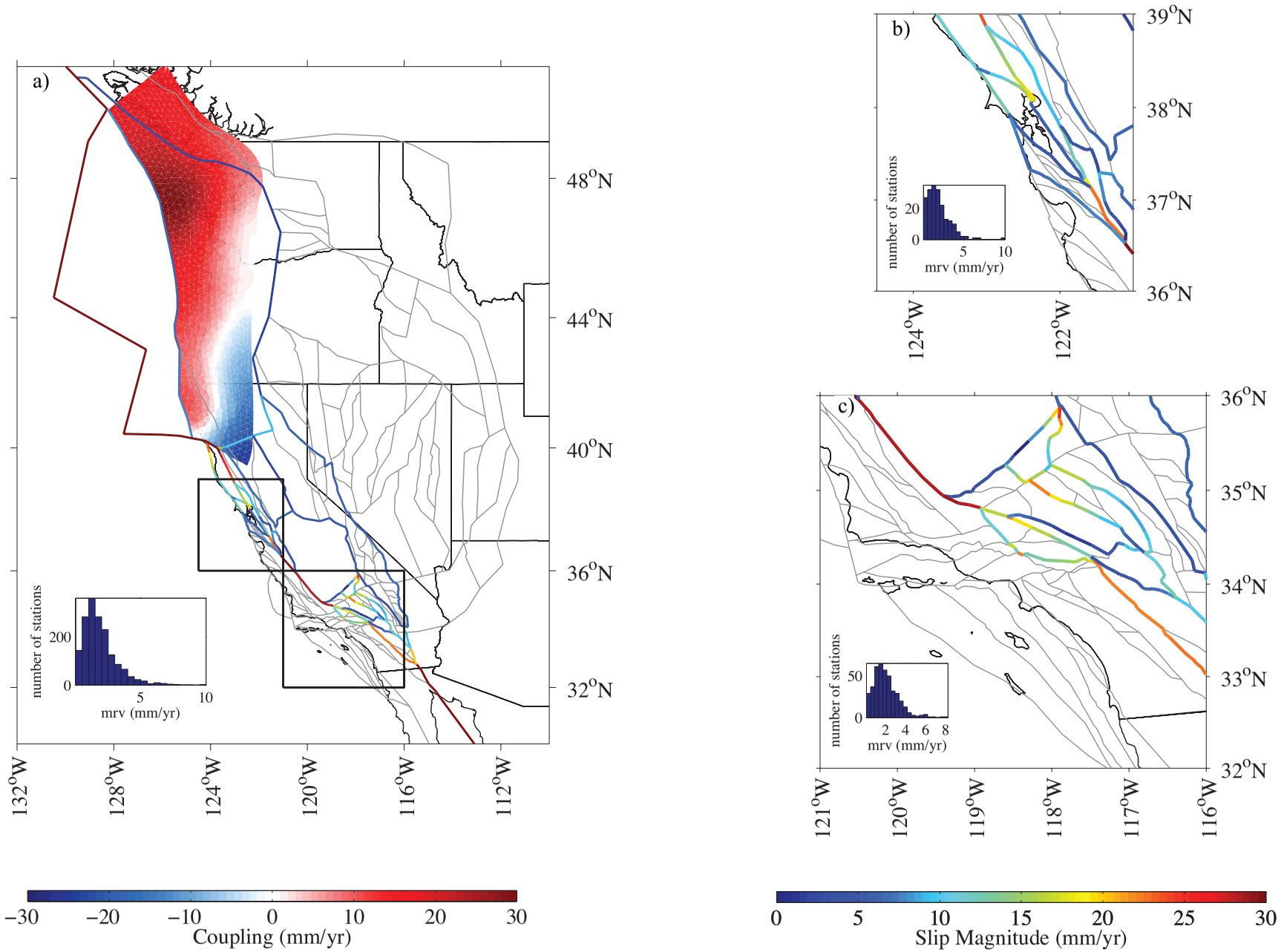

Figure 5.18: Slip rates for $\lambda = 900$ solution a) in Western U.S. b) in San Francisco Bay Area c) in Southern California. Insets show histograms of residual velocity magnitudes on the region shown.

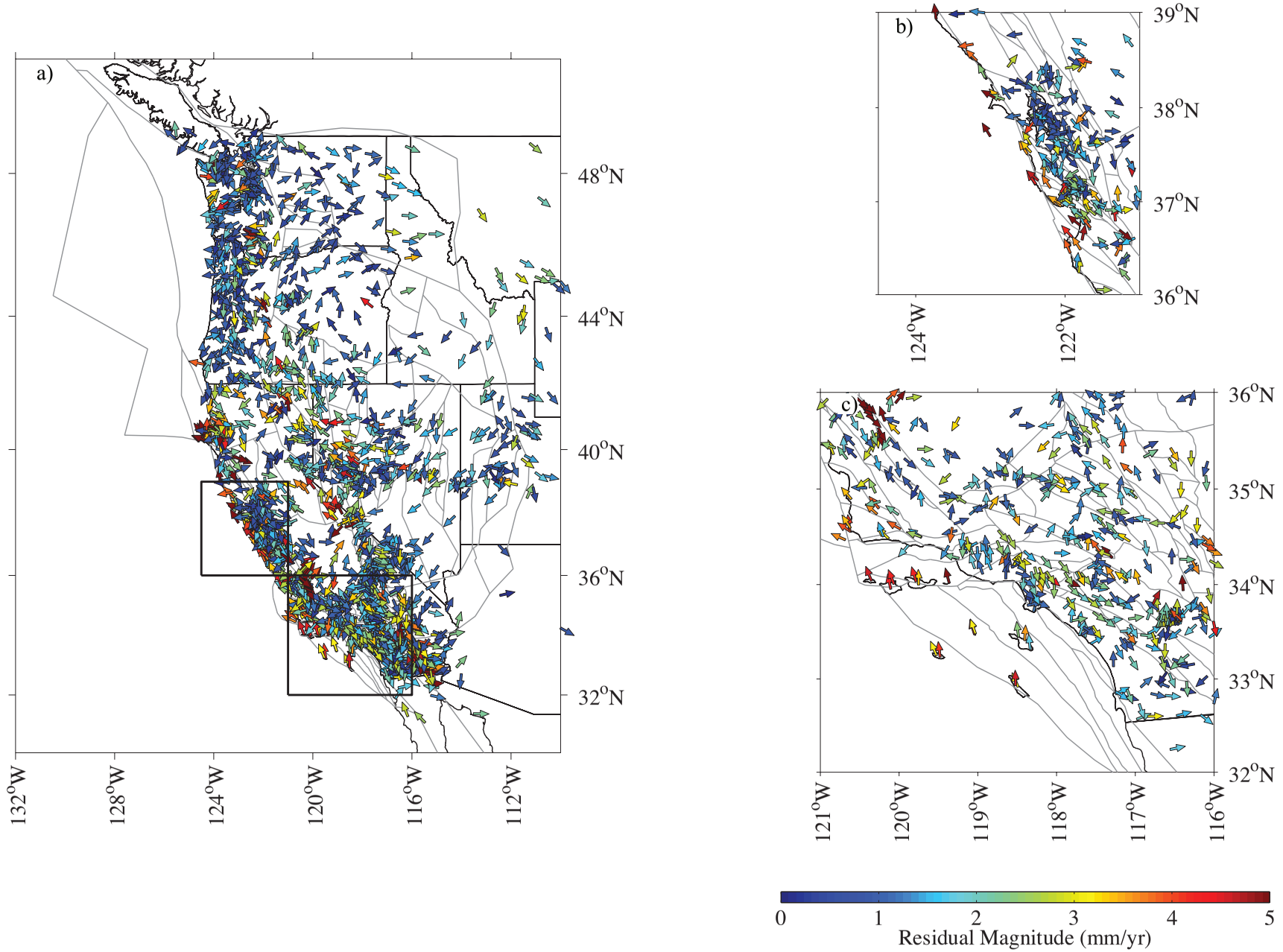

Figure 5.19: Residual velocities for $\lambda = 900$ solution a) in Western U.S. b) in San Francisco Bay Area c) in Southern California
.

California is generally narrower. In this case, the San Jacinto fault accommodates most the slip in the south, but no other structures are active west of the San Andreas, and the Goldstone fault is not active in the Eastern California Shear Zone (ECSZ). This narrowing of the boundary appears to lead to increased complexity in the interior of the region. None of the models considered contain an active Garlock fault, although all contain the White Wolf fault, consistent with high strain rate observations here [Bawden et al., 1997].

The southern San Andreas fault is active along its entire trace in all of the models. However all of the models also estimate high slip rates on the San Jacinto fault of up to 23 mm/yr ($\lambda = 610$ and 900), higher than the 9-12 mm/yr estimated on the San Andreas. This rate is consistent with the 25 mm/yr slip rate estimated by Lundgren et al. [2009], who estimated $\sim$17 mm/yr on the San Andreas, and comparable to Fialko [2006]'s estimate of 19-20 mm/yr. Other geodetic studies [Lisowski et al., 1991; Lindsey et al., 2013] estimate slip rates of $\sim$10 mm/yr and lower. We estimate a slip rate as low as 18 mm/yr when $\lambda = 550$. In addition, we estimate low (<2 mm/yr) slip rates on the San Bernadio segment, consistent with previous block model solutions [Meade and Hager, 2005; Loveless and Meade, 2011b], although this rate is higher, 8 mm/yr, when $\lambda = 900$.

Both models that fit Southern California data with <2 mm/yr mean residual velocity ($\lambda = 550$ and $\lambda = 610$) contain an active San Gabriel fault. In the $\lambda = 610$ reference model, this is the only active structure within the Los Angeles basin, and it accommodates more slip than the Mojave segment of the San Andreas fault, with a right-lateral slip rate of up to 15.5 mm/yr, and up to 20 mm/yr of shortening. We estimate only 6 mm/yr of right lateral slip on the Mojave segment of the San Andreas fault. Allowing additional structures

($\lambda = 550$) does not significantly change the slip rates on the San Gabriel fault, although this model places more slip on the San Andreas (12.5 mm/yr on the Mojave segment, more consistent with Meade and Hager [2005]). The denser $\lambda = 550$ block model identifies an active Newport-Inglewood fault in the Los Angeles basin, which transfers 6 mm/yr of slip to the San Gabriel fault via shortening on the Sierra Madre fault. Also in the $\lambda = 550$ model, we estimate 18 mm/yr of slip west of the central San Andreas fault on the San Juan fault zone, which tranfers to shortening in the Transverse ranges with 30 mm/yr of slip on the Pine mountain fault. West of this, the Santa Ynez structure is active with a right lateral slip rate of 2 mm/yr, connecting with the Santa Lucia Bank fault zone west of the Hosgri fault.

None of the block models considered contain active structures in the Los Angeles basin or offshore into the Santa Barbara channel. This lack of fault activity in and northeast of the Los Angeles basin is surprising, given recent observations of the actively uplifting Compton thrust [Leon et al., 2009], the Palos Verdes fault [Brankman and Shaw, 2009], the Puente Hills blind thrust [Leon et al., 2007] and the Elysian Park thrust [Davis et al., 1989]. These fault geometries suggest that our goal of identifying the simplest (i.e., containing the fewest blocks) block model with mean residual velocities of 2 mm/yr is not precise enough to recover deforming structures in the Los Angeles basin. The highest estimated slip rate on these faults is 4 mm/yr on the Palos Verdes fault [Brankman and Shaw, 2009], possibly indicating a limit on slip rates identifiable by this method. Indeed, all of the models fit the data west of the San Andreas poorly, with systematic northward residuals of up to 3.5-5.7 mm/yr ($\lambda = 550$ and 900, respectively) (Figures 5.15, 5.17, and 5.19). We also note that

data coverage is relatively poor offshore and in the transverse ranges. So although residuals indicate active deformation between the Pacific and the San Andreas, the data likely cannot uniquely distinguish between many slowly slipping (<∼4 mm/yr) faults in and around the Los Angeles basin. The block model that satisfies the requirement of fewest blocks to explain the geodetic observations is the one that attributes all deformation to the Pine Mountain fault and San Gabriel fault. Enforcing more strict data-fitting constraints, and modifying the block model formulation to incorporate a-priori fault slip rates may be essential for developing block models with reasonable hazard applications.

East of the San Andreas fault, we estimate little deformation between the San Andreas and the ECSZ. The $\lambda = 610$ reference model estimates 6 mm/yr of convergence across the Llano fault adjacent to the San Andreas [Jennings, 1994]. We estimate localized slip on only 4 of the possible 10 faults included in the dense fault geometry, demonstrating that continuous deformation is not required in the ECSZ. The next active faults to the east are the Lenwood/Lockhart faults, with 6 mm/yr of right lateral slip, and up to 10 mm/yr of extension. In the reference model, we estimate 5 mm/yr of right lateral slip and 6 mm/yr of shortening on the Blackwater/Calico faults, which is comparable to the ∼7mm/yr of right lateral slip estimated by Peltzer et al. [2001]. Unlike Peltzer et al. [2001], however, the Blackwater fault is not the only active structure in the ECSZ. Our results in the ECSZ are more consistent with previous results in which slip is distributed across several faults [McClusky et al., 2001; Meade and Hager, 2005]. We estimate 6 mm/yr and 3 mm/yr of right lateral slip on the Goldstone and Eastern Mojave fault, respectively. These rates are similar: 7 mm/yr, and 2 mm/yr, in the $\lambda = 550$ comparison model. The reference model also

estimates shortening on the Goldstone fault (9 mm/yr). We estimate 8 mm/yr of extension on the Eastern Mojave fault, consistent with this fault being the westernmost fault in the Basin and Range (4 mm/yr of extension for $\lambda = 550$).

When $\lambda = 900$, the tectonic structure of Southern California rearranges itself, with more deformation in the interior of the region. In this case, we observe comparable extension on the East Mojave fault (6 mm/yr), no activity on the Goldwater fault, and activation of left-lateral slip (3 mm/yr) and extension (12 mm/yr) on the Mirage Valley fault. The large mean residual velocities in this model indicate that the total variation constraint when $\lambda = 900$ in this region is too strong to effectively reproduce the geodetic data, possibly leading to nonphysical block motions on the remaining blocks.

In the reference model, the San Andreas fault is the only fault transferring slip from Southern California to the San Francisco bay area fault system. In the $\lambda = 550$ model, the San Juan fault zone and Santa Lucia Bank fault zone are active the west of the southern central San Andreas fault, connecting with the central San Andreas and San Gregorio faults, respectively. In the $\lambda = 900$ model, the San Andreas fault is the only fault transferring slip between southern California and the central San Andreas fault, where some slip transfers east to the Ortigalita fault zone.

San Francisco Bay Area

For the reference model ($\lambda = 610$) and comparison models ($\lambda = 550$, $\lambda = 900$), slip in the San Francisco Bay Area is partitioned across 3-7 active faults. Active faults in the reference model are the San Andreas fault, the Calaveras and West Napa faults, the San Gregorio fault, the Greenville fault, the Hayward and Rodgers Creek faults. East of the Greenville

and West Napa faults is a fault following San Joaquin fault and Vaca fault zone [U.S. Geological Survey et al., 2006] (Figure 5.14). Additional structures are actively transferring slip between the San Andreas/southern Calaveras faults and the San Gregorio fault, between the Hayward/Rodgers Creek fault and the Northern San Andreas fault, and a small, slow slipping structure between the Greenville fault and the northern Calaveras. On the San Francisco peninsula, slip is not estimated on the main trace of the San Andreas fault, but instead follows the San Gregorio fault to the West and an unnamed fault immediately adjacent to the bay. In models with $\lambda < 550$, the main trace of the San Andreas fault is active and slipping $\sim$10 mm/yr, suggesting that its absence in models with higher λ may have more to do with an inability to differentiate between overlapping elastic signals on the peninsula.

In the reference model south of the San Francisco peninsula, a fault west of the San Andreas fault transfers 7.5 mm/yr of slip from the central San Andreas fault across the Santa Cruz mountains to the San Gregorio fault. This rate is 6.2 ($\lambda = 900$) and 10 ($\lambda = 550$) in the comparison models. Previous block models of the San Francisco bay area have not included this structure [Murray and Segall, 2001; d'Alessio et al., 2005; Evans et al., 2012], and its presence in the reference and comparison block models is particularly interesting as this is near the off-San Andreas location of the 1989 Loma Prieta earthquake [e.g., Shaw et al., 1994].

We allow the Hayward fault to creep at its full estimated rate in all of the models by setting its locking depth to zero. Our slip rate estimate on the Hayward fault is 5.6 mm/yr in the reference model, similar to estimates from studies allowing partial creep [e.g., Evans

et al., 2012; d'Alessio et al., 2005; Schmidt et al., 2005; Bürgmann et al., 2000]. This rate is also comparable in the comparison models, ranging from 5.4 ($\lambda = 550$) to 6.1 mm/yr ($\lambda = 900$).

In the reference and comparison models, the largest slip rates are estimated on the Calaveras fault. In the reference model, we estimate a slip rate on the Calaveras fault of 14.6 mm/yr, which is faster than the geologic slip rate estimate of 5.6 mm/yr [Simpson et al., 1999], and geodetic estimates of 6.2 to 9.0 mm/yr [d'Alessio et al., 2005; Evans et al., 2012]. However, in the $\lambda = 550$ and $\lambda = 900$ models, this slip rate is lower, 14.0 and 8.8 mm/yr, respectively.

In the east San Francisco bay area, the reference and comparison models estimate low slip rates (<2 mm/yr) in the Greenville fault. In the reference and $\lambda = 550$, the easternmost bay area faults along the San Joaquin fault and Vaca fault zone also slip at <2 mm/yr. This rate is 7 mm/yr when $\lambda = 900$, possibly accommodating some slip from the Basin and Range province, which is not active for this model.

Basin and Range

Slip partitioning across the Basin and Range province differs considerably among the reference and comparison models. In our reference model ($\lambda = 610$), Slip is bounded on the west side of the province by several faults in the Eastern California Shear Zone and up through the Walker Lane Belt, and on the east by the Wasatch fault. A fault following the Central Nevada seismic belt [Wallace, 1984] remains active in the western portion of the interior of the province. The $\lambda = 550$ model estimates similar slip partitioning, although easternmost deformation follows the Strawberry fault east of the Wasatch fault in southern

Utah, and along the intermountain seismic belt in southwest Utah [Smith and Sbar, 1974], and an additional fault remains active in the Central Nevada seismic belt. The $\lambda = 900$ model does not estimate any active faults east of Walker Lane.

In the reference and comparison models, slip rates in the Basin and Range are very small. In the reference model, the largest strike slip rates transfer abount 5 mm/yr of slip up from the Eastern California Shear zone through the eastern Walker Lane fault zone, with right lateral rates up to 6.3 mm/yr, consistent with estimates of total shear in Walker lane of $\sim$7 mm/yr [Hammond and Thatcher, 2007]. These are also the location of the highest tensile slip rates, with up to $\sim$8 mm/yr of extension along the south eastern edge of the Sierras, although adjacent faults also have estimated slip rates of $\sim$8 mm/yr of shortening, indicating that we may be over-fitting the data in this region. While active and included in this block geometry, the Wasatch fault accommodates only 2.3 mm/yr of extension. The interior structure along the Central Nevada Seismic belt accommodates a similar magnitude of extension, up to 4.4 mm/yr. This set of active structures is similar to those described by Bennett et al. [2003], although we estimate consistently smaller slip rates, similar to Niemi et al. [2004]. These small deformation rates are also consistent with Thatcher et al. [1999]'s hypothesis that little-to-no active deformation takes place within the Basin and Range (and we estimate none when $\lambda = 900$). Estimating slip partitioning in the Basin and Range province is particularly challenging because even those structures estimated to be active with $\lambda = 550$ and $\lambda = 610$ are slipping very slowly. The lack of Basin and Range faults at $\lambda = 900$ demonstrates that differentiating between slow structures and inactive structures may not be possible at the $\sim$2 mm/yr GPS resolution level. Indeed, residuals in the northern

Basin and Range are systematically oriented to the northeast at rates of ∼2 mm/yr (Figure 5.19).

Pacific Northwest and Cascadia subduction

For the full block model inversion we estimate spatially variable coupling rates on triangular dislocation elements [Meade, 2007] representing the Cascadia subduction zone (geometry from McCrory et al. [2009]) in addition to block rotation rates and fault slip rates. For simplicity, we identify a single smoothing parameter $\beta = 1000$, which we apply to all models, although this may be varied as well to obtain desired smoothness and goodness of fit properties of the subduction zone solution. On the subduction zone we estimate coupling rates up to 23 mm/yr. This increases to 31 mm/yr in the $\lambda = 900$ model. This range is consistent with the coupling rates estimated by McCaffrey et al. [2007]. The coupling distribution varies slightly as the block geometry varies, however all coupling distributions estimate the highest coupling rates near the trench of the subduction zone, similar to previous estimates of strain accumulation on the subduction zone [e.g., McCaffrey et al., 2007; McCaffrey, 2009]. The coupling distribution in our reference model is equivalent to a moment accumulation rate of a $M_W = 9.2$ earthquake every 600 yrs, consistent with paleoseismic and recurrence interval estimates [Satake et al., 2003; Goldfinger et al., 2003; McCaffrey et al., 2007].

Although we do not include faults in western Oregon that may accommodate additional right lateral strike slip [e.g., McCaffrey et al., 2007], we estimate right lateral strike-slip coupling rates of 10 mm/yr on the subduction zone adjacent to Oregon and Southern Washington, which is consistent with ongoing right-lateral motion in this region. The coupling rates on the subduction zone are most sensitive to the block geometry in the northern

Basin and Range, and the higher coupling rates for $\lambda = 900$ are likely related to the lack of active structures in the Basin and Range.

In the reference model ($\lambda = 610$), we identify 6 actively rotating blocks in the Pacific Northwest region: the Juan de Fuca plate, a coast range block, a small southern Oregon block, a block containing central Washington and Vancouver island, a large oblong block containing eastern Oregon, western Washington and northern Idaho, and a basin and range block. This geometry is very similar in the $\lambda = 550$ model, with slightly more complexity in the Basin and Range (§5.4.2). These block locations and geometries are consistent with deformation accommodated by block rotation in southern Oregon [McCaffrey et al., 2007], as the fastest slip rates occur on a fault between California and Oregon, and on the small southern Oregon block. In contrast, the $\lambda = 900$ model contains only two blocks: the Juan de Fuca plate and the coast range block. This model does not fit Pacific Northwest velocities in the northern Basin and Range as well as the reference and $\lambda = 550$ model, and also estimates higher coupling rates on the Cascadia subduction zone. Residuals in the northern Basin and Range are systematically oriented to the northeast at rates of $\sim$2 mm/yr (Figure 5.19).

Even with five rotating blocks in the Pacific Northwest, we find little evidence of pervasive deformation in the region, as slip rates on block-bounding faults are low in the models considered (0 to 5 mm/yr) [McCaffrey et al., 2007]. As in the Basin and Range, the lack of faults in the Pacific northwest at $\lambda = 900$ demonstrates that differentiating between slow structures and inactive structures may not be possible at the $\sim$2 mm/yr GPS resolution level.

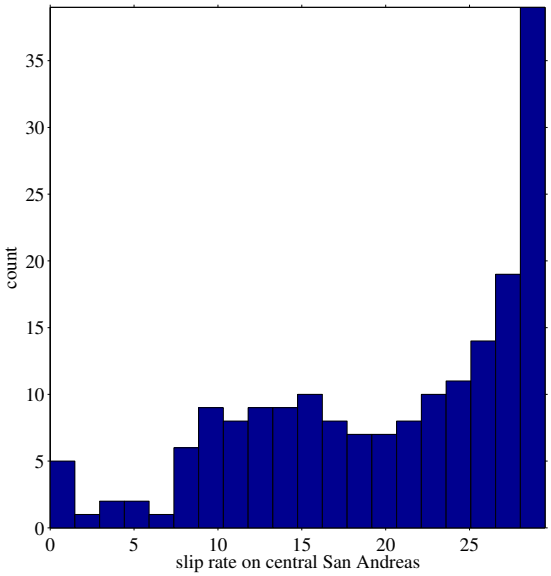

Figure 5.20: Probability distribution of central SAF slip rates

5.5 Discussion and conclusions

The total variation denoising (TVDN) estimator allows us to identify the simplest block models that fit geodetic observations at a given resolution level. Traditionally, block models interpret an interseismic velocity field in terms of block rotations where the block model geometry is pre-defined based on human interpretation of fault maps. TVDN allows interseismic velocity observations to guide block model construction by algorithmically selecting the most important block boundaries from a dense initial block geometry. The block model determined algorithmically here is similar to many previous studies of crustal deformation in western North America. Increasing λ in the total variation denoising algorithm causes overall narrowing of the plate boundary, leading to eastward migration of small-scale fault structures in California, and westward shutting off of faults in the Basin and Range.

Here we have selected block models based on their slip rates in a total variation denoising

estimator, and our slip rate estimates are based on a single block model solution for that geometry. It may be more appropriate to quantify plate boundary complexity based on the distribution of slip rates as estimated directly from TVDN over all values of λ. For example, for 185 values of λ between $\lambda = 50$ and $\lambda = 2300$ shown in Figure 5.5, slip rate on the Central San Andreas fault ranges between 0 and 30 mm/yr with a distribution shown in Figure 5.20 (calculated within the TVDN estimator, not with the traditional blocks formulation). It may be more appropriate to report slip rates based on these types of slip probability distributions, as opposed to selecting single representative models at a single λ value. To illustrate this concept, we calculate mean slip rates over all 185 λ values, and the standard deviation on each of these distributions. These slip rates are shown in Figure 5.21, colored by slip rate as before, and the width of each segment is proportional to the standard deviation of slip rates on that fault. This type of analysis requires a few caveats: 1) many of the slip rate distributions are not normally distributed (e.g. the slip rate distribution on central San Andreas shown in Figure 5.20), so mean slip rate and standard deviations may be problematic metrics, and 2) aggregate slip rates no longer ensure kinematic consistency across the boundary. However, this type of probabilistic analysis may be a powerful tool for providing a more complete picture of the epistemic uncertainties present in block model analysis.

We use the TVDN estimator only to select block model geometries. Ideally, this estimator would be integrated into the block model to estimate both quantized block motions and smooth spatially variable slip on the Cascadia subduction zone, however this is beyond the capabilities of the modified 1-D TVreg algorithm at this point. This means that the

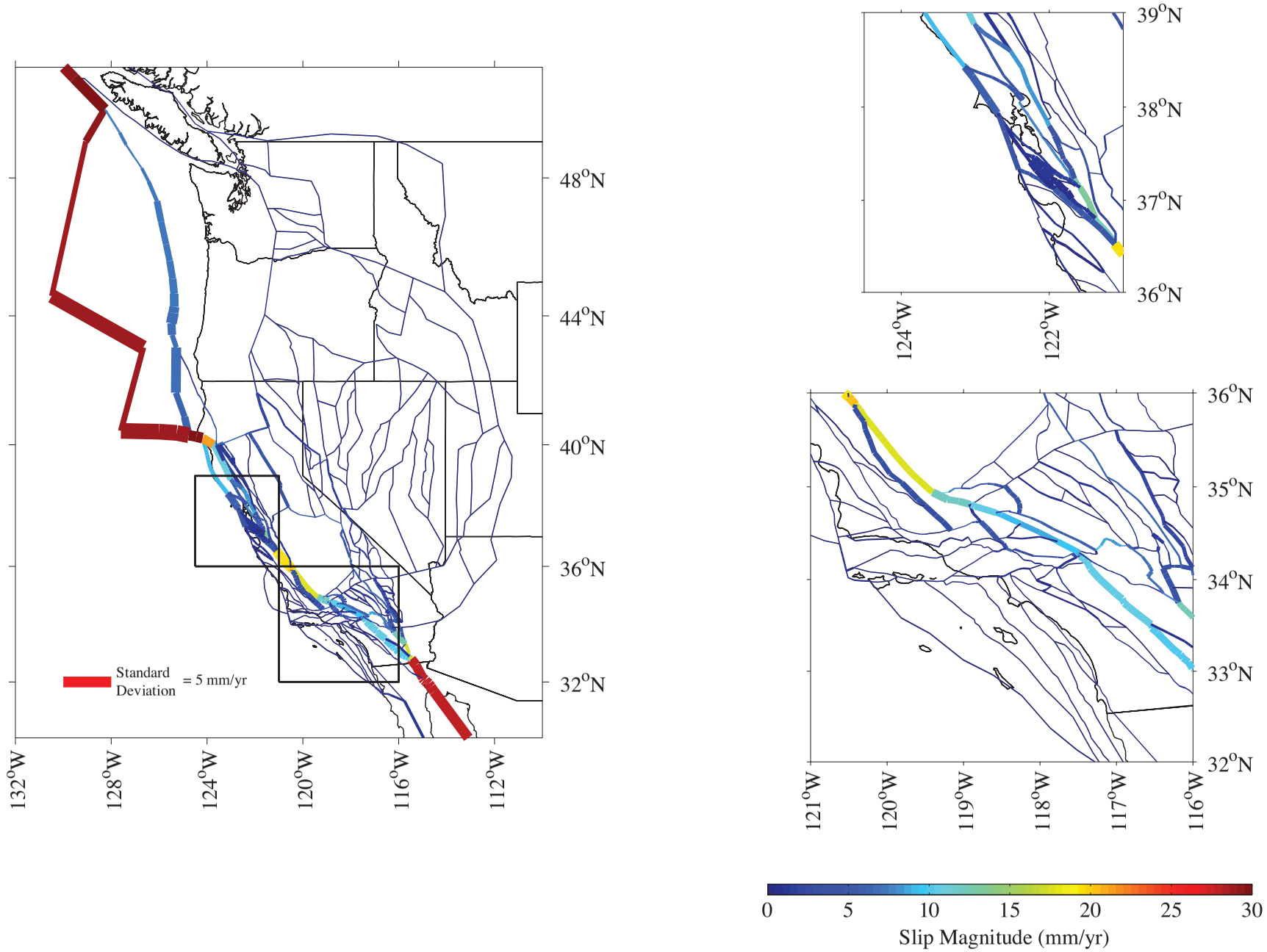

Figure 5.21: Probabilistic slip rates. Color-coded by slip rate, width is proportional to standard deviation. a) in Western U.S. b) in San Francisco Bay Area c) in Southern California

.

type of probabilistic analysis discussed above cannot currently incorporate spatially variable coupling on the subduction zone.

The inability of the TVDN regularization to identify faults slipping at $<\sim$4 mm/yr in dense fault systems such as the Los Angles basin (§5.4.2) brings up an important issue with this method. The philosophical question of "How many blocks do we need" to fit geodetic observations within a desired degree of uncertainty is fundamentally different than "which faults are important for seismic hazard". Addressing earthquake hazard more directly with TVDN methods would require: 1) the ability to incorporate a-priori geologic slip rates into the TVDN estimator, especially where slip rates are low and well studied, 2) redesigning our decision-making criteria to fit data more precisely in specific regions, and 3) better than 2 mm/yr GPS resolution to resolve slow-slipping faults.

Regardless of the precise block geometries selected in this study, allowing geodetic data to guide block model selection provides a framework for understanding continental complexity. If deformation in western North America were best approximated by the densest possible solution considered (144 blocks), then we might conclude that the plate boundary is in fact better represented as continuous. However, these very dense block models over-fit the data with short-wavelength changes in sense of slip (Figure 5.7). Instead, block models with as few as 20 blocks are capable of reproducing GPS observations with mean residual velocity of 2 mm/yr (Figures 5.18 and 5.19). This approach reveals that even in the presence of a diversity of possible fault system geometries, the majority of deformation in western North America is well approximated by slip on a subset of structures at a residual level of 2 mm/yr.

Chapter 6

Conclusions

Geodetic observations provide unprecedented quantitative constraints on the behavior of tectonically active fault systems. Using these observations to image the kinematic behavior of a fault or fault system allows us to make predictions that can be tested against other observables and hypotheses about fault mechanics, and gain a deeper understanding of earthquake phenomenology and physics.

In Chapter 2, we invert GPS and InSAR data with a kinematically consistent block model of the San Francisco Bay Area fault system to estimate Bay Area fault slip rates and spatially variable slip deficit rates on the Hayward fault. Slip estimates on the Hayward fault are consistent with independent observations of surface creep, historical seismicity, and geology. We identify a strongly coupled asperity with a slip deficit rate of 3.7±1.2 mm/yr at the surface near San Leandro, CA. Spatial correlation between high slip deficit rates and gabbroic fault surfaces adjacent to the mapped surface trace of the 1868 M_W=6.9-7.0 suggests that partially creeping fault behavior may be associated with complex lithologically modulated variations in frictional properties. Further insight into whether or not geodetically imaged asperities limit the rupture extent of future earthquakes on the Hayward fault may

be gained through dynamic slip models that are evolved forward in time from present day conditions.

In Chapters 3 and 4, we explore the ability of compressed sensing estimation techniques to recover compact and sharply varying slip distributions. Sparse regularization techniques fit geodetic observations as well as smoothed distributions, and allow quantitative assessment of the spatial relationship between coseismic slip and the rest of the earthquake cycle. Sparsity promoting estimates of slip in the great Tohoku earthquake identify a linear trend of slip between 20 and 40 km depth with a maximum coseismic slip of 64 m, and a narrow transition zone between coseismic slip and postseismic afterslip at depths of 40-50 km. Interpreted as a transition in idealized temperature-dependent frictional behavior from velocity weakening to velocity strengthening, this depth range is consistent with the warmest limit of estimated temperature profiles of the Japan trench subduction zone. In this sense, the ability to image sharp boundaries to co- and post-seismic slip provides new images of earthquake cycle processes that may be used to constrain the thermal structure of subduction zones and the depth profile of frictional behavior. Additionally, we estimate postseismic afterslip following the 2011 Tohoku earthquake that occurs almost completely down-dip of the coseismic rupture and does not migrate significantly for at least one year after the earthquake. By producing slip distributions that are localized, sparsity promoting slip estimates contain almost completely positive sense slip and are consistent with Coulomb failure stress change predictions. In this sense, sparse estimation methods may be more appropriate than traditional ℓ_2 regularized estimators.

In Chapter 5, we apply similar compressed sensing methods to kinematic block models

of interseismic deformation. Integrated with interseismic GPS velocities, compressed sensing methods allow the most important faults to be selected algorithmically, and allowing geodetic data to guide block model selection provides a framework for understanding continental complexity. If deformation western North America was best approximated by the densest possible solution considered (144 blocks), then we might conclude that the plate boundary is in fact better represented as continuous. Instead, block models with as few as 20 blocks are capable of reproducing GPS observations with mean residual velocity of 2 mm/yr.

Bibliography

2007 Working Group on California Earthquake Probabilities, 2008. The Uniform California Earthquake Rupture Forecast. Tech. Rep. 2007-1437, U.S. Geological Survey.

Argus, D. F., Gordon, R. G., 1990. Pacific North-American Plate Motion From Very Long Base-Line Interferometry Compared with Motion Inferred From Magnetic-Anomalies, Transform Faults, and Earthquake Slip Vectors. Journal of Geophysical Research 95 (B11), 17315–17324.

Argus, D. F., Heflin, M. B., 1995. Plate Motion and Crustal Deformation Estimated with Geodetic Data From the Global Positioning System. Geophysical Research Letters 22 (15), 1973–1976.

Bakun, W. H., Jun. 1999. Seismic activity of the San Francisco Bay region. Bulletin of the Seismological Society of America 89 (3), 764–784.

Barbot, S., Fialko, Y., Bock, Y., 2009. Postseismic deformation due to the Mw 6.0 2004 Parkfield earthquake: Stress-driven creep on a fault with spatially variable rate-and-state friction parameters. Journal of Geophysical Research: Solid Earth (1978–2012) 114 (B7).

Bawden, G. W., Donnellan, A., Kellogg, L. H., Dong, D. N., Rundle, J. B., 1997. Geodetic measurements of horizontal strain near the White Wolf fault, Kern County, California, 1926-1993. Journal of Geophysical Research 102 (B3), 4957–4967.

Becker, T. W., Hardebeck, J. L., Anderson, G., Feb. 2005. Constraints on fault slip rates of the southern California plate boundary from GPS velocity and stress inversions. Geophysical Journal International 160 (2), 634–650.

Bennett, R. A., Rodi, W., Reilinger, R. E., 1996. Global positioning system constraints on fault slip rates in southern California and northern Baja, Mexico. Journal of Geophysical Research 101 (B10), 21943–21960.

Bennett, R. A., Wernicke, B. P., Davis, J. L., Elosegui, P., Snow, J. K., Abolins, M. J., House, M. A., Stirewalt, G. L., Ferrill, D. A., 1997. Global positioning system constraints on fault slip rates in the Death Valley region, California and Nevada. Geophysical Research Letters 24 (23), 3073–3076.

Bennett, R. A., Wernicke, B. P., Niemi, N. A., Friedrich, A. M., Davis, J. L., 2003. Contemporary strain rates in the northern Basin and Range province from GPS data. Tectonics 22 (2), 1008.

Berger, G. W., Sawyer, T. L., Unruh, J. R., May 2010. Single- and Multigrain Luminescence Dating of Sediments Related to the Greenville Fault, Eastern San Francisco Bay Area, California. Bulletin of the Seismological Society of America 100 (3), 1051–1072.

Bilham, R., Whitehead, S., 1997. Subsurface creep on the Hayward Fault, Fremont, California. Geophysical Research Letters 24 (11), 1307–1310.

Bird, P., 2003. An updated digital model of plate boundaries. Geochemistry, Geophysics, Geosystems 4 (3), 1027.

Bird, P., 2009. Long-term fault slip rates, distributed deformation rates, and forecast of seismicity in the western United States from joint fitting of community geologic, geodetic, and stress direction data sets. Journal of Geophysical Research: Solid Earth 114 (B11).

Bird, P., Baumgardner, J., 1984. Fault Friction, Regional Stress, and Crust-Mantle Coupling in Southern-California From Finite-Element Models. Journal of Geophysical Research 89 (NB3), 1932–1944.

Bird, P., Kong, X., Feb. 1994. Computer simulations of California tectonics confirm very low strength of major faults. Geological Society of America Bulletin 106 (2), 159–174.

Blanpied, M. L., Lockner, D. A., Byerlee, J. D., 1995. Frictional slip of granite at hydrothermal conditions. Journal of Geophysical Research: Solid Earth (1978–2012) 100 (B7), 13045–13064.

Borchardt, G. S., David, L., Willis, C. J., 1999. Holocene slip rate of the Concord fault at Galindo Creek in Concord, California. Tech. rep., U.S. Geological Survey, Reston, Va.

Boyd, S. P., Vandenberghe, L., 2004. Convex Optimization. Cambridge University Press.

Brankman, C. M., Shaw, J. H., 2009. Structural Geometry and Slip of the Palos Verdes Fault, Southern California: Implications for Earthquake Hazards. Bulletin of the Seismological Society of America 99 (3), 1730–1745.

Budding, K. E., Schwartz, D. P., Oppenheimer, D. H., 1991. Slip rate, earthquake recurrence, and seismogenic potential of the Rodgers Creek Fault Zone, northern California: Initial results. Geophysical Research Letters 18 (3), 447–450.

Bürgmann, R., Hilley, G., Ferretti, A., Novali, F., 2006. Resolving vertical tectonics in the San Francisco Bay Area from permanent scatterer InSAR and GPS analysis. Geology 34 (3), 221.

Bürgmann, R., Kogan, M. G., Steblov, G. M., Hilley, G., Levin, V. E., Apel, E., 2005. Interseismic coupling and asperity distribution along the Kamchatka subduction zone. Journal of Geophysical Research: Solid Earth (1978–2012) 110 (B7).

Bürgmann, R., Schmidt, D., Nadeau, R. M., d'Alessio, M., Fielding, E., Manaker, D., McEvilly, T. V., Murray, M. H., Aug. 2000. Earthquake Potential Along the Northern Hayward Fault, California. Science 289 (5482), 1178–1182.

Bürgmann, R., Segall, P., Lisowski, M., Svarc, J., 1997. Postseismic strain following the 1989 Loma Prieta earthquake from GPS and leveling measurements. Journal of Geophysical Research 102 (B3), 4933–4955.

Candès, E. J., Romberg, J. K., Tao, T., 2006. Stable signal recovery from incomplete and inaccurate measurements. Communications on Pure and Applied Mathematics 59 (8), 1207–1223.

Chambolle, A., 2004. An Algorithm for Total Variation Minimization and Applications. Journal of Mathematical imaging and vision 20 (1-2), 89–97.

Chlieh, M., Avouac, J.-P., Hjorleifsdottir, V., Song, T.-R. A., Ji, C., Sieh, K., Sladen, A., Hebert, H., Prawirodirdjo, L., Bock, Y., Galetzka, J., Jan. 2007. Coseismic Slip and Afterslip of the Great Mw 9.15 Sumatra–Andaman Earthquake of 2004. Bulletin of the Seismological Society of America 97 (1A), S152–S173.

Chlieh, M., De Chabalier, J. B., Ruegg, J. C., Armijo, R., Dmowska, R., Campos, J., Feigl, K. L., 2004. Crustal deformation and fault slip during the seismic cycle in the North Chile subduction zone, from GPS and InSAR observations. Geophysical Journal International 158 (2), 695–711.

Claerbout, J., Muir, F., Oct. 1973. Robust modeling with erratic data. Geophysics 38 (5), 826–844.

Comninou, M., 1973. Angular dislocation in a half space. Ph.D. thesis, Northwestern University, Chicago, Ill.

Cross, R. S., Freymueller, J. T., Mar. 2007. Plate coupling variation and block translation in the Andreanof segment of the Aleutian arc determined by subduction zone modeling using GPS data. Geophysical Research Letters 34 (6), L06304.

d'Alessio, M. A., Johanson, I. A., Bürgmann, R., Schmidt, D. A., Murray, M. H., 2005. Slicing up the San Francisco Bay Area: Block kinematics and fault slip rates from GPSderived surface velocities. Journal of Geophysical Research: Solid Earth (1978–2012) 110 (B6), 403.

Davis, T. L., Namson, J., Yerkes, R. F., 1989. A Cross-Section of the Los-Angeles Area - Seismically Active Fold and Thrust Belt, the 1987 Whittier-Narrows Earthquake, and Earthquake Hazard. Journal of Geophysical Research 94 (B7), 9644–9664.

DeMets, C., Gordon, R. G., Argus, D. F., Stein, S., 1994. Effect of Recent Revisions to the Geomagnetic Reversal Time-Scale on Estimates of Current Plate Motions. Geophysical Research Letters 21 (20), 2191–2194.

Desbrun, M., Meyer, M., Schröder, P., Barr, A. H., Jul. 1999. Implicit fairing of irregular meshes using diffusion and curvature flow. ACM Press/Addison-Wesley Publishing Co., New York, New York, USA.

Diao, F., Xiong, X., Wang, R., Zheng, Y., Walter, T. R., Weng, H., Li, J., Dec. 2013. Overlapping post-seismic deformation processes: afterslip and viscoelastic relaxation following the 2011 Mw 9.0 Tohoku (Japan) earthquake. Geophysical Journal International 196 (1), 218–229.

Donoho, D., Tanner, J., Oct. 2009. Observed universality of phase transitions in high-dimensional geometry, with implications for modern data analysis and signal processing. Philosophical Transactions of the Royal Society A: Mathematical, Physical and Engineering Sciences 367 (1906), 4273–4293.

Donoho, D. L., 2006. For most large underdetermined systems of linear equations the minimal 1norm solution is also the sparsest solution. Communications on Pure and Applied Mathematics 59 (6), 797–829.

Efron, B., Jan. 1979. Bootstrap Methods: Another Look at the Jackknife. The annals of Statistics 7 (1), 1–26.

Evans, E. L., Loveless, J. P., Meade, B. J., 2012. Geodetic constraints on San Francisco Bay Area fault slip rates and potential seismogenic asperities on the partially creeping Hayward fault. Journal of Geophysical Research: Solid Earth (1978–2012) 117 (B3).

Evans, E. L., Meade, B. J., 2012. Geodetic imaging of coseismic slip and postseismic afterslip: Sparsity promoting methods applied to the great Tohoku earthquake. Geophysical Research Letters 39 (11).

Fialko, Y., 2006. Interseismic strain accumulation and the earthquake potential on the southern San Andreas fault system. Nature 441 (7096), 968–971.

Flesch, L. M., Holt, W. E., Haines, A. J., Shen Tu, B., Feb. 2000. Dynamics of the Pacific-North American Plate Boundary in the Western United States. Science 287 (5454), 834–836.

Fletcher, H. J., Freymueller, J. T., 2003. New constraints on the motion of the Fairweather fault, Alaska, from GPS observations. Geophysical Research Letters 30 (3).

Freymueller, J. T., Murray, M. H., Segall, P., Castillo, D., 1999. Kinematics of the Pacific-North America Plate Boundary Zone, northern California. Journal of Geophysical Research: Solid Earth (1978–2012) 104 (B4), 7419–7441.

Freymueller, J. T., Woodard, H., Cohen, S. C., Cross, R., Elliott, J., Larsen, C. F., Hreinsdóttir, S., Zweck, C., 2008. Active Deformation Processes in Alaska, Based on 15 Years of GPS Measurements. Vol. 179 of Geophysical Monograph Series. American Geophysical Union, Washington, D. C.

Fujii, Y., Satake, K., Sakai, S., Shinohara, M., Kanazawa, T., 2011. Tsunami source of the 2011 off the Pacific coast of Tohoku Earthquake. Earth, Planets and Space 63 (7), 815–820.

Fukuda, J., Kato, A., Kato, N., Aoki, Y., Jul. 2013. Are the frictional properties of creeping faults persistent? Evidence from rapid afterslip following the 2011 Tohoku-oki earthquake. Geophysical Research Letters 40 (14), 3613–3617.

Goldfinger, C., Nelson, C. H., Johnson, J. E., Party, S. S., 2003. Holocene earthquake records from the Cascadia subduction zone and northern San Andreas Fault based on precise dating of offshore turbidites. Annual Review of Earth and Planetary Sciences 31 (1), 555–577.

Graymer, R. W., Ponce, D. A., Jachens, R. C., Simpson, R. W., Phelps, G. A., Wentworth, C. M., 2005. Three-dimensional geologic map of the Hayward fault, northern California: Correlation of rock units with variations in seismicity, creep rate, and fault dip. Geology 33 (6), 521.

Graymer, R. W., Sarna-Wojcicki, A. M., Walker, J. P., McLaughlin, R. J., Fleck, R. J., Dec. 2002. Controls on timing and amount of right-lateral offset on the East Bay fault system, San Francisco Bay region, California. Geological Society of America Bulletin 114 (12), 1471–1479.

Hall, N. T., Wright, R. H., Clahan, K. B., 1999. Paleoseismic studies of the San Francisco Peninsula segment of the San Andreas fault zone near Woodside, California. Journal of Geophysical Research 104 (B10), 23215–23236.

Hammond, W. C., Thatcher, W., 2005. Northwest basin and range tectonic deformation observed with the global positioning system, 1999-2003. Journal of Geophysical Research 110 (B10).

Hammond, W. C., Thatcher, W., 2007. Crustal deformation across the Sierra Nevada, northern Walker Lane, Basin and Range transition, western United States measured with GPS, 2000-2004. Journal of Geophysical Research: Solid Earth 112 (B5).

Hardebeck, J. L., Michael, A. J., Brocher, T. M., Jun. 2007. Seismic Velocity Structure and Seismotectonics of the Eastern San Francisco Bay Region, California. Bulletin of the Seismological Society of America 97 (3), 826–842.

Harris, R. A., Segall, P., 1987. Detection of a locked zone at depth on the Parkfield, California, segment of the San Andreas Fault. Journal of Geophysical Research: Solid Earth (1978–2012) 92 (B8), 7945–7962.

Hashimoto, M., Jackson, D. D., 1993. Plate-Tectonics and Crustal Deformation Around the Japanese Islands. Journal of Geophysical Research 98 (B9), 16149–16166.

He, C., Wang, Z., Yao, W., 2007. Frictional sliding of gabbro gouge under hydrotherynal conditions. Tectonophysics 445 (3-4), 353–362.

Heki, K., Feb. 2004. Space geodetic observation of deep basal subduction erosion in northeastern Japan. Earth and Planetary Science Letters 219 (1-2), 13–20.

Hoechner, A., Sobolev, S. V., Einarsson, I., Wang, R., Jul. 2011. Investigation on afterslip and steady state and transient rheology based on postseismic deformation and geoid change caused by the Sumatra 2004 earthquake. Geochemistry, Geophysics, Geosystems 12 (7).

Hsu, Y.-J., Bechor, N., Segall, P., Yu, S.-B., Kuo, L.-C., Ma, K.-F., Aug. 2002. Rapid afterslip following the 1999 Chi-Chi, Taiwan Earthquake. Geophysical Research Letters 29 (16).

Hsu, Y.-J., Simons, M., Avouac, J.-P., Galetzka, J., Sieh, K., Chlieh, M., Natawidjaja, D., Prawirodirdjo, L., Bock, Y., Jun. 2006. Frictional Afterslip Following the 2005 Nias-Simeulue Earthquake, Sumatra. Science 312 (5782), 1921–1926.

Hu, Y., Wang, K., May 2012. Spherical-Earth finite element model of short-term postseismic deformation following the 2004 Sumatra earthquake. Journal of Geophysical Research 117 (B5).

Humphreys, E. D., Weldon, R. J., 1994. Deformation across the western United States: A local estimate of PacificNorth America transform deformation. Journal of Geophysical Research: Solid Earth (1978–2012) 99 (B10), 19975–20010.

Ide, S., Baltay, A., Beroza, G. C., Jun. 2011. Shallow Dynamic Overshoot and Energetic Deep Rupture in the 2011 Mw 9.0 Tohoku-Oki Earthquake. Science 332 (6036), 1426–1429.

Ishibe, Mar. 2011. Correlation between Coulomb stress changes imparted by large historical strike-slip earthquakes and current seismicity in Japan. Earth, Planets and Space 63 (3), 301–314.

Ito, T., Ozawa, K., Watanabe, T., Sagiya, T., 2011. Slip distribution of the 2011 off the Pacific coast of Tohoku Earthquake inferred from geodetic data. Earth, Planets and Space 63 (7), 627–630.

Jennings, C. W., 1994. Fault activity map of california and adjacent areas with locations and ages of recent volcanic eruptions. Tech. Rep. 1, California Division of Mines and Geology.

Jensen, T. L., Jorgensen, J. H., Hansen, P. C., Jensen, S. H., Jun. 2012. Implementation of an optimal first-order method for strongly convex total variation regularization. Bit Numerical Mathematics 52 (2), 329–356.

Jeyakumaran, M., Rudnicki, J. W., Keer, L. M., Oct. 1992. Modeling slip zones with triangular dislocation elements. Bulletin of the Seismological Society of America 82 (5), 2153–2169.

Johanson, I. A., Bürgmann, R., Jul. 2005. Creep and quakes on the northern transition zone of the San Andreas fault from GPS and InSAR data. Geophysical Research Letters 32 (14).

Johnson, K. M., Fukuda, J., 2010. New methods for estimating the spatial distribution of locked asperities and stressdriven interseismic creep on faults with application to the San

Francisco Bay Area, California. Journal of Geophysical Research: Solid Earth (1978–2012) 115 (B12), B12408.

Johnson, K. M., Fukuda, J., Segall, P., 2012. Challenging the ratestate asperity model: Afterslip following the 2011 M9 Tohoku-oki, Japan, earthquake. Geophysical Research Letters.

Kaneko, Y., Avouac, J.-P., Lapusta, N., Apr. 2010. Towards inferring earthquake patterns from geodetic observations of interseismic coupling. Nature Geoscience 3 (5), 363–369.

Kaneko, Y., Lapusta, N., Dec. 2008. Variability of earthquake nucleation in continuum models of rate-and-state faults and implications for aftershock rates. Journal of Geophysical Research 113 (B12), B12312.

Kelson, K. I., Simpson, G. D., Lettis, W. R., Haraden, C. C., 1996. Holocene slip rate and earthquake recurrence of the northern Calaveras fault at Leyden Creek, northern California. Journal of Geophysical Research 101 (B3), 5961–5975.

Kido, M., Osada, Y., Fujimoto, H., Hino, R., Ito, Y., 2011. Trenchnormal variation in observed seafloor displacements associated with the 2011 TohokuOki earthquake. Geophysical Research Letters 38 (24).

King, G. C. P., Stein, R. S., Lin, J., Jun. 1994. Static stress changes and the triggering of earthquakes. Bulletin of the Seismological Society of America 84 (3), 935–953.

Kiser, E., Ishii, M., 2012. The March 11, 2011 Tohokuoki earthquake and cascading failure of the plate interface. Geophysical Research Letters 39 (7).

Kogan, M. G., Vasilenko, N. F., Frolov, D. I., Freymueller, J. T., Steblov, G. M., Levin, B. W., Prytkov, A. S., Mar. 2011. The mechanism of postseismic deformation triggered by the 2006-2007 great Kuril earthquakes. Geophysical Research Letters 38 (6).

Kogan, M. G., Vasilenko, N. F., Frolov, D. I., Freymueller, J. T., Steblov, G. M., Prytkov, A. S., Ekström, G., Jul. 2013. Rapid postseismic relaxation after the great 2006-2007 Kuril earthquakes from GPS observations in 2007-2011. Journal of Geophysical Research: Solid Earth 118 (7), 3691–3706.

Koketsu, K., Yokota, Y., Nishimura, N., Yagi, Y., Miyazaki, S., Satake, K., Fujii, Y., Miyake, H., Sakai, S., Yamanaka, Y., Okada, T., Oct. 2011. A unified source model for the 2011 Tohoku earthquake. Earth and Planetary Science Letters 310 (3-4), 480–487.

Konca, A. O., Avouac, J.-P., Sladen, A., Meltzner, A. J., Sieh, K., Fang, P., Li, Z., Galetzka, J., Genrich, J., Chlieh, M., Natawidjaja, D. H., Bock, Y., Fielding, E. J., Ji, C., Helmberger, D. V., Dec. 2008. Partial rupture of a locked patch of the Sumatra megathrust during the 2007 earthquake sequence. Nature 456 (7222), 631–635.

Lawson, A. C., 1908. The California Earthquake of April 18, 1906.

Lay, T., Kanamori, H., 1980. Earthquake Doublets in the Solomon-Islands. Physics of the Earth and Planetary Interiors 21 (4), 283–304.

Lee, S. J., Huang, B. S., Ando, M., Chiu, H. C., Wang, J. H., 2011. Evidence of large scale repeating slip during the 2011 TohokuOki earthquake. Geophysical Research Letters 38 (19).

Leon, L. A., Christofferson, S. A., Dolan, J. F., Shaw, J. H., Pratt, T. L., 2007. Earthquake-by-earthquake fold growth above the Puente Hills blind thrust fault, Los Angeles, California: Implications for fold kinematics and seismic hazard. Journal of Geophysical Research 112 (B3).

Leon, L. A., Dolan, J. F., Shaw, J. H., Pratt, T. L., 2009. Evidence for large Holocene earthquakes on the Compton thrust fault, Los Angeles, California. Journal of Geophysical Research 114 (B12).

Lienkaemper, J. J., Jun. 1997. Creep Response of the Hayward Fault to Stress Changes Caused by the Loma Prieta Earthquake. Science 276 (5321), 2014–2016.

Lienkaemper, J. J., Borchardt, G., 1996. Holocene slip rate of the Hayward fault at Union City, California. Journal of Geophysical Research 101 (B3), 6099–6108.

Lienkaemper, J. J., Galehouse, J. S., Nov. 1998. New Evidence Doubles the Seismic Potential of the Hayward Fault. Seismological Research Letters 69 (6), 519–523.

Lienkaemper, J. J., Galehouse, J. S., Simpson, R. W., 2001. Longterm monitoring of creep rate along the Hayward Fault and evidence for a lasting creep response to 1989 Loma Prieta Earthquake. Geophysical Research Letters 28 (11), 2265–2268.

Lienkaemper, J. J., Williams, P. L., Guilderson, T. P., Sep. 2010. Evidence for a Twelfth Large Earthquake on the Southern Hayward Fault in the Past 1900 Years. Bulletin of the Seismological Society of America 100 (5A), 2024–2034.

Lindsey, E. O., Sahakian, V. J., Fialko, Y., Bock, Y., Barbot, S., Rockwell, T. K., 2013. Interseismic Strain Localization in the San Jacinto Fault Zone. Pure and Applied Geophysics, 1–18.

Lisowski, M., Savage, J. C., Prescott, W. H., 1991. The velocity field along the San Andreas Fault in central and southern California. Journal of Geophysical Research: Solid Earth (1978–2012) 96 (B5), 8369–8389.

Liu, Y., Rice, J. R., Sep. 2009. Slow slip predictions based on granite and gabbro friction data compared to GPS measurements in northern Cascadia. Journal of Geophysical Research 114 (B9), B09407.

Loveless, J. P., Meade, B. J., 2010. Geodetic imaging of plate motions, slip rates, and partitioning of deformation in Japan. Journal of Geophysical Research: Solid Earth 115 (B2).

Loveless, J. P., Meade, B. J., Sep. 2011a. Spatial correlation of interseismic coupling and coseismic rupture extent of the 2011 M_W= 9.0 Tohoku-oki earthquake. Geophysical Research Letters 38 (17).

Loveless, J. P., Meade, B. J., Oct. 2011b. Stress modulation on the San Andreas fault by interseismic fault system interactions. Geology 39 (11), 1035–1038.

Lubis, A. M., Hashima, A., Sato, T., Dec. 2012. Analysis of afterslip distribution following the 2007 September 12 southern Sumatra earthquake using poroelastic and viscoelastic media. Geophysical Journal International 192 (1), 18–37.

Lundgren, P., Hetland, E. A., Liu, Z., Fielding, E. J., 2009. Southern San Andreas-San Jacinto fault system slip rates estimated from earthquake cycle models constrained by GPS and interferometric synthetic aperture radar observations. Journal of Geophysical Research: Solid Earth (1978–2012) 114 (B2), B02403.

Maeda, T., Furumura, T., Sakai, S., Shinohara, M., 2011. Significant tsunami observed at ocean-bottom pressure gauges during the 2011 off the Pacific coast of Tohoku Earthquake. Earth, Planets and Space 63 (7), 803–808.

Maerten, F., Resor, P., Pollard, D., Maerten, L., Oct. 2005. Inverting for Slip on Three-Dimensional Fault Surfaces Using Angular Dislocations. Bulletin of the Seismological Society of America 95 (5), 1654–1665.

Malservisi, R., Furlong, K. P., Gans, C. R., 2005. Microseismicity and creeping faults: Hints from modeling the Hayward fault, California (USA). Earth and Planetary Science Letters 234 (3-4), 421–435.

Malservisi, R., Gans, C., Furlong, K. P., Jan. 2003. Numerical modeling of strike-slip creeping faults and implications for the Hayward fault, California. Tectonophysics 361 (1-2), 121–137.

Manaker, D. M., Apr. 2005. Subsurface Structure and Kinematics of the Calaveras-Hayward Fault Stepover from Three-Dimensional Vp and Seismicity, San Francisco Bay Region, California. Bulletin of the Seismological Society of America 95 (2), 446–470.

Manaker, D. M., Bürgmann, R., Prescott, W. H., Langbein, J., 2003. Distribution of interseismic slip rates and the potential for significant earthquakes on the Calaveras fault, central California. Journal of Geophysical Research 108 (B6), 2287.

Marone, C., 1998. Laboratory-derived friction laws and their application to seismic faulting. Annual Review of Earth and Planetary Sciences 26, 643–696.

Marone, C., Cox, S., 1994. Scaling of Rock Friction Constitutive Parameters - the Effects of Surface-Roughness and Cumulative Offset on Friction of Gabbro. Pure and Applied Geophysics 143 (1-3), 359–385.

Marone, C. J., Scholtz, C. H., Bilham, R., 1991. On the mechanics of earthquake afterslip. Journal of Geophysical Research: Solid Earth (1978–2012) 96 (B5), 8441–8452.

Matsu'ura, M., Jackson, D. D., Cheng, A., 1986. Dislocation Model for Aseismic Crustal Deformation at Hollister, California. Journal of Geophysical Research 91 (B12), 2661–2674.

McCaffrey, R., 2002. Crustal block rotations and plate coupling. Geodynamics Series 30, 101–122.

McCaffrey, R., 2005. Block kinematics of the Pacific-North America plate boundary in the southwestern United States from inversion of GPS, seismological, and geologic data. Journal of Geophysical Research 110 (B7).

McCaffrey, R., Apr. 2009. Time-dependent inversion of threecomponent continuous GPS for steady and transient sources in northern Cascadia. Geophysical Research Letters 36 (7), L07304.

McCaffrey, R., Qamar, A. I., King, R. W., Wells, R., Khazaradze, G., Williams, C. A., Stevens, C. W., Vollick, J. J., Zwick, P. C., Jun. 2007. Fault locking, block rotation and crustal deformation in the Pacific Northwest. Geophysical Journal International 169 (3), 1315–1340.

McClusky, S. C., Bjornstad, S. C., Hager, B. H., King, R. W., Meade, B. J., Miller, M. M., Monastero, F. C., Souter, B. J., 2001. Present day kinematics of the Eastern California Shear Zone from a geodetically constrained block model. Geophysical Research Letters 28 (17), 3369–3372.

McCrory, P. A., Blair, J. L., Oppenheimer, D. H., Walter, S. R., 2009. Depth to the Juan de Fuca slab beneath the Cascadia subduction margin - A 3-D model sorting earthquakes. Tech. rep., U.S. Geological Survey.

Meade, B. J., 2005. Block models of crustal motion in southern California constrained by GPS measurements. Journal of Geophysical Research 110 (B3), B03403.

Meade, B. J., Aug. 2007. Algorithms for the calculation of exact displacements, strains, and stresses for triangular dislocation elements in a uniform elastic half space. Computers & Geosciences 33 (8), 1064–1075.

Meade, B. J., Hager, B. H., 2005. Block models of crustal motion in southern California constrained by GPS measurements. Journal of Geophysical Research: Solid Earth (1978–2012) 110 (B3).

Meade, B. J., Loveless, J. P., Dec. 2009. Block Modeling with Connected Fault-Network Geometries and a Linear Elastic Coupling Estimator in Spherical Coordinates. Bulletin of the Seismological Society of America 99 (6), 3124–3139.

Menke, W., 1984. Geophysical Data Analysis. Vol. 45. Academic Press, Palisades, NY.

Miller, M. M., Johnson, D. J., Rubin, C. M., Dragert, H., Wang, K., Qamar, A., Goldfinger, C., 2001. GPS-determination of along-strike variation in Cascadia margin kinematics: Implications for relative plate motion, subduction zone coupling, and permanent deformation. Tectonics 20 (2), 161–176.

Minster, J. B., Jordan, T. H., 1987. Vector Constraints on Western United-States Deformation From Space Geodesy, Neotectonics, and Plate Motions. Journal of Geophysical Research 92 (B6), 4798–4804.

Miyazaki, Sep. 2011. Seismic and aseismic fault slip before and during the 2011 off the Pacific coast of Tohoku Earthquake. Earth, Planets and Space 63 (7), 637–642.

Miyazaki, S., 2004. Space time distribution of afterslip following the 2003 Tokachi-oki earthquake: Implications for variations in fault zone frictional properties. Geophysical Research Letters 31 (6), L06623.

Miyazaki, S., Larson, K. M., 2008. Coseismic and early postseismic slip for the 2003 Tokachioki earthquake sequence inferred from GPS data. Geophysical Research Letters 35 (4), L04302.

Molnar, P., 1988. Continental Tectonics in the Aftermath of Plate-Tectonics. Nature 335 (6186), 131–137.

Moreno, M., Rosenau, M., Oncken, O., Sep. 2010. 2010 Maule earthquake slip correlates with pre-seismic locking of Andean subduction zone. Nature 467 (7312), 198–202.

Mori, N., Takahashi, T., Yasuda, T., Yanagisawa, H., 2011. Survey of 2011 Tohoku earthquake tsunami inundation and runup. Geophysical Research Letters 38 (7).

Morrow, C. A., Lockner, D. A., 2001. Hayward fault rocks: Porosity, density and strength measurements. Tech. Rep. 01-421, U.S. Geological Survey.

Murray, M. H., Segall, P., 2001. Modeling broadscale deformation in northern California and Nevada from plate motions and elastic strain accumulation. Geophysical Research Letters 28 (22), 4315–4318.

Murray-Moraleda, J. R., Simpson, R. W., Sep. 2009. Geodetically Inferred Coseismic and Postseismic Slip due to the M 5.4 31 October 2007 Alum Rock Earthquake. Bulletin of the Seismological Society of America 99 (5), 2784–2800.

Natawidjaja, D. H., Sieh, K., Ward, S. N., Cheng, H., Edwards, R. L., Galetzka, J., Suwargadi, B. W., 2004. Paleogeodetic records of seismic and aseismic subduction from central Sumatran microatolls, Indonesia. Journal of Geophysical Research 109 (B4).

Niemi, N. A., Wernicke, B. P., Friedrich, A. M., Simons, M., Bennett, R. A., Davis, J. L., Dec. 2004. BARGEN continuous GPS data across the eastern Basin and Range province, and implications for fault system dynamics. Geophysical Journal International 159 (3), 842–862.

Niemi, T. M., Hall, N. T., Mar. 1992. Late Holocene Slip Rate and Recurrence of Great Earthquakes on the San-Andreas Fault in Northern California. Geology 20 (3), 195–198.

Nishida, K., Kawakatsu, H., Obara, K., 2008. Three-dimensional crustal S wave velocity structure in Japan using microseismic data recorded by Hinet tiltmeters. Journal of Geophysical Research: Solid Earth (1978–2012) 113 (B10).

Nishimura, T., Hirasawa, T., Miyazaki, S., Sagiya, T., Tada, T., Miura, S., Tanaka, K., May 2004. Temporal change of interplate coupling in northeastern Japan during 1995-2002 estimated from continuous GPS observations. Geophysical Journal International 157 (2), 901–916.

Nur, A., Ron, H., Beroza, G. C., Jul. 1993. The Nature of the Landers-Mojave Earthquake Line. Science 261 (5118), 201–203.

Okada, Y., Aug. 1985. Surface deformation due to shear and tensile faults in a half-space. Bulletin of the Seismological Society of America 75 (4), 1135–1154.

Okada, Y., Apr. 1992. Internal deformation due to shear and tensile faults in a half-space. Bulletin of the Seismological Society of America 82 (2), 1018–1040.

Ozawa, S., Nishimura, T., Munekane, H., Suito, H., Kobayashi, T., Tobita, M., Imakiire, T., Jul. 2012. Preceding, coseismic, and postseismic slips of the 2011 Tohoku earthquake, Japan. Journal of Geophysical Research 117 (B7), B07404.

Ozawa, S., Nishimura, T., Suito, H., Kobayashi, T., Tobita, M., Imakiire, T., Jul. 2011. Coseismic and postseismic slip of the 2011 magnitude-9 Tohoku-Oki earthquake. Nature 475 (7356), 373–376.

Panet, I., Pollitz, F., Mikhailov, V., Diament, M., Banerjee, P., Grijalva, K., Jun. 2010. Upper mantle rheology from GRACE and GPS postseismic deformation after the 2004 Sumatra-Andaman earthquake. Geochemistry, Geophysics, Geosystems 11 (6).

Park, S.-C., Mori, J., 2007. Are asperity patterns persistent? Implication from large earthquakes in Papua New Guinea. Journal of Geophysical Research 112 (B3).

Paul, J., Lowry, A. R., Bilham, R., Sen, S., Smalley Jr., R., Oct. 2007. Postseismic deformation of the Andaman Islands following the 26 December, 2004 Great Sumatra–Andaman earthquake. Geophysical Research Letters 34 (19), L19309.

Peacock, S. M., Wang, K., Oct. 1999. Seismic Consequences of Warm Versus Cool Subduction Metamorphism: Examples from Southwest and Northeast Japan. Science 286 (5441), 937–939.

Peltzer, G., Crampe, F., Hensley, S., Rosen, P., Nov. 2001. Transient strain accumulation and fault interaction in the Eastern California shear zone. Geology 29 (11), 975–978.

Pollitz, F., 2004. A physical model for strain accumulation in the San Francisco Bay region: Stress evolution since 1838. Journal of Geophysical Research 109 (B11), B11408.

Pollitz, F. F., Bürgmann, R., Banerjee, P., 2011. Geodetic slip model of the 2011 M9.0 Tohoku earthquake. Geophysical Research Letters 38 (7).

Pollitz, F. F., Sacks, I. S., May 2002. Stress Triggering of the 1999 Hector Mine Earthquake by Transient Deformation Following the 1992 Landers Earthquake. Bulletin of the Seismological Society of America 92 (4), 1487–1496.

Ponce, D. A., Simpson, R. W., Graymer, R. W., Jachens, R. C., Jul. 2004. Gravity, magnetic, and high-precision relocated seismicity profiles suggest a connection between the Hayward and Calaveras Faults, northern California. Geochemistry, Geophysics, Geosystems 5 (7).

Pritchard, M. E., Simons, M., Rosen, P. A., Hensley, S., Webb, F. H., Aug. 2002. Co-seismic slip from the 1995 July 30 Mw=8.1 Antofagasta, Chile, earthquake as constrained by InSAR and GPS observations. Geophysical Journal International 150 (2), 362–376.

Rousset, B., Barbot, S., Avouac, J.-P., Hsu, Y.-J., Dec. 2012. Postseismic deformation following the 1999 Chi-Chi earthquake, Taiwan: Implication for lower-crust rheology. Journal of Geophysical Research 117 (B12), B12405.

Rudin, L. I., Osher, S., Fatemi, E., Nov. 1992. Nonlinear total variation based noise removal algorithms. Physica D: Nonlinear Phenomena 60 (1-4), 259–268.

Sammis, C. G., Rice, J. R., Jun. 2001. Repeating earthquakes as low-stress-drop events at a border between locked and creeping fault patches. Bulletin of the Seismological Society of America 91 (3), 532–537.

Santosa, F., Symes, W., Oct. 1986. Linear Inversion of Band-Limited Reflection Seismograms. SIAM J. Sci. and Stat. Comput. 7 (4), 1307–1330.

Satake, K., Wang, K. L., Atwater, B. F., 2003. Fault slip and seismic moment of the 1700 Cascadia earthquake inferred from Japanese tsunami descriptions. Journal of Geophysical Research 108 (B11).

Sato, M., Ishikawa, T., Ujihara, N., Yoshida, S., Fujita, M., Mochizuki, M., Asada, A., Jun. 2011. Displacement Above the Hypocenter of the 2011 Tohoku-Oki Earthquake. Science 332 (6036), 1395–1395.

Savage, J. C., 1983. A Dislocation Model of Strain Accumulation and Release at a Subduction Zone. Journal of Geophysical Research 88 (NB6), 4984–4996.

Savage, J. C., Burford, R. O., 1973. Geodetic Determination of Relative Plate Motion in Central California. Journal of Geophysical Research 78 (5), 832–845.

Savage, J. C., Lisowski, M., 1993. Inferred depth of creep on the Hayward Fault, central California. Journal of Geophysical Research: Solid Earth (1978–2012) 98 (B1), 787–793.

Schmalzle, G., Dixon, T., Malservisi, R., Govers, R., 2006. Strain accumulation across the Carrizo segment of the San Andreas Fault, California: Impact of laterally varying crustal properties. Journal of Geophysical Research 111 (B5), B05403.

Schmidt, D. A., Bürgmann, R., Nadeau, R. M., d'Alessio, M., 2005. Distribution of aseismic slip rate on the Hayward fault inferred from seismic and geodetic data. Journal of Geophysical Research: Solid Earth (1978–2012) 110 (B8).

Scholz, C. H., Jan. 1998. Earthquakes and friction laws. Nature 391 (6662), 37–42.

Schwartz, D. P., Coppersmith, K. J., 1984. Fault Behavior and Characteristic Earthquakes - Examples From the Wasatch and San-Andreas Fault Zones. Journal of Geophysical Research 89 (NB7), 5681–5698.

Segall, P., Jan. 2002. Integrating Geologic and Geodetic Estimates of Slip Rate on the San Andreas Fault System. International Geology Review 44 (1), 62–82.

Shaw, J. H., Bischke, R. E., Suppe, J., 1994. The Loma Prieta, California, earthquake of October 17, 1989: Earthquake occurence. United States Geological ....

Shen, Z. K., Agnew, D. C., King, R. W., Dong, D., Herring, T. A., Wang, M., Johnson, H., Anderson, G., Nikolaidis, R., van Domselaar, M., Hudnut, K. W., D, J. D., 2003. SCEC crustal motion map. Tech. rep., Southern California Earthquake Center.

Shen Tu, B., Holt, W. E., Haines, A. J., 1998. Contemporary kinematics of the western United States determined from earthquake moment tensors, very long baseline interferometry, and GPS observations. Journal of Geophysical Research: Solid Earth (1978–2012) 103 (B8), 18087–18117.

Shimizaki, K., Nakata, T., 1980. Time-Predictable Recurrence Model for Large Earthquakes. Geophysical Research Letters 7 (4), 279–282.

Simons, M., Minson, S. E., Sladen, A., Ortega, F., Jiang, J., Owen, S. E., Meng, L., Ampuero, J.-P., Wei, S., Chu, R., Helmberger, D. V., Kanamori, H., Hetland, E., Moore, A. W., Webb, F. H., Jun. 2011. The 2011 Magnitude 9.0 Tohoku-Oki Earthquake: Mosaicking the Megathrust from Seconds to Centuries. Science 332 (6036), 1421–1425.

Simpson, G. D., Baldwin, J. N., Kelson, K. I., Lettis, W. R., Oct. 1999. Late holocene slip rate and earthquake history for the northern Calaveras fault at Welch Creek, eastern San Francisco Bay area, California. Bulletin of the Seismological Society of America 89 (5), 1250–1263.

Simpson, G. D., Thompson, S. C., Noller, J. S., Lettis, W. R., Oct. 1997. The northern San Gregorio fault zone: Evidence for the timing of late Holocene earthquakes near Seal Cove, California. Bulletin of the Seismological Society of America 87 (5), 1158–1170.

Simpson, R. W., Lienkaemper, J. J., Galehouse, J. S., 2001. Variations in creep rate along the Hayward Fault, California, interpreted as changes in depth of creep. Geophysical Research Letters 28 (11), 2269–2272.

Sleep, N. H., Fujita, K., 1997. Principles of geophysics. John Wiley and Sons Ltd.

Smith, R. B., Sbar, M. L., Aug. 1974. Contemporary Tectonics and Seismicity of the Western United States with Emphasis on the Intermountain Seismic Belt. Geological Society of America Bulletin 85 (8), 1205–1218.

Souter, B. J., 1998. Comparisons of geologic models to GPS observations in southern California. Ph.D. thesis, Massachussets Institude of Technology, Cambridge, MA.

Steacy, S., Marsan, D., Nalbant, S. S., McCloskey, J., 2004. Sensitivity of static stress calculations to the earthquake slip distribution. Journal of Geophysical Research: Solid Earth (1978–2012) 109 (B4).

Stein, R. S., King, G. C. P., Lin, J., Sep. 1994. Stress Triggering of the 1994 M = 6.7 Northridge, California, Earthquake by Its Predecessors. Science 265 (5177), 1432–1435.

Suito, H., Freymueller, J. T., Nov. 2009. A viscoelastic and afterslip postseismic deformation model for the 1964 Alaska earthquake. Journal of Geophysical Research 114 (B11), B11404.

Suito, H., Nishimura, T., Tobita, M., Imakiire, T., 2011. Interplate fault slip along the Japan Trench before the occurrence of the 2011 off the Pacific coast of Tohoku Earthquake as inferred from GPS data. Earth, Planets and Space 63 (7).

Templeton, D. C., Nadeau, R. M., Bürgmann, R., Feb. 2008. Behavior of Repeating Earthquake Sequences in Central California and the Implications for Subsurface Fault Creep. Bulletin of the Seismological Society of America 98 (1), 52–65.

Thatcher, W., 1990. Order and diversity in the modes of CircumPacific Earthquake recurrence. Journal of Geophysical Research: Solid Earth (1978–2012) 95 (B3), 2609–2623.

Thatcher, W., 1995. Microplate Versus Continuum Descriptions of Active Tectonic Deformation. Journal of Geophysical Research 100 (B3), 3885–3894.

Thatcher, W., 2009. How the Continents Deform: The Evidence From Tectonic Geodesy. Annual Review of Earth and Planetary Sciences 37 (1), 237–262.

Thatcher, W., Foulger, G. R., Julian, B. R., Svarc, J., Quilty, E., Bawden, G. W., 1999. Present-day deformation across the basin and range province, western United States. Science 283 (5408), 1714–1718.

Thomas, A. L., 1993. Poly3D: A three-dimensional, polygonal element, displacement discontinuity boundary element computer program with applications to fractures, faults, and cavities in the earth's crust. Master's thesis, Stanford University, Palo Alto, CA.

Tibshirani, R., Jan. 1996. Regression Shrinkage and Selection via the Lasso. Journal of the Royal Statistical Society. Series B (Methodological) 58 (1), 267–288.

Toppozada, T., Branum, D., Dec. 2004. California earthquake history. Annals of Geophysics 47 (2-3).

Tse, S. T., Rice, J. R., 1986. Crustal earthquake instability in relation to the depth variation of frictional slip properties. Journal of Geophysical Research: Solid Earth (1978–2012) 91 (B9), 9452–9472.

Ueda, H., 2003. Postseismic crustal deformation following the 1993 Hokkaido Nansei-oki earthquake, northern Japan: Evidence for a low-viscosity zone in the uppermost mantle. Journal of Geophysical Research 108 (B3), 2151.

U.S. Geological Survey, Arizona Geological Survey, California Geological survey, Colorado Geological Survey, Idaho Geological Survey, Montana Bureau of Mines and Geology, Nevada Bureau of Mines and Geology, New Mexico Bureau of Mines and Mineral Resources, Utah Geological Survey, 2006. Quaternary fault and fold database for the United States. Tech. rep., U.S. Geological Survey.

van den Berg, E., Friedlander, M. P., Jan. 2009. Probing the Pareto Frontier for Basis Pursuit Solutions. SIAM Journal on Scientific Computing 31 (2), 890–912.

Vigny, C., Socquet, A., Peyrat, S., Ruegg, J. C., Métois, M., Madariaga, R., Morvan, S., Lancieri, M., Lacassin, R., Campos, J., Carrizo, D., Bejar-Pizarro, M., Barrientos, S., Armijo, R., Aranda, C., Valderas-Bermejo, M. C., Ortega, I., Bondoux, F., Baize, S., Lyon-Caen, H., Pavez, A., Vilotte, J. P., Bevis, M., Brooks, B., Smalley, R., Parra, H., Baez, J. C., Blanco, M., Cimbaro, S., Kendrick, E., Jun. 2011. The 2010 Mw 8.8 Maule Megathrust Earthquake of Central Chile, Monitored by GPS. Science 332 (6036), 1417–1421.

Waldhauser, F., 2002. Fault structure and mechanics of the Hayward Fault, California, from double-difference earthquake locations. Journal of Geophysical Research 107 (B3), 2054.

Waldhauser, F., Ellsworth, W. L., 2002. Fault structure and mechanics of the Hayward Fault, California, from double-difference earthquake locations. Journal of Geophysical Research 107 (B3), 2054.

Wallace, L. M., Beavan, J., McCaffrey, R., Darby, D., 2004. Subduction zone coupling and tectonic block rotations in the North Island, New Zealand. Journal of Geophysical Research: Solid Earth (1978–2012) 109 (B12).

Wallace, R. E., 1984. Patterns and Timing of Late Quaternary Faulting in the Great-Basin Province and Relation to Some Regional Tectonic Features. Journal of Geophysical Research 89 (NB7), 5763–5769.

Weber, G. E., Nolan, J. M., Zinn, E. N., Jan. 1993. Determination of late Pleistocene - Holocene slip rates along the San Gregorio fault zone, San Mateo County, California. Tech. rep., Weber, Hayes and Associates, Watsonville, CA.

Weldon, R., Humphreys, E., 1986. A Kinematic model of southern California. Tectonics 5 (1), 33–48.

Wells, D. L., Coppersmith, K. J., Aug. 1994. New empirical relationships among magnitude, rupture length, rupture width, rupture area, and surface displacement. Bulletin of the Seismological Society of America 84 (4), 974–1002.

Wernicke, B., Davis, J. L., Niemi, N. A., Luffi, P., Bisnath, S., 2008. Active megadetachment beneath the western United States. Journal of Geophysical Research: Solid Earth (1978–2012) 113 (B11).

Williams, R. A., 2005. Seismic reflection evidence for a northeast-dipping Hayward fault near Fremont, California: Implications for seismic hazard. Geophysical Research Letters 32 (13), 301.

Williams, T. B., Kelsey, H. M., Freymueller, J. T., 2006. GPS-derived strain in northwestern California: Termination of the San Andreas fault system and convergence of the Sierra Nevada-Great Valley block contribute to southern Cascadia forearc contraction. Tectonophysics 413 (3-4), 171–184.

Wiseman, K., Bürgmann, R., Feb. 2011. Stress and Seismicity Changes on the Sunda Megathrust Preceding the 2007 Mw 8.4 Earthquake. Bulletin of the Seismological Society of America 101 (1), 313–326.

Yabuki, T., Matsu'ura, M., 1992. Geodetic data inversion using a Bayesian information criterion for spatial distribution of fault slip. Geophysical Journal International 109 (2), 363–375.

Yagi, Y., Kikuchi, M., Nishimura, T., 2003. Co-seismic slip, post-seismic slip, and largest aftershock associated with the 1994 Sanriku-haruka-oki, Japan, earthquake. Geophysical Research Letters 30 (22).

Yamanaka, Y., Kikuchi, M., 2004. Asperity map along the subduction zone in northeastern Japan inferred from regional seismic data. Journal of Geophysical Research 109 (B7), 307.

Yao, H., Gerstoft, P., Shearer, P. M., Mecklenbräuker, C., 2011. Compressive sensing of the TohokuOki Mw 9.0 earthquake: Frequencydependent rupture modes. Geophysical Research Letters 38 (20).

Yokota, Y., Koketsu, K., Fujii, Y., Satake, K., Sakai, S., Shinohara, M., Kanazawa, T., 2011. Joint inversion of strong motion, teleseismic, geodetic, and tsunami datasets for the rupture process of the 2011 Tohoku earthquake. Geophysical Research Letters 38 (7).

Yu, E., Segall, P., 1996. Slip in the 1868 Hayward earthquake from the analysis of historical triangulation data. Journal of Geophysical Research: Solid Earth (1978–2012) 101 (B7), 16101–16118.

Yue, H., Lay, T., 2011. Inversion of highrate (1 sps) GPS data for rupture process of the 11 March 2011 Tohoku earthquake (Mw 9.1). Geophysical Research Letters 38 (7).

Zebker, H. A., Rosen, P. A., Goldstein, R. M., Gabriel, A., Werner, C. L., 1994. On the Derivation of Coseismic Displacement-Fields Using Differential Radar Interferometry - the Landers Earthquake. Journal of Geophysical Research 99 (B10), 19617–19634.